MULTIPLE MINERALIZATION EVENTS IN THE ZACATECAS Ag-Pb-Zn-Cu-Au DISTRICT, AND THEIR RELATIONSHIP TO THE TECTONOMAGMATIC EVOLUTION OF THE MESA CENTRAL, MEXICO

by

Osbaldo Zamora Vega

A thesis submitted in partial fulfillment of the requirements for the degree of

Doctor of Philosophy

Department of Earth and Atmospheric Sciences

University of Alberta

Abstract

Mineralization in the Zacatecas district is polymetallic (Ag, Zn, Pb, Cu, and Au) and occurs as skarn-type and epithermal veins formed in different metallogenetic stages. The oldest mineralization in the district is skarn-type, Cu-rich with lesser Zn-Pb-Ag, and is considered to be close in age to felsic dikes and plugs dated at ~51 Ma. Epithermal mineralization is present as both low- and intermediate-sulfidation deposits. Intermediate-sulfidation veins (the Veta Grande, Mala Noche, El Bote, and La Cantera veins) are polymetallic, Ag-rich, hosted in ESE- to SE-striking structures, and were formed at 42.36 ± 0.18 Ma ($^{40}Ar/^{39}Ar$ adularia isochron age; 2σ; MSWD = 0.76). The low-sulfidation system (El Orito) is Au-rich with minor silver, and lacks base metal sulfides; it is hosted by predominantly N–S-trending structures and was formed at 29.19 ± 0.20 Ma ($^{40}Ar/^{39}Ar$ adularia isochron age; 2σ; MSWD = 1.8), which indicates that these two styles of epithermal mineralization are temporally unrelated.

The skarn-type and intermediate-sulfidation mineralization is broadly coeval with Eocene subduction-related magmatism in the Zacatecas area, which is constrained by zircon U-Pb ages for igneous rocks between 51–42 Ma. The emplacement of these magmas was controlled by the same regional-scale, ESE- to SE-trending, transtensional structures that controlled the skarn-type and intermediate-sulfidation deposits. This mineralization is thus interpreted to be related to the last stages of subduction-related volcanism in central Mexico, under neutral to mildly extensional stress conditions. In contrast, no nearby magmatism is clearly related to the Oligocene low-sulfidation system. However, its age and structural orientation (N–S), combined with a regional change in magma composition from Eocene calc-alkaline to Oligocene bimodal volcanism in central Mexico, suggest that the low-sulfidation mineralization is related to post-

subduction continental extension processes, reflecting the beginning of Basin and Range tectonics.

The mineral paragenesis of the Mala Noche deposit consists of early skarn-type Cu mineralization overprinted by later epithermal Pb-Zn-Ag veins. Skarn-type minerals include relicts of prograde silicate minerals (diopside, hedenbergite, and garnet), retrograde silicate minerals (ilvaite, grunerite, stilpnomelane, epidote, clinochlore), and ore minerals (chalcopyrite, pyrite, sphalerite, galena, magnetite, wolframite, and minor bismuthinite). Epithermal mineralization is characterized by layered to vuggy quartz veins and breccias, with variable amounts of base metal sulfides (sphalerite, galena, pyrite, minor chalcopyrite, and rare acanthite and stromeyerite) intergrown with quartz, calcite, dolomite, and ankerite. Fluid inclusion and stable isotope data, combined with mathematical modelling, indicate that ore formation, was caused by a magmatic fluid (~340°C, ~14 wt.% NaCl eq., $\delta^{18}O$ = +5 to +8 ‰), which boiled and mixed with isotopically exchanged, moderately saline ground water (~150°C, ~4 wt.% NaCl eq., $\delta^{18}O$ = +0.9 to +2.9).

The Veta Grande mineralization was emplaced in two main stages of Ag-rich quartz veining. Stage I consist of pyrite, followed by sphalerite, galena, and lesser chalcopyrite, acanthite, pyrargyrite, and jamesonite, intergrown with quartz, calcite, and scarce adularia. Fluids from stage I (180°–260°C, 6–10 wt.% NaCl eq., $\delta^{18}O$ = +2 to +2.8‰) are interpreted to be isotopically exchanged formation waters that boiled during ascent and depressurization. Stage II mineral paragenesis is similar to stage I but contains less sulfides, shows supergene alteration, and is characterized by amethystine quartz. Stage II fluids are of bimodal composition (6–13 and <1 wt.% NaCl eq.) and show a wide range of homogenization temperatures (150°–280°C). Ore

minerals are interpreted to have precipitated by boiling of the hot and saline, possibly magmatic fluid, end member (~320°C, ~13 wt.% NaCl eq., $\delta^{18}O$ = +4.6 to +10.1 ‰).

The ore mineral paragenesis of the El Compas vein, which represents the El Orito System, consists of scarce pyrite followed by aguilarite, naumannite, electrum, and native gold with a gangue of quartz, adularia, calcite, and chalcedony. This mineralization was deposited in a single stage from a dominantly meteoric fluid boiling at a temperature of ~210°C, and with a salinity of <1 wt.% NaCl eq., and $\delta^{18}O$ = -1.4 and +3.1 ‰.

Preface

This thesis is the result of a research conducted by Osbaldo Zamora Vega under the supervision of Professor Jeremy Richards in the Department of Earth and Atmospheric Sciences at the University of Alberta. This an original work except were references are made to previous work. I collected all the samples during field visits to the Zacatecas area in 2009, 2010, and 2015. Dr. Jeremy Richards contributed to data interpretation and edited the manuscript. Terry Spell conducted the $^{40}Ar/^{39}Ar$ isotopic analysis at the Nevada Isotope Geochronology Laboratory, University of Nevada. Andrew Dufrane conducted the U-Pb analysis at the Radiogenic Isotope Facility, University of Alberta. Richard Stern directed the cathodoluminescence and in-situ oxygen isotope analyses at the Canadian Centre for Isotopic Microanalysis and Karlis Muehlenbachs the BrF_5 oxygen isotope analyses at the stable isotopes research laboratory, University of Alberta. Daniel Moncada contributed to RAMAN and LA-ICPMS analyses at the Fluids Research Laboratory, Virginia Tech University. Mark Reed and Jim Palandri provided the software CHIM-XPT, SOLVEQ, GEOCAL, and MINTAB, and contributed to the mathematical modeling of chemical processes.

To the memory of my father, †Jose Refugio Zamora Mendez “Don Cuco” (1927 – 2013).

Acknowledgments

The author would like to thank North Country Gold for financing this research project, and especially to John Williamson for his encouragement to develop and complete this project. Thanks to Adrienne Ross, Peter Kleespies, and Simeon Robinson for their support at the beginning of my program. The Society of Economic Geologist Canada Foundation also provided partial financial support for fieldwork through a student research grant. Thanks to Consejo Nacional de Ciencia y Tecnologia for the scholarship No. 305391 granted to Osbaldo Zamora Vega. I would like to thank Capstone Gold, Oro Silver Resources, and Mr. Jose Parga for access to drillcore and underground sampling. Mineral separation was done with the help of Mark Labbe and at the University of Alberta facilities. Thank you very much to Carlos Linares for his help doing preliminary microprobe analyses at the National University of Mexico. Many thanks to Mark Reed and Jim Palandry for their warm welcoming to the University of Oregon and their training and support using the different software applied for geochemical modeling.

I would like to thank the members of my thesis committee, Karlis Muehlenbachs, Sarah Gleeson, and Tom Chacko for trusting on me, and especially to my supervisor Jeremy Richards for his patience on guiding me to conclude this work satisfactorily. Thank you very much to Rob Bodnar for his kind welcoming to the VT Fluid Research Lab.

Thanks to Miguel Morales-Gamez, Rares Bistran, Andreas Enggis and Meg, Ali Imer, Mary Borrero, Guadalupe Maldonado, Gideon Lambiv and Nelson Bernal for the memorable times together.

Finally, my heart goes to Laura, Nadia, and Monserrat, my wife and daughters. Thanks for walking along with me this long and tough path. *"Though the mountains be shaken and the hills be removed, yet my unfailing love for you will not be shaken" (Isaiah, 54:10).*

Table of Contents

List of Tables

List of Figures

1. Introduction

Mexico has been one of the largest primary silver-producing countries in the world for more than five centuries, with historic production from 1521 to 2008 amounting to over 283 million kg of silver and almost 2 million kg of gold (Clark and Fitch, 2009). The known silver mineralization of Mexico surpasses the rest of the world (Fig. 1; Gemmel, 2009). In 2016, Mexico led the world's silver production with 5.3 million kg of silver (http://www.silverinstitute.org/production.php, visited in December 2017). Zacatecas is the most important Ag mining state within Mexico, and accounted for 45% of that production. This study is focused on the Zacatecas mining district, which for more than three centuries (1548–1900) ranked as the third most important silver producing district in Mexico (Ponce and Clark 1988).

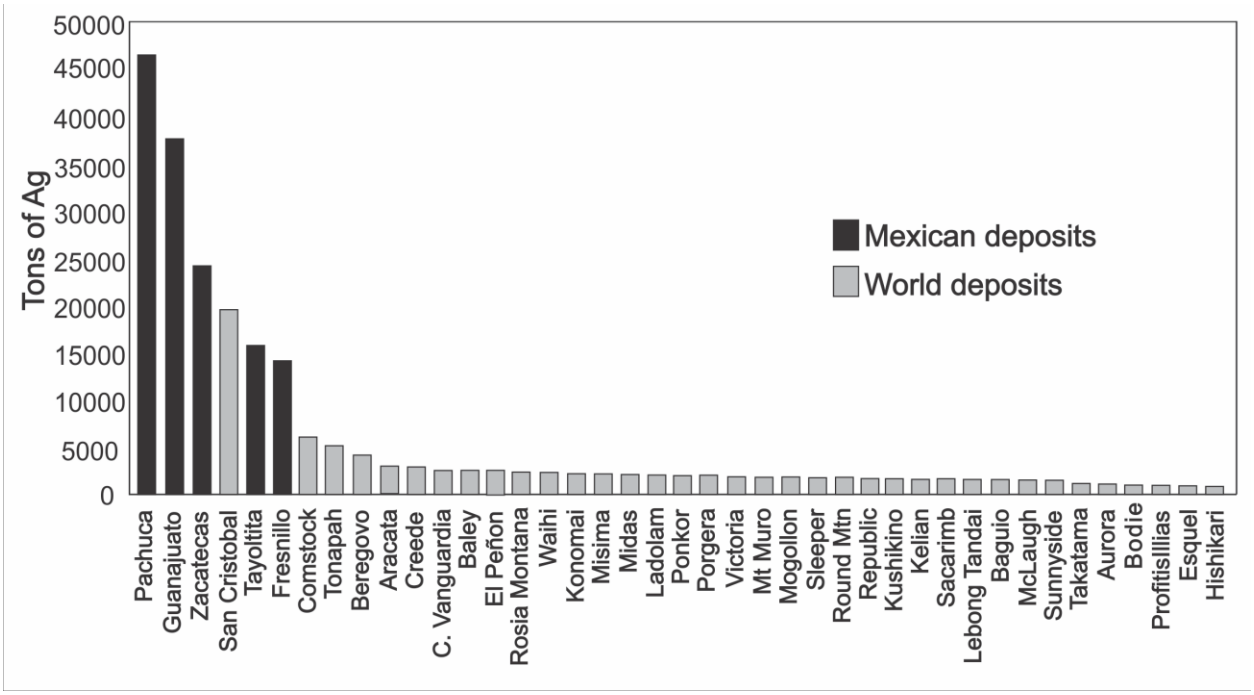

Figure 1. Metric tonnes of Ag contained in 41 of the world's most important silver deposits known up to 2009 (Gemmel, 2009).

The Zacatecas district lies within the Mexican Silver Belt, which constitutes the largest silver province in the world. Silver mineralization occurs mainly in epithermal veins, with lesser amounts in related skarn and manto-type replacement bodies. Consequently, epithermal deposits are a major target for precious metal exploration, and understanding their evolution and links with associated intrusive and volcanic rocks is crucial for the development of exploration guides.

Epithermal gold and silver deposits have been classified as high-, intermediate-, and low-sulfidation types based on the sulfidation states of the observed hypogene sulfide assemblages (Hedenquist et al., 2000; Sillitoe and Hedenquist, 2003). The defining characteristics of each epithermal style have been related directly to their magmatic roots within specific volcanotectonic settings. The distance from hypothetical source plutons and interactions with the country rock have also been invoked to explain the differences in chemistry of the ore-forming fluids from different epithermal styles of mineralization (Simmons et al., 2005; Camprubi and Albinson, 2007).

Previous studies have documented spatial, and in some cases, genetic relationships between intermediate- and high-sulfidation epithermal deposits, and underlying porphyry-type deposits (Sillitoe, 1999; Hedenquist et al., 2000). Other studies have shown that there is a transition from one type to another (Einaudi et al., 2003). In contrast, low-sulfidation epithermal deposits are generally not considered transitional to intermediate- or high-sulfidation epithermal systems, because they are largely formed in distinct tectonic settings, and are less clearly related to magmatism (Hedenquist et al., 2000; John, 2001; Sillitoe and Hedenquist, 2003). However, Camprubi and Albinson (2007) noted that several of the Mexican deposits have characteristics of both intermediate- and low-sulfidation mineralization styles and, therefore, cannot be classified straightforwardly within the scheme proposed by Hedenquist et al. (2000). Camprubi and

Albinson (2007) therefore proposed a new empirical classification scheme for the Mexican deposits based on their depth of formation with respect to the paleo-water table as determined by fluid inclusion studies (Albinson et al., 2001). This scheme considers three types of deposit (A, B, and C): type A was formed at greater depths (>1000 m) from relatively high-salinity brines, and displays only intermediate-sulfidation characteristics; type B was formed at intermediate depths (400–1000 m), and displays combined characteristics of intermediate- and low-sulfidation mineralization; type C exhibits only low-sulfidation characteristics and was formed at shallow depths (<500 m) from dilute fluids. Under this scheme, the Zacatecas, Guanajuato, and Fresnillo ore deposits are classified as type B. The concurrence of intermediate- and low-sulfidation characteristics within a district and even within a single vein was explained by Camprubi and Albinson (2007) as reflecting a transition from one mineralization style to the other, due to progressive neutralization of the mineralizing fluids by chemical reactions with country rocks.

The Zacatecas district hosts both low- and intermediate-sulfidation deposits, which are spatially related to each other. Based on this fact, and on whole rock K-Ar dates of different veins from the Zacatecas district, Camprubi and Albinson (2007) proposed that the Zacatecas district represents a single prolonged hydrothermal system, which evolved from an intermediate-sulfidation state (Mala Noche and stage I of the Veta Grande vein systems) to a low-sulfidation state (El Orito vein system and stage II of the Veta Grande vein). This model implies that both intermediate- and low-sulfidation systems were formed under the same tectonic regime, and differs from the model developed for the Great Basin metallogenic province in the southwestern USA, where intermediate- and low-sulfidation mineralization have been related to separate calc-alkaline magmatic arc and extensional tectonics, respectively (John, 2001; Sillitoe and Hedenquist, 2003). In contrast, in this study we use $^{40}Ar/^{39}Ar$ dating of adularia from the Veta

Grande and the El Compas (El Orito system) veins, and U-Pb dating of zircons from associated subvolcanic rocks to show that there are different ages of mineralization in the Zacatecas district that may be linked to the tectonomagmatic evolution of the Mesa Central.

This study has two main objectives: (1) to test the hypothesis that the different mineralization styles in the Zacatecas district were formed at different times and are associated with specific tectonic stress regimes; and (2) at a local scale, to contribute to the understanding of the geochemical and temporal evolution of the hydrothermal fluids, and the mechanisms of precipitation of ore minerals in the Zacatecas mining district.

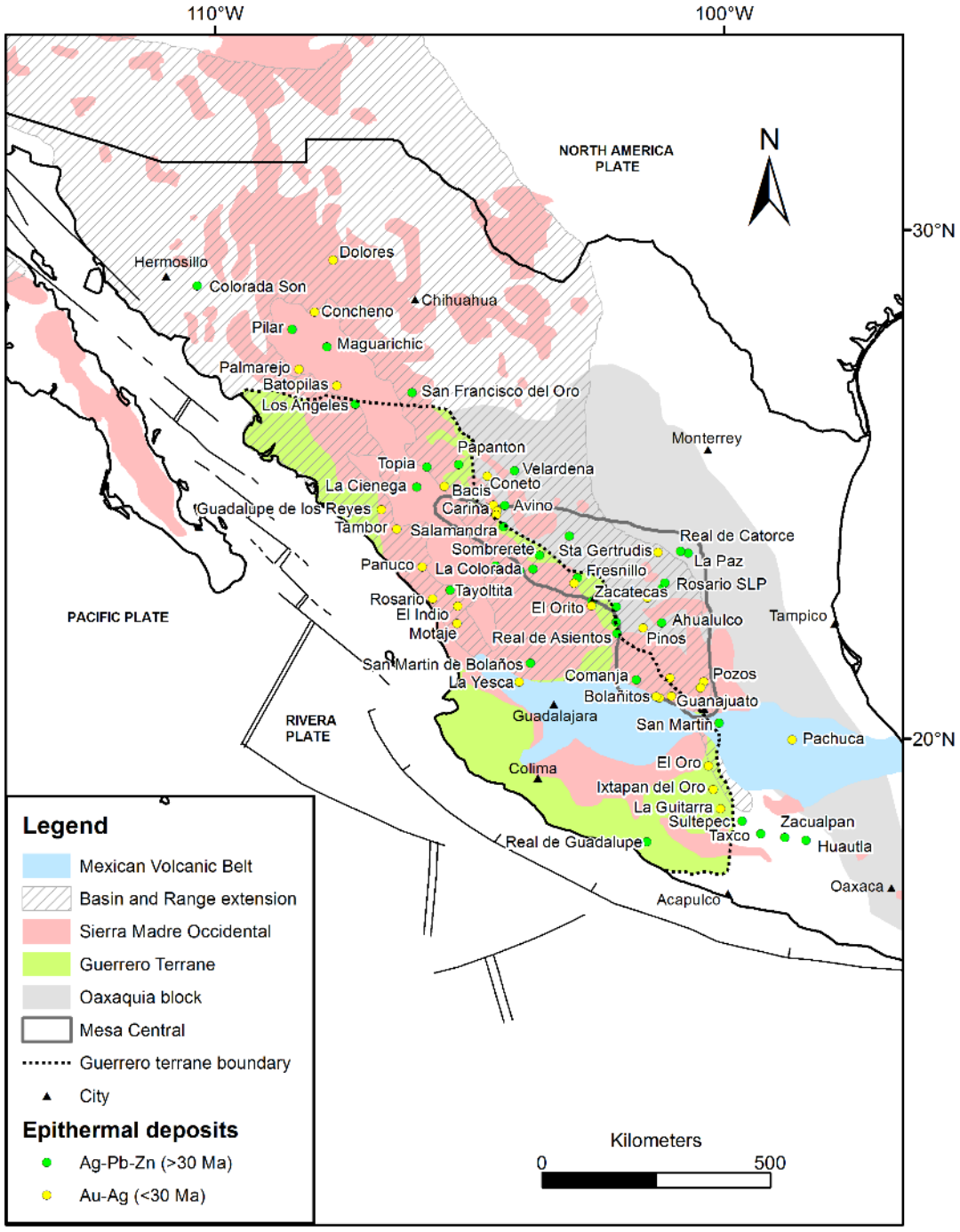

Figure 2. Geology of northern Mexico showing epithermal deposits of the Mexican Silver Belt, key terrane boundaries, and Basin and Range extension with associated mid-Cenozoic rhyolites of the Sierra Madre Occidental (based on maps from Ortega-Gutiérrez et al., 1995; Albinson et al., 2001; Ferrari et al., 2002, 2007; Aguirre-Diaz and Labarthe- Hernandez, 2003; Nieto-Samaniego et al., 2007).

2. Regional Geodynamic Setting

The Zacatecas mining district lies on the western border of the Mesa Central physiographic province (Fig. 2). The Mesa Central is an elevated plateau located in central Mexico. It is bounded to the south by the Mexican Volcanic Belt and partially overlaps the Sierra Madre Occidental. The Sierra Madre Occidental formed during the Cretaceous–Miocene as a result of magmatic and tectonic events related to the subduction of oceanic crust (Farallon plate) beneath the North American continent, and intracontinental Basin and Range extension (Ferrari et al., 2007). Eocene–Oligocene mineralization in the Zacatecas district is located within the western part of the Mesa Central, and is closely linked to the tectonic evolution of this region.

The basement in the western part of the Mesa Central consists of volcano-sedimentary successions of the Guerrero terrane. The Oaxaquia block underlies the eastern part of the Mesa Central (Fig. 2). The western limit of this block represents the early Mesozoic continental margin of Mexico (Ortega-Gutiérrez et al., 1995; Keppie et al., 2003; Centeno-García et al., 2008). Siliciclastic turbidites derived from the paleocontinent formed the basement of the Guerrero terrane in the Triassic. This siliciclastic sequence was deformed and metamorphosed to greenschist facies during the first accretion of the Guerrero terrane to the continent in the Early Jurassic (Fig. 3; Centeno-García, 2005; Centeno-García et al., 2008, 2011). The Zacatecas Formation is part of this sequence. In the Middle–Late Jurassic, continental-arc subvolcanic rocks, red beds, and shallow-marine limestone were deposited unconformably on the crystalline basement of Oaxaquia (Jones et al., 1995; Barboza-Gudiño et al., 2004). In the Late Jurassic–Early Cretaceous, rifting of the back-arc basins produced partial detachment of the previously accreted Guerrero terrane, and volcano-sedimentary successions along with volcanogenic massive sulfides were deposited in fringing basins (Centeno-García et al., 2011). The units that

represent this event in the Zacatecas district are described below as volcano-sedimentary rocks. Some of these volcano-sedimentary sequences, which are part of the Guerrero terrane, have been dated between 157.4 ± 4.1 and 139.7 ± 2.5 Ma (U-Pb on zircon; Mortensen et al., 2008). These volcano-sedimentary successions were finally accreted to the paleocontinental margin during the Late Cretaceous in a compressional arc tectonic setting (Fig 3; Centeno-García, 1993; Talavera-Mendoza et al., 1995; Centeno-García and Silva-Romo, 1997; Centeno-García et al., 2008, 2011). The alternating stages of subduction-collision and rifting produced structurally weak planes that may have served as channels for Eocene magma ascent and the flow of hydrothermal fluids.

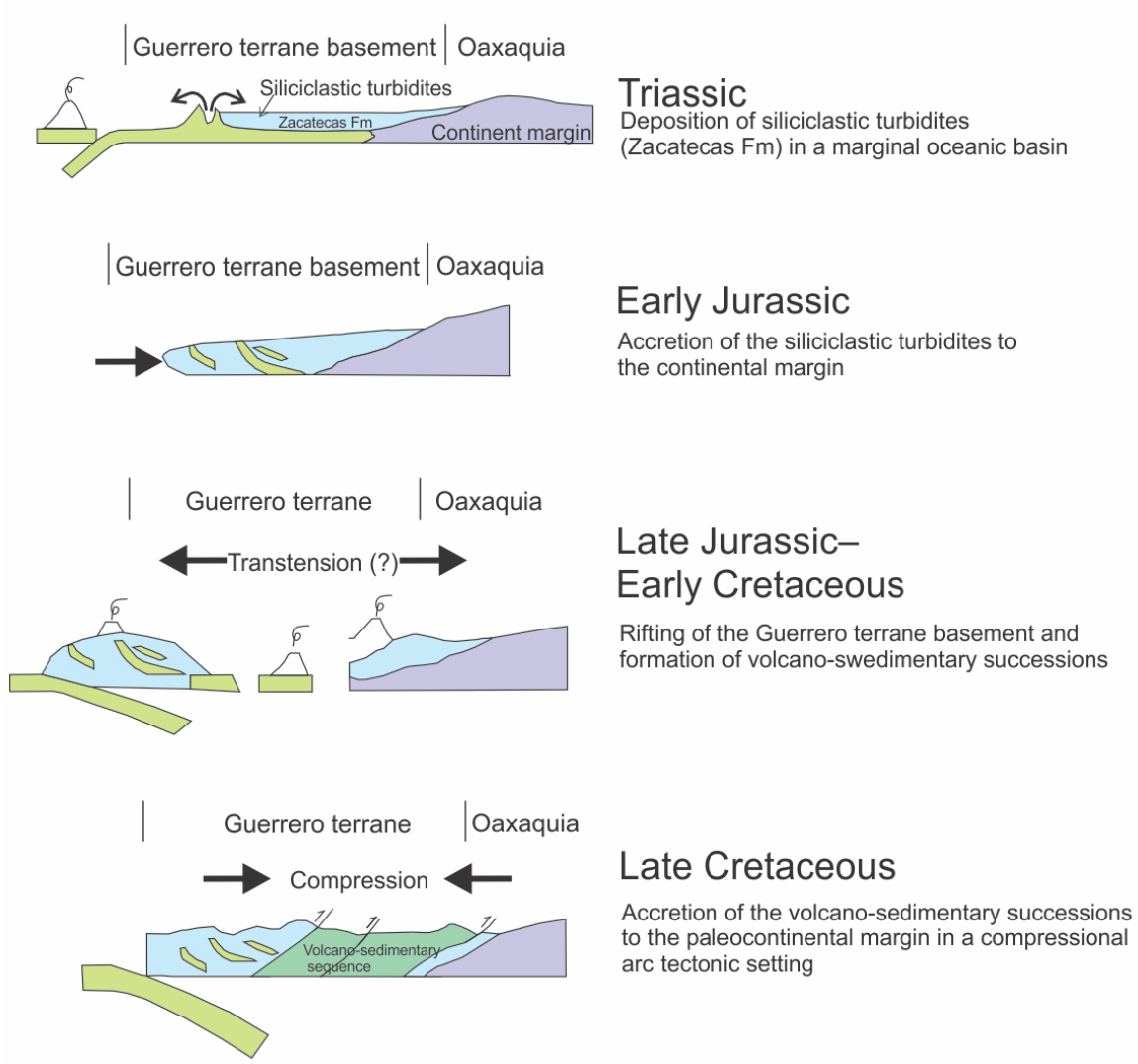

Figure 3. Tectonic model for the evolution of the Guerrero Terrane (Modified from Centeno et al., 2008)

Eocene clastic sedimentary and volcanic rocks overlie the Mesozoic basement in southern and western areas of the Mesa Central. Eocene–Oligocene mineralization in the Zacatecas district is located within the Guerrero terrane and is closely related in space and time with the tectonic evolution of the Eocene units. The Tertiary tectono-magmatic history of the Mesa Central has been elucidated based on relationships between sedimentation, faulting, magmatism, and volcanism (Edwards, 1955; Diaz and Labarthe-Hernandez, 2003; Nieto-

Samaniego et al., 2005, 2007; Aranda-Gomez, 2007; Aguillon-Robles et al., 2009; Tristan-Gonzalez et al., 2009). A brief description is given below of the sequence of volcano-tectonic and structural events that took place in the Mesa Central, from Late Cretaceous to Oligocene.

2.1 Late Cretaceous–Early Cenozoic (Laramide Orogeny)

The final accretion of the Guerrero terrane to the Mexican continental margin took place during the Late Cretaceous–early Cenozoic as part of the Laramide orogeny, and caused deformation and eastward shortening of the epicontinental Mesozoic sequences (Fig. 3; Centeno-García, 1993; Talavera-Mendoza et al., 1995; Centeno-García and Ortega-Gutierrez, 2007; Centeno-García et al., 2008). The mechanism most commonly invoked to explain the Laramide deformation is flattening of the subducting Farallon slab beneath the North American plate (Coney and Reynolds, 1977; Dickinson and Snyder, 1978; Humphreys et al., 2003). Flattening of the subducting slab caused migration of the volcanic arc towards the east under a compressional arc stress regime between 80 and 45 Ma (Coney and Reynolds, 1977; Damon et al., 1981; Clark et al., 1982; Ferrari, 2003; Ferrari et al., 2007).

The timing of the end of the Laramide compression in northern Mexico and the Mesa Central has been constrained by K-Ar and $^{40}Ar/^{39}Ar$ ages of undeformed intrusive rocks to between 55 and 43 Ma (Butler, 1972; Mujica-Mondragon and Jacobo-Albarran, 1983; Stein et al., 1993; Aranda-Gomez et al., 2007; Sole et al., 2007; Tristan-Gonzalez, 2008; Tristan-Gonzalez et al., 2009). The El Peñón Blanco granite dated by the $^{40}Ar/^{39}Ar$ method on muscovite (50.94 ± 0.47 Ma; Aranda-Gomez et al., 2007) is the example nearest to the Zacatecas district (~100 km SE). At the end of this orogenic period, a change from compressional to tensional stress occurred in Mexico, likely due to a return to steep subduction with a resultant westward

shift of arc magmatism (Damon et al., 1981; Clark et al., 1982; McDowell et al., 1989; Atwater, 1990; Aguirre-Díaz and McDowell, 1991; Nieto-Samaniego et al., 1997; Aranda-Gomez and McDowell, 1998; Aranda-Gómez et al., 2000).

2.2 Eocene Continental Sedimentation and Volcanism (Transitional Tectonics)

Sedimentary basins associated with normal and/or strike-slip faults were developed throughout central and southern Mexico during the Eocene after the end of the Laramide orogeny as a result of the change in stress regime (Fig. 4; Edwards, 1955; Aranda-Gomez and McDowell, 1998; Aranda-Gomez et al., 2007; Tristan-Gonzalez, 2009). These basins were filled with detritus eroded from basement rocks, granites, and volcanic rocks to produce red-bed conglomerates.

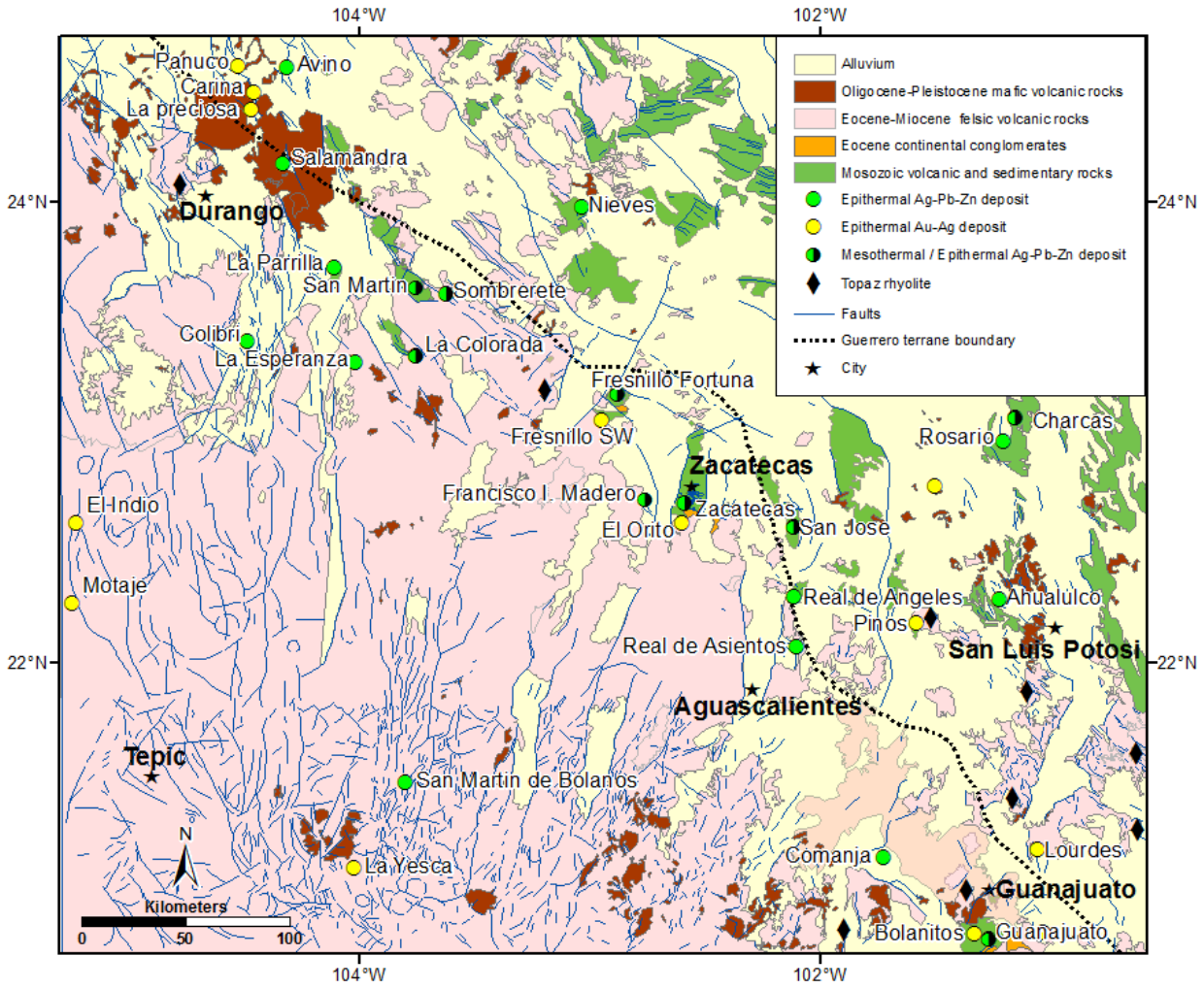

Figure 4. Map of central Mexico showing the distribution of Eocene red-bed conglomerates, combined mesothermal - epithermal deposits, topaz-bearing rhyolites (32–27 Ma), and grabens and NNE- and NNW-trending normal faults related to Basin and Range extension. Mesothermal deposits include skarn-, chimney-, and manto-type deposits.

The presence of clasts of Laramide-type granite in these conglomerate sequences confirms that exhumation and denudation happened after the end of the compressional regime (Edwards, 1955; Aranda-Gomez et al., 2007). These conglomerates have been interpreted to be fanglomerates deposited near normal faults, and related to the first period of extension immediately after the Laramide orogeny (Edwards, 1955; De Cserna and Fries, 1981; De Cserna, 1989; Yta and Moreno-Tovar, 1997; Aranda-Gómez and McDowell, 1998). According to

Tristan-Gonzales et al. (2009), the Eocene shift from compression (Laramide orogeny) to extension (Basin and Range) in the Mesa Central was separated by a period of crustal stress relaxation. Dextral strike-slip movements produced uplift of NNE-oriented ranges in the Mesa Central, and subsequent ESE- to SE-trending high-angle normal faults cut these ranges in the middle Eocene (Tristan-Gonzalez, 2008; Tristan-Gonzalez et al., 2009). These faults served as channelways for the emplacement of dikes and domes of felsic rocks, and for the formation of associated intermediate-sulfidation hydrothermal systems.

Andesitic lava flows and felsic pyroclastic rocks intercalated with red beds at different levels show that volcanism was episodic during the life of the basins. In the Guanajuato district, mafic volcanic lavas intercalated with clastic sedimentary sequences were dated at 49.3 ± 1.0 Ma (K-Ar on whole rock; Aranda-Gomez and McDowell, 1998). The oldest volcanic unit overlying the Fresnillo conglomerate has been dated at 44.73 ± 0.04 Ma ($^{40}Ar/^{39}Ar$ on sadinine; Velador et al., 2010). In the Zacatecas district, pyroclastic rocks interfingered with red bed layers on top of the conglomeratic sequence were dated at 46.8 Ma (K-Ar on biotite; Ponce and Clark, 1988; no error reported). These pyroclastic rocks were followed by effusive felsic volcanism emplaced along reactivated SE-trending faults (Tristan-Gonzalez et al., 2009). These dates are confirmed here by U-Pb zircon ages for felsic hypabyssal and volcanic rocks in the Zacatecas district ranging from 51–42 Ma (see below).

These Eocene calc-alkaline intermediate to felsic magmas appear to have been generated during the last stages of subduction of the Farallon plate beneath the North American plate, in a mildly extensional continental margin arc (Atwater, 1989; Aguirre-Díaz and McDowell, 1991; Ferrari et al., 1999; Tristan-Gonzalez et al., 2009). Early stages of skarn-type,

manto replacement, and epithermal Ag-Pb-Zn-Cu mineralization are spatially related to this magmatism and a temporal relationship is inferred.

2.3 Basin and Range

The Basin and Range province extends from the northern Rocky Mountains in the United States to the Trans-Mexican volcanic belt, and includes the Mesa Central province (Fig. 2; Henry and Aranda-Gomez, 1992; Stewart, 1998; Aranda-Gómez et al., 2000). This physiographic province is characterized by alternating NNW- to NNE-trending narrow mountain ranges and block-faulted valleys, produced by extensional tectonics that began in the Eocene or as early as Paleocene (Stewart, 1998; Aranda-Gomez et al., 2000). Extension was initiated in western North America by collision of the East Pacific spreading center with the North American plate (Atwater, 1989; Aguirre-Díaz and McDowell, 1991; Henry and Aranda-Gomez, 1992; Dickinson, 2006; Ferrari et al., 2007), which produced a change from a subduction to a transform boundary along the plate margin. During and after the waning stages of subduction, extension developed gradually and episodically with systematically different timing, style, and magnitude from one area to another along the Basin and Range province (Stewart, 1998; Aranda-Gomez et al., 2000). Stewart (1998) divided the Basin and Range province into eleven regions based on their physiographic and structural characteristics, including the Mesa Central within a region that extends from near the Mexican border with the USA to Guanajuato in central Mexico, and is structurally characterized by grabens, half grabens, horsts, and locally tilted blocks concentrated on the eastern margin of the Sierra Madre Occidental (Figs 2 and 4; Aranda-Gomez, 1989; Aranda-Gomez et al., 1989; Henry et al., 1989; Henry and Aranda-Gomez, 1992; Stewart, 1998).

The timing of the onset of Basin and Range extension in the Mesa Central has been constrained by dating of extensional hydrothermal veins and tilting, and is considered to have

started between 32 and 28 Ma (Henry and Aranda-Gomez, 1992; Aguirre-Diaz and McDowell, 1993). Late Au-rich epithermal mineralization in Zacatecas is here dated at 29.19 ± 0.20 Ma (see below), and appears to be related to the start of this extensional tectonic phase.

Magma composition also changed at this time from dominantly felsic subalkaline to felsic peraluminous and/or to bimodal styles, with the extrusion of rhyolitic and basaltic magmas along NNE- and NNW-trending normal faults related to grabens at about 29 Ma (Orozco-Esquivel et al., 2002; Rodriguez-Rios et al., 2007; Tistan-Gonzalez et al., 2009). The main bimodal volcanic events occurred between 28 and 26 Ma, but several younger pulses occurred intermittently until the Quaternary (Fig. 4; McDowell and Keizer 1977; Nieto-Samaniego et al., 2007). In the northwestern part of the Mesa Central (Durango state area), basalt lava flows coeval with rhyolitic tuff have been dated on 29 ± 0.60 Ma (McDowell and Keizer 1977), whereas in the southeastern part (San Luis Potosi state area) a rhyolite intercalated with basaltic lavas was dated at 27.6 ± 0.60 Ma (Orozco-Esquivel et al., 2002). No bimodal volcanic rocks of this age occur in the immediate Zacatecas area, but Oligocene rhyolitic and basaltic rocks have been mapped ~20 km to the southwest of Zacatecas.

Measurements of heat flow in the states of Chihuahua, Durango, and Zacatecas, which are comparable to those associated with the Rio Grande Rift anomaly in New Mexico, suggest the presence of an incipient rift in the Mesa Central (Smith and Jones, 1979). This inference is consistent with the interpretation from seismic and gravimetric studies that the crust under the Mesa Central is thinner (~8 km) than adjacent areas (Nieto-Samaniego et al., 2005).

Topaz-bearing rhyolites enriched in silica, potassium, and fluorine in the Mesa Central, have been compared with the fluorine-rich rhyolites genetically associated with the extensional regimes of the Rio Grande rift and the Basin and Range Province in western USA (Christiansen

et al., 1986; Orozco-Esquivel et al., 2002; Rodriguez-Rios et al., 2007). Topaz rhyolites in Mexico are between 32 and 27 Ma-old and are widely distributed near the eastern limit of the Sierra Madre Occidental Volcanic Province in the states of Durango, Zacatecas, and San Luis Potosí (Fig. 4; Orozco-Esquivel et al., 2002; Rodriguez-Rios et al., 2007). In the southern part of Mesa Central (San Luis Potosí and Guanajuato), eruption of effusive rhyolites geochemically similar to these topaz-bearing rhyolites recorded a change in magma composition at about 30 Ma (Orozco-Esquivel et al., 2002). This geochemical marker has allowed the distinction between lower and upper felsic volcanic sequences. The lower felsic volcanic sequence is similar to high-K felsic rocks of the eastern Sierra Madre Occidental and hypabyssal rocks of the Zacatecas district. The upper volcanic sequence is characterized by high-silica peraluminous rhyolites with strong enrichment in fluorine and lithophile elements (Rb, La, Sm, Yb, Y, Th, U, Nb, Ta), and strong depletion in Sr, Ba, and Eu (Orozco-Esquivel et al., 2002). These geochemical changes are attributed to high melting rates in the lower crust promoted by the beginning of crustal extension at high strain rates, documented for the Mesa Central at about 30–29 Ma (Christiansen et al., 1986; Orozco-Esquivel et al., 2002; Rodriguez-Rios et al., 2007; Tristan-Gonzalez et al., 2009). The low-sulfidation epithermal system in the Zacatecas district was developed within this period of time (see below).

2.4 The Mexican Silver Belt

Silver mineralization in central Mexico occurs as skarn, manto-type replacements bodies, chimney-like bodies, and epithermal veins, and is widely distributed from Sonora to Oaxaca. The systems define a ~1500 km-long NW-trending belt that includes the world-class mining districts of Zacatecas, Guanajuato, and Fresnillo along the east border of the Mesa Central (Fig. 2). The

belt includes both Ag-Pb-Zn and Au-Ag metallogenic provinces (as defined by Clark et al., 1982) and is spatially and temporally associated with the Sierra Madre Occidental volcanic province (Fig. 2; Damon et al., 1981; Clark et al., 1982; Camprubi et al., 2003; Camprubi and Albinson, 2007; Camprubi, 2009).

The Mexican epithermal deposits have been characterized based on their fluid inclusion compositions and relative metal contents, and grouped broadly into polymetallic (Ag-Pb-Zn) and Au-Ag-rich deposits (Fig. 5; Albinson et al., 2001). The Au-Ag-rich deposits are characterized by the lower salinity fluids (0 to ~7.5 wt.% NaCl eq.), whereas polymetallic deposits have fluids with higher salinities between ~7.5 and 23 wt.% NaCl eq. (Albinson et al., 2001; Camprubi and Albinson, 2007). Camprubi and Albinson (2007) classified the Au-Ag-rich deposits as type C, equivalent to low-sulfidation type according to the criteria of Hedenquist et al. (2000), and the polymetallic deposits as type A and/or B (equivalent to intermediate-sulfidation type or combined intermediate- and low-sulfidation, respectively). Under this scheme, the Zacatecas, Guanajuato, and Fresnillo ore deposits are classified as type B.

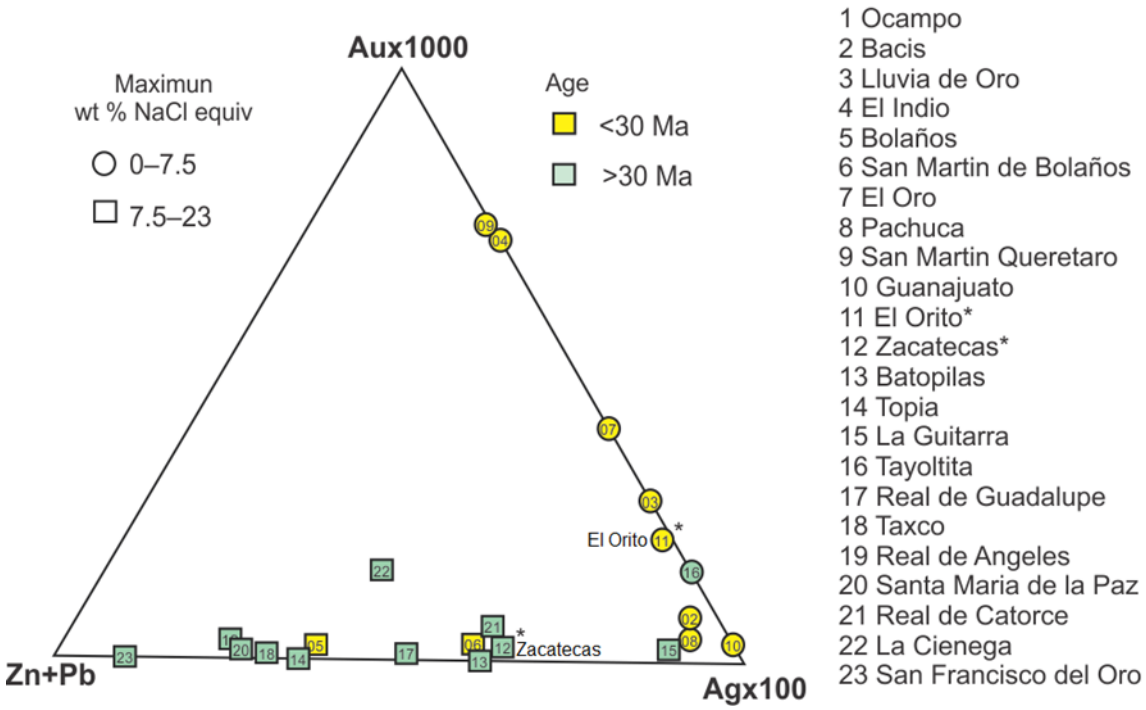

Figure 5. Relative metal contents and fluid inclusion salinities of various Mexican epithermal deposits (compositional data from Albinson et al., 2001; ages compiled by Camprubí et al., 2003, and references therein; * this study).

A compilation of ages for Mexican epithermal deposits shows that low-sulfidation Au-Ag-rich deposits are mostly younger than ~30 Ma, whereas the intermediate-sulfidation polymetallic deposits are mostly older than this age (Fig. 5; Albinson et al., 2001; Camprubi et al., 2003; this study), indicating a regional change in metallogenic style.

The formation of the various types of epithermal mineralization in Mexico has been related to periods of subduction-related, continental arc magmatism (Clark et al., 1982; Simmons, 1991; Randall et al., 1994; Camprubi et al., 2003; Camprubi and Albinson, 2007; Velador et al., 2010). Although this model fits for the polymetallic mineralization, the Au-Ag deposits appear instead to be related to later, post-subduction continental extension processes (see below).

2.4.1 Eocene Ag-Pb-Zn-Cu Mineralization

Eocene Ag-Pb-Zn-Cu mineralization in the Mesa Central occurs as skarn, chimney-, and manto-type deposits, and ESE–SE-trending epithermal Ag-Pb-Zn intermediate-sulfidation veins that locally overprint skarn-type mineralization (Albinson, 1988; Lang et al., 1988; Rubin and Kyle, 1988; Yta et al., 2003; Nieto-Samaniego et al., 2007; Pinto-Linares et al., 2008; Cannet et al., 2009). This mineralization is related to intermediate–felsic subvolcanic and intrusive bodies dated between 32 and 46.6 Ma (e.g., the San Martin, Francisco I. Madero, La Colorada, Fresnillo-Fortuna, Guanajuato, Charcas, and La Paz deposits; Fig. 4).

The San Martin skarn deposit and associated epithermal veins have been genetically related to a 46.2 ± 1 Ma quartz monzonite stock (K-Ar on biotite; Damon et al., 1983; Rubin and Kyle, 1988). Skarn-type mineralization in the La Colorada and Francisco I. Madero deposits has been related to porphyritic sills and ESE–SE-trending dikes that range in composition from diorite to tonalite, and granite (Moller et al., 2001; Cannet et al., 2009).

In the Fresnillo district, mesothermal Ag-Pb-Zn skarn and manto-type replacement bodies are related to a quartz-monzonite stock. Crosscutting relationships between the stock, manto, and veins indicate that the richer epithermal Ag-Pb-Zn veins are younger than the mesothermal deposits (De Cserna, 1976). Epithermal silver-rich mineralization has been interpreted to be formed in two separate hydrothermal pulses between 31.0 ± 0.6 and 29.1 ± 0.6 Ma (whole rock K-Ar), associated with subduction-related magmatism (Lang et al., 1988).

A similar succession of mineralizing events occurred in the Guanajuato district, starting with skarn development at 55 ± 4 Ma (K-Ar; Randall et al., 1994) related to a granite intrusion. The oldest Ag-Pb-Zn epithermal system has been dated between 30.7 ± 3 and 28.3 ± 5 Ma, and the youngest between 29.2 ± 2 and 27.0 ± 0.4 Ma (whole rock K-Ar ages; Gross, 1975).

However, these dates may not be accurate because the younger hydrothermal systems may have caused disturbance of the K-Ar system. The age of the older mineralization is probably greater than the reported age, and has been related to volcanic activity that ranges from 37.0 ± 3 to 32.1 ± 1 Ma (Gross, 1975).

Based on K/Ar dating of volcanic rocks, intrusive bodies, and hydrothermal alteration, Albinson (1988) has estimated a preferred age range of between 35 and 30 Ma for the formation of epithermal Ag-Pb-Zn mineralization in the Mesa Central.

In the Zacatecas area, previous studies have indicated ages for Ag-Pb-Zn mineralization of between 35.5 and 31.1 Ma (K/Ar, no uncertainty reported; Krueger, 2000, reported in Camprubi and Albinson, 2007). However, a new date of 42.36 ± 0.18 Ma ($^{40}Ar/^{39}Ar$ on adularia; see details below) indicates an older timing for mineralization in the area.

2.4.2 Oligocene Au-Ag Mineralization

Gold-rich mineralization in the Mesa Central occurs principally in low-sulfidation epithermal deposits. This style of mineralization occurs as Au-Ag-rich quartz veins mainly controlled by NNE–NNW-striking normal faults (e.g., Bolañitos in Guanajuato, and Pinos and El Orito System in Zacatecas; Figs. 6 and 7; Steel, 2012; Munroe, 2014). Low-sulfidation styles of mineralization also occur in paragenetically late stages of NW-striking Ag-Pb-Zn veins (e.g., Fresnillo-Southwest area; Velador, 2010), or in late NE-striking veins crosscutting Ag-Pb-Zn

intermediate-sulfidation veins at high angles (e.g., Guanajuato; Randall et al., 1994).

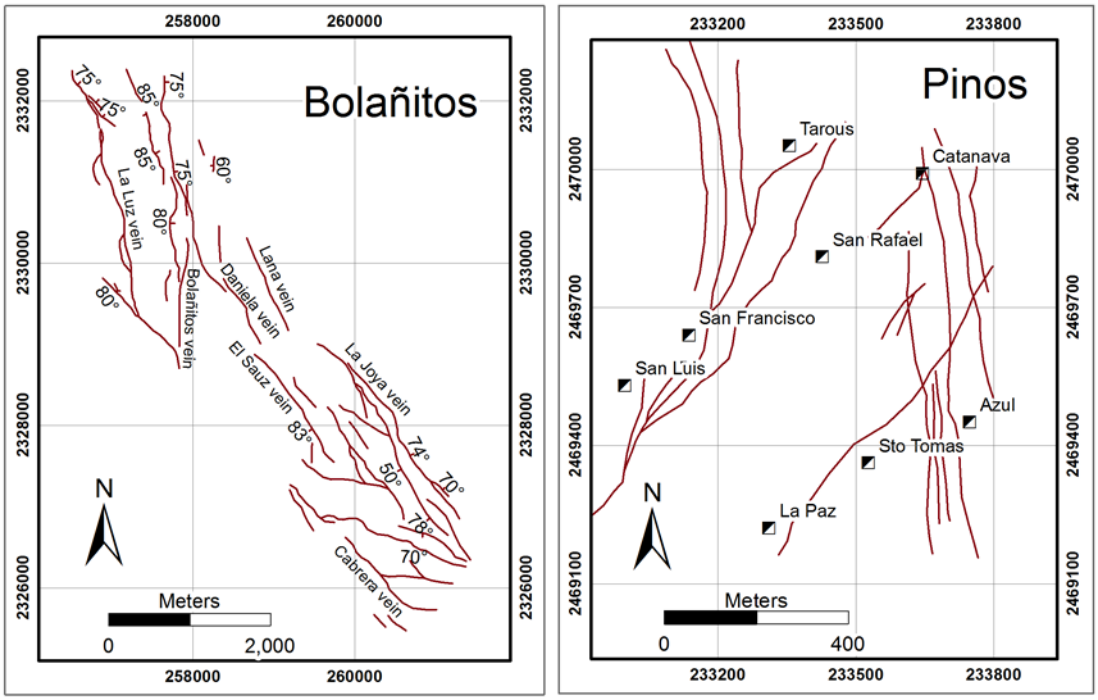

Figure 6. Maps showing veins infilling NNE- and NNW-striking normal faults in the Bolañitos (Guanajuato) and Pinos (Zacatecas) low-sulfidation deposits (modified from: Steel, 2012, and Munroe, 2014).

Radiometric ages of mineralization in the Mesa Central have been reported only from the Fresnillo, Guanajuato, and Zacatecas areas. In the Fresnillo-Southwest area, Au-Ag-rich quartz veins that paragenetically postdate the main stage of Ag-Pb-Zn mineralization have been dated at 29.75 ± 0.12 and 29.68 ± 0.10 Ma ($^{40}Ar/^{39}Ar$ on adularia; Velador, 2010; Velador et al., 2010). The youngest volcanic event in the Fresnillo district occurred at 31.04 ± 0.05 Ma ($^{40}Ar/^{39}Ar$ on sanidine; Velador et al., 2010), suggesting that the Au-Ag-rich mineralization is not temporally associated with local volcanism. In the Guanajuato district, the San Nicolas mid-Oligocene Au-Ag-rich deposit is also low-sulfidation in style; it is rich in Se-bearing minerals, electrum, and adularia, and practically devoid of base metal sulfides. The mineralization occurs in veins controlled by NE-trending normal faults, and crosscuts older SE-striking Ag-Pb-Zn veins. It is

spatially related to coeval latite and rhyolitic dikes and domes controlled by similar NE-trending structural systems (Randall et al., 1994).

In the Zacatecas area, the Au-Ag-rich low-sulfidation El Orito system was formed in predominantly N–S-striking normal faults, cross-cutting the ESE- to SE-striking strike-slip faults that controlled the Eocene Ag-Pb-Zn intermediate-sulfidation veins. Four K-Ar ages obtained from adularia-rich samples of the El Compas veins range from 26.9 ± 0.7 to 32.7 ± 0.8 (Kapusta, 2005). However, in this study, we obtained an age of 29.19 ± 0.20 Ma ($^{40}Ar/^{39}Ar$ on adularia; see details below) from one of these veins, suggesting that they in fact belong to the Oligocene metallogenetic stage.

3. Geology of the Zacatecas District

The Zacatecas mining district is located in the central part of the state of Zacatecas in central Mexico, and comprises the mineralized zones of El Orito, El Bote, La Cantera, Mala Noche, and Veta Grande (Fig. 7). Several authors have described the geology of the Zacatecas mining district since its discovery in 1546 (Burckhardt, 1906; Maldonado-Koerdell, 1948; Perez-Martinez et al., 1961; Ponce and Clark, 1988; Caballero-Martinez, 1999). The litho-stratigraphic units that crop out in the district range from Triassic to Oligocene. All of these units host epithermal vein mineralization, but the majority of veins are located in the Jurassic–Cretaceous sequence or along faulted contacts with the Zacatecas conglomerate (Fig. 7).

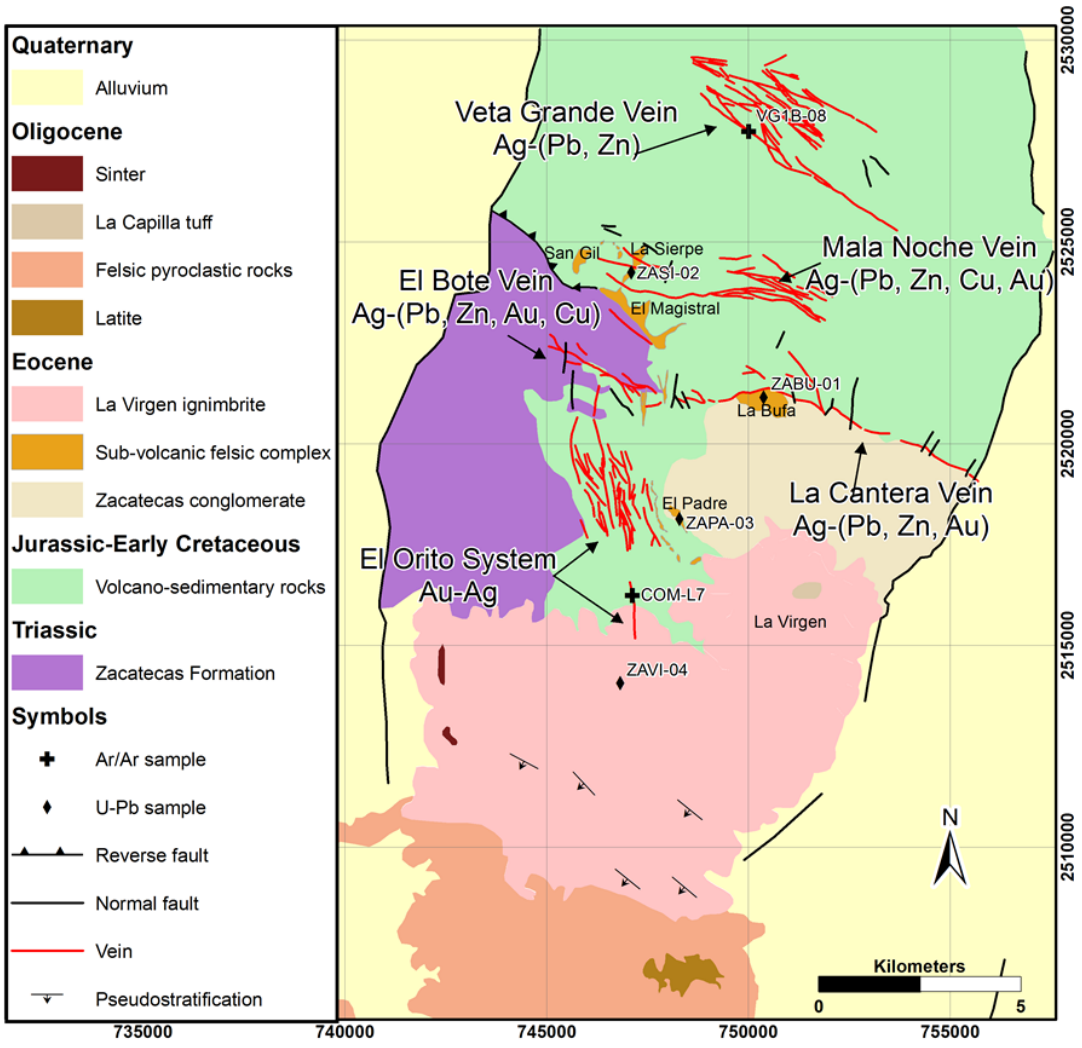

Figure 7. Geological map of the Zacatecas district showing the main vein systems and sample locations (modified from Perez-Martinez et al., 1961; Ponce et al., 1988; Mexican Geological Service maps Zacatecas F13-B58_GM, Guadalupe F13-B68_GM, and Jerez F13-B67_GM.

3.1 Triassic

The Triassic Zacatecas Formation is a clastic marine sequence, and crops out in a tectonic window near the city of Zacatecas (Fig. 7). It consists of metamorphosed (greenschist facies) pelites, sandstone, and conglomerate, with minor recrystallized limestone and basaltic pillow lavas (Fig. 8a; Ranson, 1975; Ranson et al., 1982; Centeno-Garcia and Silva-Romo, 1997).

Abundant fossil content indicates a Late Triassic (Carnian) age for this formation (Burckhardt, 1906; Maldonado-Koerdell, 1948). This formation has been interpreted to be the basement of the Guerrero terrane in the Mesa Central (Centeno-Garcia et al., 2008) and is unconformably overlain by Late Jurassic–Early Cretaceous marine volcano-sedimentary successions.

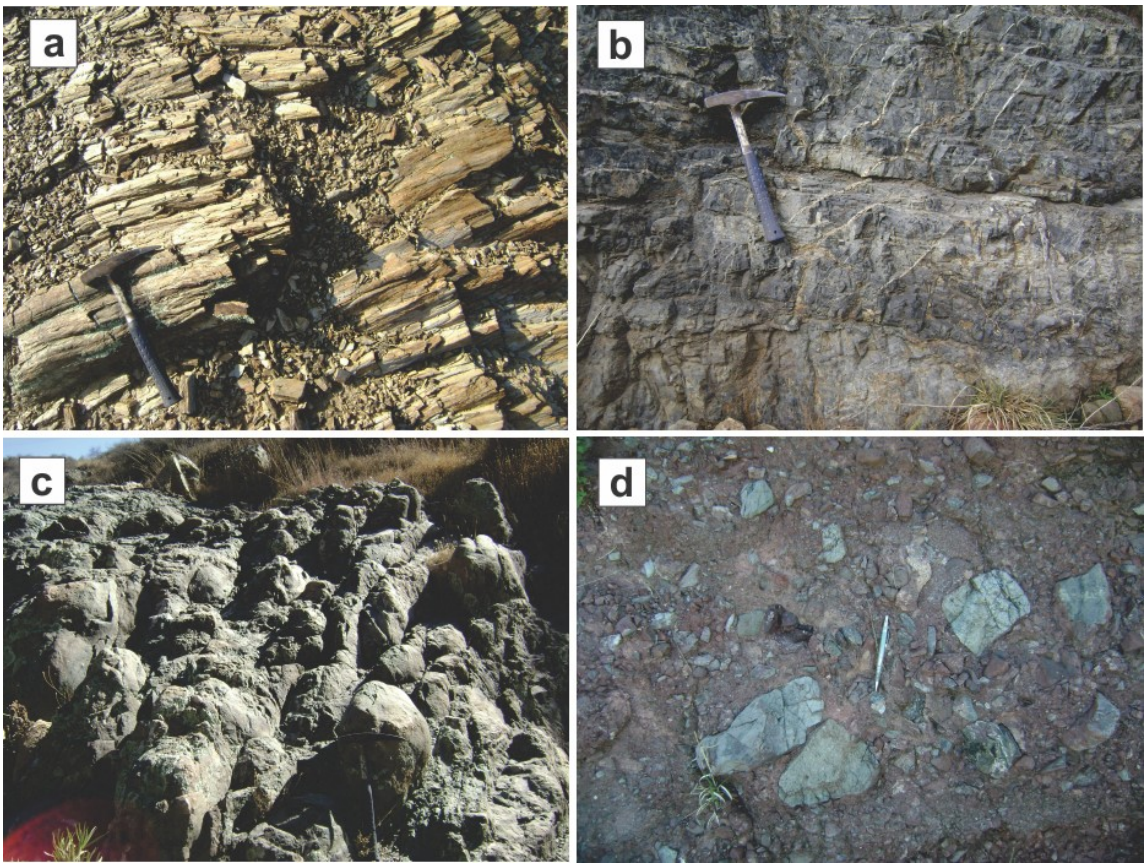

Figure 8. Photographs of Zacatecas district rocks: a) Metamorphosed clastic sediments of the Triassic Zacatecas Formation (746689E, 2523038N); Late Jurassic–Early Cretaceous volcano-sedimentary rocks b) lenses of impure limestone (747365E, 2523876N) and c) andesitic to basaltic pillow lavas (746787E, 2523891N); d) Eocene Zacatecas red conglomerate showing clasts of andesitic rocks, phyllite, and schist in a reddish sandy matrix (748466E, 2518169N).

3.2 Jurassic–Cretaceous

Late Jurassic–Early Cretaceous volcano-sedimentary rocks tectonically overlie the Zacatecas Formation (Burckhardt, 1906; Gutiérrez-Amador, 1908; Martínez-Pérez, 1961; Centeno-Garcia and Silvia Romo, 1997). These rocks consist of a sequence of andesitic to

basaltic lava flows and pillow lavas metamorphosed to greenschist facies, interstratified with marine clastic and volcaniclastic rocks, limestone lenses, and thin layers of chert (Fig. 8b–c; Centeno-Garcia and Silvia Romo, 1997). The lava flows are green in colour, and vary in texture from aphanitic to porphyritic. Porphyritic textures consist of plagioclase phenocrysts (~3mm) in a groundmass of plagioclase microlites and accessory ferromagnesian minerals including olivine, augite, rare biotite, and traces of opaque minerals. Zeolites filling amygdales are common (Fig. 9a–c). The dominant meta-sedimentary lithology of this succession is shale that ranges in colour from grey to black. The rock consists of well-compacted and homogeneous mud-sized particles commonly with very fine-grained pyrite with framboidal texture that suggest a bacterial origin (Fig. 9d–f).

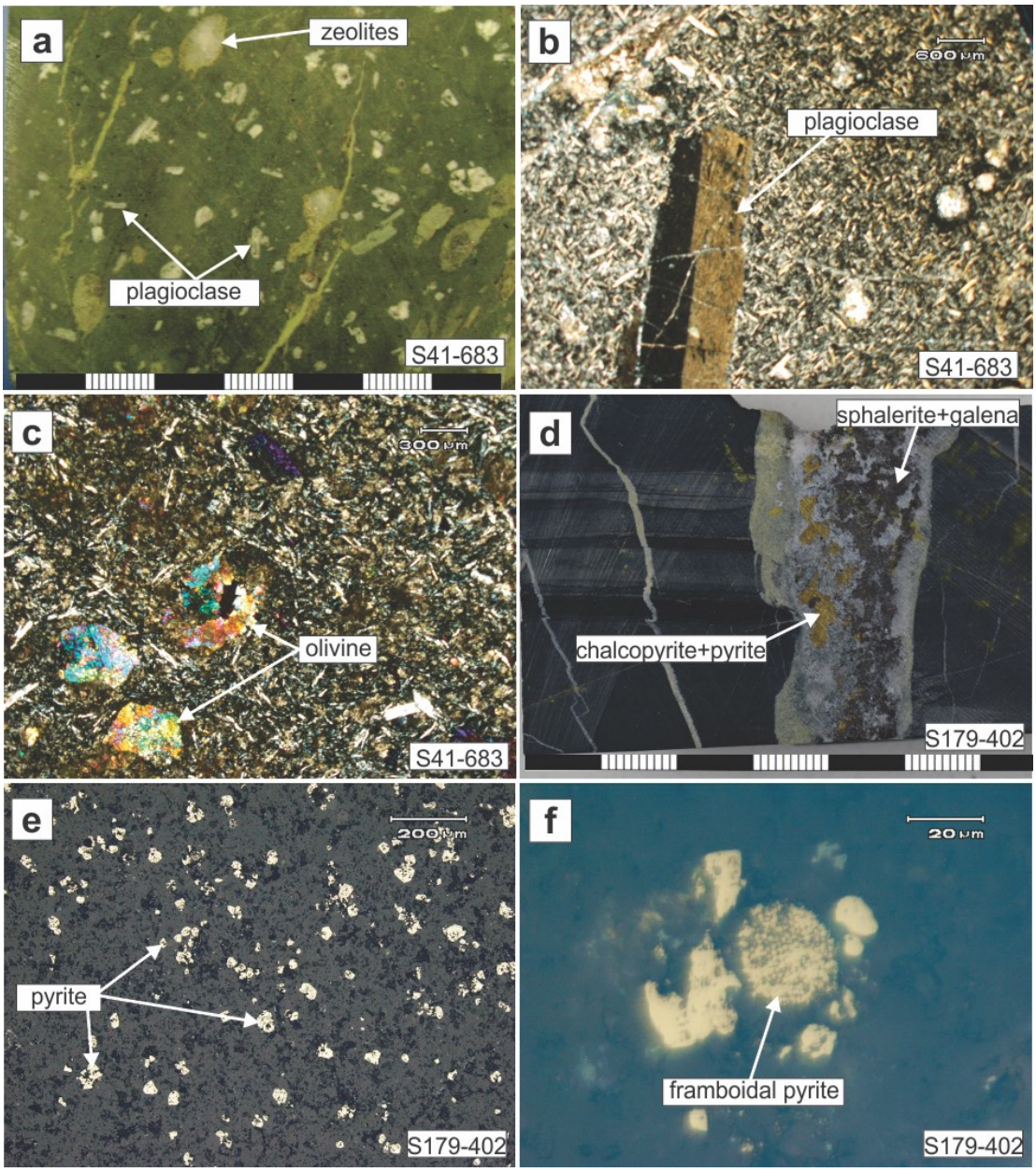

Figure 9. Hand samples and photomicrographs of representative Late Jurassic–Early Cretaceous volcano-sedimentary lithologies. (a–c) Sample of basaltic andesite (S41-683; 747355E, 2524201N) showing porphyritic texture in hand sample (a) and phenocrysts of of plagioclase (b) and olivine (c) in a groundmass of plagioclase microlites. (d) Sample of shale (S179-402; 747225E, 25242350N) showing grey and black laminations crosscut by a vein; (e) fine-grained disseminated and (f) framboidal pyrite in shale.

Some authors have interpreted the porphyritic facies of this succession as a diorite intrusion that is part of the continental Sierra Madre Occidental volcanic complex with an age of between 77 and 72 Ma (Ranson, 1975, 1982; Ponce and Clark, 1988). However, stratigraphic,

geochemical, and age correlations between the Jurassic–Cretaceous volcano-sedimentary rocks of the Zacatecas district and other successions at different localities in the State of Zacatecas (Fresnillo, La Borda, El Saucito) have established that this unit was deposited in a back-arc tectonic setting and is part of the Guerrero terrane (De Cserna, 1976; Lapierre et al., 1992; Centeno-Garcia and Silva-Romo, 1997).

3.3 Eocene Sedimentary Rocks

The Eocene Zacatecas conglomerate unconformably overlies the Mesozoic rocks in the Zacatecas district (Edwards, 1955). It is a polymictic conglomerate containing ~60% pebbles of basaltic-andesitic lava, with the remainder comprised of phyllite, schist, slate, sandstone, limestone, felsic volcanic rocks, and granite, in a reddish sandy matrix (Fig. 8 d). The fragments are rounded to subrounded and range in size from 3 to 30 cm. Blocks up to 1.5 m across have been reported at the top of this unit (Caballero-Martinez, 1999).

The Zacatecas conglomerate has been correlated with other red bed sequences that crop out elsewhere in central and southern Mexico (Edwards, 1955; Aranda-Gomez and McDowell, 1998; Aranda-Gomez et al., 2007; Tristan-Gonzalez et al., 2009). Although not necessarily coeval, these conglomerates are interpreted to have been deposited under similar subaerial conditions, and as a result of the same sequence of geological events: uplift, extensional faulting, erosion, and volcanism after the end of the Laramide orogeny in central Mexico (Edwards, 1955; Aranda-Gomez and McDowell, 1998; Aranda et al., 2007; Tristan-Gonzalez et al., 2009).

3.4 Eocene Igneous Rocks

Eocene volcanism in the Zacatecas district is part of the voluminous igneous activity of the Sierra Madre Occidental silicic province (Aguirre-Diaz and Labarthe–Hernandez 2003). Rhyolitic ignimbrites, lava domes, plugs, and dikes unconformably overlie or intrude older rocks. Magmatism spanned a ~9 m.y. time period from 50.8 to 41.7 Ma (see below).

The oldest event is a complex of rhyolitic plugs and dikes spatially associated with the Mala Noche vein system, and includes the San Gil and La Sierpe plugs and dikes (which intrude the Jurassic–Cretaceous volcano-sedimentary sequence) and the El Magistral plug (which is emplaced along the contact between the Jurassic–Cretaceous volcano-sedimentary sequence and the Zacatecas Formation). The rhyolites are pale gray to whitish in color and vary in texture from aphanitic with flow banding and aligned xenoliths to porphyritic at deeper levels (Fig. 10a–b). The main phenocrysts are 1–7% of euhedral quartz and plagioclase (~1 mm in size) and minor euhedral biotite (1–3 mm in size) set in a devitrified matrix commonly with disseminations of very fine-grained pyrite (Fig. 10b and 11b). Quartz shows rounded and embayed textures indicating partial resorption during rise of the magma. Plagioclase shows moderate sericitic alteration and biotite is oxidized (Fig. 11b).

Both magmatic and hydrothermal breccias are observed in dikes. Magmatic breccias are located close to the contact with the volcano-sedimentary succession, are barren, and show globular peperitic texture (Busby-Spera and White, 1987) that consists of rounded and lobate clasts of grey to white porphyritic rhyolite in a matrix of black fine-grained metasediments (Fig 10c). Hydrothermal breccias consist of sharply angular fragments of white rhyolite, cemented by chalcopyrite-pyrite bearing quartz (Fig 10d).

Three samples, one taken from La Sierpe plug and two from a dike associated to Cu-rich mineralization yielded U-Pb zircon ages of 50.73 ± 0.37 Ma, and 50.19 ± 0.53 Ma and 50.40 ± 0.45 Ma, respectively (see below).

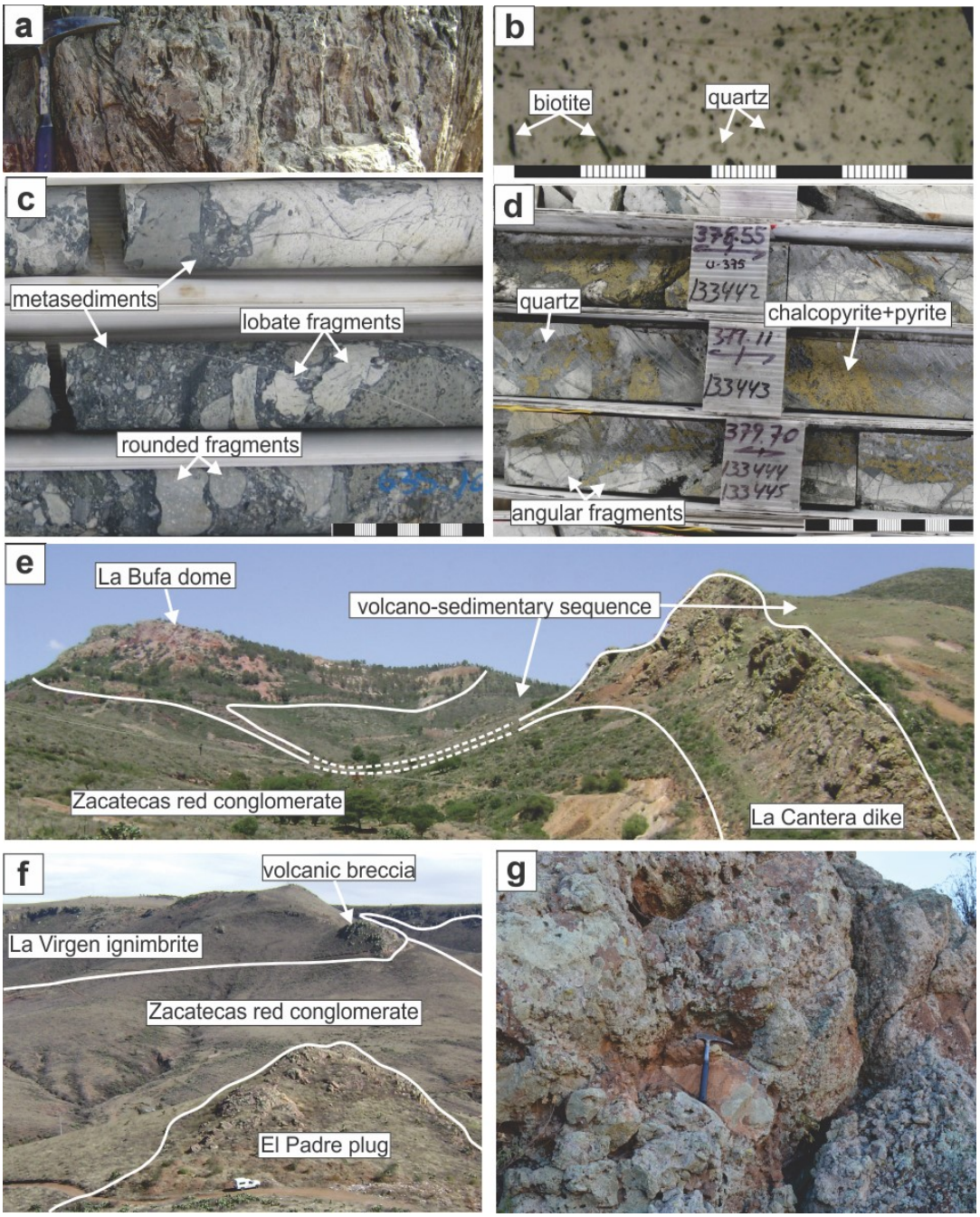

Figure 10. Photographs showing Eocene igneous rocks. (a) Surface outcrop of the La Sierpe plug showing vertical flow-banded texture (vertical face 746966E, 2523906N). (b) Sample of drillcore (drillhole COS-41 at 896 m depth; 747372E, 2524200N) showing porphyritic texture of the La Sierpe plug at depth. (c) Magmatic breccia with globular peperitic texture of grey rounded and white lobate clasts of porphyritic rhyolite in a matrix of black fine-

grained metasediments (DDH S-179 from 633–636m). (d) Breccia with angular fragments of rhyolite cemented by chalcopyrite-pyrite-bearing quartz (DDH U-375). (e) Panoramic view looking northwest showing the eastern end of the la Bufa dome and its continuation to the east as the La Cantera dike (751947E, 2520682N). (f) Panoramic view to the southeast sowing the El Padre plug intruding the Zacatecas red conglomerate, the La Virgen ignimbrite lying discordantly on top of the Zacatecas red conglomerate, and the volcanic breccia at the base of the La Virgen ignimbrite (748328E, 2518097N). (g) Close up of the volcanic breccia outcrop in d showing rock blocks up to 40 cm wide (748887E, 2517362N). All coordinates are in UTM, ITRF92 datum, zone 13.

The La Bufa rhyolite dome is structurally controlled by the La Cantera fault, which down-drops the Zacatecas conglomerate against the Jurassic-Cretaceous volcano-sedimentary sequence. The dome continues to the east as a narrow dike (too narrow to show on Fig. 7) emplaced along the fault, and is crosscut by the La Cantera vein (Perez-Martinez et al., 1961; Ponce and Clark, 1988). The La Bufa rhyolite is pale gray to pinkish in color, and contains ~5% phenocrysts (1–2 mm in size) of sanidine, quartz, orthoclase, and rare biotite in a partially devitrified glassy matrix. Feldspars are selectively argillized and the clay washed out during preparation of the thin section; biotite is replaced by hematite; and the matrix is partially devitrified (Fig. 11a). This alteration is considered to be deuteric, caused by volatiles released during late stages of solidification. A K-Ar whole rock date for this intrusion of 49.9 ± 1.0 Ma (Tristan-Gonzales, 2008) is similar to the U-Pb zircon age of 48.64 ± 0.50 Ma obtained in this study (see below).

The El Padre intrusion is an elongated rhyolitic plug associated with NNW-oriented dikes of the same composition. It crosscuts the Zacatecas conglomerate and the Jurassic-Cretaceous volcano-sedimentary sequence on the south side of the district (Fig. 10d). The rock is purple to reddish in color with vertical flow banding, and locally contains xenoliths. It contains ~5% phenocrysts (up to 3 mm in size) of orthoclase, quartz, and fine-grained biotite set in a partially devitrified matrix. Orthoclase phenocrysts show a dirty texture due to partial alteration to

sericite, and biotite shows minor oxidation (Fig. 11c). The El Padre rhyolitic plug has been dated in this study at 45.32 ± 0.47 Ma (U-Pb on zircon; see below).

The La Virgen ignimbrite is a voluminous pyroclastic unit, ~200 m thick, which extends from the southern part of the El Orito vein system to the south for more than 5 km (Figs. 7 and 10d). Its base in the northern portion is a volcanic breccia that consists of angular, poorly sorted rock fragments that range in size from 0.5 to 50 cm (Fig. 10e). The largest blocks are exposed in a thick (~25 m) outcrop that forms a prominent hill on the northeastern flank of the La Virgen ignimbrite, suggesting that the vent is located close to this area (Fig. 10d). This breccia grades laterally to the south and southeast into a bedded (<1 m thick) medium- to fine-grained ash flow tuff with cross bedding that has been interpreted as a pyroclastic surge deposit (Tristan-Gonzalez, 2008). The base of this ignimbrite locally exhibits argillic (kaolinite) alteration. This alteration continues neither vertically nor laterally and is interpreted to be local weathering. The upper part of the ignimbrite is welded with rare lithic fragments. The texture is pyroclastic with broken crystals of quartz, sanidine, eutaxitic pumice, and accessory biotite. The matrix is dominantly glassy with preserved glass shards and scarce isolated spherulites denoting minor devitrification (Figs. 11d–f). Concentrations of eutaxitic pumice and crystals form layers up to 20 cm thick (pseudostratification) within the welded ignimbrite that dip 10–15° SW. Tristan-Gonzalez (2008) obtained a whole rock K-Ar age of 37.1 ± 0.9 Ma for this unit but in this study, we obtained an older U-Pb zircon age of 41.72 ± 0.45 (see below).

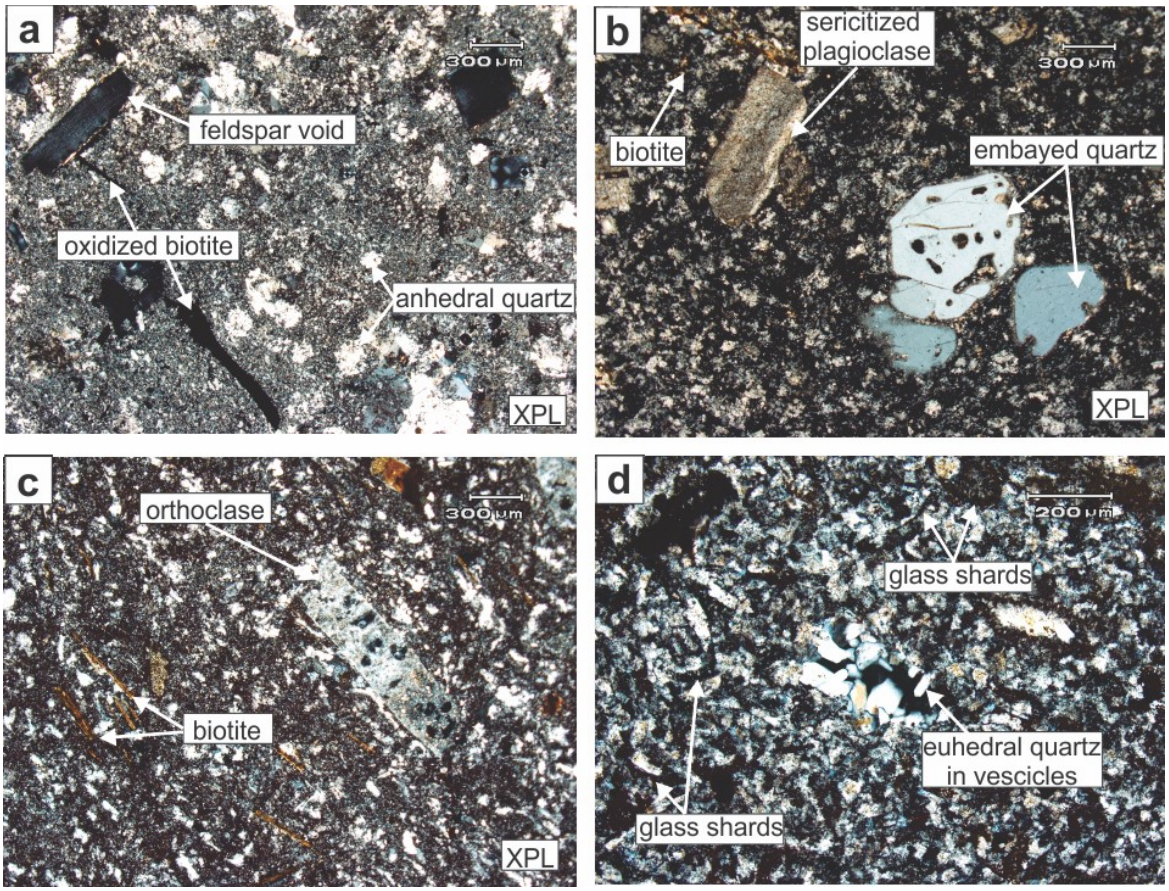

Figure 11. Photomicrograph of the Eocene igneous rocks samples showing their degree of alteration. (a) Sample from the La Bufa rhyolitic dome (ZABU-01) showing cavities after leached feldspars and oxidized biotite in a glassy matrix (UTM NAD27: 750195E, 2520755N). (b) Sample from the La Sierpe rhyolitic plug (ZASI-02) showing sericitized plagioclase, oxidized biotite, and partially reabsorbed quartz phenocrysts set in a cryptocrystalline matrix (DDH S-41 at 896 m; UTM NAD27: 747327E, 2524177N). (c) Sample ZAPA-03 from the El Padre rhyolitic plug showing fine-grained oxidized biotite and dusty aspect of altered orthoclase in a partially devitrified matrix (UTM NAD27: 748383E, 2517921N). (d) Sample from the La Virgen ignimbrite (ZAVI-04) showing preserved glass shards in a partially devitrified matrix and euhedral quartz crystals growing in vesicles (UTM NAD27: 746915E, 2515212N).

Based on radiogenic isotope compositions, the origin of these magmas has been interpreted to be a mix of mantle- and crust-derived magmas evolved through fractional crystallization in shallow-level magma chambers (Verma, 1984).

3.5 Oligocene Rocks

In the southern half of the district, latitic and rhyolitic volcanic rocks and sinters have been mapped as Oligocene, although no radiogenic ages are available. The latite is a small unit exposed only in the southern portion of the area (Fig. 7), whereas rhyolitic rocks are voluminous and widespread to the south of Zacatecas (Fig. 7), and consist mainly of pyroclastic deposits. These include ash flow tuffs, lithic and lapilli breccias, and crystal-rich and vitric ignimbrites (Ponce et al., 1988).

The youngest bedded stratigraphic unit is an unaltered rhyolite crystal ash-flow tuff, the La Capilla tuff, which unconformably overlies the Eocene La Virgen ignimbrite (Fig. 7).

Sinter deposits also occur locally within the Oligocene rocks on the western flank of the La Virgen ignimbrite, and consist of stratiform siliceous N–S-elongated bodies ~750 m in length, 60 m wide, and up to 24 m thick (Fig. 7; Ponce et al., 1988). These deposits consist of subhorizontal bands (0.3–10 cm thick) of alternating light grey, white, and reddish amorphous silica (Fig. 12a), and contain abundant well-preserved circular and polygonal shaped mud-crack structures, indicating formation at or near the paleosurface (Fig. 12b–c). The deposition of these sinters was possibly controlled by the same N–S-trending structural system that controlled the low-sulfidation El Orito veins, and might represent hot-spring activity concurrent with that hydrothermal system.

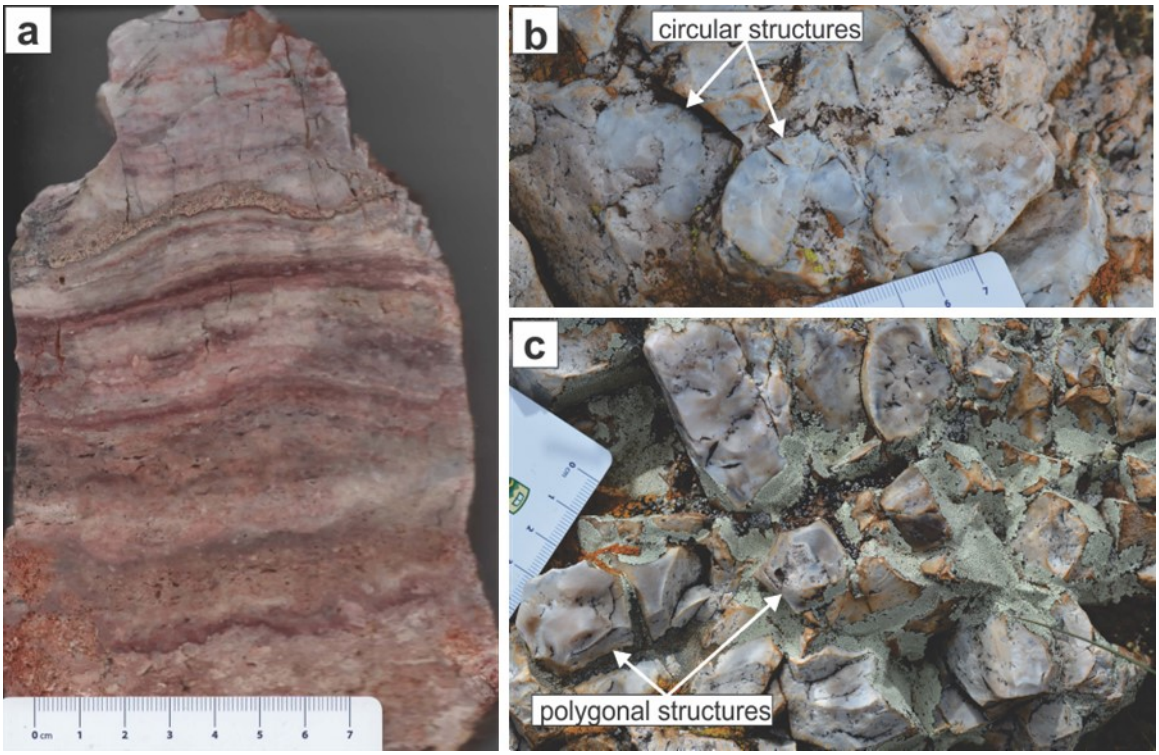

Figure 12. Photographs showing macroscopic textures of sinter deposits. (a) Vertical section of a sample of sinter showing subhorizontal bands of amorphous silica. (b, c) Plan view showing circular and polygonal mud-crack structures, respectively (E742718, N2512882).

3.6 Wall-rock alteration

The Jurassic–Cretaceous volcano-sedimentary sequence and the Eocene volcanic and subvolcanic rocks are the most important host of mineralization in the Zacatecas district. All these rocks exhibit some degree of alteration. Minerals were identified with the aid of X-ray diffraction analysis (Appendix A).

Jurassic–Cretaceous volcano-sedimentary rocks are affected by greenschist-facies regional metamorphism, leading to the formation of chlorite, epidote, and minor calcite and disseminated pyrite. Additionally, there is local evidence within the Mala Noche area for contact metamorphic alteration that includes hornfels, marble, and skarn-type minerals, although no causative pluton has been identified to date. Hornfels consists of laminations of hardened grey to

black shale and fine-grained quartzite, with chlorite–epidote-rich horizons locally replaced by sphalerite or pyrite (Fig. 13a–d). Marble is rare and has been observed only in drill hole CGS198 (E745320, N2524,692; depth 267.40–269.50 m) located ~500 m west of the San Gil rhyolite plug (Fig. 7). It is white, compact with a roughly equigranular texture, and is composed primarily of recrystallized calcite and dolomite (Fig. 13e–f). Skarn-type minerals occur locally in proximity to high copper grades in the Mala Noche mine (Fig. 14). Prograde alteration minerals include wolframite associated with magnetite and remnants of anhydrous silicates (garnets and hedenbergite) that have been obliterated by intense retrograde skarn-type alteration and late epithermal overprints. Retrograde minerals include abundant chlorite–epidote (dominantly clinochlore) and lesser amounts of ilvaite, Fe-hydroxides, nontronite, siderite, stilpnomelane, and laumontite among others (see section 3.8).

Eocene subvolcanic and volcanic felsic rocks are affected only by hydrothermal or deuteric alteration. The dominant alteration of rhyolitic plugs and dikes spatially associated with the Mala Noche vein system is phyllic (quartz, sericite-illite, and pyrite). The La buffa dome shows local slicification associated to vertical fractures due to vapour phase alteration, and development of argillic alteration associated to the Cantera fault on the northern edge of the dome. This alteration is suspected to be supergene because there is no evidence to continue at depth. The La Virgen ignimbrite shows dominantly deuteric alteration including partial devitrification of the matrix and vapor phase silicification indicated by euhedral quartz crystals in vesicles (Figs. 11d–f).

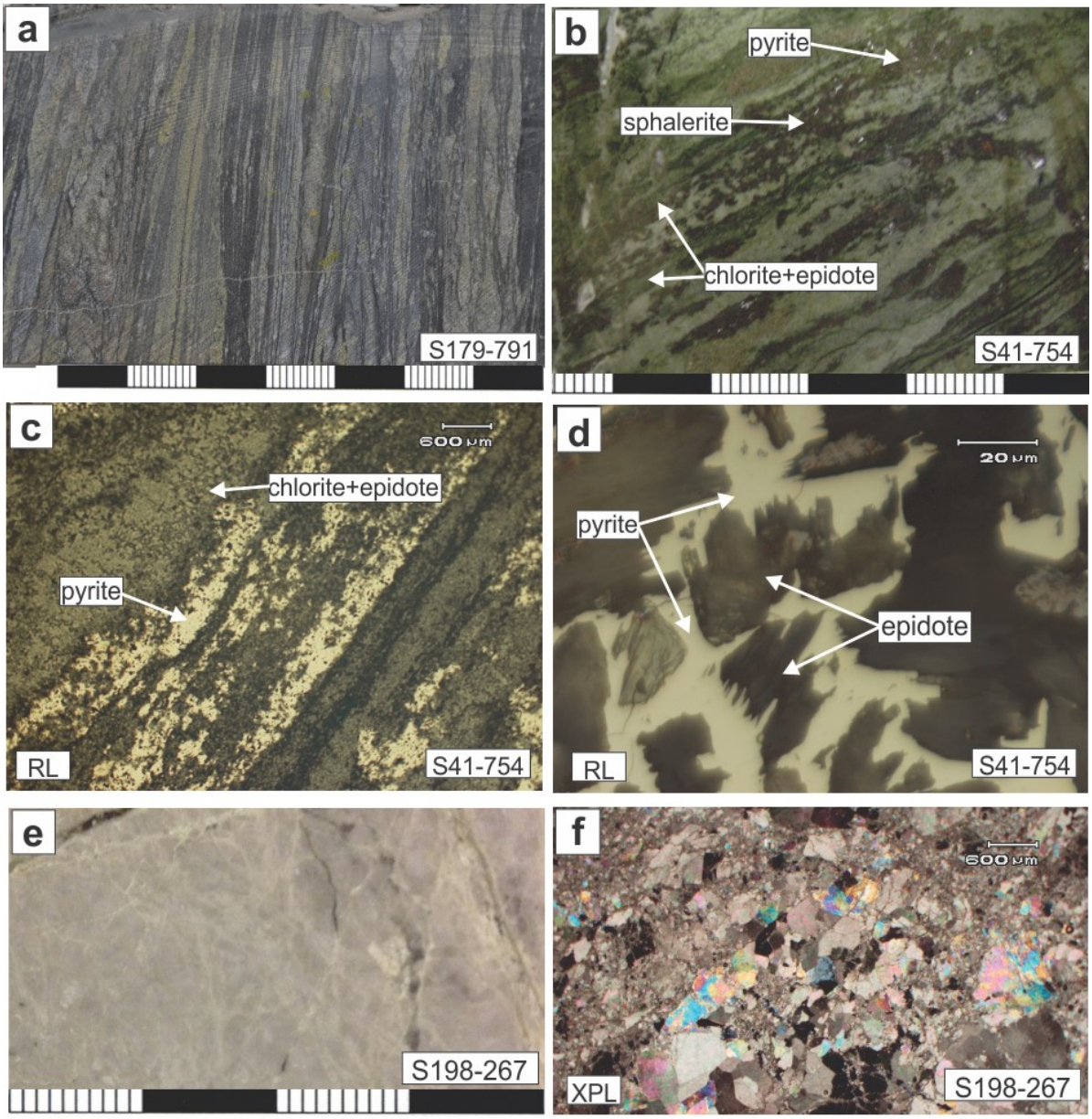

Figure 13. Hand sample photographs and photomicrographs from the Mala Noche drill core showing alteration of Jurassic–Cretaceous volcano-sedimentary rocks. (a) Hornfels consist of laminations of hardened grey to black shale and fine-grained quartzite interbanded with chlorite-epidote layers. (b) Pyrite and sphalerite replacing chlorite-epidote laminations (DDH S-41 at 754 m; 747355E, 2524201N). (c) Polished section of b showing chlorite-epidote and pyrite in plane polarized reflected light (RL). (d) Close up of c showing pyrite replacing epidote crystals in reflected light. (e) Sample of marble (DDH S198 at 267m; E745320, N2524,692). (f) Photomicrograph of e showing a roughly equigranular mosaic of calcite and dolomite

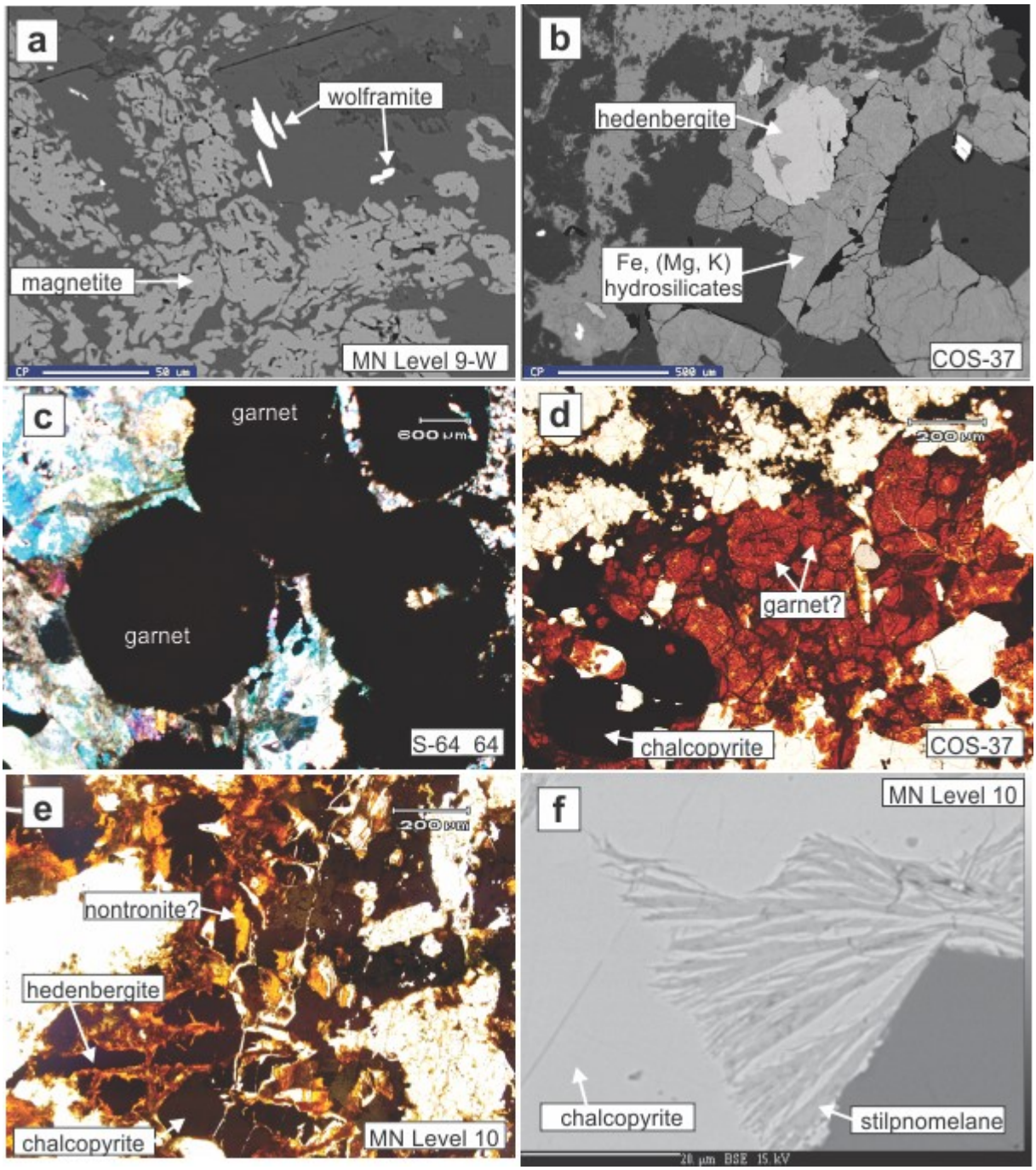

Figure 14. Back scattered electron images and photomicrographs showing skarn-type alteration minerals from the Mala Noche mine and drill core samples: (a) Back scattered electron image of wolframite associated to magnetite; sample from underground mine level 9-W (747445E, 2523630N at 2205 masl). (b) Back scattered electron image of sample Cos-37 (DDH U-37 at 164 m; 747779E, 2523876N) showing hedenbergite altered to Fe-Mg hydrosilicates (grunerite–cummingtonite). (c) Photomicrograph of sample S-64 (DDH S-64 at 64 m; 747172E, 2523732N) showing extinction of subhedral garnet crystals (possible andradite) under crossed nicols. (d) Rounded crystals altered to Fe-hydrosilicates and replaced by chalcopyrite (sample Cos-37). (e) Photomicrograph of sample from underground level 10 (748139E, 2523400N at 2154 masl) showing hedenbergite retrograded to nontronite and replaced by chalcopyrite, and (f) back scattered electron image of stilpnomelane replacing chalcopyrite.

3.7 Mineral Deposits

Mineral deposits in the Zacatecas district have been mined since 1548 for silver, gold, lead, zinc, and copper (Ponce et al., 1988). Copper has been mined as a main product only from the Mala Noche deposit. The bulk of the silver and base metal mineralization has been mined from epithermal veins in ESE- to SE-striking structures (Fig. 7). The main ore minerals are native silver, acanthite, silver sulfosalts, galena, sphalerite, chalcopyrite, and minor bornite, with ubiquitous pyrite, and locally pyrrhotite and magnetite in skarn assemblages. Gangue minerals include amethystine quartz (characteristic of the Veta Grande system but also present in the Mala Noche vein), colourless quartz, chalcedony, calcite, ankerite, and rare adularia. These types of vein in the Zacatecas area have been classified by Camprubi and Albinson (2007) as intermediate-sulfidation Ag-(Pb-Zn-Cu-Au), with the Veta Grande system being specifically described as containing both low- and intermediate-sulfidation styles.

The highest gold grades in the district occur in the El Orito vein system, which differs in orientation and mineralogy from the intermediate-sulfidation Ag-(Pb-Zn-Cu-Au) vein systems. The El Orito vein system is located in the southwestern part of the district and has a predominantly N–S trend (Fig. 7). This vein system has been described as the auriferous southern zone (Perez-Martinez et al., 1961), the Au-Ag-(Se) system (Ponce and Clark, 1988), or the El Orito system (Caballero-Martinez, 1999), and is classified as low-sulfidation Au-Ag by Camprubi and Albinson (2007).

The following sections provide descriptions of three of the most important mineral deposits in the district: The Mala Noche deposit, which is Cu-rich and includes skarn-type and epithermal mineralization in WNW-striking veins; the intermediate-sulfidation Veta Grande vein, which is representative of the polymetallic, Ag-rich, WNW- to NW-striking veins; and the

low-sulfidation El Compas vein which is part of the Au-rich and predominantly N–S-trending El Orito system.

3.7.1 Mala Noche

The Mala Noche deposit, located in the central part of the Zacatecas district, is the only deposit where Cu has been mined as the main commodity, with Ag, Pb, and Zn as byproducts. Although the mineralization is dominantly in epithermal veins hosted by the Jurassic–Cretaceous volcano-sedimentary sequence, Cu-rich zones show skarn characteristics and are spatially related to felsic plugs and dikes from the sub-volcanic complex.

Skarn-type mineralization. This mineralization style contains high grades of Cu (e.g., drillhole U-39 with 8% Cu over 4 m) and is characterized by replacement and/or semi-massive textures of chalcopyrite associated with pyrrhotite, magnetite, lesser sphalerite and galena, minor wolframite and/or relicts of silicate minerals (Figs. 14–16).

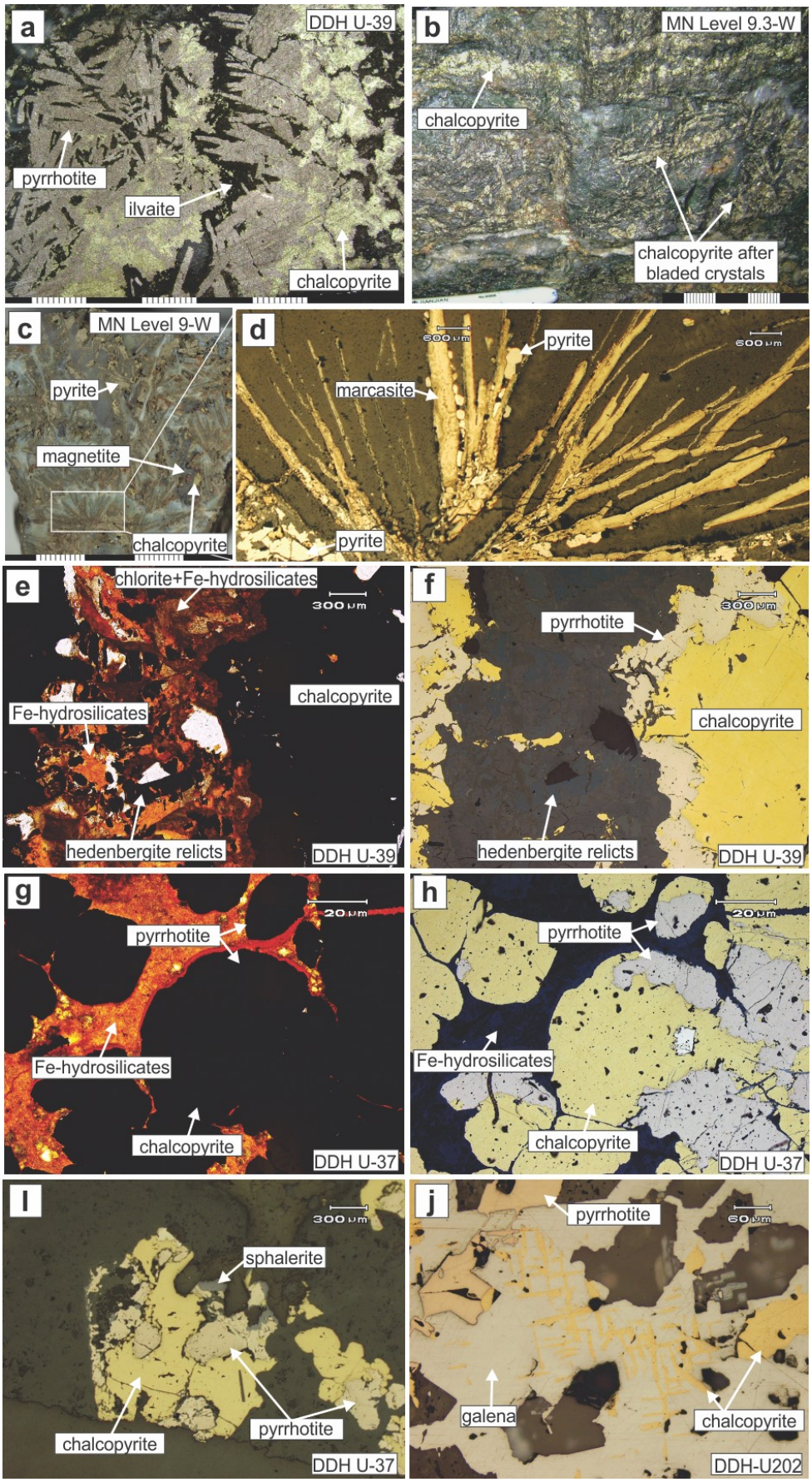
a
DDH U-39
pyrrhotite
ilvaite
chalcopyrite
b
MN Level 9.3-W
chalcopyrite
chalcopyrite after bladed crystals
c
MN Level 9-W
pyrite
magnetite
chalcopyrite
d
500 µm
pyrite
marcasite
pyrite
e
chlorite+Fe-hydrosilicates
300 µm
chalcopyrite
Fe-hydrosilicates
hedenbergite relicts
DDH U-39
f
300 µm
pyrrhotite
chalcopyrite
hedenbergite relicts
DDH U-39
g
20 µm
pyrrhotite
Fe-hydrosilicates
chalcopyrite
DDH U-37
h
20 µm
pyrrhotite
Fe-hydrosilicates
chalcopyrite
DDH U-37
I
300 µm
sphalerite
chalcopyrite
pyrrhotite
DDH U-37
j
pyrrhotite
60 µm
galena
chalcopyrite
DDH-U202

Figure 15. Photographs and reflected light photomicrographs of the Mala Noche skarn-type high Cu grade samples showing mineral associations and textures: (a) Sample from DDH U-39 (E748097, N2523786 at 173.5 m) showing pyrrhotite replacing chalcopyrite and intergrown with ilvaite crystals. (b) Photo from underground wall level 9.3–W, showing semi-massive chalcopyrite replacing tabular bladed crystals (probably amphiboles). (c) Mineral association of pyrite, magnetite, and chalcopyrite in a groundmass of grey quartz (sample from underground level 9 west). (d) Close-up of C showing texture of marcasite and pyrite replacing radially elongated crystals of possible amphibole precursors. (e–f) Photomicrographs showing alteration and remnants of hedenbergite replaced by chalcopyrite and rimmed by pyrrhotite (e, transmitted light and f reflected light; sample from DDH U-39; E748097, N2523786 at 171 m). (g–h) Photomicrographs in transmitted and reflected light, respectively, showing rounded silicate(?) crystals replaced by chalcopyrite and pyrrhotite surrounded by Fe-hydrosilcates (from DDH U-37; E747779, N2523876 at 162 m). (i) Euhedral isometrically shaped crystal (probably garnet) replaced by chalcopyrite, pyrrhotite, and minor sphalerite (DDH U-37; E747779, N2523876 at 162 m). (j) Sample from DDH U-202 (E747827, N2523550) showing pyrrhotite and chalcopyrite replacing galena along cleavage planes.

The silicates are commonly altered to Fe-hydrosilicates and replaced by pyrrhotite, chalcopyrite, and pyrite (Figs. 14 and 15). Pyrrhotite is characteristic of this stage and occurs closely associated with ilvaite and replacing chalcopyrite (Fig. 15a). Chalcopyrite is the most abundant ore mineral and occurs in different mineral associations: associated with pyrrhotite and ilvaite (Fig. 15a); after bladed and acicular radial crystals (possibly amphibole) in association with magnetite, pyrite, and marcasite (Figs. 15b–d); replacing silicates including hedenbergite and rounded isometrically shaped crystals (possibly garnet) altered to Fe-hydrosilicates (Figs. 14f, 15e–i). Chalcopyrite is commonly rimmed and replaced by pyrrhotite. Pyrite and marcasite are found replacing radial acicular and bladed tabular crystals (Fig. 15 c–d). Sphalerite and galena are both late in the mineral paragenesis. Sphalerite is found rimming and replacing pyrrhotite (Fig. 15i). Chalcopyrite, which has a wide spectrum of deposition within the paragenesis, is observed replacing galena along cleavage planes (Fig. 15j). Quartz, siderite, calcite, and ankerite are the main gangue minerals (Fig. 16). Quartz is typically fine-grained with a distinct grey color in hand sample.

The association of high Cu-grades with replacement textures, remnants of calc-silicate minerals, and high temperature minerals such as wolframite, as well as the presence of marble distal to the Mala Noche Cu-rich mineralization indicates skarn-type mineralization. The calc-

silicate mineral assemblage that defines a skarn (Meinert et al., 2005) is not clearly observed because it has been almost completely obliterated by retrograde alteration and later epithermal overprint. However, abundant tabular or acicular crystals with radial textures, and rounded and isometric minerals replaced by sulfides may represent precursor pyroxene, amphibole, and garnet, characteristic of skarn assemblages. Some samples of this stage of mineralization show evidence of post-mineral tectonic deformation including sheared massive sulfides with distorted galena crystals and deformed triangular cleavage pits, sigmoidal shaped segregations of pyrite and chalcopyrite, cataclastic deformation textures in pyrite, and lineaments of quartz grains with undulose extinction. These textures suggest that strike-slip faulting disturbed this mineralization, further obscuring the spatial distribution and possible zoning of alteration minerals characteristic of skarns (Figs. 16 and 17 a–f; Meinert et al., 2005).

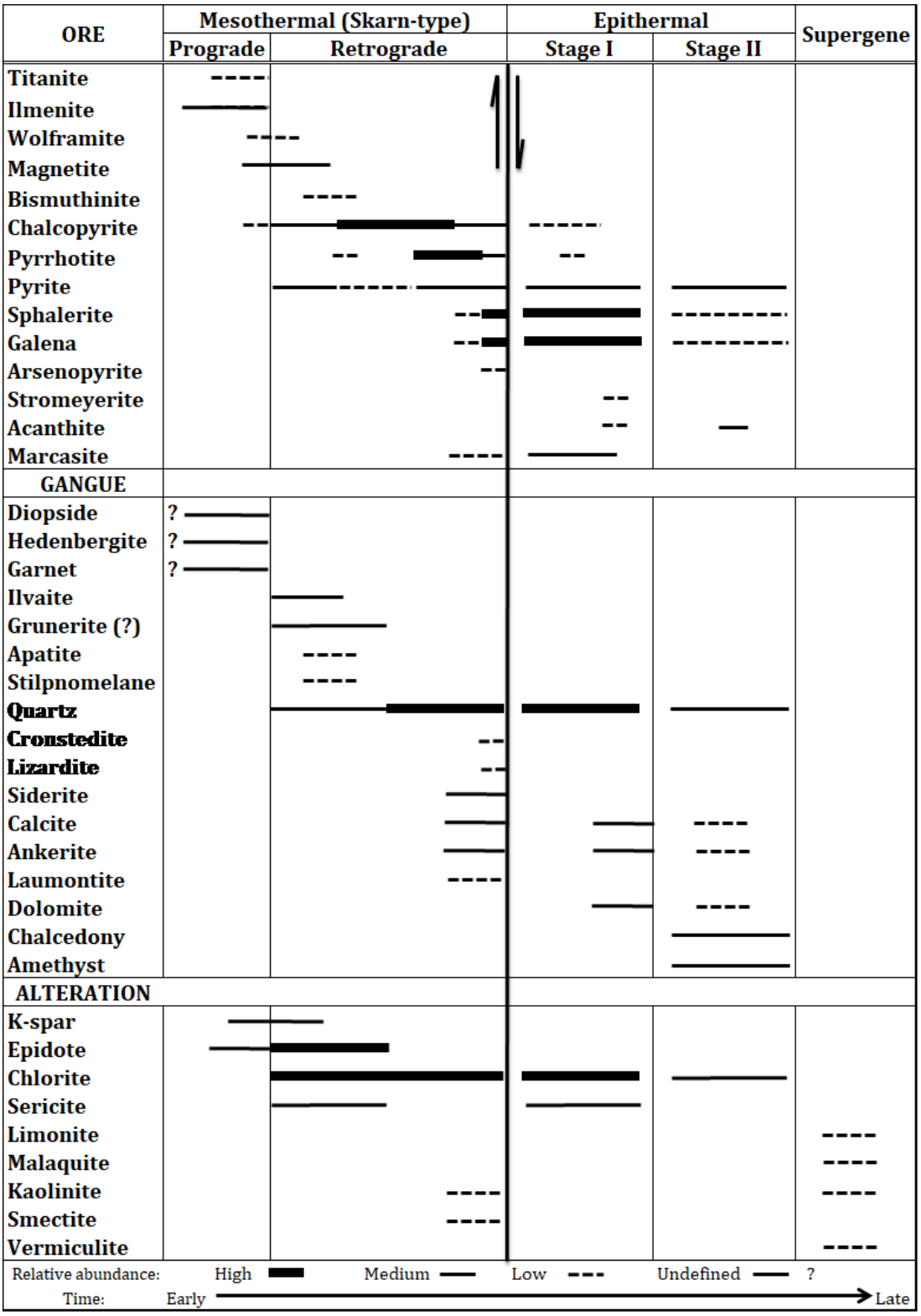

Figure 16. Mineral paragenesis of the Mala Noche skarn- and intermediate-sulfidation epithermal-type mineralization.

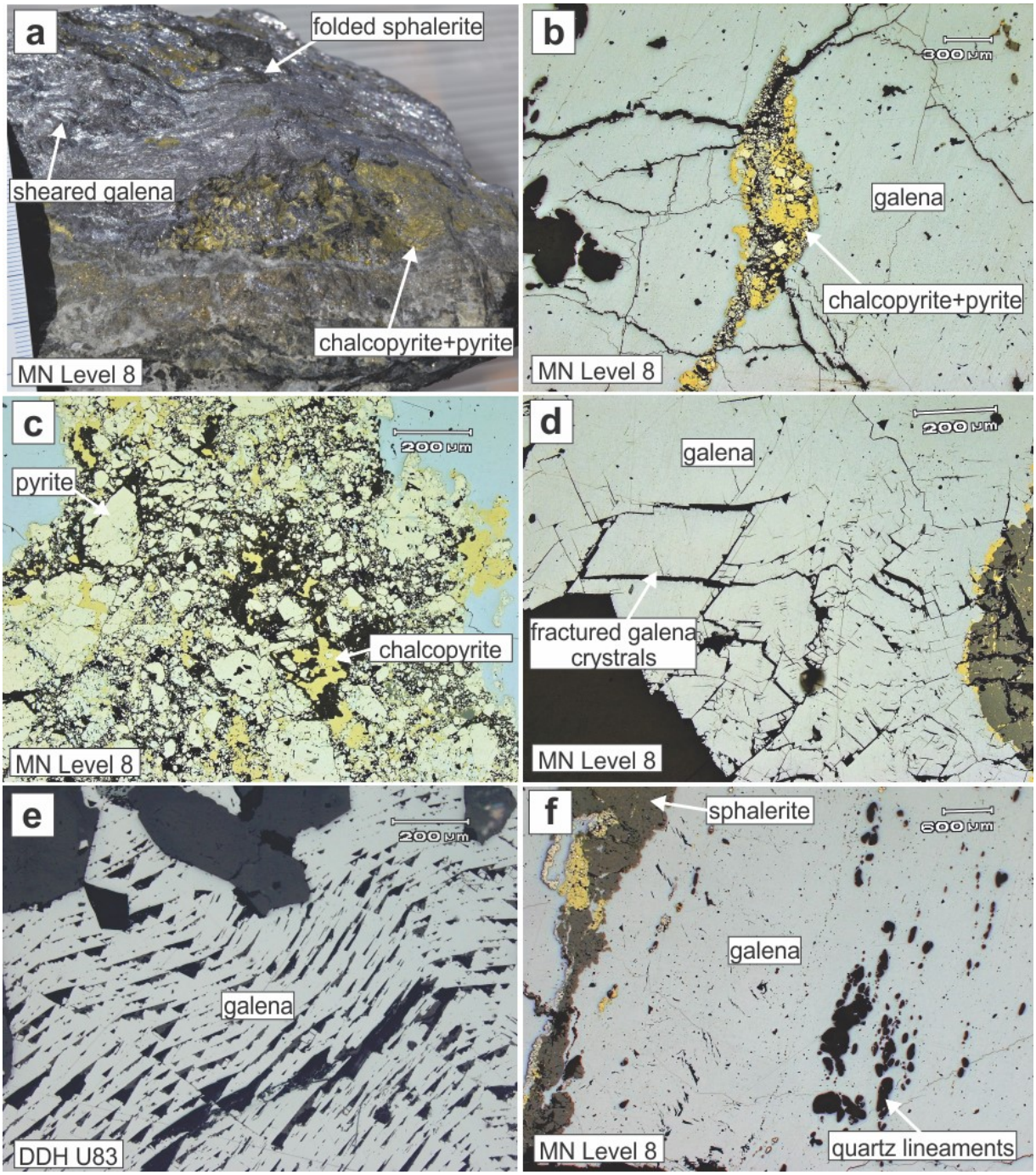

Figure 17. Photographs and reflected light photomicrographs of the Mala Noche skarn-type mineralization showing post-mineral deformational textures in massive sulfides: (a) Sheared galena with a folded band of sphalerite, and sigmoidal shaped lens of chalcopyrite and pyrite. (b) Sigmoidal shaped aggregate of chalcopyrite and pyrite. (c) Cataclastic texture in pyrite and chalcopyrite. (d) Fractured crystals of galena. (e) Deformation of triangular cleavage pits in galena. (f) Lineaments of rounded quartz grains that exhibit undulose extinction in transmitted light.

Epithermal mineralization. This mineralization is dominantly Zn-Pb-Ag-rich with low Cu grades and is characterized by open space textures (crustiform and cockade banding, breccias, and vuggy cavities; Fig. 18a–c). Sulfides form discontinuous bands associated with crustiform quartz, or infill interstitial spaces between gangue minerals. The first stages in the mineral paragenesis are sulfide-rich and lack amethystine quartz, whereas late stages are similar to the Veta Grande stage II with abundant amethystine quartz and chalcedony, and sparse sulfides (Figs. 18a and b, respectively). In the cockade texture, crustiform quartz coats pre-existing fragments of mineralization, and meta-sedimentary or volcanic rocks (Fig. 18c). The main ore mineral association is sphalerite, galena, pyrite, and minor chalcopyrite, with acanthite as blebs in sphalerite or galena, or associated with sphalerite in micro-veinlets of quartz (Fig. 18d–e). This mineralization does not show evidence of deformation and clearly overprints Cu-rich skarn-type mineralization (Figs. 18e–f). The main gangue minerals are clear coarse-grained euhedral quartz, amethystine quartz, calcite, and chalcedony.

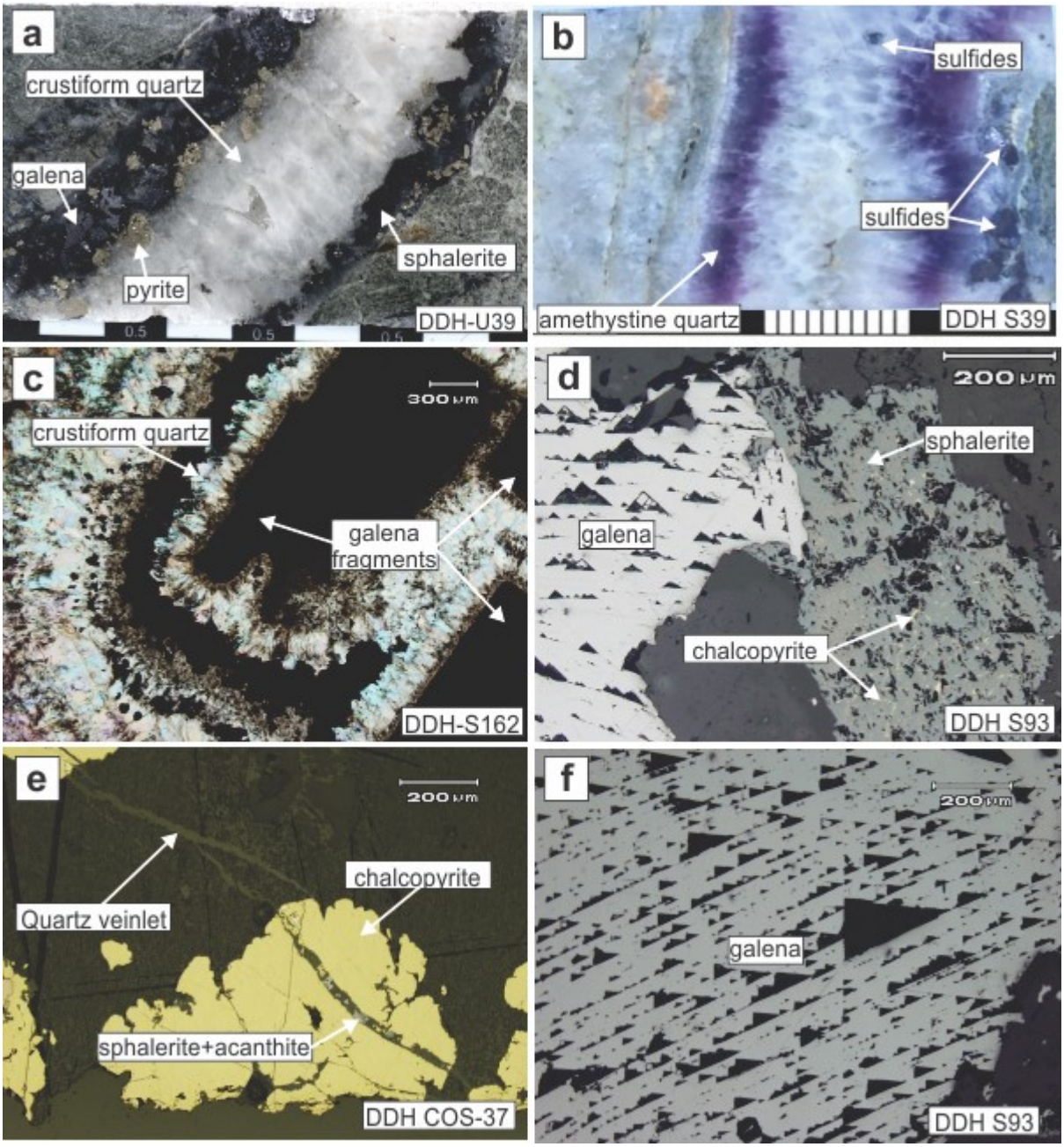

Figure 18. Photographs and photomicrographs of the Mala Noche Zn-Pb-Ag-rich intermediate-sulfidation epithermal mineralization showing textures and ore mineral associations: (a) Early sulfide-rich vein showing discontinuous bands of sphalerite, galena, pyrite, and crustiform quartz with vuggy cavities at the center. (b) Later sulfide-poor vein showing crustiform amethystine quartz. (c) Cockade texture formed by crustiform quartz that coats pre-existing fragments of galena. (d) Mineral association of galena, sphalerite, and blebs of chalcopyrite. (e) Micro-veinlet of quartz with sphalerite and acanthite crosscutting chalcopyrite and associated alteration minerals. (f) Photomicrograph showing undeformed triangular cleavage pits in galena.

Metal Zoning. Figure 19 shows the Cu and Zn metal content distribution of the Mala Noche vein. Zones of high Cu metal content, which is calculated by multiplying width by average grade (W*Cu% > 30) have irregular to elongated shapes up to 200m long with no preferential orientation along the vein (Fig. 19a). These zones are concentrated in the center of the vein with some smaller (up to 100m) ore shoots spread in the west. The eastern section of the vein shows no significant Cu content discovered to date. Medium Cu grades (W*Cu% 5–30) form irregular shaped halos that extend up to 300m around high Cu grade ore shoots. Low Cu content (W*Cu% 0.6–5) is present along the entire lateral extent of the vein. Vertically, the high Cu content is apparently restricted to between 2200–1900 meters above sea level (masl), however medium contents continue deeper in the central section and remain open to depth.

The Zn metal content shows a wider and more continuous vertical and lateral distribution than Cu. High Zn content (W*Zn% > 10) continues horizontally almost along the entire extent of the vein and remains open to the east (Fig. 19b). Vertically, Zn mineralization extends from surface to 1850 masl in the central and remains open to depth in the eastern section. The spatial distribution of Pb and Ag (not shown in the figures) show a similar distribution to Zn. Local sporadic intersections of Au have been reported.

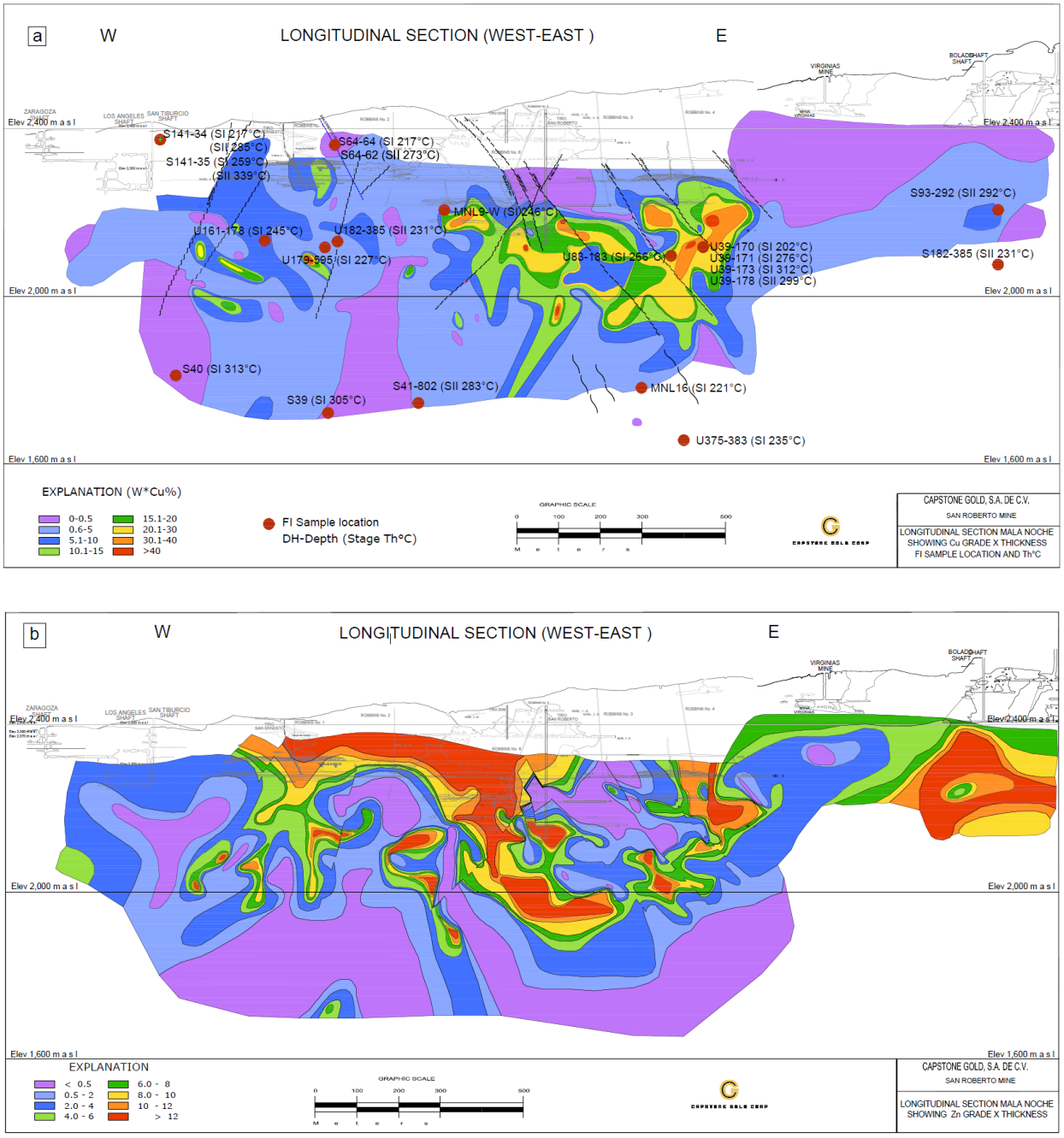

Figure 19. Longitudinal section of the Mala Noche vein showing (a) the distribution of Cu content, calculated as average grade x thickness, and location of fluid inclusion samples showing maximum temperature FIA averages (see below), and (b) the distribution of Zn content.

3.7.2 Veta Grande

The Veta Grande vein is the most prominent single vein (2 to 30 m wide including breccia and stockwork zones and averaging ~10 meters; ~7,000 m long) in a system that strikes northwest and dips ~70° to the southwest. The Veta Grande vein has two main stages of mineralization with contrasting textures and gangue mineralogy (Figs. 20–22).

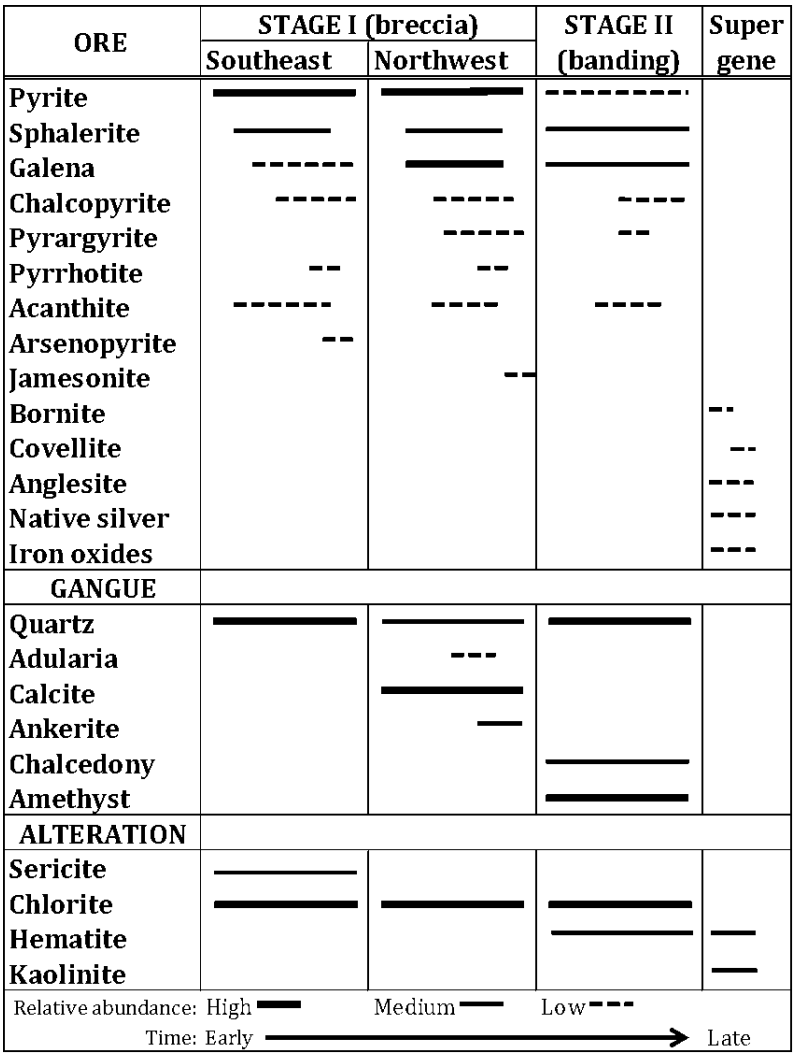

Figure 20. Mineral paragenesis of the Veta Grande Vein.

Stage I consists of a breccia with fragments up to 4 cm long of volcanic and metasedimentary rocks, cemented by gray microcrystalline quartz, calcite, scarce adularia, and

fine-grained sulfides (~5% pyrite-sphalerite-galena; Fig. 21a–d). The breccia shows some differences along the vein length: volcanic fragments and silica gangue are dominant to the southeast (Fig. 21a), whereas to the northwest, fragments of metasedimentary rocks are more abundant, and the gangue is dominated by carbonates (calcite, ankerite, dolomite, and scarce adularia; Fig. 21b–d). The sulfide mineralogy consists of variable percentages of pyrite, sphalerite, galena, with minor acanthite as inclusions in galena or pyrite, and minor chalcopyrite and pyrrhotite as blebs within sphalerite (Fig. 21e–f). Sphalerite shows growth zoning with iron contents ranging from 0.7–0.9 mole percent FeS (from electron microprobe analyses; Appendix B). Additionally, jamesonite and pyrargyrite associated with calcite are present in the northwest breccia.

The dominant alteration assemblage related to this mineralization stage is quartz-sericite and occurs as moderate to pervasive replacement of rock fragments within the breccia (Fig. 21a), and as haloes (<1 mm) around quartz veinlets within the wall rock. Carbonatization (calcite, ankerite, and dolomite) is also important in the northwest breccia (Fig. 21b). Propylitization consisting of chlorite, epidote, and disseminated pyrite is widespread in the volcano-sedimentary host rock, although it is not clear whether this alteration is related to hydrothermal processes or greenschist facies regional metamorphism. Based on the iron content in sphalerite, the abundance of base metal sulfides, the lack of high sulfidation-state minerals (e.g., enargite, digenite, and covellite), and the quartz-sericite vein wallrock alteration, this stage of mineralization can be classified as intermediate-sulfidation according to the classification scheme proposed by Hedenquist et al. (2000).

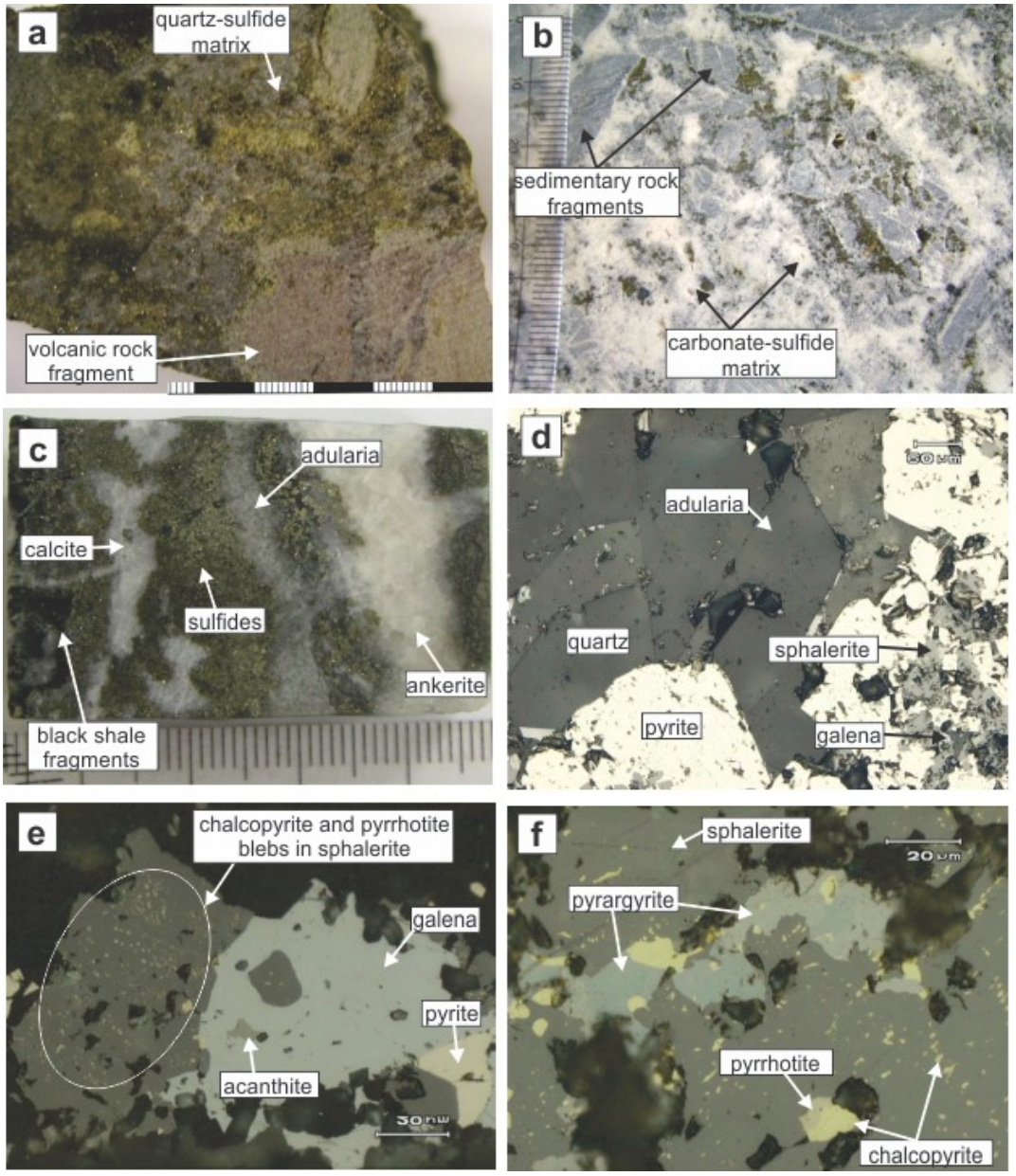

Figure 21. Hand samples and photomicrographs showing representative features of the Veta Grande stage mineralization. (a) Southeast breccia showing fragments of volcanic rocks and a quartz-sulfide matrix (sample SA-1 from the El Refugio level; 752468E, 2526042N). (b) Northwest breccia showing fragments of sedimentary rocks and carbonate-sulfide matrix (sample OSDH6-S14 from drillhole 08VGX006; 750090E, 2527129). (c) Sample of intermediate-sulfidation vein showing the dated adularia associated with sulfides, ankerite, and calcite (sample VG1B-S8 from drillhole 08VGX001B; 750738E, 2526639). (d) Reflected light microphotograph of sample shown in c showing euhedral quartz and adularia crystals associated with pyrite, sphalerite, and galena. (e, f) Reflected light microphotographs showing the association of Ag-bearing minerals with base-metal sulfides (samples OSDH1B-S4 from drillhole 08VGX001B, and DP-04 from the Santa Rita level, 749815E, 2527748N, respectively).

Stage II consists of rhythmically banded silica, with discontinuous bands containing minor sulfides, sulfosalts, and native silver. This second stage occurs as veins crosscutting the stage I breccia, and locally contains clasts of that breccia (Fig. 22a–b). The main silver minerals are acanthite and pyrargyrite (associated with galena and sphalerite). Gangue minerals include amethyst and clear crystalline quartz with crustiform, cockade, and vuggy textures, and chalcedony. Quartz pseudomorphs after bladed calcite (indicating boiling conditions) were also observed locally. The alteration in the host rock is mainly chlorite and hematite.

Replacement of pyrite by iron oxides, galena by anglesite, chalcopyrite by bornite and covellite, and native silver in late fractures and vugs show evidence of supergene replacement in this stage of mineralization (Fig. 22c–f). This stage was preferentially oxidized with respect to stage I due to the higher permeability of the vuggy veins, whereas the lack of permeability in the highly cemented matrix of stage I breccias largely precluded oxidation by downward percolation of groundwaters. Despite supergene oxidation, the general similarity of hypogene sulfide mineralogy between stages I and II suggests a common intermediate sulfidation state.

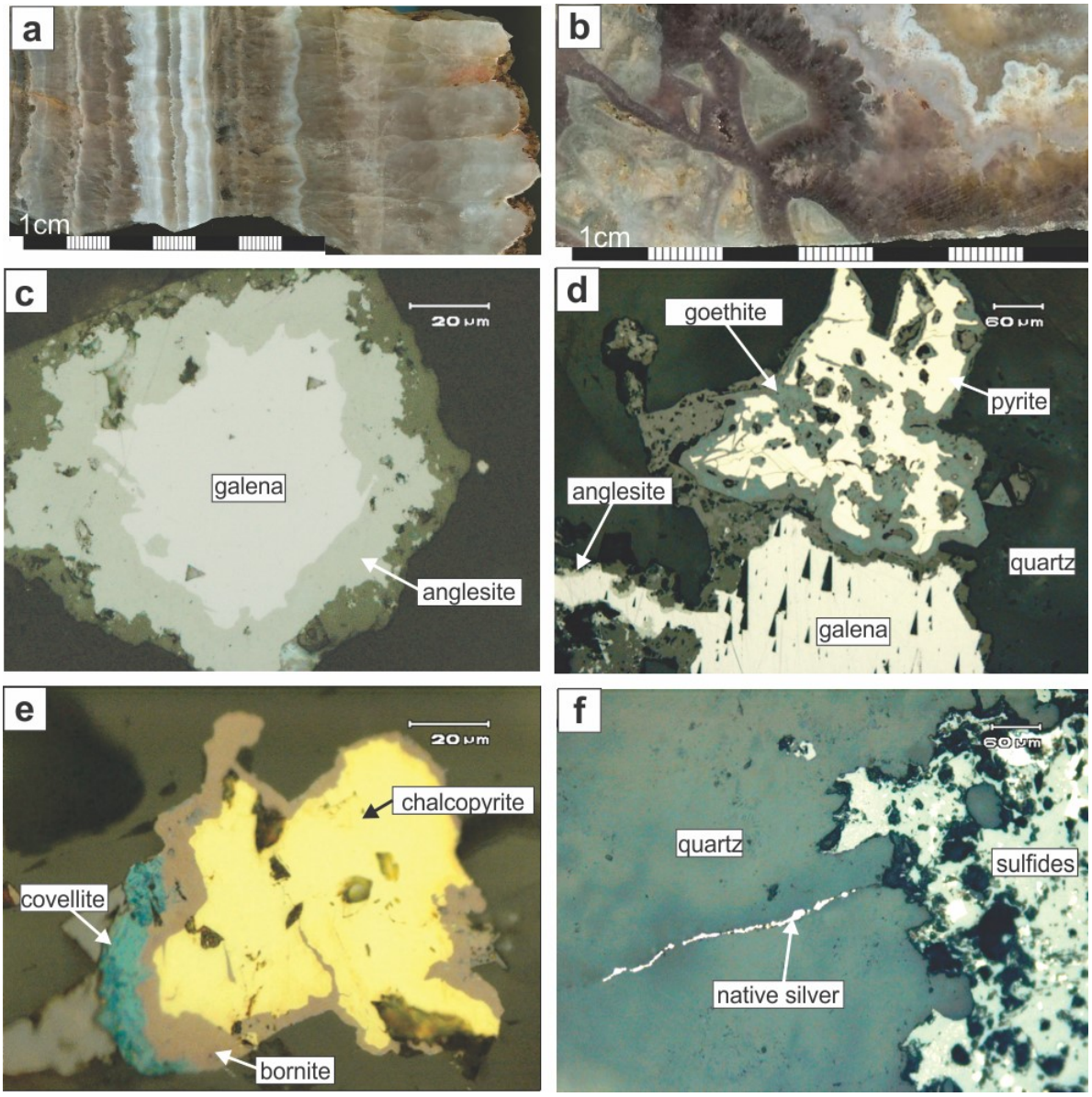

Figure 22. Hand samples and microphotographs showing representative features of the Veta Grande stage II mineralization. (a) Crustiform banding and prismatic crystalline quartz, amethyst, and chalcedony, with discontinuous bands containing sulfides and sulfosalts (dark bands; sample SA-3; 751685E, 2526286N). (b) Stage II quartz enclosing fragments of stage I breccia (sample from drillhole SAD9536; 751678E, 2526252N). Reflected light microphotographs: (c) Supergene replacement of galena by anglesite. (d) Supergene oxidation of pyrite to goethite associated with a halo of supergene anglesite replacing galena. (e) Supergene replacement of chalcopyrite by bornite, and bornite by covellite. (f) Native silver in a fracture associated with oxidized sulfides.

3.7.3 El Orito System

The El Compas vein is one of the principal veins in the El Orito System. The vein is gold-rich with minor silver, and lacks significant base metal sulfides. The vein consists of a single stage of mineralization, with multiple bands of alternating calcite and green to white fine-grained quartz intergrown with adularia in varying proportions (Fig. 23). The bands with higher proportions of adularia (~90%) are creamy in color and stain yellow with sodium cobaltinitrite (Fig. 24a). Textures such as bladed calcite replaced by quartz in late substages, and colloform, flamboyant, and plumose quartz are common (Figs. 24b–d; cf. Moncada et al., 2012). Ore minerals occur as black patches intergrown with bands of adularia and fine-grained quartz (Fig. 24e–f). Electron microprobe analyses show that gold occurs in the form of native gold and electrum (68 wt.% Au, 32 wt.% Ag; Appendix B), and silver occurs as electrum and in the selenide minerals aguilarite (Ag_4SeS) and naumannite (Ag_2Se). Pyrite is present only in trace amounts and is commonly replaced by supergene iron oxides. Gangue minerals are quartz, chalcedony, adularia, and calcite. The alteration in the host rock consist mainly of silicification and minor illite. This type of mineralization is classified as low-sulfidation according to the scheme proposed by Hedenquist et al. (2000).

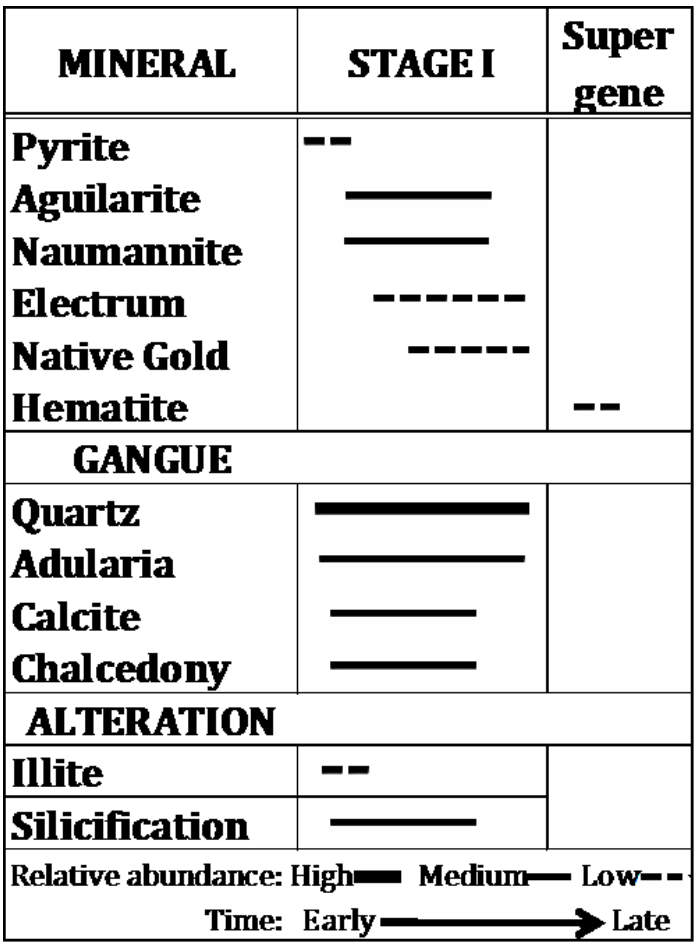

Figure 23. Mineral paragenesis of the El Compas Vein.

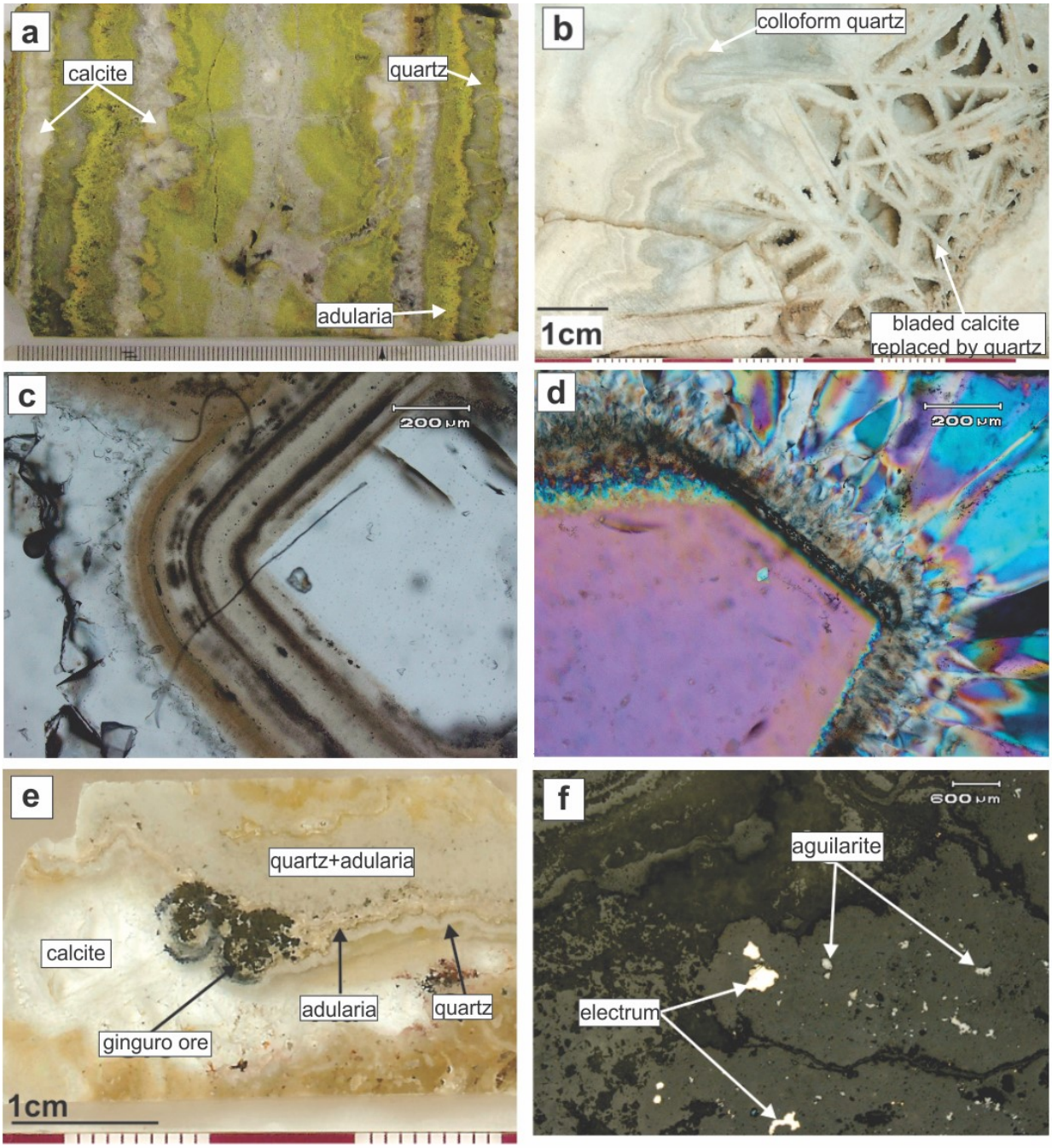

Figure 24. Hand samples and microphotographs showing representative features of the El Compas vein (El Orito System). (a) Hand sample stained with sodium cobaltinitrite showing alternating bands of greenish to white quartz, calcite, and adularia (stained yellow; sample from the El Compas underground mine, level 7). (b) Hand specimen showing bladed calcite texture with interstitial microcrystalline quartz and pinacoids of calcite (sample from the El Compas mine dump; 747259E, 2515568N). (c,and d) Thick section of sample from the El Compas underground mine showing flamboyant and plumose textures, in plane- and cross-polarized light. (e) Scanned thick section showing electrum, aguilarite, and naumannite related to bands of microcrystalline quartz and adularia (sample from drillhole 09COM043 at 63 m). (f) Close up of c showing aguilarite and electrum grains set in a matrix of quartz and adularia (68 wt.% Au, 32 wt.% Ag).

3.8 Structural Geology

Two main fault systems that host mineralized veins in the Zacatecas district have been mapped by Ponce et al. (1988), Caballero-Martinez (1999), and Tristán-González et al. (2012) (Figs. 7 and 25). The majority of the veins occur in the oldest system, which consists of ESE- to SE-striking faults that dip between 50° and 70° SW and NE, respectively. These faults have a maximum strike length of 16 km, and associated breccia widths of up to 20 m. This fault system is considered to have first formed in the Eocene because it crosscuts the Jurassic-Cretaceous volcano-sedimentary sequence and the La Sierpe and La Bufa domes, but does not affect the La Virgen ignimbrite (Fig. 7). Two different stages of activity have been identified based on kinematic indicators on the Veta Grande, Mala Noche, and La Cantera fault planes. Fault arrangements, horizontal slickenlines, and grooves on fault planes indicate that the first and principal stage of activity was dextral strike-slip (Figs. 25 and 26a; Tristán-González et al., 2012). The horizontal slickenlines are overprinted by oblique slickenlines, which indicates that the second stage of movement was normal-left oblique. A breccia containing fragments of vein in the hanging-wall of the La Cantera fault/vein indicates that this normal fault reactivation occurred after the initial mineralizing event (Fig. 26b). Pyroclastic breccias at the base of the mid-Eocene La Virgen ignimbrite also contain vein fragments indicating that pyroclastic volcanism continued after mineralization, which is consistent with the dates obtained in this study.

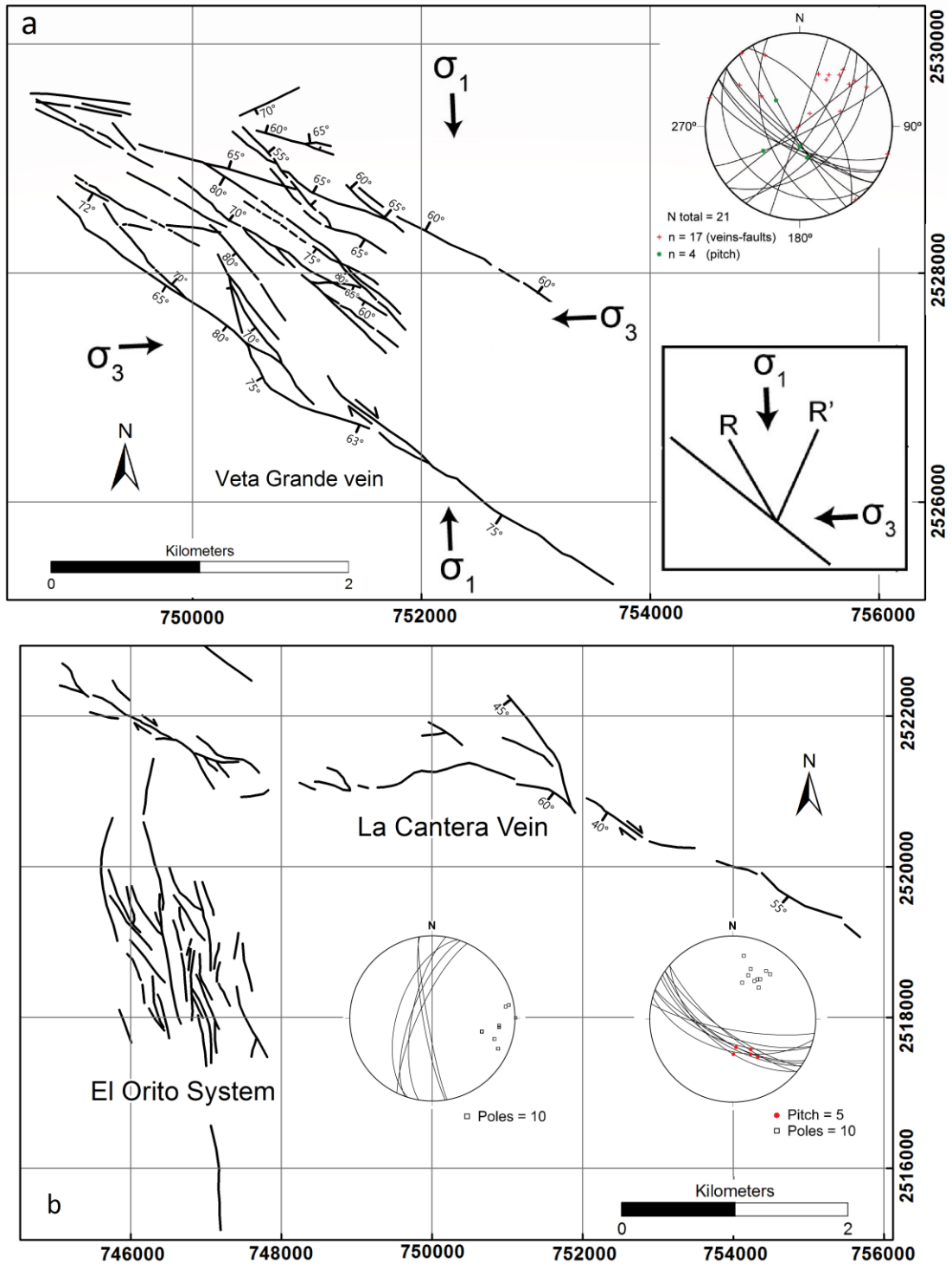

Figure 25. Structural maps of the (a) Veta Grande and La Cantera ENE-striking dextral strike-slip fault systems, and (b) El Orito N–S-striking normal fault system (modified from Perez-Martinez et al., 1961). In (a) the stereonet shows 30°–35° NW- and 20°–30° NE-striking secondary faults (R and R', respectively), and planes from the main Veta Grande fault/vein measured in the field by Tristan-Gonzalez et al. (2012). The Riedel diagram shows a model for these data. In (b) the stereonet represents data from the La Cantera fault/vein measured in the field by Tristan-Gonzalez et al. (2012).

The younger of the two main fault systems strikes N–S with vertical to steep westerly dips (Fig. 25b). This system cuts both the Jurassic–Cretaceous volcano-sedimentary sequence and the La Virgen ignimbrite. Veins filling this fault system show anastomosing arrangements where hosted by the Jurassic-Cretaceous volcano-sedimentary sequence. Here, individual veins range in thickness from 1 to 4 m, and multiple parallel vein sets occur over widths of up to 22 m in the El Compas mine, separated by ~2 m-wide panels of wall rock. Conversely, where the veins occur within the La Virgen Ignimbrite, they are typically planar, less than 1 m thick, and less mineralized relative to within the Jurassic-Cretaceous volcano-sedimentary sequence.

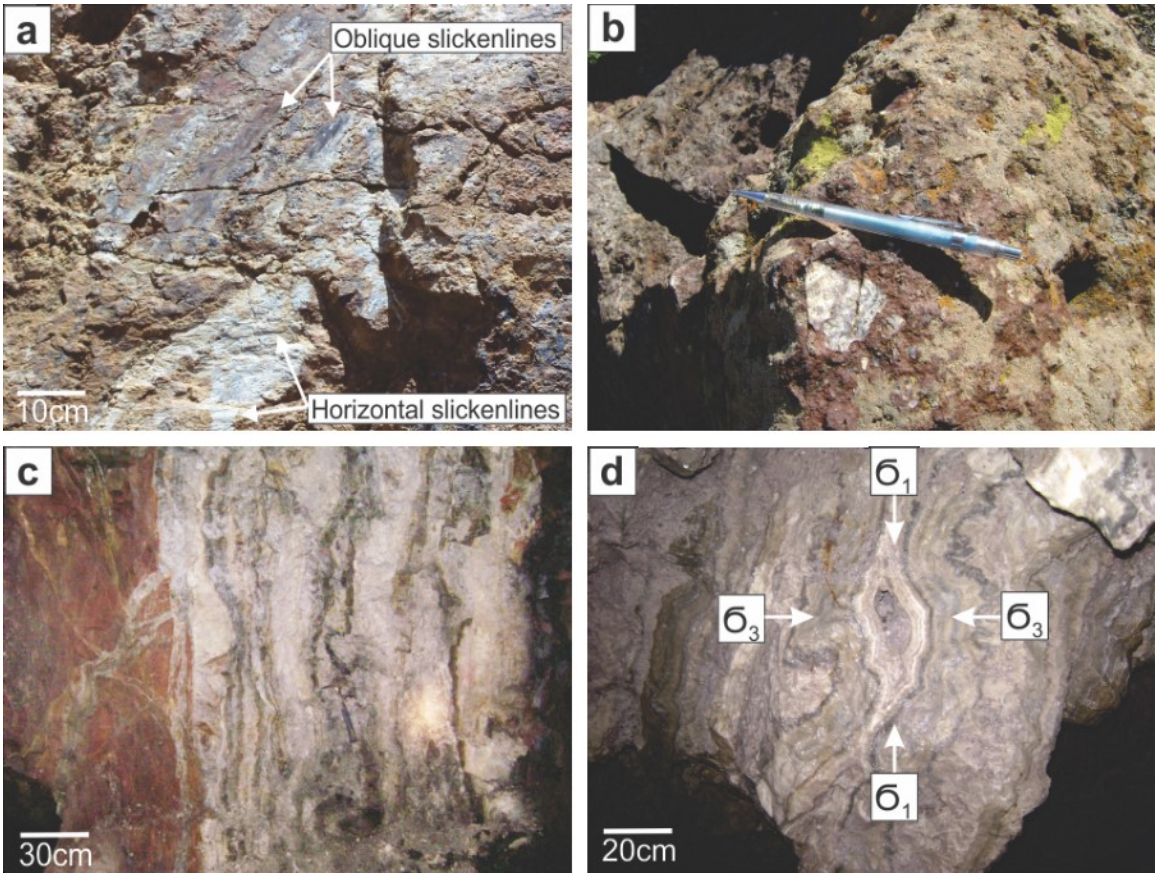

Figure 26. Oblique slickenlines overprinting horizontal slickenlines on a fault plane of the Mala Noche fault (photo courtesy of Tristan-Gonzalez). (b) Fragments of quartz vein in a fault breccia in the hangingwall of the La Cantera fault/vein (E749645, N2521109). (c) Underground vertical stope wall showing the El Compas vein filling a vertical extensional fault, and (d) vertical face of a dilational fault jog in the El Compas vein (level 4; E747109, N2515904).

Kinematic indicators, structural data collected from the El Compas underground mine, and surface mapping of vein arrangements show that these veins formed in dominantly extensional normal faults with a sinistral component. Steeply dipping to vertical extension faults and dilatational fault jogs with vertical principal stress direction (σ_1) and horizontal least principal stress direction (σ_3) are typical features in the El Compas vein (Fig 26c–d). A sinistral strike-slip component is interpreted from NW-striking horsetail splays (Fig. 26; Nelson, 2005). The age of these faults and related veins is considered to be early Oligocene, based on an age obtained for adularia from a vein in this structural system (29.19 ± 0.20 Ma; see below).

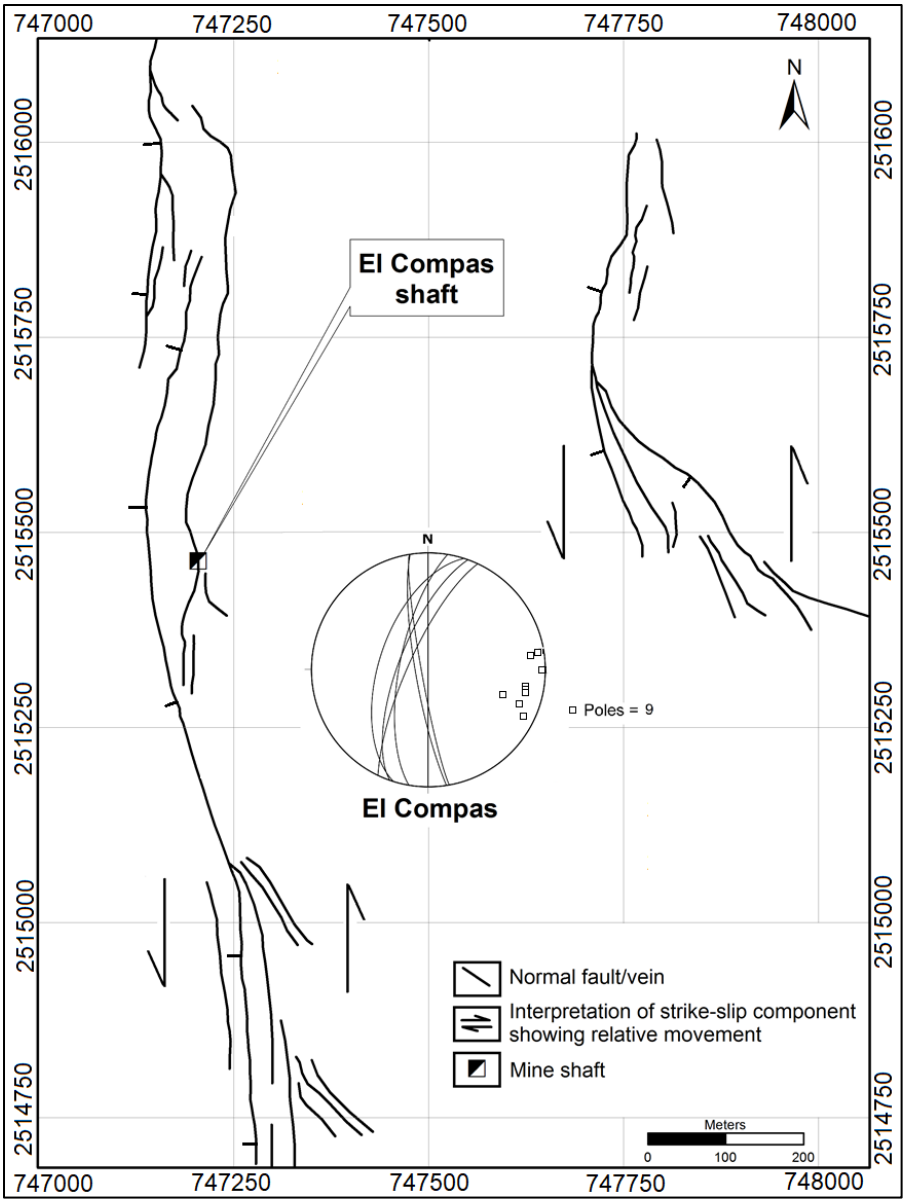

Figure 27. Surface map of the El Compas veins showing second-order NW-striking vein patterns. The stereoplot shows data collected from the El Compas underground mine by Nelson (2005).

4. Analytical Methods and Samples

Locations and descriptions of samples analyzed for geochemistry and geochronology are listed in Table 1.

Sample	Location	UTM Easting (NAD-27)	UTM Northing (NAD-27)	Sample type/Drill hole name (depth)	Analysis	Description
ZABU-01	La Bufa dome	750195	2520755	Outcrop	Litho-geochemistry; U-Pb	Gray pale to pinkish rhyolite with an average of 2% phenocrysts (1–2 mm) of sanidine, quartz, orthoclase, and rare biotite, in a vitreous matrix.
ZASI-02	La Sierpe dike	747327	2524177	Drill hole S38 (750–758 m)	Litho-geochemistry; U-Pb	Gray to whitish rhyolite, varying in texture from aphanitic to flow banded, with <1% quartz, K-feldspar, and accessory biotite, set in a microcrystalline matrix, commonly with disseminations of very fine-grained pyrite.
ZAPA-03	El Padre dome	748383	2517921	Outcrop	Litho-geochemistry; U-Pb	Pink to reddish rhyolite with ~3% phenocrysts of sanidine, quartz, orthoclase (up to 3 mm long), and fine-grained biotite. The matrix is vitreous and shows vertical flow banding surrounding xenoliths.
ZAVI-04	La Virgen ignimbrite	746915	2515212	Outcrop	Litho-geochemistry; U-Pb	Pinkish rhyolitic welded ignimbrite containing pumice with eutaxitic texture and broken crystals of quartz, sanidine, and biotite in a partially devitrified matrix.
ZAC1-07	MalaNoche Volcano-sediments	748702	2524005	Drill hole CGS151 (15.4–27.8 m)	Litho-geochemistry	Basaltic-andesite with porphyritic texture formed by plagioclase phenocrysts in a cryptocrystalline matrix. Sample taken from the volcano-sedimentary succession.
ZAC2-08	MalaNoche Volcano-sediments	749485	2523575	Drill hole CGS154 (396– 399 m)	Litho-geochemistry	Basaltic-andesite with porphyritic texture formed by plagioclase phenocrysts in a cryptocrystalline matrix. Sample taken from the volcano-sedimentary succession.

Sample	Location	UTM Easting (NAD-27)	UTM Northing (NAD-27)	Sample type/Drill hole name (depth)	Analysis	Description
ZAC4-10	Sierpe dike	747358	2524160	Drill hole CGS41 (100– 102 m)	Litho-geochemistry	Gray rhyolite with aphanitic flow banded texture and disseminations of very fine-grained pyrite
ZA01-11	El Compas Volcano-sediments	746945	2515958	Drill hole 08-COM-34 (50-50.6m)	Litho-geochemistry	Redish colour andesite with porphyritic texture formed by microlites of plagioclase in a vitreous matrix with oxidized pyrite finely disseminated
ZA02-12	El Compas Volcano-sediments	747322	2516410	Drill hole 08-COM-31 (143.5-144m)	Litho-geochemistry	Grey colour porphyritic andesite with ~10% phenocrysts of plagioclase (~3 mm in size) set in a vitreous matrix.
CGS139-210	Mala Noche dikes	746850	2523925	Drill hole CGS139 (210.30–211.3 m)	Litho-geochemistry; U-Pb	Sample of pale gray to whitish rhyolitic dike. The main phenocrysts are ~1% plagioclase (~1 mm in size) set in a cryptocrystalline silica groundmass with fine-grained disseminated pyrite. Plagioclase shows strong pervasive sericitic alteration.
CGS139-288	Mala Noche dikes	746850	2523925	Drill hole CGS139 (288.5–291.10 m)	Litho-geochemistry; U-Pb	Sample of pale gray to whitish rhyolitic dike. Phenocrysts of plagioclase (~1 mm in size) are set in a cryptocrystalline silica groundmass with fine-grained disseminated pyrite, and altered to sericite.
CGS198	Mala Noche dikes	745320	2524692	Drill hole CGS198 (267.40–269.50 m)	Litho-geochemistry	White, compact marble with a roughly equigranular texture, composed primarily of recrystallized calcite.
COM-L7	El Compas vein	747109	2515904	Level 7 underground mine (70 m)	40Ar/39 Ar	Banded vein consisting of greenish quartz inter-banded with white quartz, creamy adularia, and calcite bands.

Sample	Location	UTM Easting (NAD-27)	UTM Northing (NAD-27)	Sample type/Drill hole name (depth)	Analysis	Description
VG1B-S8	Veta Grande vein	750738	2526639	Drill hole 08VGX01B (420m)	40Ar/39 Ar	Breccia vein cemented by >5% sulphides (pyrite>sphalerite>galena>argentite) and gangue minerals (quartz, calcite, adularia, and late ankerites)
COS39	Mala Noche vein	747158	2524175	Drill hole S39 (689m)	RAMAN /LA-ICP	Hydrothermal breccia which consist of sharply angular fragments of white rhyolite, cemented by quartz-chalcopyrite-pyrite veins
TVG	Veta Grande vein	751680	2526285	Grab sample/ surface	RAMAN / LA-ICP	Sample of amethystine quartz crystals showing crustiform banding with discontinuous bands containing sulfides and sulfosalts

Table 1. Whole-Rock geochemistry, $^{40}Ar/^{39}Ar$, and U-Pb geochronological sample locations and descriptions.

4.1 Electron Microprobe Analyses

Quantitative analyses of sulfides and selenides were obtained by wavelength dispersive spectrometry (WDS) using a JEOL 8900 electron microprobe at the University of Alberta. The Mala Noche and Veta Grande sulfides were analyzed for S, As, Ag, Au, W, Pb, Bi, Fe, Sb, Cu, and Zn and the El Compas vein selenides were analyzed for S, Ag, Au, Br, Se, Cl, and Hg. The instrument was operated at an accelerating voltage of 20 kV and current of 20 nA, with peak and background count times at 20 and 10 s, respectively. A CAMECA-SX-100 electron microprobe was used under the energy dispersive spectroscopy (EDS) mode to aid in the identification of silicate and oxide minerals and to obtain images under the back-scattered electron (BSE) mode.

The operating conditions of the instrument were an accelerating voltage of 15 kV and a current of 20 nA.

4.2 Whole Rock Geochemistry

Major- and trace-element compositions of eleven samples of volcanic host rock were analyzed at Actlabs Laboratories in Ontario, Canada. Four samples of basaltic lava flows are from the Jurassic-Cretaceous volcano-sedimentary succession, and the other six are from the Eocene subvolcanic and volcanic rocks. The analytical package used was 4E-research, which includes a combination of inductively coupled plasma (ICP), inductively coupled plasma emission mass spectrometry (ICP-MS), and instrumental neutron activation analysis (INAA) methods. Detection limits for each element along with full analyses are listed in Table 2. Replicate analyses of certificated standards indicate accuracy to within 5 relative percent for

major elements and 10 relative percent for trace elements.

Analyzed Symbol	Unit	Analysis Method	Detection Limit	ZABU-01	ZASI-02	ZAPA-03	ZAVI-04	ZAC1-07	ZAC2-08	ZAC4-10	ZA01-11	ZA02-12	CGS139
SiO2	%	FUS-ICP	0.01	74.17	73.75	78.83	81.94	46.19	50.67	74.34	46.19	47.18	72.12
Al2O3	%	FUS-ICP	0.01	12.87	12.14	10.44	9.01	15.94	16.87	13.13	16.35	15.72	11.80
Fe2O3(T)	%	FUS-ICP	0.01	1.88	1.36	1.86	1.46	10.24	9.38	1.93	9.89	10.16	4.99
MnO	%	FUS-ICP	0.001	0.03	0.03	0.03	0.01	0.20	0.19	0.04	0.16	0.17	0.04
MgO	%	FUS-ICP	0.01	0.27	0.48	0.07	0.04	5.54	4.95	0.59	6.35	9.10	0.17
CaO	%	FUS-ICP	0.01	0.42	0.68	0.08	0.10	9.80	11.37	0.73	11.46	10.02	0.07
Na2O	%	FUS-ICP	0.01	1.45	1.23	0.21	0.58	3.49	1.95	1.32	2.87	1.79	0.17
K2O	%	FUS-ICP	0.01	7.27	7.23	8.28	6.86	0.83	0.75	5.86	1.32	0.71	8.74
TiO2	%	FUS-ICP	0.001	0.09	0.07	0.08	0.07	1.21	0.92	0.10	1.37	1.58	0.10
P2O5	%	FUS-ICP	0.01	0.03	0.02	0.04	0.01	0.12	0.13	0.02	0.13	0.16	0.01
LOI	%	FUS-ICP		1.44	1.87	0.77	0.34	6.31	3.43	2.55	4.86	3.84	0.40
Total	%	FUS-ICP	0.01	99.93	98.85	100.70	100.40	99.87	100.60	100.60	100.90	100.40	98.61
Au	ppb	INAA	1	< 1	< 1	< 1	64.00	< 1	< 1	< 1	< 1	< 1	22.00
Ag	ppm	INAA / TD-ICP	0.5	< 0.5	0.70	< 0.5	< 0.5	< 0.5	< 0.5	< 0.5	< 0.5	< 0.5	< 0.5
As	ppm	INAA	1	102.00	35.00	33.00	27.00	< 1	9.00	2.00	18.00	3.00	90.00
Ba	ppm	FUS-ICP	1	938.00	1473.00	901.00	97.00	63.00	135.00	954.00	90.00	187.00	1850.00
Be	ppm	FUS-ICP	1	4.00	< 1	1.00	1.00	< 1	< 1	4.00	< 1	< 1	2.00
Bi	ppm	FUS-MS	0.1	< 0.1	0.70	< 0.1	< 0.1	< 0.1	< 0.1	< 0.1	< 0.1	< 0.1	< 0.1
Br	ppm	INAA	0.5	< 0.5	< 0.5	< 0.5	< 0.5	< 0.5	< 0.5	< 0.5	< 0.5	< 0.5	< 0.5
Cd	ppm	TD-ICP	0.5	< 0.5	< 0.5	< 0.5	< 0.5	0.60	< 0.5	< 0.5	0.60	< 0.5	< 0.5
Co	ppm	INAA	0.1	1.40	16.00	1.20	1.30	41.40	35.00	1.40	42.70	42.90	4.10
Cr	ppm	INAA	0.5	< 0.5	6.60	9.10	4.50	55.80	166.00	6.30	305.00	233.00	105.00
Cs	ppm	FUS-MS	0.1	47.20	10.60	13.90	11.30	2.30	4.00	31.60	11.40	2.00	8.80
Cu	ppm	TD-ICP	1	4.00	42.00	10.00	12.00	53.00	42.00	1.00	47.00	49.00	415.00
Ga	ppm	FUS-MS	1	17.00	15.00	10.00	10.00	15.00	14.00	17.00	15.00	15.00	13.00
Ge	ppm	FUS-MS	0.5	1.90	1.10	1.40	1.50	1.50	2.30	1.50	1.30	1.30	0.90
Hf	ppm	FUS-MS	0.1	3.70	4.50	3.40	3.10	1.80	1.30	4.30	2.30	2.80	2.80
Hg	ppm	INAA	1	< 1	< 1	< 1	< 1	< 1	< 1	< 1	< 1	< 1	< 1
In	ppm	FUS-MS	0.1	< 0.1	< 0.1	< 0.1	< 0.1	< 0.1	< 0.1	< 0.1	< 0.1	< 0.1	< 0.1
Sb	ppm	INAA	0.1	35.40	4.10	73.40	12.90	0.70	2.50	1.70	2.00	1.60	3.40
Sc	ppm	INAA	0.01	3.47	3.96	3.01	3.21	38.80	36.70	3.76	37.20	29.60	3.27
Se	ppm	INAA	0.5	< 0.5	< 0.5	< 0.5	< 0.5	< 0.5	< 0.5	< 0.5	< 0.5	< 0.5	< 0.5
Sn	ppm	FUS-MS	1	< 1	6.00	7.00	< 1	< 1	1.00	8.00	< 1	2.00	4.00
Sr	ppm	FUS-ICP	2	75.00	74.00	19.00	38.00	196.00	348.00	65.00	231.00	248.00	120.00
Ta	ppm	FUS-MS	0.01	1.81	1.91	1.48	0.88	0.06	0.02	1.86	0.22	0.15	1.44
Th	ppm	FUS-MS	0.05	14.20	15.90	12.30	16.00	0.26	0.14	14.90	0.26	0.17	14.80
U	ppm	FUS-MS	0.01	4.09	6.68	4.56	3.66	1.10	1.00	5.76	0.23	0.08	5.65
V	ppm	FUS-ICP	5	6.00	< 5	20.00	24.00	364.00	281.00	5.00	248.00	256.00	7.00
W	ppm	INAA	1	< 1	< 1	< 1	10.00	< 1	< 1	< 1	< 1	< 1	< 1
Y	ppm	FUS-ICP	1	23.00	31.00	20.00	20.00	28.00	19.00	26.00	25.00	28.00	26.00
Zn	ppm	INAA / TD-ICP	1	49.00	14.00	16.00	11.00	80.00	46.00	80.00	64.00	73.00	60.00
Zr	ppm	FUS-MS	1	124.00	132.00	108.00	100.00	63.00	44.00	145.00	86.00	109.00	93.00
La	ppm	FUS-MS	0.05	45.30	45.30	36.40	38.40	3.74	2.79	44.90	4.83	4.53	39.40
Ce	ppm	FUS-MS	0.05	82.90	89.60	71.50	77.20	10.60	7.87	84.60	13.40	14.20	79.30
Pr	ppm	FUS-MS	0.01	9.55	10.30	7.91	8.74	1.70	1.27	9.39	2.11	2.33	8.67
Nd	ppm	FUS-MS	0.05	33.20	37.00	27.80	31.70	9.26	6.63	33.80	10.70	11.90	29.80
Sm	ppm	FUS-MS	0.01	5.58	7.18	4.85	5.84	3.09	2.27	6.09	3.32	3.88	5.58
Eu	ppm	FUS-MS	0.005	0.64	0.67	0.54	0.13	1.13	0.86	0.69	1.15	1.48	0.62
Gd	ppm	FUS-MS	0.01	4.38	5.99	3.85	4.27	4.05	2.99	5.15	4.01	4.75	4.39
Tb	ppm	FUS-MS	0.01	0.71	1.00	0.63	0.67	0.79	0.57	0.83	0.75	0.87	0.74
Dy	ppm	FUS-MS	0.01	4.01	5.87	3.77	3.66	5.15	3.71	4.66	4.78	5.60	4.48
Ho	ppm	FUS-MS	0.01	0.80	1.13	0.75	0.74	1.08	0.76	0.89	0.99	1.17	0.85
Er	ppm	FUS-MS	0.01	2.30	3.25	2.14	2.10	3.14	2.23	2.52	2.91	3.48	2.40
Tl	ppm	FUS-MS	0.05	3.96	2.75	8.88	2.88	0.08	0.18	1.84	0.47	0.16	3.01
Tm	ppm	FUS-MS	0.005	0.36	0.49	0.33	0.32	0.48	0.34	0.39	0.43	0.51	0.37
Yb	ppm	FUS-MS	0.01	2.49	3.15	2.29	2.13	3.26	2.30	2.63	2.76	3.27	2.47
Lu	ppm	FUS-MS	0.002	0.40	0.49	0.36	0.33	0.53	0.36	0.42	0.43	0.51	0.36

Table 2. Geochemical analyses of rocks from the Zacatecas district

4.3 $^{40}Ar/^{39}Ar$ Geochronology

Adularia was identified with the aid of petrography and sodium cobaltinitrite staining of drill core and underground hand samples. One sample was selected from the low-sulfidation El Orito system (COM-L7) and another from the stage I intermediate-sulfidation Veta Grande system (VG1B-S8).

Adularia is rare at Veta Grande, and where present occurs as small rhombohedral crystals up to 100 μm long intergrown with quartz and sulfides (Fig. 21c–d). To separate adularia from this sample, a roughly defined band with a high concentration of adularia mixed with sulfides was sawn off with a fine diamond saw, and then crushed and sieved to select the fraction between 85 and 100 μm. Sulfides were removed using heavy liquids (bromoform), and the sample was analyzed by XRD to check purity. Small amounts of quartz were detected, but it was too finely intergrown with the adularia to be removed without further crushing.

The sample from the El Orito system was collected from Level 7 of the El Compas mine. In this system, adularia occurs as fine-grained (<80 μm) euhedral crystals intergrown with microcrystalline quartz and calcite in banded veins (Fig. 24a). A band with the highest proportion of adularia (~90%) was carefully separated with a fine diamond saw, and crushed to hand pick aggregates of adularia in a matrix of quartz. These aggregates were crushed again and sieved to collect the fraction between 85 and 100μm. This fraction was cleaned ultrasonically and analyzed by XRD to determine purity. Small amounts of quartz and calcite were detected by XRD in addition to adularia, but it was decided not to attempt further purification because of the risk of fragmenting individual adularia crystals (which can cause mechanical homogenization of the K-Ar distribution in the sample; Richards and Noble 1998).

The two adularia samples were sent to the Nevada Isotope Geochronology Laboratory at the University of Las Vegas for Ar isotopic analysis. The samples were wrapped in aluminum foil and loaded together with neutron fluence and neutron induced argon interference monitors in sealed silica tubes. Loaded tubes were packed in an aluminum container and sent for irradiation at the U.S. Geological Survey TRIGA Reactor, Denver, CO. Neutron fluence was monitored using the Fish Canyon Tuff sanidine standard (28.02 Ma; Renne et al., 1988). Neutron induced argon interference from K and Ca was corrected using correction factors determined by repeated analysis of synthetic K-glass and optical grade CaF_2 fragments ($(^{40}Ar/^{39}Ar)_K$ = 1.74 (± 67.07%) x 10^{-2}, $(^{36}Ar/^{37}Ar)_{Ca}$ = 2.16 (± 8.78%) x 10^{-4}, and $(^{39}Ar/^{37}Ar)_{Ca}$ = 6.70 (± 1.60%) x 10^{-4}). After irradiation the samples were fused under a 20 W CO_2 beam laser using the step-heating method. The $^{40}Ar/^{39}Ar$ ratios of the gas released from each step were measured using a MAP 215-50 mass spectrometer. Atmospheric argon aliquots were analyzed repeatedly to monitor mass spectrometer discrimination and sensitivity. Measured $^{40}Ar/^{36}Ar$ ratios were 279.72 ± 0.43% during this work, thus a discrimination correction of 1.0565 (4 AMU) was applied to measured isotope ratios. Final data reduction and age calculations were performed using LabSPEC software.

4.4 U/Pb Geochronology

Six samples of Eocene volcanic and subvolcanic rocks collected from surface outcrops and drill-core were dated by the U-Pb zircon method. The zircons were separated at the University of Alberta using standard crushing and mineral separation techniques: approximately 10 kg of each sample were pulverized, and zircons were separated using a Wilfley table, a Frantz isodynamic separator, and heavy liquids (methylene iodide). A population of about 100 zircons

was selected by hand under a binocular microscope based on size, morphology, and optical clarity. Zircons are euhedral with prismatic or elongated habit and well-developed growth zoning, and range in size between 30 and 150 μm in the longest dimension. These characteristics are typical of magmatic zircons (Fig. 28; Shore and Fowler, 1996). Zircons that show textural evidence of inherited cores were avoided. The selected zircons were mounted in epoxy resin for analysis using laser ablation multicollector inductively coupled plasma mass spectrometry (LA-MC-ICP-MS) at the University of Alberta Radiogenic Isotope Facility. The laser spot used was 30 μm, the analytical procedure is described in detail by Simonetti et al. (2005). Descriptions of the samples and their locations are provided in Table 1 and summarized below.

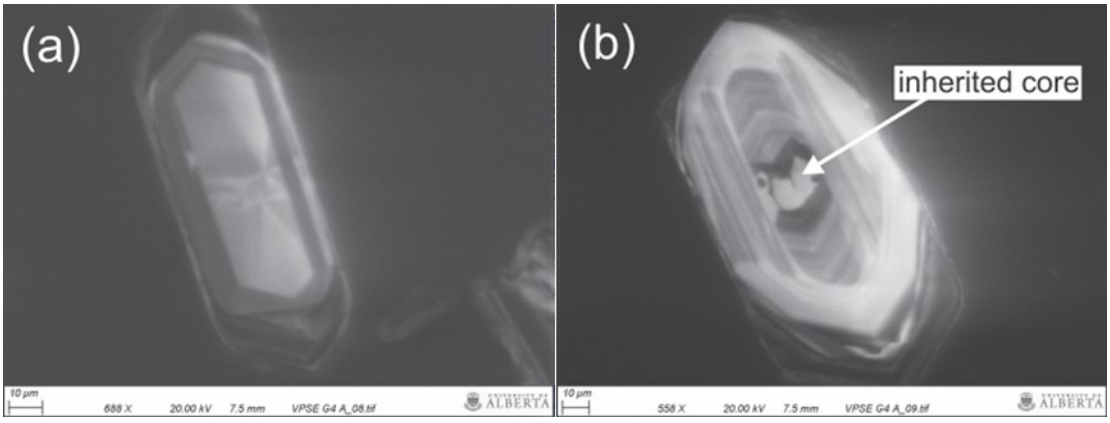

Figure 28. Cathodoluminescence images of representative zircons from sample CGS139 showing (a) prismatic habit and growth zoning typical of magmatic zircons, and (b) inherited core.

Sample ZABU-01 was taken from the top of the La Bufa dome, avoiding xenoliths and obvious alteration; surface weathering rinds were removed in the field. This sample represents the youngest volcanic flow from this dome.

Sample ZASI-02 was collected from drill core at a depth of ~750 m. The hole was drilled vertically down a feeder zone of the rhyolitic La Sierpe plug. This is inferred from the fact that

the drill hole intersects rhyolite at the top, bottom, and intermittently along the length of the hole, with vertical flow-banding textures and subvertical contacts with the metasedimentary country rock. The sample was taken from a central section of one interval of rhyolite, avoiding contacts with the metasedimentary rock and flow-banded zones containing xenoliths.

Sample ZAPA-03 was taken from an outcrop of the El Padre rhyolitic plug. The sample has a porphyritic texture with laminar fabric surrounding sparse xenoliths of andesitic rock. Surface weathering rinds were removed in the field and xenoliths were avoided as far as possible.

Sample ZAVI-04 was taken from the upper level of the La Virgen ignimbrite, where the rock is crystal rich and the number of xenoliths decreases. The sample was taken on the La Virgen plateau away from obvious hydrothermal alteration haloes or weathering.

Samples CGS139-210 and CGS139-288 were taken from drillhole CG-08-139 at 210.30–211.3 m, and 288.5–291.10 m depth, respectively. The samples are from dikes that run parallel to the Mala Noche vein and are spatially associated with Cu-rich mineralization, and consist of pale gray to whitish rhyolite with scarce phenocrysts of sericitized plagioclase set in a cryptocrystalline silica groundmass. Both samples were taken away from contacts with the metasedimentary rock and avoiding xenoliths.

4.5 Fluid Inclusions

More than 870 fluid inclusions from the Mala Noche, Veta Grande, and El Compas veins were measured microthermometrically. Most of the measured inclusions are hosted by quartz, although some inclusions from Veta Grande were also measured in calcite, adularia, and sphalerite. The measurements were performed in fluid inclusion assemblages (FIA) with similar

vapour/liquid ratios, located in the same growth zone or plane, and considered to be primary or pseudosecondary according to the criteria of Roedder (1984). A FIA is a group of inclusions that were trapped at the same time and from the same fluid, usually in a co-spatial cluster such as a growth zone (Goldstein and Reynolds, 1994). Fluid inclusions that showed petrographic evidence of post-entrapment deformation (decrepitating, leaking, necking, fracturing) were not measured except for the ice melting point in some necked inclusions (because the necking process affects only the vapour-liquid ratios, and therefore homogenization temperature, but not the salinity of the liquid in halite-undersaturated fluids). In this case, the homogenization temperatures were not measured and are reported as necked. Additionally, some secondary fluid inclusions from the Mala Noche stage I were measured for comparison purposes. The reported homogenization temperatures are not pressure-corrected and therefore represent the minimum temperature of trapping. Coexistence of liquid- and vapour-rich inclusions in the same FIA provides evidence of phase separation (boiling conditions), in which case the homogenization temperature is equal to the trapping temperature. The approximate depth of formation of a particular FIA with evidence of boiling can be estimated from boiling point curves (Hass, 1971) at the average temperature and salinity of the FIA. This method assumes a hydrostatic pressure regime in the hydrothermal system. Salinities are reported as equivalent wt. % NaCl eq. and were calculated from final ice melting temperatures using the equation of Bodnar (1993). None of the inclusions show evidence of clathrate formation, indicating lack or insignificant amounts of CO_2.

All measurements were completed at the University of Alberta using a Linkham THMSG600 microthermometric stage coupled to an Olympus BX50 microscope. The stage was calibrated using synthetic fluid inclusion standards. The temperature measurement precision and accuracy is ±0.1°C for final ice melting points and ±2°C for homogenization temperatures.

Thirty samples from drillcore intercepts and underground workings were collected and prepared as doubly polished thick sections (150 μm). All samples were observed under both reflected and transmitted light microscopy for petrography and microthermometry.

Samples from the Mala Noche vein were collected based on ore grade intercepts and represent both the vertical and horizontal extent of the mineralization. They are from two different mineralogical stages defined in terms of crosscutting relationships, mineralogy, and textures. Some samples contain both stages (stage I crosscut by stage II) and some samples contain only either stage I or II. Samples from the Veta Grande vein were selected to represent the two stages of mineralization (stage I breccia and stage II rhythmically banded silica), and samples from the El Compas vein represent the main stage mineralization.

4.6 Stable Isotopes

4.6.1 Sulfur Isotopes

The $\delta^{34}S$ isotopic compositions of sulfide minerals from 17 samples, 12 from Mala Noche and 5 from Veta Grande, were obtained at the University of Calgary. Mineral separates (~150 micrograms) were acquired either by crushing the sample and hand picking grains smaller than 1 mm, or by drilling thin section billets with a 1 mm diamond bit dremel tool. The mineral separates were powdered and sulfur isotope ratios ($^{34}S/^{32}S$) analyzed using continuous flow-isotope ratio mass spectrometry in a ISL-AGg a Carlo Erba NA 1500 elemental analyzer interfaced to a Thermo Delta+XL mass spectrometer. The samples were combusted at 1050 °C in a stream of O_2 (gas) to produce SO_2, which was separated from other contaminant gases through a gas chromatograph column and introduced to the mass spectrometer by a helium carrier stream at ~115 ml/min flow. Raw isotopic ratios were normalized to the Vienna Canyon Diablo Troilite

(VCDT) standard using the International Atomic Energy Agency S1, S2, and S3 standards. Internal laboratory standards were analyzed every ten samples within each sample set for quality control. Results are reported with a precision of ±0.3‰ (1σ). Four samples (including a replicate of sample U-202) were selected to analyze handpicked pure mineral separate pairs of co-precipitated galena and sphalerite for geothermometry. Each of these samples was analyzed 10 times to overcome instrumental memory effects, and to achieve an accuracy of ±0.1‰ (1σ). Crystallization temperatures were calculated for sphalerite-galena pairs using the fractionation factor of Rye (1974).

4.6.2 Oxygen Isotope Analyses

The isotopic composition of oxygen in quartz from 14 samples (including two duplicates) were obtained at the University of Alberta using two different methods in two laboratories.

A total of 8 $\delta^{18}O$ analyses from two samples of the Veta Grande vein stage II were obtained using the BrF_5 method of Clayton and Mayeda (1963) at the stable isotopes research laboratory, University of Alberta. These analyses are from bands of amethyst, chalcedonic, and crystalline quartz. The band thickness ranges from 0.3 to 2.5 cm. Amethyst bands vary slightly in color intensity and thickness and are usually mixed with other silica phases. These bands were carefully separated by hand, grained, and analyzed for $\delta^{18}O$. The results are reported in the δ notation as per mil related to the SMOW standard (Craig, 1961) with a precision of ±0.1‰ (2σ). The $\delta^{18}O$ values of fluids were calculated using the average homogenization temperature of the sample and the quartz-water fractionation equation of Clayton et al. (1972).

In-situ oxygen isotope analyses of vein quartz samples were obtained by secondary ion mass spectrometry (SIMS) at the Canadian Centre for Isotopic Microanalysis, University of Alberta. 125 spots were selected for analysis from 12 samples (8 from Mala Noche, 3 from Veta Grande, and 1 from El Compas veins) using doubly polished thick sections previously characterized by fluid inclusion microthermometry. The samples were mounted in epoxy along with quartz reference materials (RMs), lightly polished, washed with soap and de-ionized water, and coated with 10 nm of high-purity Au. Scanning electron microscopy (SEM) characterization was carried out with a Zeiss EVO MA15 instrument equipped with a high-sensitivity, broadband CL detector. Beam conditions were 15kV and 3 nA sample current. A further 40 nm of Au was subsequently deposited on the mount prior to SIMS analysis.

Oxygen isotopes (^{18}O, ^{16}O) in quartz were analyzed using a Cameca IMS 1280 multicollector ion microprobe. A $^{133}Cs^{+}$ primary beam was operated with impact energy of 20 keV and beam current of ~ 2.0 nA. Instrumental mass fractionation (IMF) was monitored by repeated analysis of a quartz primary reference material S0151 (UAQ1; $\delta^{18}O_{VSMOW}$ = +14.45 ‰; R. Stern, unpublished SIMS data) and two quartz secondary reference materials (Larsen and Sharp, 2003) with values of $\delta^{18}O$ = +12.5 ‰ and +18.2 ‰. One analysis of the primary and secondary RMs was taken after every 4 and 8 unknowns, respectively, to determine a standard deviation of 0.08‰. The individual spot errors related to within-spot counting statistics (between-spot geometric effects and correction for instrumental mass fractionation) average ±0.19 ‰.

The isotopic measurement of single fluid inclusions was not possible because the SIMS has no transmitted light capabilities. Therefore, analyses of quartz grains were performed within ~3 mm wide regions containing a previously well-characterized fluid inclusion assemblage. The

regions were selected to represent either saline or dilute primary FIAs, although some samples contain pseudosecondary dilute fluid inclusions within regions of primary saline FIAs. The $\delta^{18}O$ values of fluids were calculated according to the quartz-water fractionation equation of Clayton et al. (1972) using the average homogenization temperature of the FIAs within the analyzed region, and assuming that homogenization temperature approximates the trapping temperature based on evidence of boiling conditions.

Cathodoluminescence analyses help to track different generations of quartz within a grain scale. Observed textures on SEM-CL images result from variations in cathodoluminescence intensity caused by different trace element chemistry in the quartz structure produced at specific physical and chemical conditions during quartz growth (Marshall, 1988; Pagel et al., 2000; Gotze et al., 2001). Textures such as euhedral overgrowths on rounded cores of quartz and euhedral growth zones may indicate partial dissolution, reprecipitation, and recrystallization of quartz, whereas crosscutting bands and quartz-sealed cobweb- and puzzle-like fractures may indicate dilation and fracturing (Rusk and Reed, 2002). The analyzed particular spots were selected on the basis of different cathodoluminescence (CL) response, growth zones, and crosscutting relationships within the selected regions.

4.7 RAMAN and LA-ICPMS

The chemical composition of fluids from fluid inclusions of the Mala Noche, Veta Grande, and El Compas ore-stage vein samples were obtained by LA-ICPMS at Virginia Tech University. Additionally, solid phases present in some inclusions from the Mala Noche vein were identified using RAMAN spectroscopy. The purpose of these analyses was to constrain the composition of fluids from which the Zacatecas district ore deposits formed, and to use these

data to simulate the mechanisms of mineral precipitation based on thermodynamic modeling using the software CHIM-XPT (Reed, 1998). The samples, ~5 mm chips of doubly polished thick sections, were previously analyzed microthermometrically at the University of Alberta as described above.

RAMAN spectroscopy was performed prior to laser ablation at the Virginia Tech Vibrational Spectroscopy Laboratory using a high-resolution laser Raman spectrometer (JY Horiba LabRam HR; 800 mm). Fluid inclusions were excited by an air-cooled 514.529 nm Laser Physics 100S-514 Ar+laser. The diameter of the laser beam was ~1 μm using a 40x objective lens. Liquid, gas, and solid phases trapped in the inclusions were analyzed with the purpose of identifying the solid phases and the presence of CO_2 or other gases. This technique can be used to measure CO_2 densities in fluid inclusions with a precision of ±0.02 g/cm^3 (Rosso and Bodnar, 1995). The limit of detection is based on the pressure of CO_2 in the inclusion, which is a factor of the volume % vapour and size of the fluid inclusion. Usually, RAMAN can detect CO_2 in a moderately-sized inclusion (~50 μm) if the CO_2 pressure is in the range of about 2-4 bars (Bodnar, personal communication, 2017).

After RAMAN spectroscopy, LA-ICP-MS analyses were conducted using an Agilent 7500ce quadrupole ICP-MS and a Lambda Physik GeoLas 193 nm Excimer laser ablation system with He gas flow. The diameter of the ablating laser beam was adjusted from 10 to 40 μm according to the size of the inclusions. Transient signals of 26 elements were measured in time-resolved mode. The background signal was measured with the laser off for ~50 s and immediately followed by progressive ablation of the sample for another 3–4 min. The sections of the signal corresponding to background and fluid inclusion analysis were adjusted manually after visual inspection of the spectra using the AMS analytical software (Mutchler et al., 2008; Fig.

29). Analyses of single moderately saline fluid inclusions typically yielded short transient signals (3–10s) with a single sharp peak for Na, which was used to identify the initial opening of the fluid inclusion. During ablation, some samples cracked and several inclusions (including some diluted inclusions) were opened simultaneously. These analyses yielded dispersed and extended (>20s) transient signals with either smooth or multiple Na peaks and were not used in the modelling simulations. In the case where several inclusions located at different depths were opened during the same run, only the first opened inclusion was considered for the simulation because of the risk of contamination for the others. The chemical composition of dilute fluid inclusions could not be obtained.

The glass standard NIST 610 was measured 4 times (two at the beginning and two at the end of each run) to compensate for instrumental drift. The AMS software integrates background, fluid inclusion, and external standard signals with the ice melting point, previously determined from microthermometry, using Na as an internal standard to calculate concentration of the elements in ppm, limits of detection, and concentration in weight percent of the chloride salt containing the element. Analytical precision using Na as an internal standard is typically within 20% (Gunther et al., 1998; Heinrich et al., 2003).

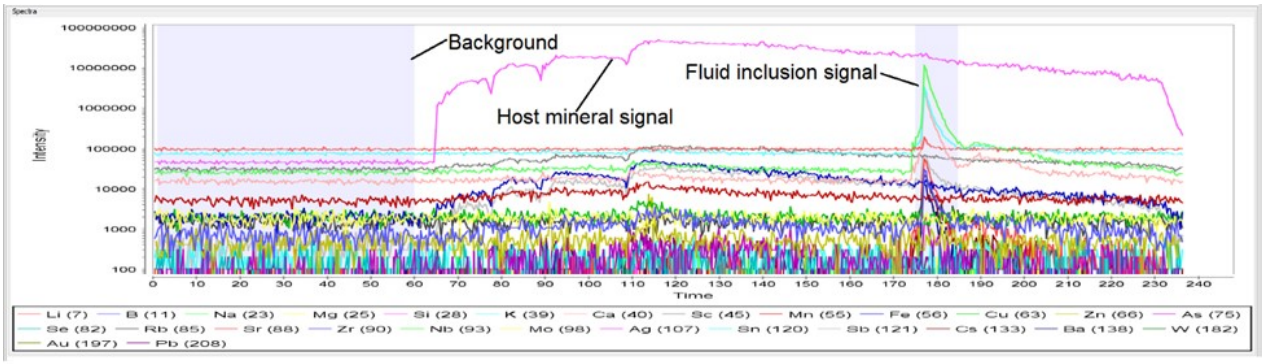

Figure 29. A time-resolved signal for a sample TVG9-P10, showing selected windows for the background and for the fluid inclusion.

4.8 CHIM-XPT Modeling

Chemical processes that controlled the mineral deposition of the Mala Noche vein stage I and the Veta Grande vein stage II were modelled mathematically using the software CHIM-XPT, an expanded version of CHILLER (Reed, 1998). The software CHIM-XPT computes simultaneous equilibrium among minerals, gases, and aqueous phase under progressively changing physicochemical conditions (composition X, pressure P, and temperature T), based on thermodynamic data contained in the database SOLTHERM (Reed and Palandri, 2010) and given starting XPT parameters. The software GEOCAL and SOLVEQ (Reed, 1982, 1998) were used to estimate the initial water composition to be used in CHIM-XPT simulations. GEOCAL was used to convert concentration of cations in ppm obtained from selected LA-ICP-MS analyses into an input file for SOLVEQ with concentrations in total moles. Average gas concentrations obtained from the literature for an amethyst quartz sample, which corresponds to the Veta Grande stage II were also included (except for CH_4) using GEOCAL (Table 3; Albinson, 2001). Methane was reported by Albinson (2001) to have an average concentration of 0.56 mole percent, but it was not possible to reach equilibrium with this value using GEOCAL, and attempts to titrate the methane using SOLVEQ or CHIM-XPT were unsuccessful. Therefore, we used values of CH_4 computed from equilibrium between the other measured components in boiling simulations. Because there is evidence of boiling, the steam fraction (X) was obtained based on the enthalpy balance equation below assuming that boiling took place at constant enthalpy (no heat loss or added) as commonly observed in active geothermal systems (Henley et al., 1984):

$$m_{liqT_1}\overline{H}_{liq,T_1} = m_{steam,T_2}\overline{H}_{steam,T_2} + m_{liq,T_2}\overline{H}_{liq,T_2}$$

where $\overline{H}$ refers to the enthalpy per gram (of steam or liquid water), *m* refers to grams of liquid or steam, T_1 refers to the initial temperature of the pure liquid at depth, and T_2 refers to the temperature of the liquid and steam after they ascend and boil. The enthalpy for both liquid and vapour phase have been determined for pure water at temperatures from 0–374°C (Keenan et al., 1969). Although the Veta Grande vein fluids are saline, we can use these enthalpy constraints to obtain an approximated fraction of steam because the effects of salinity on the enthalpy of water are small (Reed, 1988). Evidence of boiling for the Veta Grande vein was observed at 280°C, but the fluids likely started boiling at slightly higher temperature. For modelling purposes, the starting boiling temperature was set at 320°C. Under these conditions, the steam fraction is calculated to be 15 wt.%. This result is comparable to the 35 wt.% steam fraction released at the Broadlands geothermal system surface (Spycher and Reed, 1989).

	Sample Veta Grande 93-1 Surface (Quartz)													
Run	**5456A**	**5456B**	**5456C**	**5456D**	**5456E**	**5456F**	**5456I**	**5456J**	**5457A**	**5457B**	**5457C**	**5457D**	**5457E**	**Average (n=13)**
H_2	0.119500	0.031990	0.095120	0.04071	0.11794	0.07601	0.60523	0.14203	0.02375	0.032420	0.06980	0.12964	0.16144	0.126583
CH_4	0.129400	0.155000	0.256540	0.21474	0.50732	0.39763	3.38087	0.88920	0.04658	0.128250	0.24776	0.44250	0.57252	0.566793
N_2	0.028000	0.166530	0.072180	0.04405	0.06670	0.06321	0.20946	0.10457	0.01726	0.020500	0.07135	0.09118	0.10811	0.081777
O_2	0.003480	0.013900	0.007330	0.00306	0.00283	0.00456	0.00645	0.00043	0.00155	0.003040	0.00412	0.00434	0.00483	0.004610
H_2S	0.000340	0.000250	0.000220	0.00024	0.00003	0.00033	0.00025	0.00034	0.00011	0.000047	0.00020	0.00017	0.00035	0.000222
C_nH_n	0.000800	0.000710	0.000990	0.00083	0.00163	0.00116	0.01104	0.00184	0.00047	0.000850	0.00076	0.00173	0.00256	0.001952
CO_2	0.311001	0.128430	0.129630	0.21366	0.26164	0.26140	0.32041	0.37911	0.17642	0.209340	0.31063	0.40624	0.53262	0.280041
SO_2	0.000048	0.000067	0.000099	0.00004	0.00015	0.00016	0.00026	0.00055	0.00011	0.000058	0.00011	0.00008	0.00013	0.000144

Table 3. Average gas concentrations reported in mole percent from the Veta Grande stage II amethystine quartz (Albinson et al., 2001).

SOLVEQ was applied to compute the distribution of aqueous species in the fluid at a given temperature based on microthermometric analyses. The initial pH and total mole concentrations of Al were estimated forcing equilibrium with muscovite. Because quartz is a ubiquitous mineral, the concentration of Si was set for quartz saturation. The total concentration

of Cl^- in solution was calculated by SOLVEQ to account for charge balance and readjusted by CHIM-XPT in each run. Arbitrary concentrations of oxidized and reduced sulfur were used initially in CHIM-XPT, and entries were adjusted by trial and error to prevent the precipitation of sulfate minerals. Multiple runs for boiling, mixing, cooling, and water-rock reaction simulations were applied to each starting fluid, and the results compared with the observed mineral paragenesis to validate potential mechanisms of ore precipitation. The results were plotted to show the sequence and relative amounts of minerals precipitated, variations in the total concentrations of dissolved components, pH, and in individual aqueous species relative to understand redox variations along the reaction path.

CHIM-XPT can simulate systems where precipitated minerals are not removed (fractionated), allowing them to remain in contact and react with the fluid (i.e., closed systems), or where precipitated minerals are fractionated and do not react with evolved fluids (i.e., open systems). The water-rock reaction simulations were run without mineral fractionation assuming a very low infiltration rate and allowing precipitated minerals to react with the fluid. The boiling, cooling, and mixing scenarios, were run with mineral fractionation, assuming rapid fluid flow and gas escape through fractures. For comparison purposes some experiments were run without fractionation, but very similar results were obtained, possibly because the precipitated minerals were not re-dissolved under the new physicochemical conditions (Spycher and Reed, 1989).

Boiling was modeled assuming constant enthalpy (as observed in active geothermal systems; Henley et al., 1984) with temperature decrements of 5°C, and total pressure set slightly lower than the saturation pressure, which was obtained from an earlier run on CHIM-XPT where boiling was prevented. Lacking the chemical composition of dilute fluid inclusions, mixing was simulated by progressively adding 0.5 kg of 150°C pure water into 1 kg of the starting solution,

assuming that the mixing component was heated meteoric water. Water-rock reactions were simulated by titrating 1 kg of basaltic andesite into 1 kg of the starting hydrothermal fluid. The whole-rock composition used for the reaction was from sample ZAC2-08 (Tables 2 and 5).

5. Results

5.1 Whole-Rock Geochemistry

The results of whole-rock geochemical analyses are reported in Table 2. Major-element compositions were recalculated to 100% on a volatile-free basis for plotting on geochemical classification diagrams (loss-on-ignition values range from 3.43–5.91 wt.% for Jurassic-Cretaceous rocks and 0.34 to 1.87 wt. % for Eocene rocks).

5.1.1 Jurassic–Cretaceous volcanic rocks

Jurassic–Cretaceous volcanic rocks show evidence for propylitic alteration and contain varying amounts of chlorite, epidote, calcite, and disseminated pyrite. This is reflected in high LOI values (3.4–5.9 wt. %). Despite this alteration and low grades of regional metamorphism (greenschist facies), the samples plot in the basalt field in a TAS diagram (Fig. 30a). This is consistent with the immobile element (Zr/TiO_2 vs Nb/Y) classification diagram of Winchester and Floyd (1977), where the samples fall within the range andesite/basalt (Fig. 30b).

Chondrite-normalized rare earth element (REE) patterns for the Jurassic–Cretaceous basalts are flat, at between 10 and 30 times chondritic values (Fig. 31a; normalization values of Sun and McDonough, 1989). These patterns are characteristic of back-arc basalts, which is the

tectonic setting proposed for these rocks by different authors (Tardy et al., 1991; Yta, 1992; Lapierre et al., 1992; Centeno-Garcia and Silva-Romo, 1997). The samples show low normalized abundances on an extended trace-element diagram (Fig. 31b) with flat patterns for Zr, Ti, and Y (~5 times primitive mantle values), and small negative Nb and Th anomalies, with minor enrichments of the large ion lithophile elements (Rb, Ba, K, and Sr; between 10 and 100 times primitive mantle values).

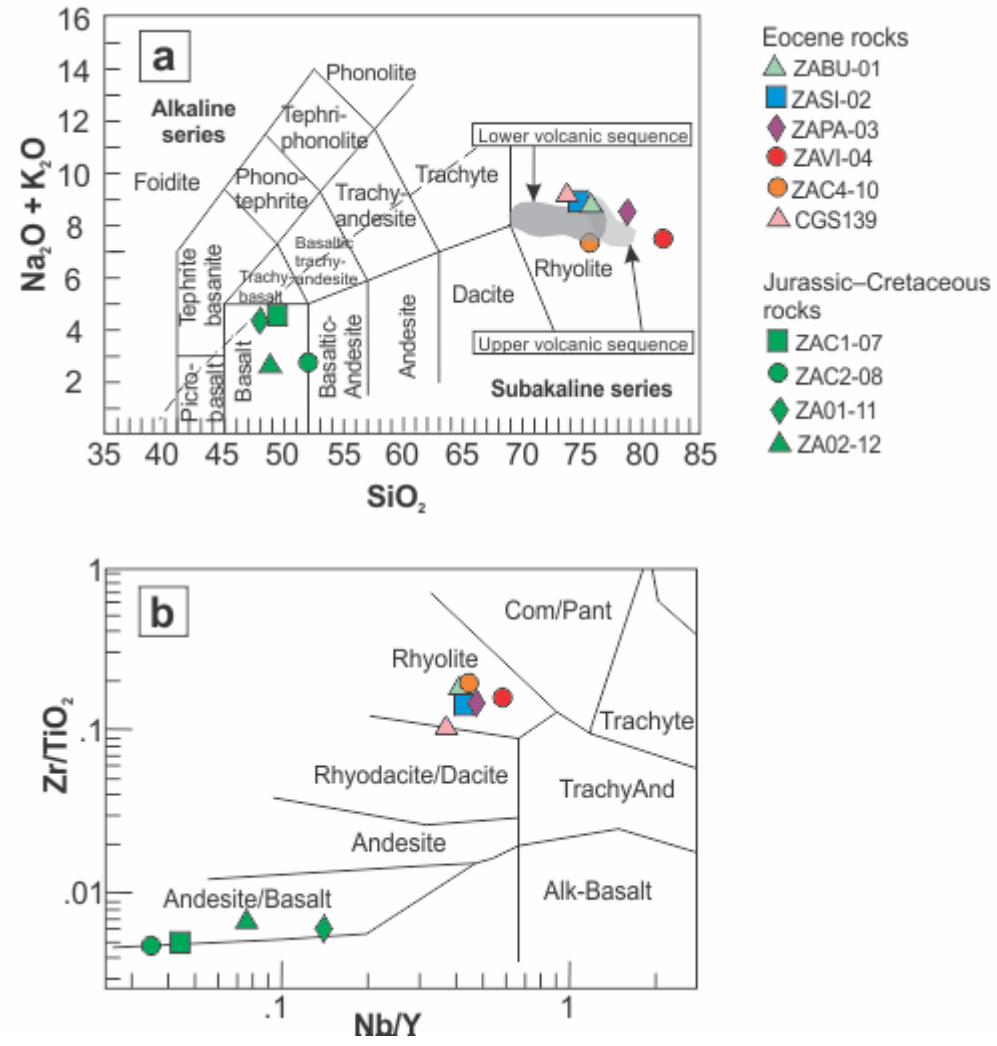

Figure 30. (a) Total alkali vs. silica diagram (LeBas et al., 1986); alkaline-subalkaline boundary from Irvine and Baragar (1971) showing the major element classification of the Jurassic–Cretaceous lava flows and Eocene volcanic and hypabyssal rocks from the Zacatecas district and (b) Zr/TiO_2 vs. Nb/Y diagram (Winchester and Floyd 1977) showing their corresponding trace element classification.

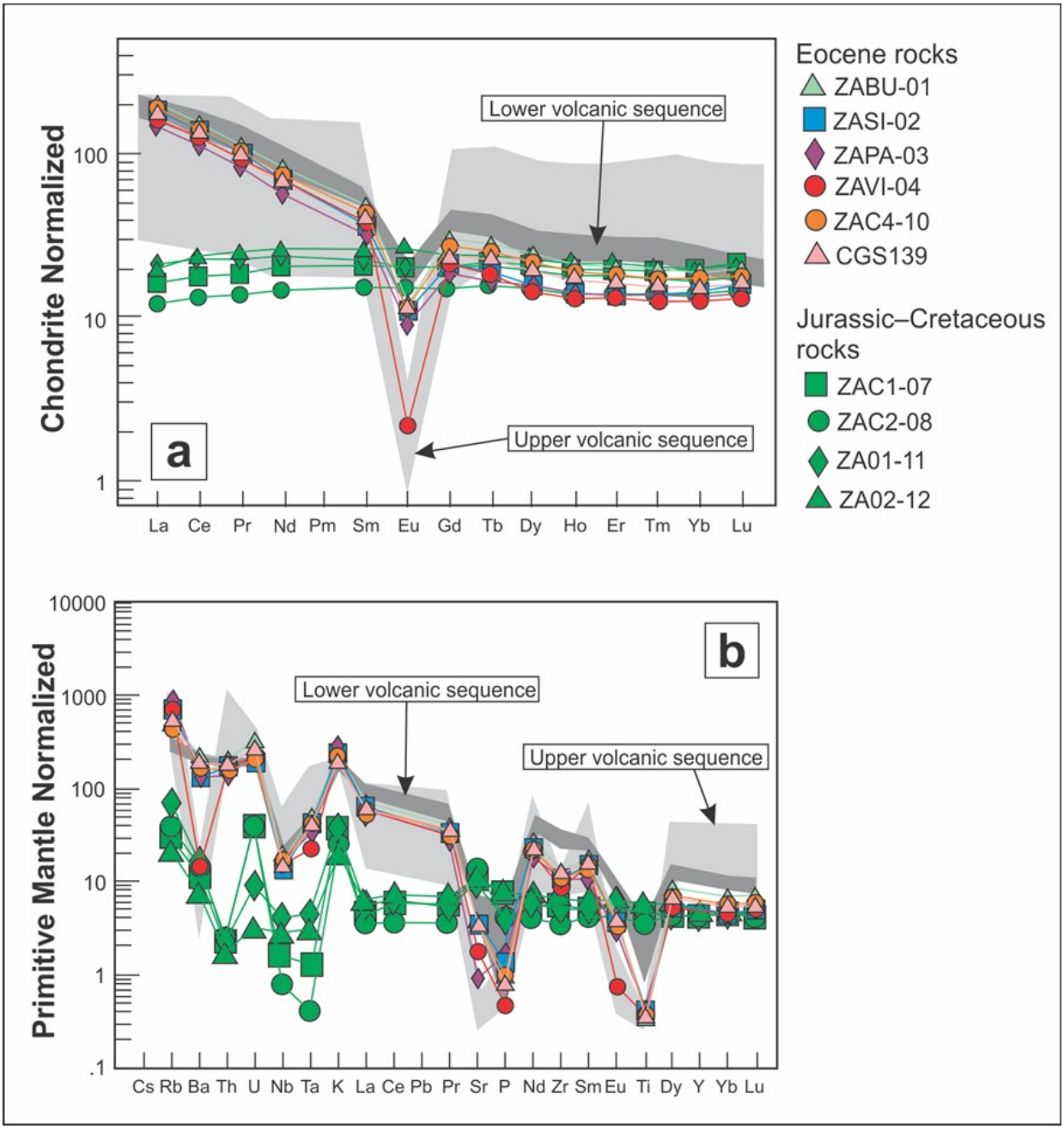

Figure 31. (a) Chondrite-normalized REE diagram (normalization values of Sun and McDonough, 1989) and (b) primitive mantle-normalized extended trace element diagram for samples from the Zacatecas district (normalization values of Sun and McDonough, 1989). The composition ranges of the lower and upper volcanic sequences of the southern Mesa Central are shown in dark and light gray, respectively (data from Orozco-Esquivel et al., 2002).

5.1.2 Eocene Igneous Rocks

Samples of Eocene felsic volcanic rocks and domes plot in the rhyolite field on TAS and immobile trace-element diagrams (Fig. 30). The anomalously high silica content of sample ZAVI-04 (81.9 wt. % SiO_2) is likely due to deuteric silicification, as indicated by euhedral quartz crystals growing in vesicles within its partially devitrified matrix (Fig. 11d). All samples show high K (6.86–8.28 wt. % K_2O) and low Na contents (0.21–1.45 wt.% Na_2O), which are thought to broadly reflect their primary magmatic compositions, despite evidence for minor sericitic and argillic alteration of feldspars. A high-K calc-alkaline rhyolite composition is therefore proposed for these felsic volcanic rocks.

When plotted on a chondrite-normalized REE diagram (Fig. 31a) the suite shows strong enrichment of LREE with respect to heavy rare earth elements (HREE), and pronounced negative Eu anomalies that increase with SiO_2 content, indicating higher degrees of plagioclase fractionation from more evolved rhyolites. On a normalized extended trace-element diagram (Fig. 31b) the suite shows strong enrichments in large ion lithophile elements, and negative anomalies for Nb, Ta, and Ti, which are characteristic of subduction-related magmas (Gill, 1981; Brenan et al., 1994; Stolz et al., 1996). Strong negative anomalies for Sr and Eu suggest extensive fractionation of plagioclase (as noted above), and large negative anomalies for P and Ti are likely due to fractionation of apatite and Fe-Ti oxide minerals, respectively.

5.2 $^{40}Ar/^{39}Ar$ Geochronology

Apparent age spectra and inverse isochron plots are presented in Figure 32, and full analytical data are reported in Appendix C. Errors for ages are reported at the ±2σ level in the text and ±1σ in the plots.

Sample VG1B-S8 from an early-stage intermediate-sulfidation vein at Veta Grande produced a spectrum with high initial apparent ages that decrease to a plateau (steps 3–9: 94% of the ^{39}Ar released; Fig. 32a) with an age of 46.49 ± 0.44 Ma (slightly younger than the total gas age of 47.80 ± 0.42 Ma). Both plateau and total gas ages are considered to be anomalously old due to the presence of minor excess ^{40}Ar, as indicated by the high apparent ages of the initial steps, and the slightly upward-stepping "plateau" section. The inverse isochron age of 42.36 ± 0.18 Ma (MSWD = 0.76) provides a better estimate of the sample's true age because it accounts for the presence of excess ^{40}Ar, which is indicated by a slightly elevated initial $^{40}Ar/^{36}Ar$ ratio of 297.7 ± 1.2 (expected atmospheric ratio is 295.5). Low and uniform Ca/K ratios (see Appendix B) indicate outgassing of a pure, unaltered adularia mineral separate.

The apparent age spectrum for sample COM-L7 from the El Compas vein (El Orito system; Fig. 32b) shows a characteristic saddle shape indicating the presence of significant amounts of excess ^{40}Ar. The early steps show high apparent ages that decrease progressively until step 5, and from there apparent ages increase again until the last step. Steps 3 through 6 (53% of the ^{39}Ar released) define an approximate plateau with an age of 32.63 ± 0.40 Ma, but this age likely represents a maximum age for the sample due to excess ^{40}Ar. In contrast, a well-constrained inverse isochron (steps 1–11: 99.8% of the ^{39}Ar released) defines a distinctly younger age of 29.19 ± 0.20 Ma (MSWD = 1.8). The initial $^{40}Ar/^{36}Ar$ ratio of 302.5 ± 2.8

calculated from this isochron is significantly higher than the atmospheric value (295.5), and confirms the presence of excess ^{40}Ar. The inverse isochron age therefore provides the most reliable date for this sample. The excess ^{40}Ar likely comes from fluid inclusions present in contaminant quartz that could not be separated from the fine-grained adularia. Fluid inclusions tend to decrepitate at relatively low temperatures, and can yield high apparent ages for early steps if some ^{40}Ar is present in the fluid at the time of trapping (Rama et al., 1965; Harrison and McDougall, 1980; Heizler and Harrison, 1988; Richards and McDougall, 1990). Uniform Ca/K ratios (see Appendix C) indicate outgassing of a homogeneous, unaltered, adularia mineral separate; therefore, these anomalies are not caused by other K- or Ca-bearing contaminant

minerals.

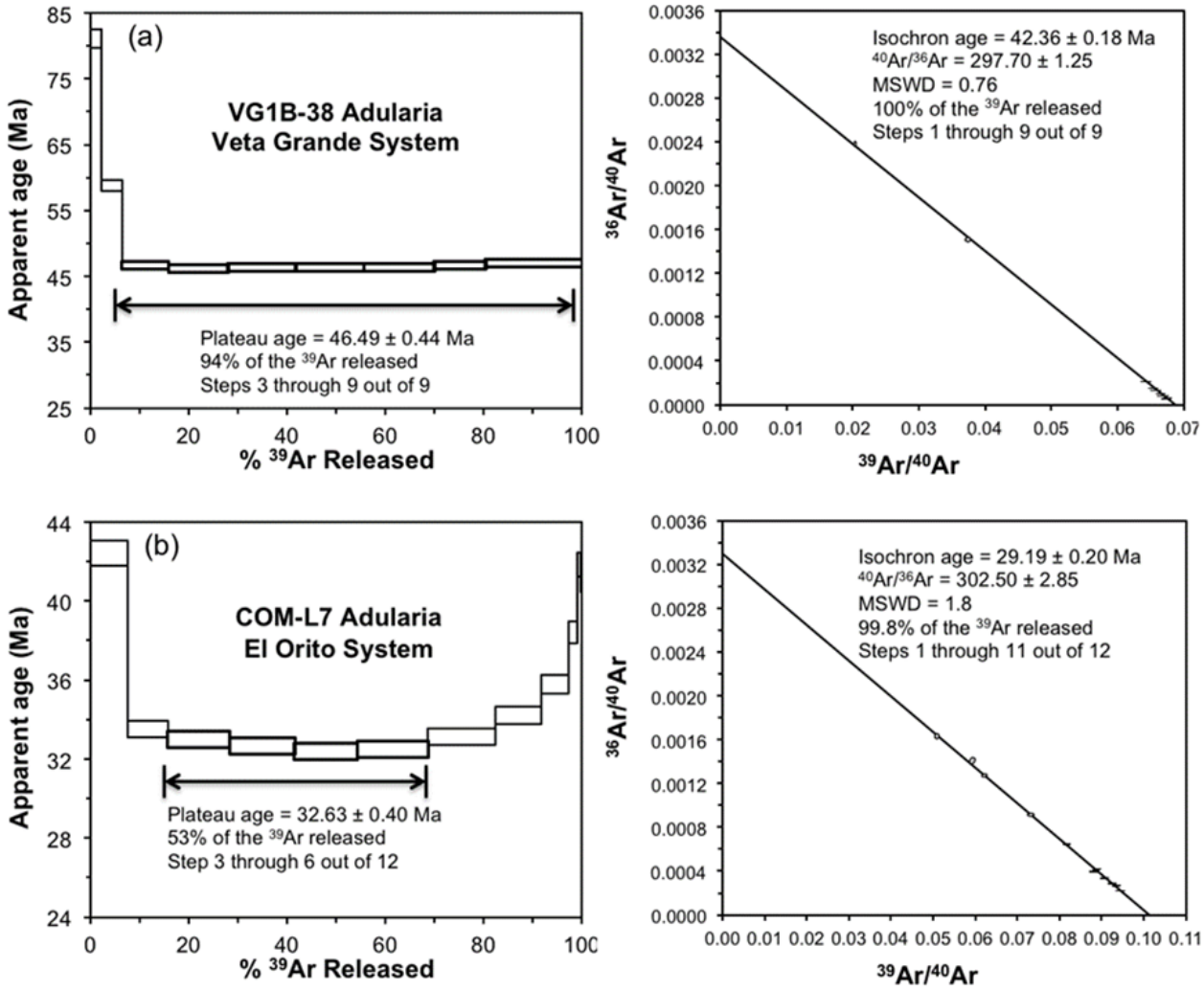

Figure 32. Apparent $^{40}Ar/^{39}Ar$ age spectra and inverse isochron diagrams for adularia samples from (a) the Veta Grande vein (VG1B-08), and (b) the El Compas vein (COM-L7). All errors are drawn at 1σ error, but calculated ages are reported to 2σ.

5.3 U/Pb Geochronology

Zircon U-Pb geochronological results are illustrated on Tera-Wasserburg Concordia plots in Figure 33, and the full analytical data are reported in Appendix D; errors are reported at the

±2σ level. The ^{207}Pb / ^{206}Pb ratios are not corrected for common Pb, but the Concordia intercept is the common Pb corrected age. A brief discussion of each result is provided below.

Thirty grains of zircon from sample ZABU-01 from the La Bufa rhyolite dome produced a weighted mean $^{238}U/^{206}Pb$ age of 48.54 ± 0.49 Ma (MSWD = 0.62), and a Tera-Wasserburg Concordia intercept age of 48.64 ± 0.50 Ma (MSWD = 0.59; Fig. 33a). Both results are very similar, but we report the Concordia intercept age given the slightly lower MSWD value.

Thirty-seven zircons from sample ZASI-02 from the La Sierpe rhyolite plug yielded a weighted mean $^{238}U/^{206}Pb$ age of 50.73 ± 0.37 Ma (MSDW = 1.03), but the best estimate of the crystallization age of this rock is given by the Tera-Wasserburg Concordia intercept age of 50.81 ± 0.50 Ma (MSDW = 0.66; Fig. 33b).

Twenty-eight zircons from sample ZAPA-03 from the El Padre rhyolitic plug yielded two populations of zircons (Fig. 33c–e). Four grains gave a Tera-Wasserburg Concordia intercept age of 136 ± 13 Ma (MSWD = 4.4; Fig. 32d); this age is interpreted to record the age of andesitic xenoliths that are relatively abundant in this rhyolite. The other 24 grains yielded a Tera-Wasserburg Concordia intercept age of 45.32 ± 0.47 Ma (MSWD = 1.3; Fig. 33e), which is interpreted to represent the crystallization age of the El Padre plug.

Sample ZAVI-04 from the La Virgen ignimbrite contains no xenoliths, and yielded a weighted mean $^{238}U/^{206}Pb$ age for 25 grains (all within the 2σ error) of 42.04 ± 0.51 Ma (MSWD = 1.18), and a Tera-Wasserburg Concordia intercept age of 41.72 ± 0.45 Ma (MSWD = 1.08; Fig. 33f); for consistency, we report the latter age as the crystallization age of this sample.

Sample 139-210 is from a felsic dike that runs parallel to a Cu-rich zone in the Mala Noche vein, and yielded a Tera-Wasserburg Concordia intercept age of 50.19 ± 0.53 Ma (MSDW = 1.4; Fig. 33g) with 23 out of 25 analyzed zircons. This age reflects the crystallization

age of the sampled dike. The other two zircons are much older (~150–200 Ma) and were likely entrained as xenocrysts from the Jurassic–Cretaceous volcano-sedimentary country rocks.

Sample 139-288 is also from a felsic dike parallel to the Mala Noche vein, and has a similar age to samples S139-210 and ZASI-02 (Figs. 33g and b, respectively). Twenty-five out of 28 analyzed zircons yielded a Tera-Wasserburg intercept age of 50.40 ± 0.45 Ma (MSDW = 1.1; Fig. 33h), whereas the other three zircons are inherited from Mesozoic basement rocks.

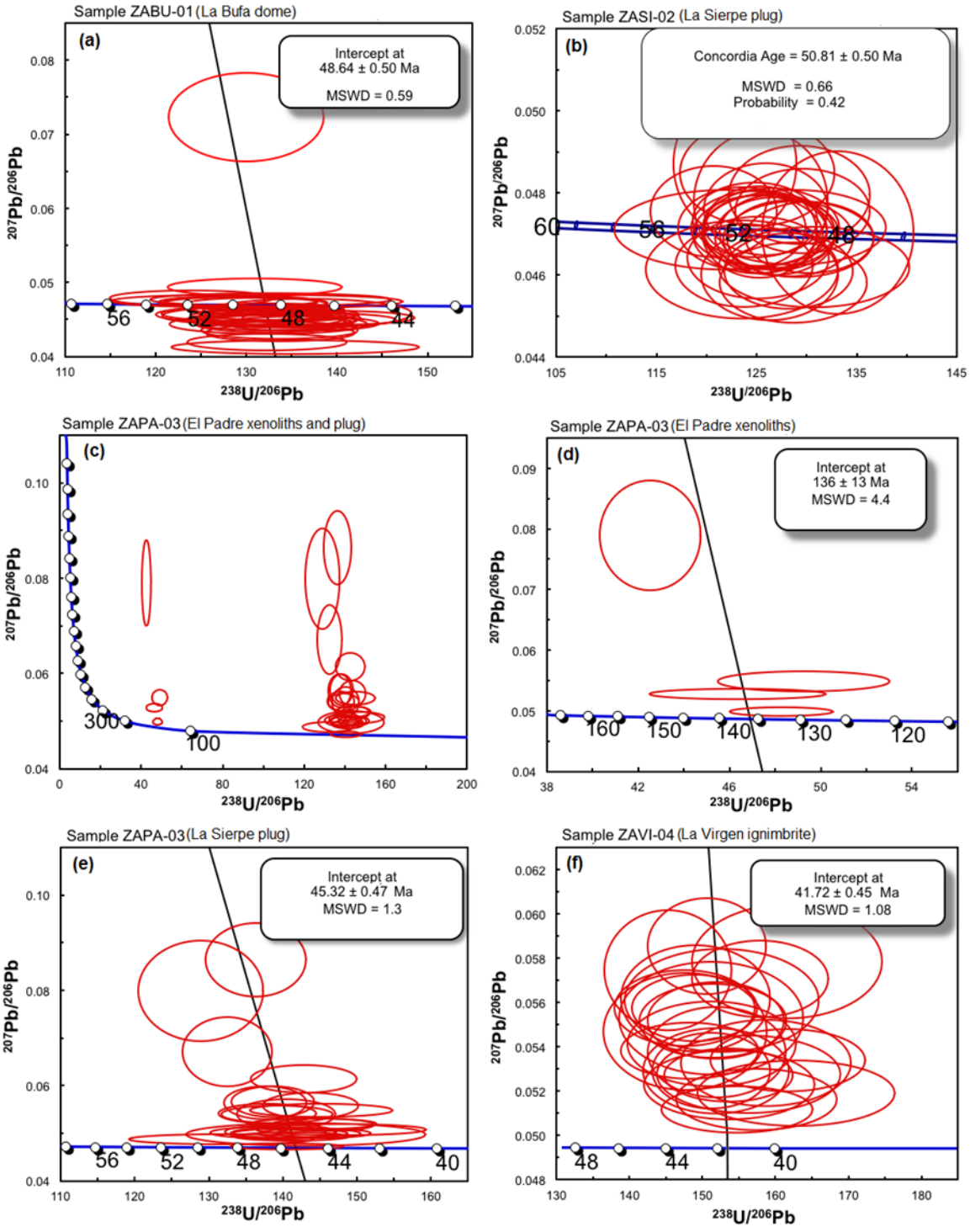
Sample ZABU-01 (La Bufa dome)
(a)
Intercept at
48.64 ± 0.50 Ma
MSWD = 0.59
Sample ZASI-02 (La Sierpe plug)
(b)
Concordia Age = 50.81 ± 0.50 Ma
MSWD = 0.66
Probability = 0.42
Sample ZAPA-03 (El Padre xenoliths and plug)
(c)
Sample ZAPA-03 (El Padre xenoliths)
(d)
Intercept at
136 ± 13 Ma
MSWD = 4.4
Sample ZAPA-03 (La Sierpe plug)
(e)
Intercept at
45.32 ± 0.47 Ma
MSWD = 1.3
Sample ZAVI-04 (La Virgen ignimbrite)
(f)
Intercept at
41.72 ± 0.45 Ma
MSWD = 1.08
207Pb/206Pb
238U/206Pb

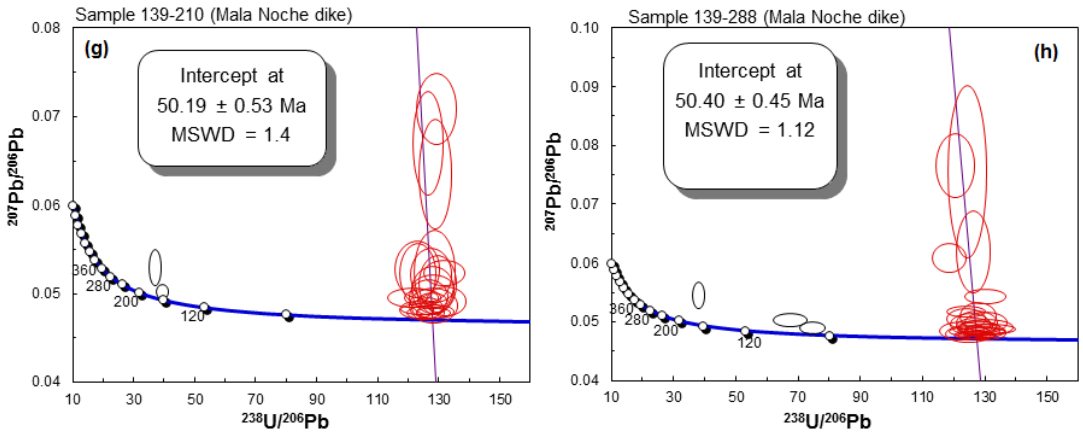

Figure 33. Tera-Wasserburg concordia diagrams for volcanic and hypabyssal rocks of the Zacatecas district. See text for details.

5.4 Fluid Inclusion Petrography

5.4.1 Mala Noche Vein

Fluid inclusions in stage I quartz range in size from 5 to 50 µm with regular or negative crystal shapes and are of two types: liquid-rich (L) with >70% liquid; vapour-rich (V) with >90% vapour. No daughter minerals were observed in fluid inclusions from this stage. Stage I quartz from sample MNL16 shows petrographic evidence of deformation (micro-fracturing and undulose extinction) and contains abundant secondary fluid inclusions, which were avoided. Pseudosecondary vapour- and liquid-rich inclusions were observed in stage I quartz from sample U161-178 (Fig. 34 a–d).

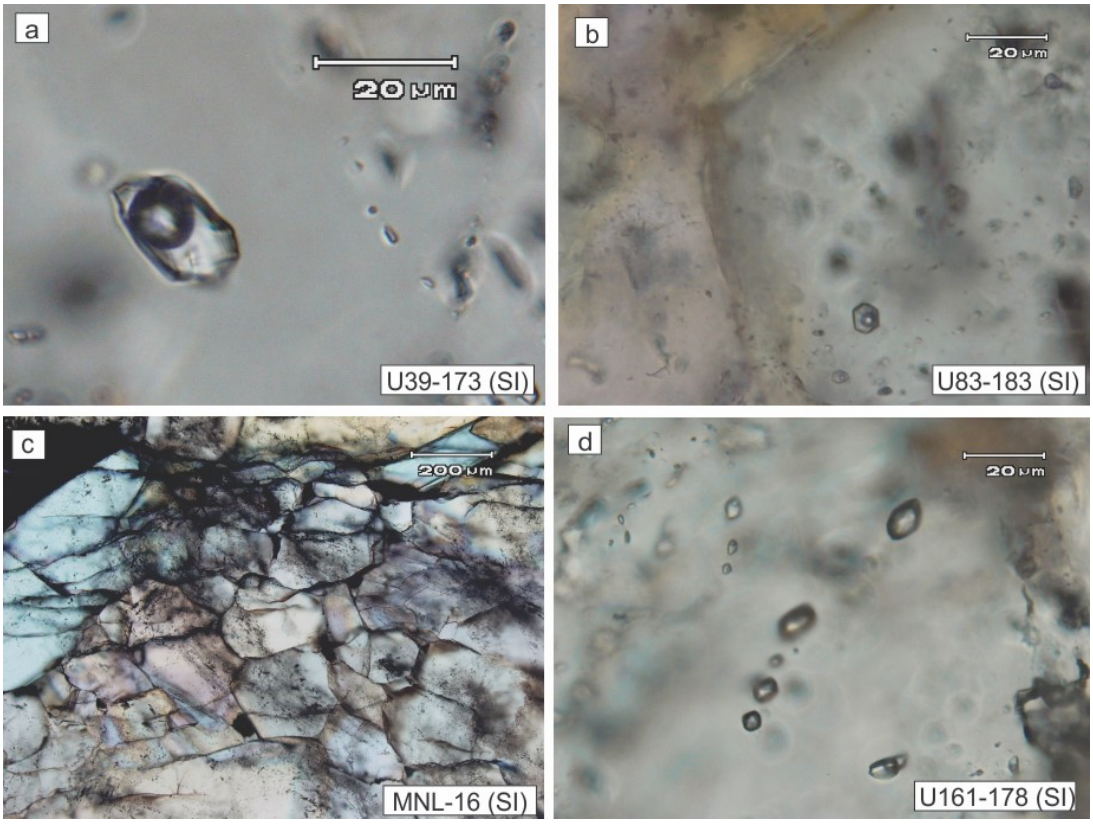

Figure 34. Photomicrographs of fluid inclusions in Mala Noche stage I quartz veins: (a) large primary fluid inclusion with regular shape; (b) small primary fluid inclusion with negative crystal shape; (c) mosaic of fine-grained fractured quartz with abundant secondary fluid inclusions; (d) adjacent trails of liquid- and vapor-rich pseudosecondary fluid inclusions.

Stage II inclusions hosted by quartz and sphalerite are petrographically similar to those in stage I: liquid-rich (L) and vapour-rich (V), with the difference that vapour-rich inclusions are generally larger (up to 60 μm). Illite and sphalerite accidental solid inclusions (identified by Raman spectroscopy) were observed in fluid inclusions in quartz samples S141-35 and MNL-16, respectively (Fig. 35a–b). Vapour-rich inclusions coexisting with liquid-rich inclusions (indicating boiling conditions) were observed in samples U30-178, S141-35, and S141-34 (Fig. 35c–d).

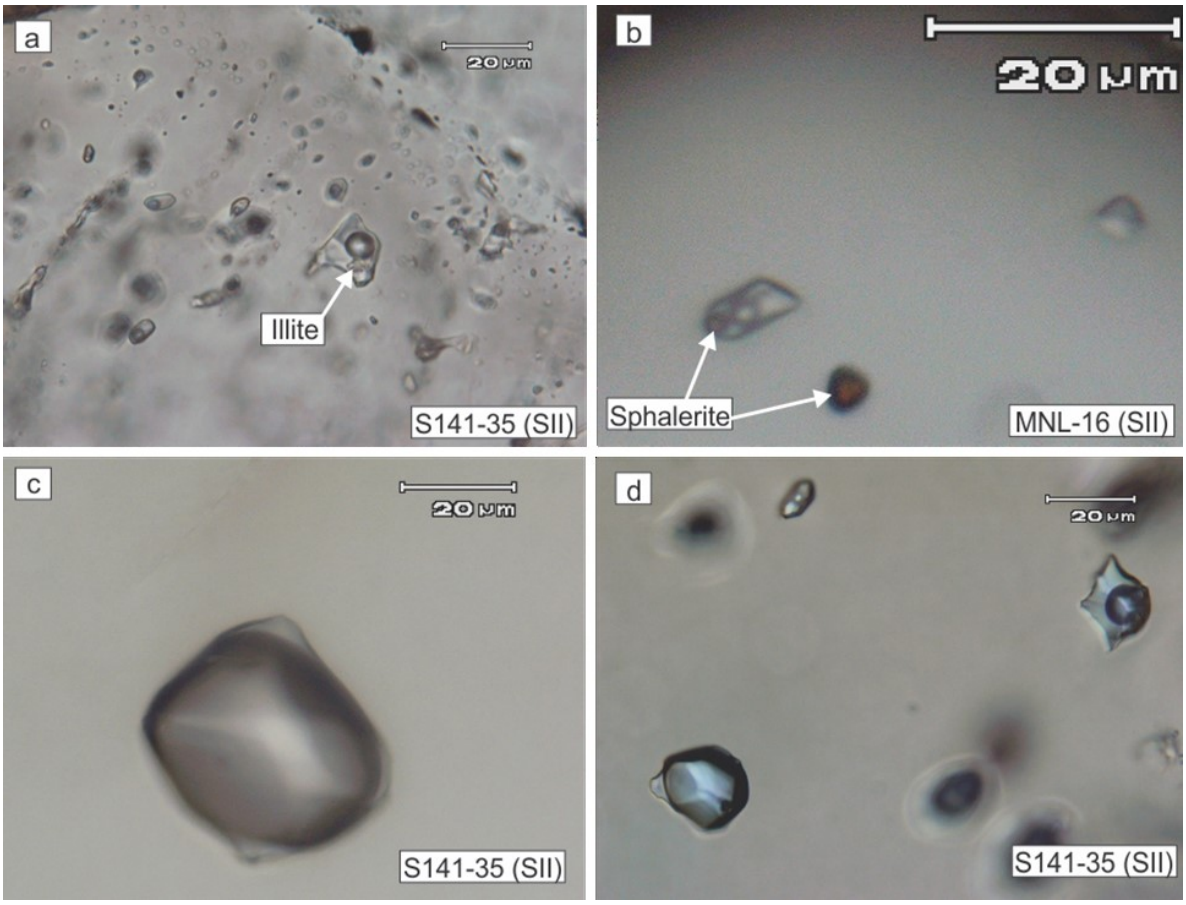

Figure 35. Photomicrographs of primary fluid inclusions in stage II quartz: (a) assemblage of primary fluid inclusions in a growth zone showing accidental illite in one inclusion; (b) liquid-rich fluid inclusion with an accidental crystal of sphalerite besides a solid inclusion of sphalerite in quartz; (c) large vapor-rich primary fluid inclusion; (d) primary liquid-rich fluid inclusions coexisting with vapor-rich fluid inclusions indicative of boiling conditions.

5.4.2 Veta Grande Vein

Fluid inclusions in the Veta Grande stage I are hosted mainly by quartz and calcite although sphalerite and adularia also contain some measurable inclusions. They range in size from 3 to 30 μm and have a regular shape when hosted by quartz and calcite, and elongated when hosted by adularia (Figs. 36a–b). Most of the inclusions are liquid-rich (70–80% liquid). Vapour-rich inclusions (>90% vapour) coexisting with liquid-rich inclusions (indicating boiling conditions) were observed only in calcite (sample OSDH1B; Fig. 36a).

Measurable primary fluid inclusions in stage II are hosted only by quartz. Three different groups of fluid inclusions were observed in this stage: (1) liquid-rich with ~80% liquid, regular to irregular shaped, between 3 and 50 μm in size, and commonly hosted along crystal growth planes (Figs. 36c–d); (2) vapour-rich with >90% vapour, rounded shape, and up to 10 μm in size coexisting with liquid-rich inclusions of similar shape and size or slightly bigger (Fig. 36e); and (3) liquid-rich with ~90% liquid, up to 120 μm in size, and notably irregular shaped that commonly show evidence for necking or beginning of a necking process (Fig. 36f).

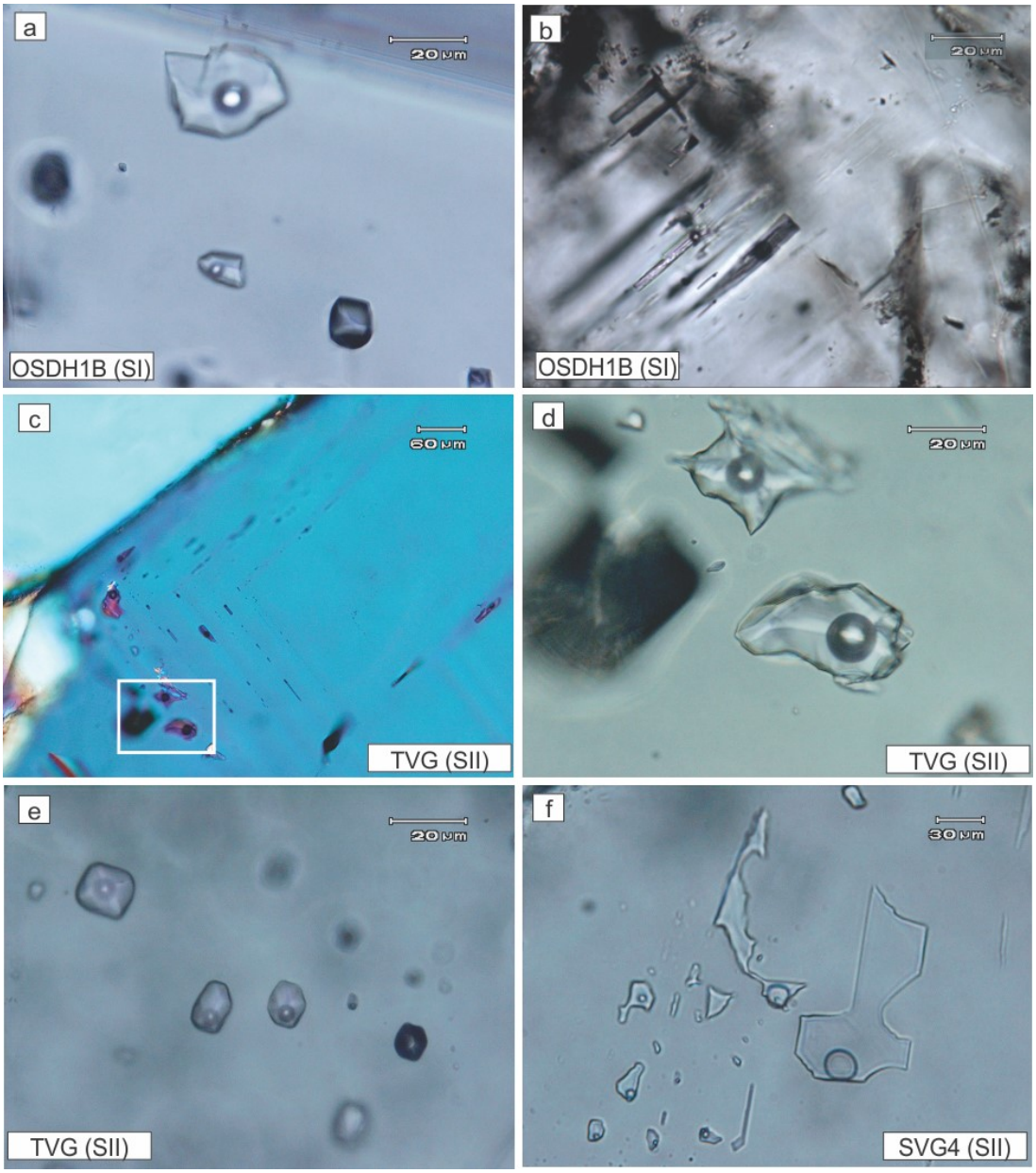

Figure 36. Photomicrographs of primary and pseudosecondary fluid inclusions in the Veta Grande stages I and II: (a) primary liquid-rich fluid inclusions coexisting with vapor-rich fluid inclusions in stage I calcite; (b) elongated primary fluid inclusions in adularia; (c) primary fluid inclusions hosted in quartz growth planes; (d) close up of (c) showing shape and size of primary fluid inclusions; (e) primary liquid-rich fluid inclusions coexisting with vapor-rich fluid inclusions in stage II quartz; (f) large irregular shaped pseudosecondary fluid inclusions showing evidence of necking in stage II quartz.

5.4.3 El Compas Vein

Fluid inclusions in the El Compas vein are hosted mainly by quartz and calcite. Inclusions in calcite are of regular shape, liquid-rich (~85% liquid), and range in size between 5 and 30 μm, whereas inclusions in quartz are usually larger (up to 70 μm) with irregular shapes, and similar liquid-vapor ratios (~85% liquid). Coexisting vapour- and liquid-rich fluid inclusions are commonly observed in quartz, indicating boiling conditions, consistent with the presence of bladed calcite texture (Fig. 37a–d).

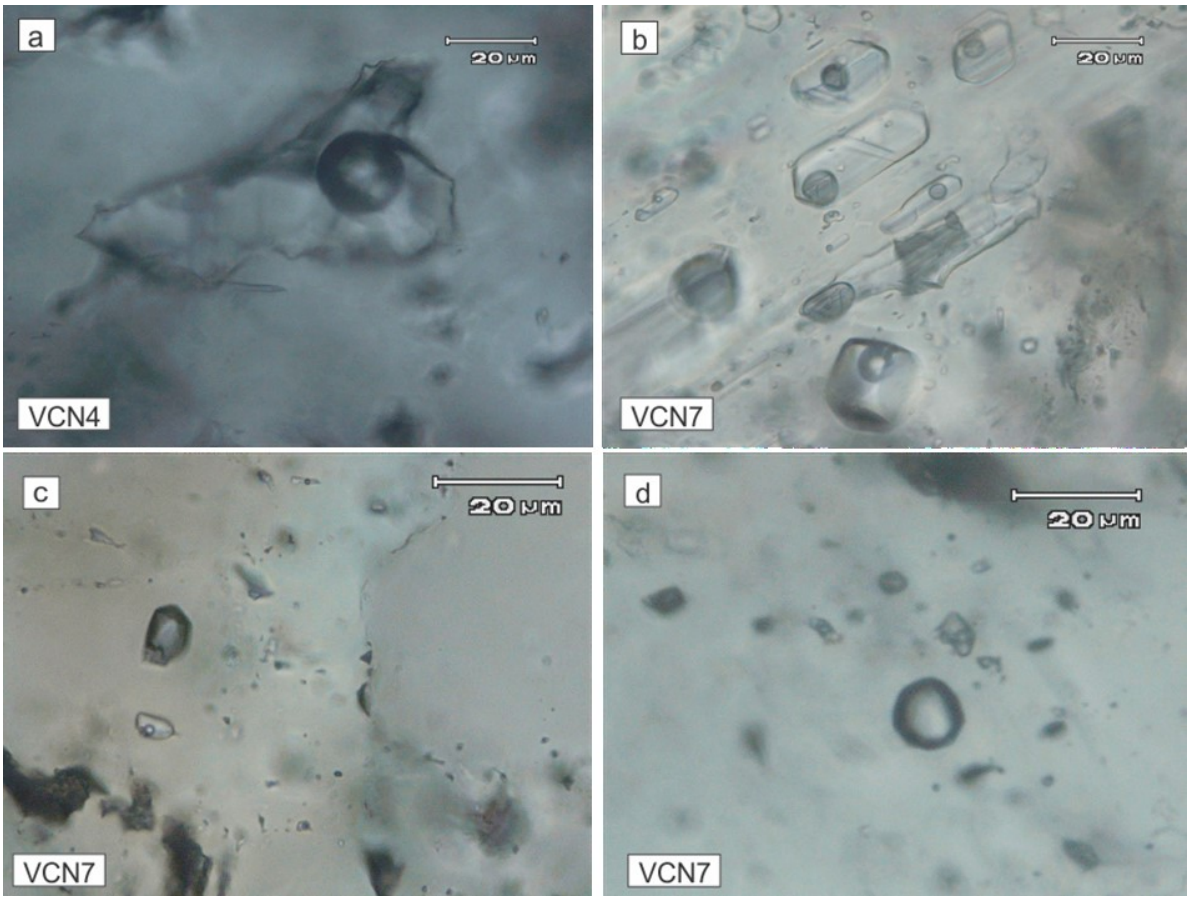

Figure 37. Photomicrographs of primary fluid inclusions in the El Compas vein quartz: (a) large irregular shaped primary fluid inclusion in quartz; (b) assemblage of regular shaped primary fluid inclusions in calcite; (c and d) examples of primary liquid-rich fluid inclusions coexisting with vapour-rich fluid inclusions in quartz indicative of boiling conditions.

5.5 Fluid Inclusion Microthermometry

5.5.1 Mala Noche vein

Homogenization temperatures (Th) and salinities were obtained from 552 fluid inclusions in 20 samples of stage I and II veins from Mala Noche. The stage I fluid inclusions range from 150 to 351°C and 0 to 14.5 wt.% NaCl eq., whereas those from stage II show a similar range from 165 to 325°C and 0 to 14 wt.% NaCl eq. (Figs. 38–40). The data from both stages show a correlated array from saline (~12–14 wt.% NaCl eq.) slightly higher homogenization temperature (250°–350°C) compositions, to low salinity (~4 wt.% NaCl eq.), and cooler (~150°C) compositions. More dilute fluids (0–3 wt.% NaCl eq.) show a wider range of homogenization temperatures (~150–350°C). These data indicate the presence of three types of fluid in the veins: 1) a warmer saline fluid, 2) a slightly cooler lower salinity fluid, and 3) a variable temperature dilute fluid. The warmer saline fluid shows evidence of boiling although not widely preserved. The second fluid shows evidence of mixing with the first one but not evidence of boiling, and the third fluid shows evidence of boiling in the high-temperature end member but no evidence of mixing (see below).

The presence of boiling fluid inclusion assemblages in both the warmer saline and dilute fluids means that fluid inclusion homogenization temperatures (Th) do not require pressure correction, and approximate the actual trapping temperature (Tt).

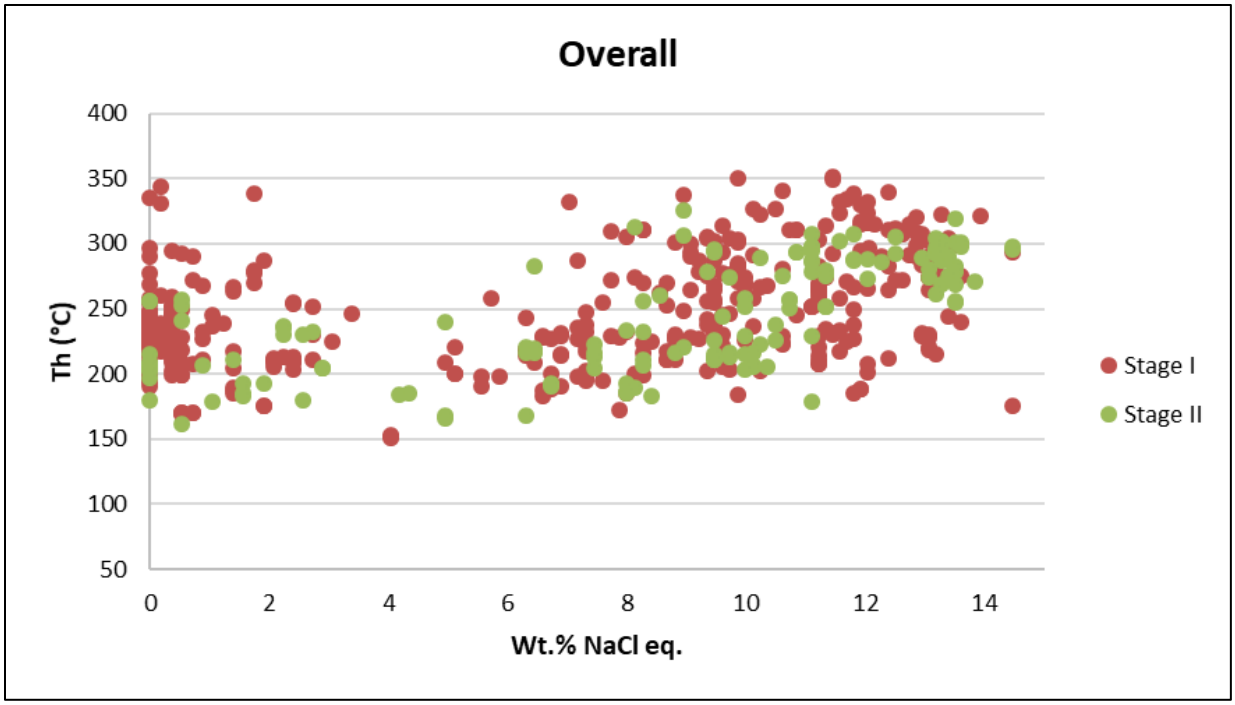

Figure 38. Homogenization temperature vs. salinity scatter plot of individual fluid inclusions from the Mala Noche Mala Noche vein stages I and II.

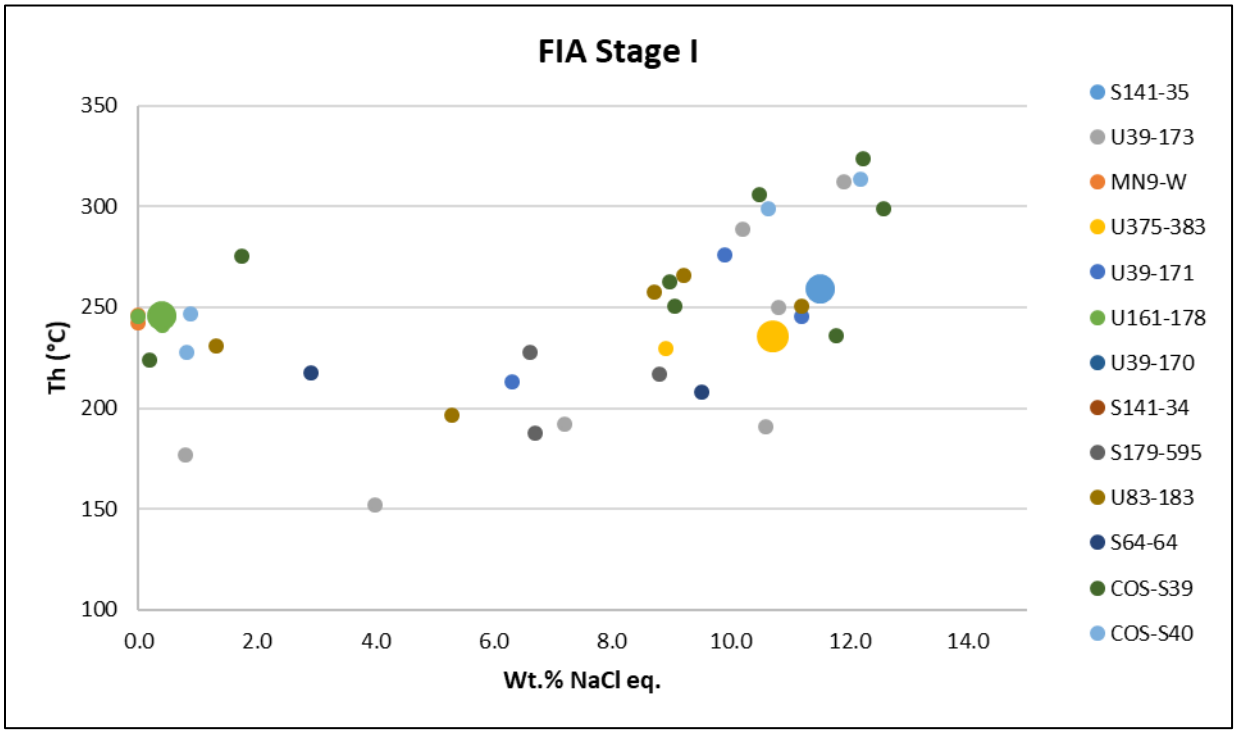

Figure 39. Homogenization temperature vs. salinity scatter plot showing the average compositions of fluid inclusion assemblages (n = 2–12 inclusions) from the Mala Noche stage I samples; enlarged circles FIA with evidence for boiling.

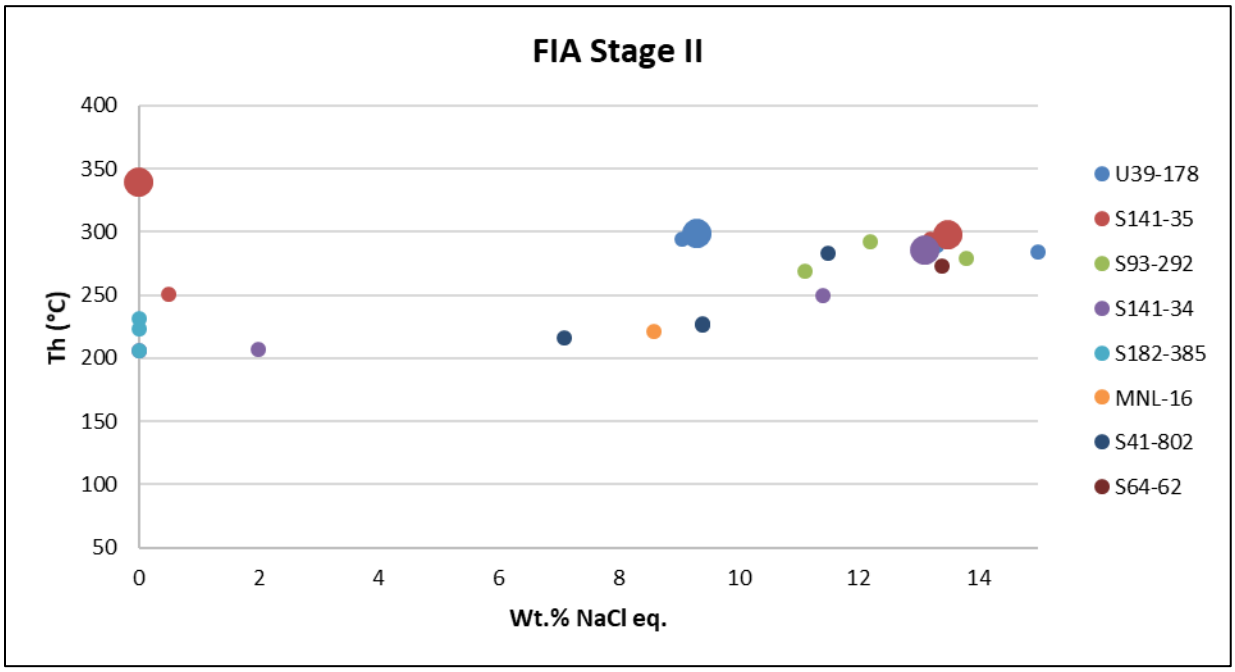

Figure 40. Homogenization temperature vs. salinity scatter plot showing the average compositions of fluid inclusion assemblages (n = 2–12 inclusions) from stage II samples; enlarged circles indicate FIA with evidence for boiling.

Correlated Th–salinity arrays within individual FIAs suggest that the warmer saline fluid mixed with the slightly cooler (~150°C) low salinity (~4 wt.% NaCl eq.) but not with the dilute fluid (Fig. 41). This correlation shows evidence of actual fluid mixing, because FIAs are interpreted to have trapped coexisting fluids. Such assemblages were observed in stage I and II samples (Fig. 41), and indicate that actual fluid mixing, as well as boiling of both the saline and low salinity fluids, occurred in the mineralized veins. Both processes can result in ore deposition (see below).

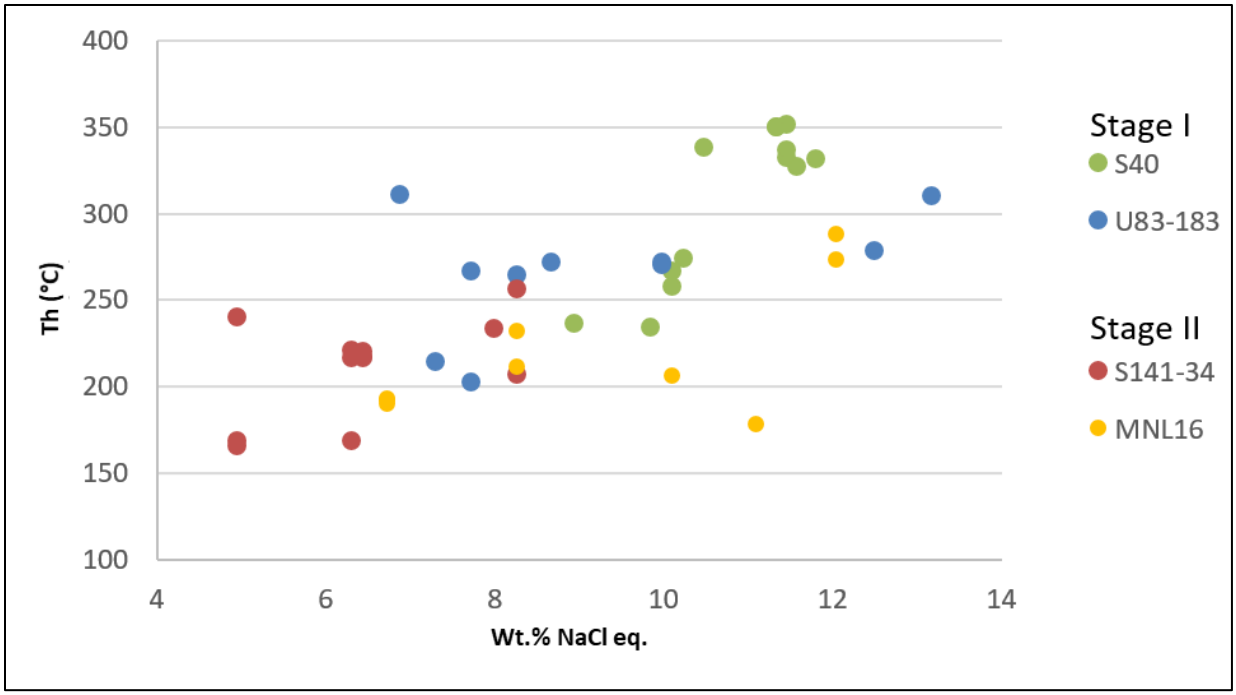

Figure 41. Homogenization temperature vs. salinity scatter plots for fluid inclusions within single FIAs from stages I and II, showing roughly correlated trends indicative of fluid mixing.

5.5.2 Veta Grande vein

Microthermometric measurements of 263 fluid inclusions were obtained from 8 samples of the Veta Grande vein stage I and II. Calcite and quartz from of stage I show moderate salinities (6–10 wt.% NaCl eq.) and homogenization temperatures that range from 180° to 260°C. Fluid inclusions in quartz from stage II show a wider range of homogenization temperatures (150°–280°C) and bimodal compositions (6–13 and <1 wt.% NaCl eq.; Fig. 42). Dilute fluids are usually trapped in distinctively large and irregular shaped fluid inclusions. Trends between saline high-temperature and dilute low-temperature fluids within a single FIA that may indicate mixing are not clearly observed in these samples, and petrographic differences suggest that saline and dilute FIA were trapped at different times. Fluid inclusion evidence of

boiling (coexistence of vapor- and liquid-rich inclusions) is present in both stages, and textural evidence (bladed calcite) has been observed in stage II quartz.

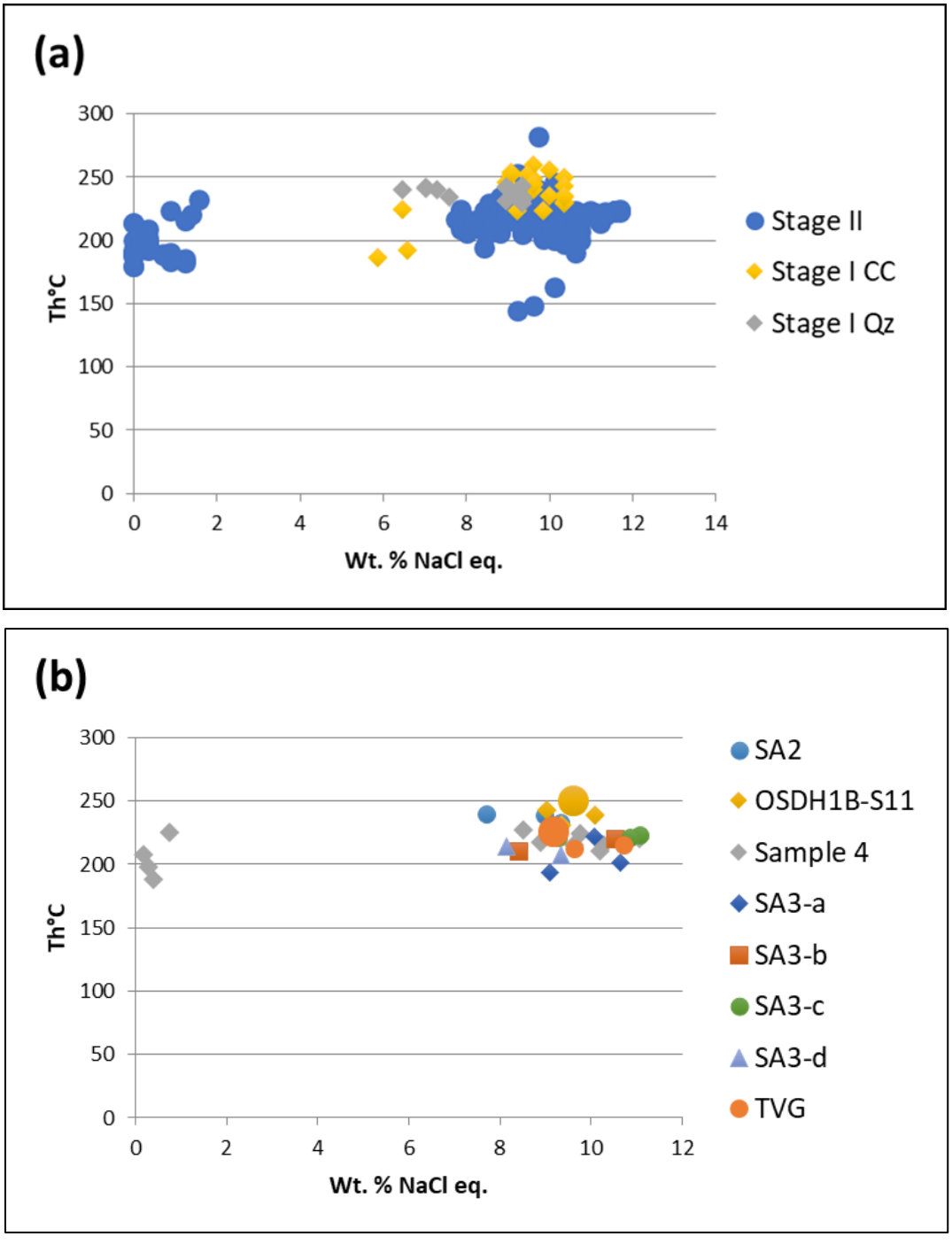

Figure 42. Homogenization temperature vs stage I in quartz and calcite and stage II in quartz: (a) individual fluid inclusion measurements and (b) average of fluid inclusion assemblages (n = 3–14 inclusions); enlarged circles indicate FIA with evidence for boiling.

5.5.3 El Compas vein

Fluid inclusion microthermometry conducted in 4 samples from the El Compas vein indicate that vein formation occurred from low temperature (average Th = 209 ± 17°C) and dilute (<1 wt.% NaCl eq.) fluids (Fig. 43). Evidence of boiling is shown by the widespread occurrence of bladed calcite textures and coexistence of vapor-rich and liquid-rich fluid inclusions in quartz.

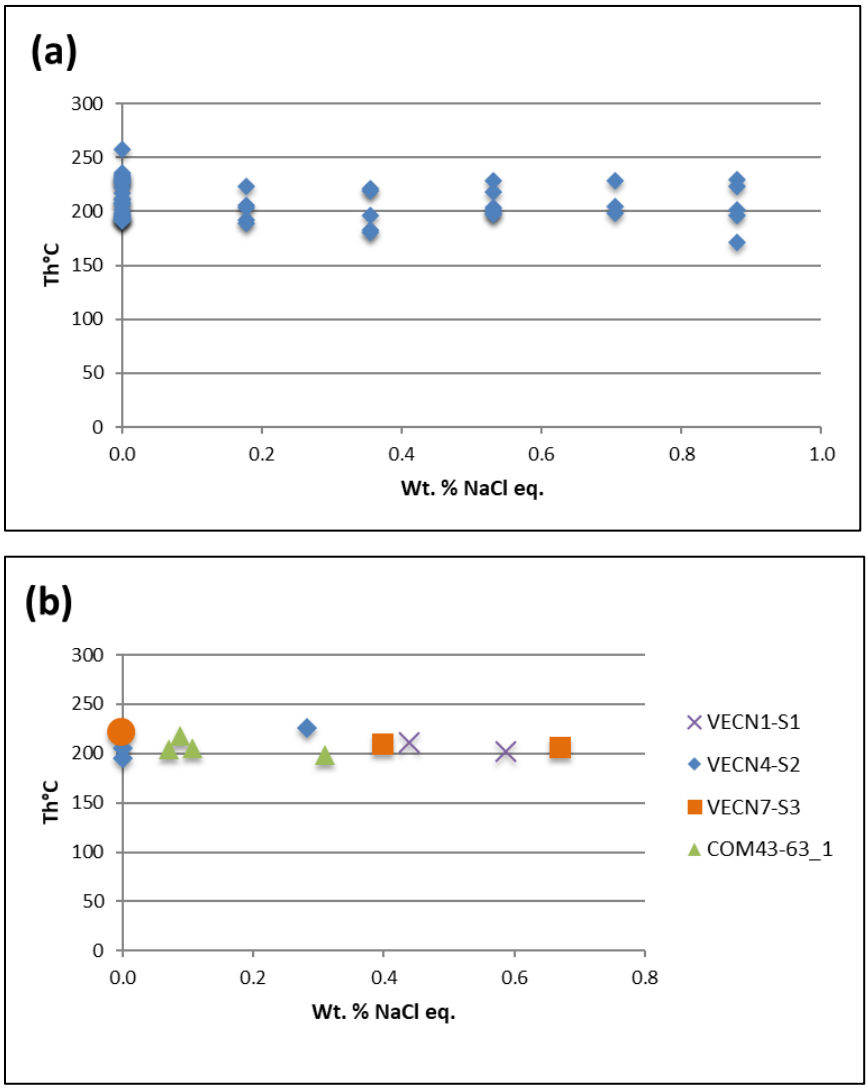

Figure 43. Microthermometric data from the El Compas vein showing a plot of salinity in wt.% NaCl eq. vs. homogenization temperature: (a) individual fluid inclusion measurements, and (b) average of fluid inclusion assemblages (n = 3–6 inclusions); enlarged circles indicate FIA with evidence for boiling.

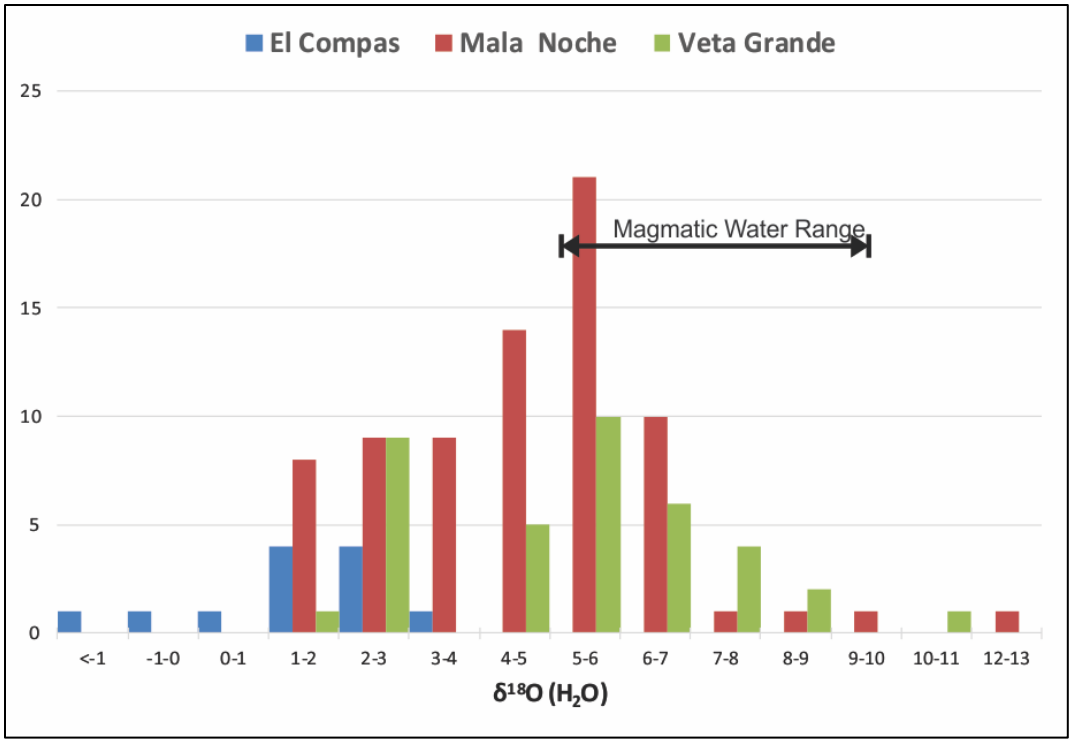

Figure 44. Histogram showing the frequency of $\delta^{18}O_{fluid}$ for the Mala Noche, Veta Grande, and El Compas veins. Global magmatic water range is shown for comparison (Sheppard, 1986). The $\delta^{18}O$ range of present-day meteoric water in central Mexico, not shown in this figure is between -4.89 and -11.75% (Aguilar-Ramírez et al., 2017).

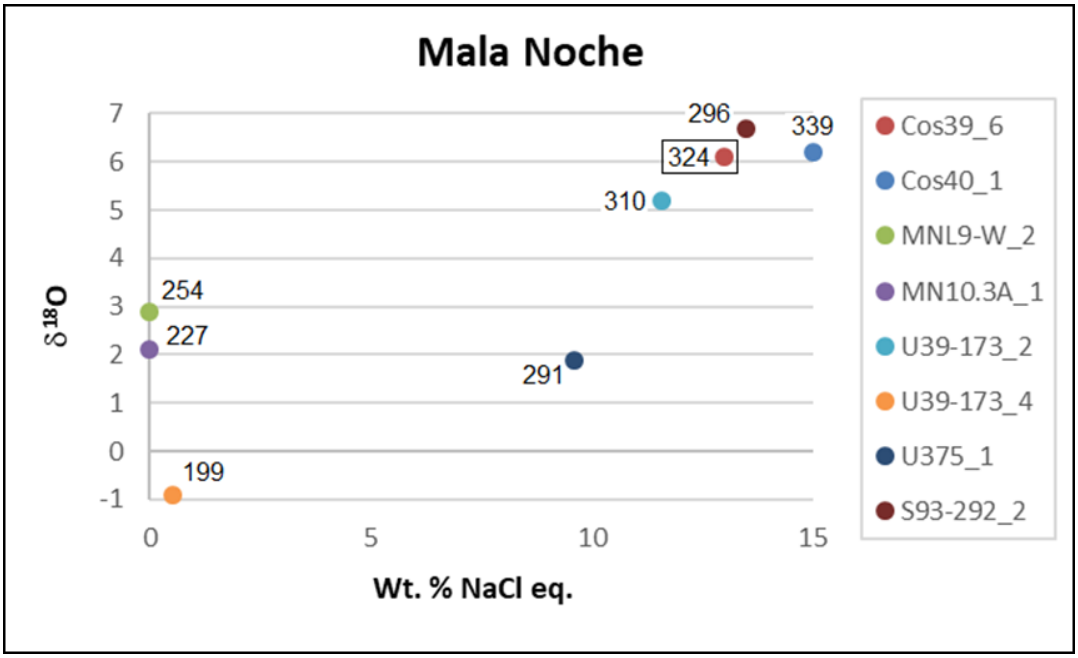

Figure 45. Plot of salinity in wt.% NaCl eq. vs. $\delta^{18}O_{fluid}$ of inclusions from the Mala Noche vein stage I in quartz and calcite and stage II in quartz. The numbers against the symbols show the average homogenization temperature used to calculate the fluid isotopic composition. The rectangle highlights the fluid inclusion assemblage that contains the inclusion analyzed by LA-ICPMS to constrain the Mala Noche vein stage I water composition for modelling.

5.6 Stable Isotopes

5.6.1 Sulfur Isotopes

Sulfur isotopic data are reported in Table 4. The $\delta^{34}S$ values of sulfide minerals from both stages of the Mala Noche and Veta Grande veins are very homogeneous. Average values from Mala Noche are -12.3 ± 0.6 ‰ in pyrite (n = 4), -14.4 ± 0.3 ‰ in galena (n = 7), and -12.5 ± 0.6 ‰ in sphalerite (n = 10), -12.9 ± 0.4 ‰ (n = 3) in chalcopyrite, and -12.1 ‰ in a single sample of pyrrhotite. Average values for Veta Grande are -14.3 ± 1.7 ‰ in pyrite (n = 5), -13.8 ± 0.4 ‰ in sphalerite (n = 5), and -16.0 ‰ in a single sample of galena.

Crystallization temperatures calculated from intergrown sphalerite-galena mineral pairs analyzed at ±0.1 ‰ accuracy and using the fractionation equation of Rye (1974) range from 403°– 514 °C for Mala Noche stage I, which is somewhat higher than the temperatures recorded by fluid inclusions (Th_{max} 351°C). However, a crystallization temperature of 298 ± 21°C calculated for a sphalerite-galena sample from the Mala Noche stage II vein (U39-178) is in better agreement with the average homogenization temperature of fluid inclusions from the same

sample (299° ± 19°C).

Vein	Sample	Stage	$\delta^{34}S$ py	$\delta^{34}S$ gn	$\delta^{34}S$ sp	$\delta^{34}S$ cpy	$\delta^{34}S$ po	Accuracy (‰)	T°C	Error (±°C)
Mala Noche	MN10.6-S4	I	-12.1	-14.6	-12.6	-12.5	-	±0.3	-	-
Mala Noche	MN10.6-S8	I	-12.6	-14.3	-12.9	-12.9	-	±0.3	-	-
Mala Noche	Cos U202	I	-12.9	-14.7	-12.9	-13.3	-	±0.3	-	-
Mala Noche	U202 Rep	I	-	-14.5	-13.0	-	-	±0.1	403	58
Mala Noche	S165-339	I	-	-14.0	-12.9	-	-	±0.1	514	95
Mala Noche	S93-303	I	-	-14.2	-12.8	-	-	±0.1	432	59
Mala Noche	U39-178	II	-	-14.6	-12.4	-	-	±0.1	298	21
Mala Noche	Cos 107	?	-11.6	-	-11.5	-	-	±0.3	-	-
Mala Noche	Cos 161	Alteration	-8.7	-		-	-	±0.3	-	-
Mala Noche	Cos 41-20	I	-	-	-12.4	-	-	±0.3	-	-
Mala Noche	Cos 41-24	?	-5.3	-	-11.2	-	-	±0.3	-	-
Mala Noche	MN11.3	I	-	-	-	-	-12.1	±0.3	-	-
Veta Grande	DP05	I	-13.7	-	-13.7	-	-	±0.3	-	-
Veta Grande	OSS11	I	-17.3	-	-13.9	-	-	±0.3	-	-
Veta Grande	OSS5	I	-13.9	-16.0	-13.5	-	-	±0.3	-	-
Veta Grande	SA1	I	-13.0	-	-13.5	-	-	±0.3	-	-
Veta Grande	SCS6	I	-13.7	-	-14.5	-	-	±0.3	-	-

Table 4. Sulfur isotopic composition of sulfides from the Mala Noche and Veta Grande veins, accuracy reported according to 1σ and crystallization temperature calculated for sphalerite-galena pairs with an accuracy of ± 0.1‰ (1σ).

5.6.2 Oxygen Isotopic Compositions of Quartz

Oxygen isotope data are reported in Appendix F. The $\delta^{18}O$ values obtained using the BrF_5 method from the Veta Grande stage II samples (+15.5 to +16.4 ‰) are consistent with the results obtained using the in-situ method (+15.7 to +16.4 ‰) for the same samples. However, the $\delta^{18}O_{fluid}$ calculated using the in-situ method and local FIAs average homogenization temperatures is more accurate. The ranges of $\delta^{18}O_{fluid}$ values (calculated at the average homogenization temperature of the FIAs within the in-situ analyzed region) for the Mala Noche, Veta Grande, and El Compas veins are shown relative to the $\delta^{18}O$ ranges of global magmatic waters in Figure 44 (Sheppard, 1986). The $\delta^{18}O$ range of present-day meteoric water in central Mexico has been estimated to be between -4.89 and -11.75‰ (Aguilar-Ramírez et al., 2017; not shown in Fig. 44).

The Mala Noche vein shows a wide range of $\delta^{18}O_{fluid}$ values from -0.9 to +8.1, which overlaps the range of magmatic waters (Fig. 44). In general, heavy isotopic compositions are

from regions within quartz veins that contain high temperature and saline FIAs, whereas lighter $\delta^{18}O_{fluid}$ values correlate with regions that contain cooler and dilute fluids (Fig. 45). Correlated arrays suggest mixing between these two types of fluids (Fig. 45). The $\delta^{18}O_{fluid}$ values of the cooler dilute fluids range between -0.9 and +2.9 (Fig. 45), and likely represent isotopically exchanged groundwaters.

The $\delta^{18}O_{fluid}$ of the Veta Grande vein shows two well-defined ranges of isotopic compositions, from +2 to +2.8 ‰ and from +4.6 to +10.1 ‰ (Fig. 44). The lighter range is from stage I quartz that contains moderately saline fluids, whereas the heavier range is from stage II quartz regions that contain saline fluid inclusions. Not enough areas of quartz containing dilute FIAs were analyzed isotopically to enable a salinity vs. $\delta^{18}O_{fluid}$ correlation for the Veta Grande vein as shown for Mala Noche in Figure 45, however fluid inclusion data does not support fluid mixing in this vein and suggest that the bimodal fluids of stage II were formed at different times.

The calculated $\delta^{18}O$ composition of the El Compas vein fluids represented by sample VNC4 cluster more tightly from -1.4 to +3.1 ‰ (Fig. 44).

Figure 46 shows CL images with the $\delta^{18}O_{fluid}$ values of analyzed spots for the Mala Noche, Veta Grande, and El Compas veins. There is no clear correlation between isotopic values and CL response except for the El Compas vein. However, different textures are revealed. The Mala Noche dilute FIAs regions with isotopically light values show euhedral quartz with growth zoning and dissolution textures (Fig. 46b), whereas regions of the Mala Noche vein that contain isotopically heavy saline fluids show either cobweb- and puzzle-like textures that indicate fracturing and dilation, or rounded quartz cores surrounded by euhedral overgrowths and crosscut by late microveinlets (Fig. 46a).

Cathodoluminescence images of the Veta Grande vein stage II samples show crystal growth zoning textures indicating fluctuations in the chemical composition of quartz. However; there is no correlation between isotopic values and cathodoluminescence response (Fig. 46c).

The CL image of quartz from the El Compas vein, sample VNC4, shows well-defined growth zonation of alternating dark, grey, and bright bands (Fig. 46d), and in general the heavier and lighter $\delta^{18}O$ compositions correlate with darker and brighter zones respectively. This sharp CL–isotopic banding suggests either that fluids with distinct trace-elements compositions flowed through the veins in pulses, or that rapid fluctuations of pressure and temperature conditions occurred during vein formation. The uniform fluid inclusion compositions (Fig. 43) are more consistent with the second interpretation.

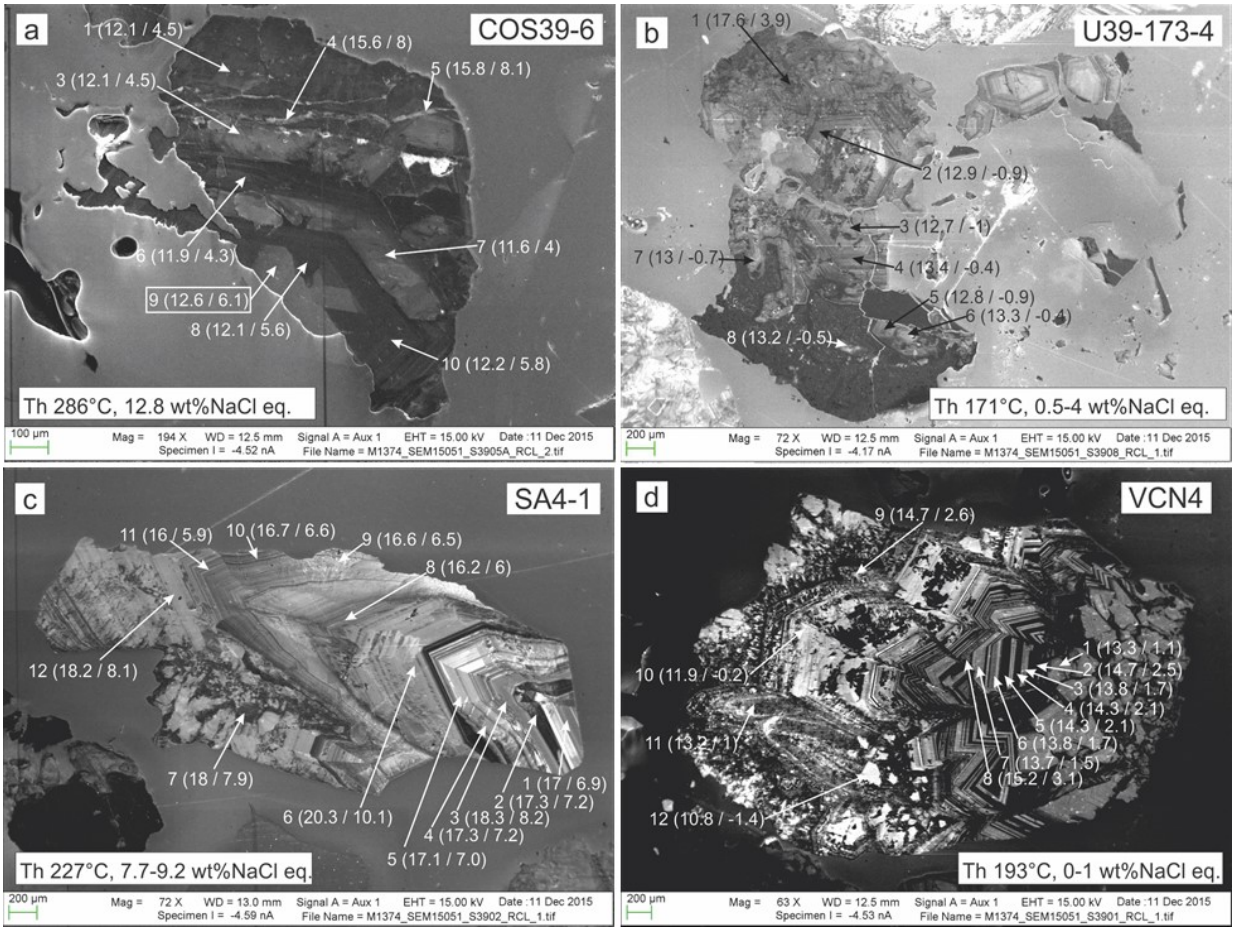

Figure 46. Cathodoluminescence (CL) images showing the spots analyzed for oxygen isotopes. In parentheses are the quartz $\delta^{18}O$ values followed by the $\delta^{18}O$ value of the fluid calculated using average homogenization temperatures of FIA from the analyzed area, and the quartz-water fractionation equation of Clayton et al. (1972). (a) Sample from the Mala Noche vein (Cos39-6) showing a region that contains saline fluid inclusions with average Th = 286°C. (b) Sample from the Mala Noche vein (U39-173-4) showing a region that contains dilute fluid inclusions with average Th = 171°C (c) Sample from the Veta Grande vein (SA4-1) showing a region that contains saline fluid inclusions with average Th = 227°C. (d) Sample from the El Compas vein (VCN4) that contains dilute fluid inclusions with average Th = 193°C.

5.7 Fluid Inclusion RAMAN Spectroscopy Results

The solid phase illite was identified with Raman spectroscopy within moderately saline (~10 wt.% NaCl eq.) liquid-rich fluid inclusions from the Mala Noche vein stage II (Fig. 47). Illite crystals vary in size from ~5 to 20 μm and more than one crystal can be found in a single

fluid inclusion. For this reason, it is interpreted that illite was trapped as a solid phase rather than a precipitated daughter mineral.

The vapour phase in both liquid- and vapour-rich fluid inclusions was analyzed for CO_2 and other gases, but none of the inclusions showed evidence for gases other than H_2O-vapour, consistent with the lack of clathrate formation during microthermometric analyses.

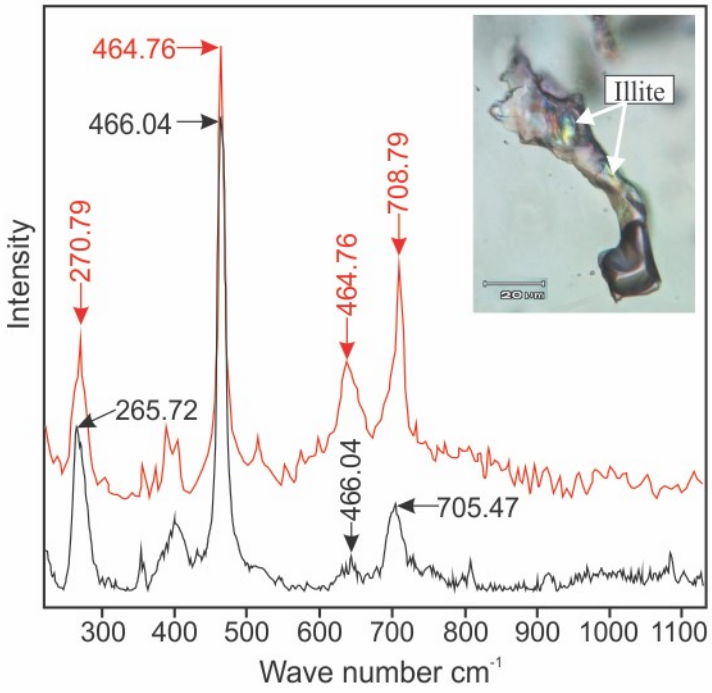

Figure 47. Raman spectrum of illite trapped in a fluid inclusion from the Mala Noche Vein sample MN10.3A (black color). The spectrum of a natural illite in red color is shown for comparison (Wenxin, 2001). The inset shows the analyzed solid phase under cross-polarized transmitted light.

5.8 Fluid Inclusion LA-ICP-MS Results

Full results of 15 LA-ICP-MS analyses of fluid inclusions from ore-stage samples of the Mala Moche, Veta Grande, and El Compas veins are reported in Appendix G. Two analyses were selected to constrain the initial water composition for modelling simulations reported in

Table 5. The analyses were selected based on the quality of ablation, visual inspection of transient signals, microthermometry constraints, and resolved concentrations above the limit of detection.

Component species	Mala Noche (Moles)	Veta Grande (Moles)	Reactant rock component	Wt%
Cl-	2.0065E+00	2.0647E+00	SiO_2	50.67
SO4--	3.3700E-05	3.4790E-05	Al_2O_3	16.87
HS-	9.9100E-03	1.4790E-02	Fe_2O_3	9.38
HCO3-	2.8030E-05	2.8030E-03	MnO	0.19
H4SiO4	9.0640E-02	1.1080E-02	CaO	11.37
Al+++	9.8830E-10	1.5000E-06	Na_2O	1.95
Ca++	1.5770E-01	1.6560E-01	K_2O	0.75
Mg++	1.0000E-14	-	MgO	4.95
Fe++	9.0420E-03	3.2260E-03		
K+	1.3100E-01	2.3230E-01		
Na+	1.5310E+00	1.4940E+00		
Mn++	2.8780E-03	1.7640E-04		
Zn++	2.5170E-04	1.4660E-04		
Cu+	1.3940E-03	1.5080E-05		
Pb++	1.9900E-04	3.2750E-04		
Ag+	-	5.0000E-05		
Sr++	2.1110E-03	1.4810E-03		
Ba++	4.7730E-04	2.7150E-04		
Sb(OH)3	1.3150E-04	4.5350E-03		
H2AsO3-	-	5.5920E-04		
Temperature	340 C	320 C		
pH	5.1	5.2		

Table 5. Constrained initial water composition for modelling simulations.

5.8.1 Mala Noche

The analysis selected to constrain the initial water composition for the Mala Noche stage I model simulations was obtained from a single fluid inclusion (Cos39_6-P7). The inclusion is from sample Cos39 described in Table 1. The analyzed inclusion's Th, salinity, and $\delta^{18}O_{fluid}$ value is highlighted on Figs. 39, 45, and 46. This inclusion yielded a short (5s) transient signal with a single sharp peak for Na and signals above detection limit for Ca, Mg, Fe, K, Na, Mn, Zn, Cu, Pb, Ag, Sr, Ba, Sb, and As, which are the metals used in the modelling simulations (P7; Appendix G).

5.8.2 Veta Grande

The analysis selected for the Veta Grande stage II quartz was obtained from a single fluid inclusion with salinity of 9.2 wt. % NaCl eq.; Th = 225°C; and located within a well-defined crystal growth plane with zoning texture (Fig. 36c-d). Regions of crystal growth zoning display a range of isotopic compositions between +6.9 and +7.2 ‰ $\delta^{18}O_{fluid}$ (Fig. 46c; SA4-1). The analysis yielded a short transient set of signals (9.5s) with a sharp peak on the signal of Na (TVG-P10; Appendix G), and signals above detection limit for the elements used in the numeric simulations (Ca, Fe, K, Na, Mn, Zn, Cu, Pb, Ag, Sr, Ba, Sb, and As).

5.8.3 El Compas vein

Ablation of a fluid inclusion from the El Compas vein (sample VCN4S3) with salinity of 0.9 wt. % NaCl eq., Th = 195°C, and located within a region with isotopic compositions that

range from +1.1 to +3.1 ‰ $\delta^{18}O_{fluid}$ between growth zone planes (Fig. 46d; VCN4), yielded a detectable signal for Na despite of its low salinity. However, most of the resolved concentrations are only just above the limit of detection, and Se (observed in aguilarite and naumannite at El Compas) was not detected (Appendix G). Therefore, mathematical simulations for this vein were not attempted.

5.9 CHIM-XPT Modelling

Results for boiling, cooling, mixing, and water-rock reaction simulations including gases released during boiling, the predicted mineral association, total concentration of components dissolved in water, and concentration of selected aqueous species relevant to understanding pH and redox changes are shown on Figures 48–55. Relative redox variations are indicated using the sulfate/sulfide (S^{6+}/ S^{2-}) ratio (Cooke and McPhail, 2001; Ronacher et al., 2004).

5.9.1 Mala Noche

The estimated starting water composition for the Mala Noche vein stage I is shown in Table 4. The temperature was set at 340°C, slightly above of the analyzed fluid inclusion homogenization temperature (324°C), and corresponding to the highest average FIA homogenization temperature measured in this sample. This starting water composition is interpreted to represent the composition of a magmatic fluid based on $\delta^{18}O$, salinity, and Th correlations (Fig. 45).

Boiling. Immediately after the solution starts boiling and gases are released (Fig 48a), the amphibole anthophyllite (polymorphic with the cummingtonite-grunerite solid solution; (Mg, Fe^{2+})$_2$(Mg, Fe^{2+})$_5Si_8O_{22}(OH)_2$) precipitates for a very narrow temperature interval slightly below 340 °C (Fig. 48b). Quartz, chalcopyrite, magnetite, and pyrite start precipitating also when boiling begins and continue until 150°C, except for magnetite which stops at 285°C. Sphalerite and galena start precipitating later in the paragenesis at 310°C and 295°C, respectively. Riebeckite ($Na_2Fe^{2+}{}_3Fe^{3+}{}_2(Si_8O_{22})(OH)_2$) precipitates between 285°C and 195°C.

Boiling normally causes a pH increase due to loss of CO_2 and H_2S, whereas cooling leads to a pH decrease (Reed and Spycher, 1985; Reed, 1998). However, in this simulation the pH decreases slightly from 5.1 to 4.9 showing that the effect of cooling is stronger than boiling on pH, likely due to the low concentration of CO_2 in the fluid (Fig. 48a and c). Most of the components concentrated in the liquid phase remain fairly constant except for HS^-, Cu, Zn, and Pb, which decrease slightly because H_2S is lost to the vapour phase and based metals are consumed by sulfide precipitation as illustrated by the galena dissolution-precipitation reaction (Fig. 48c; Reed and Palandri, 2006), and HCO_3 also decreases because of CO_2 loss to the gas phase.

$$PbS_{(galena)} + H^+_{(aq)} = Pb^{2+}_{(aq)} + HS^-_{(aq)}$$

The solution starts relatively reduced as illustrated by the S^{6+}/ S^{2-} ratio, with H_2S more abundant than SO_4, and becomes more oxidized upon boiling because H_2S and H_2 are exsolved to the gas phase. However, sulfide aqueous species remain dominant throughout the entire boiling path.

Cooling. The mineral association precipitated upon cooling is shown in Figure 49. During this simulation, sphalerite precipitates in higher proportion than chalcopyrite and along the entire cooling path. Magnetite precipitates only during the first 5 degrees of cooling down to 335°C, and quartz starts to precipitate at 340°C. Tetrahedrite ($Cu_{12}Sb_4S_{13}$) starts to precipitate at 265°C and is replaced by stibnite (Sb_2S_3) at ~230°C because chalcopyrite consumes the available Cu in solution. Galena remains in solution until 165°C, likely due to the increasingly acidic conditions (pH decreases from 5.1 to 3.1) as a result of cooling. The redox indicator (S^{6+}/ S^{2-}) decreases from -3.5 to -9 because sulfide species remain constant whereas sulfate decreases.

Mixing. Progressive mixing of 0.5 kg of 150°C pure water into 1kg of the 340°C starting solution results in dilution and cooling (down to 150°C; Fig. 50). This simulation precipitates quartz and chalcopyrite along the entire path, and anthophyllite precipitates early in the paragenesis until 278°C. Pyrite appears slightly later at 330°C, and pyrrhotite precipitates from 290–170°C followed by galena (265°C) and sphalerite (240°C). The concentrations of Cu, Pb, and Zn in solution are reduced in response to the precipitation of chalcopyrite, galena, and sphalerite, respectively. The oxidation state (indicated by log S^{6+}/ S^{2-}) decreases initially from -3.8 to a minimum of -5.7, before increasing again to ~-1.5 at the end of the simulation (150°C). Precipitation of pyrrhotite occurs only during the more reducing (lower S^{6+}/ S^{2-}) conditions.

Water-rock reaction. During reaction with basaltic andesite wall-rocks, the hydrothermal fluid precipitates silicate minerals mainly at low water/rock ratios (epidote, quartz, actinolite-tremolite, clinochlore, and microcline), whereas pyrite and chalcopyrite start to precipitate at low water/rock ratios and continue throughout the entire reaction path (Fig. 51). Microcline and clinochlore become undersaturated at water/rock ratios above 3 and 40, respectively. Stilpnomelane precipitates at water/rock ratios above 40, and sphalerite and galena precipitate

later with further addition of fluid (water/rock ratios above 80). The pH remains constant and the solution becomes more reduced at high water/rock ratios.

Comparison with the observed mineral paragenesis. The mineral paragenesis observed in the Mala Noche deposit is complex and involves multiple stages of mineralization and likely several mechanisms of precipitation. Results of the stage I starting solution modelled here is comparable with the retrograde skarn-type mineralization stage described in Fig. 17. Ore, gangue, and alteration minerals observed to precipitate significantly in this stage are first chalcopyrite, pyrite and magnetite along with quartz, the cummingtonite-grunerite solid solution amphiboles $(Mg, Fe^{2+})_2(Mg, Fe^{2+})_5Si_8O_{22}(OH)_2$), ilvaite ($CaFe^{2+}{}_3(SiO_4)_2(OH)$), and stilpnomelane followed by pyrrhotite, galena, and sphalerite. Chalcopyrite is the most abundant sulfide and is observed throughout the entire mineralization stage. Sphalerite and galena are subordinate to chalcopyrite although by the end of the mineralization stage they become more abundant. Pyrrhotite is observed to be abundant although it is restricted in space and time.

The mineral association predicted from the boiling simulation partially resembles the observed mineral paragenesis. The amphiboles anthophyllite (polymorphic with cummingtonite) and riebeckite, not observed in the mineral paragenesis, could have been replaced by sulfides accounting for the radial acicular and bladed pseudomorph textures observed in pyrite and pyrrhotite. The relative sequence and amounts of ore minerals are consistent with the observed paragenesis except that pyrrhotite is not predicted, likely because the increasingly oxidized conditions inhibited its precipitation.

The simple cooling model results do not reflect the observed mineral paragenesis because it predicts the precipitation of sphalerite in higher abundance than chalcopyrite, and the precipitation of tetrahedrite and stibnite, which are not observed in the mineral paragenesis. The

mineral association predicted from mixing is similar to the observed mineral paragenesis except that pyrrhotite overlaps sphalerite and galena, and magnetite is absent.

The water-rock reaction simulation reproduces approximately the gangue and alteration minerals observed in the wallrocks, including epidote, chlorite (clinochlore), K-feldspar (microcline), epidote, quartz, and stilpnomelane. The amphibole solid-solution actinolite-tremolite, which was not observed in the paragenesis but is predicted in the simulation, could have been replaced by sulfides in the same way as proposed for other amphiboles. Ilvaite is not predicted to precipitate in the model because its thermodynamic properties are not well known and, therefore, it is not included in the SOLTHERM database. The relative sequence and amount of sulfide precipitation is also consistent with the observed mineral paragenesis, except that pyrite is predicted to be more abundant than chalcopyrite.

Comparison between the observed and modelled mineral paragenesis suggests that boiling and mixing may have played important roles in the precipitation of ore minerals, and water-rock reactions dominated in the formation of wall-rock alteration minerals and to a lesser extent contributed to ore mineral deposition.

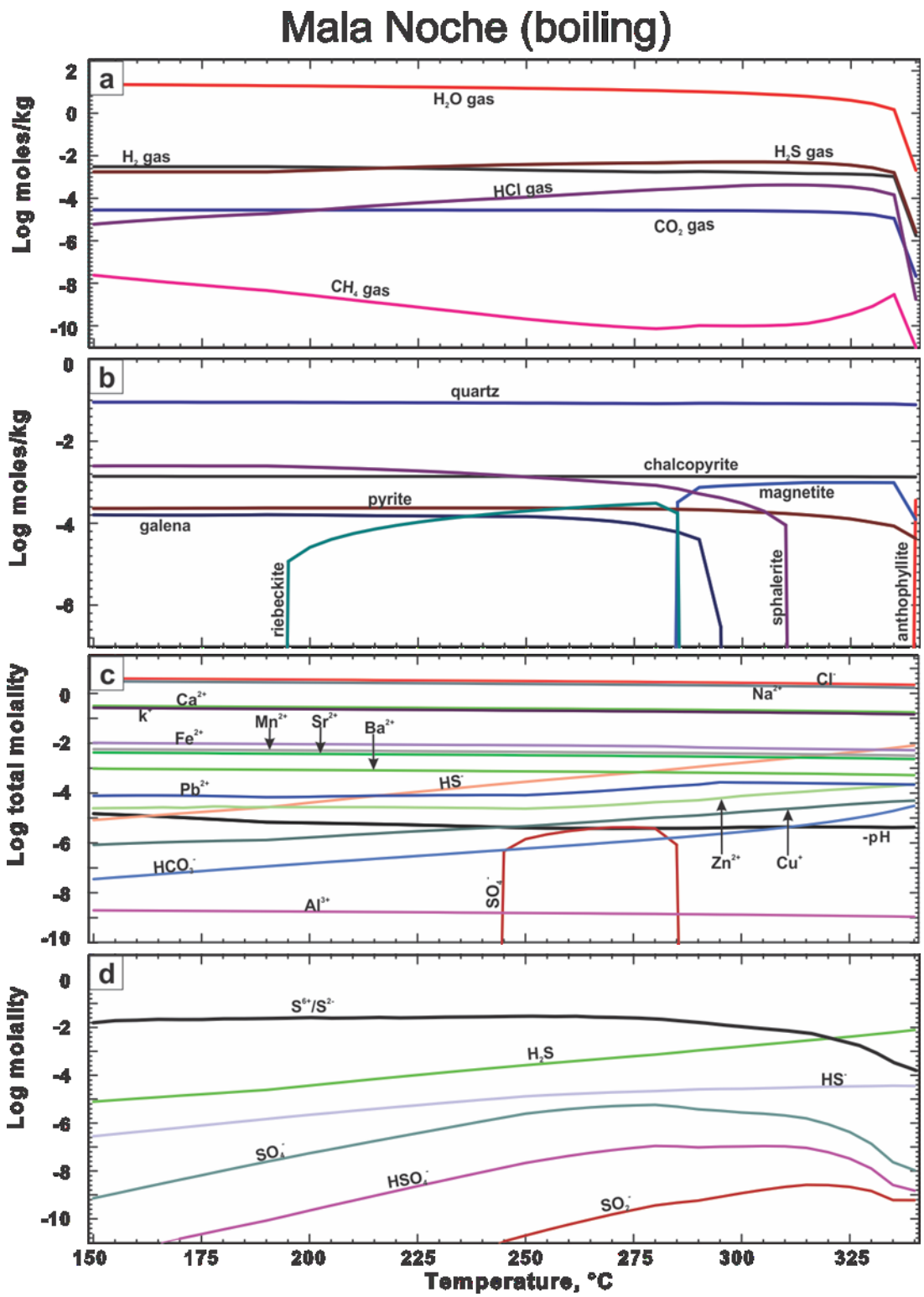

Figure 48. Results of the boiling simulation for 1 kg of the Mala Noche vein starting solution. The reactions procced from 340° to 150 °C at a constant enthalpy. (a) Gases released upon boiling. (b) Minerals precipitating from the solution (anthophyllite refers to Fe-anthophyllite). (c) Total concentration of components in the aqueous phase and pH variations along the boiling path. (d) Concentration of individual species in the aqueous phase and S^{6+}/ S^{2-} ratio indicative of redox variations (Cooke and McPhail, 2001).

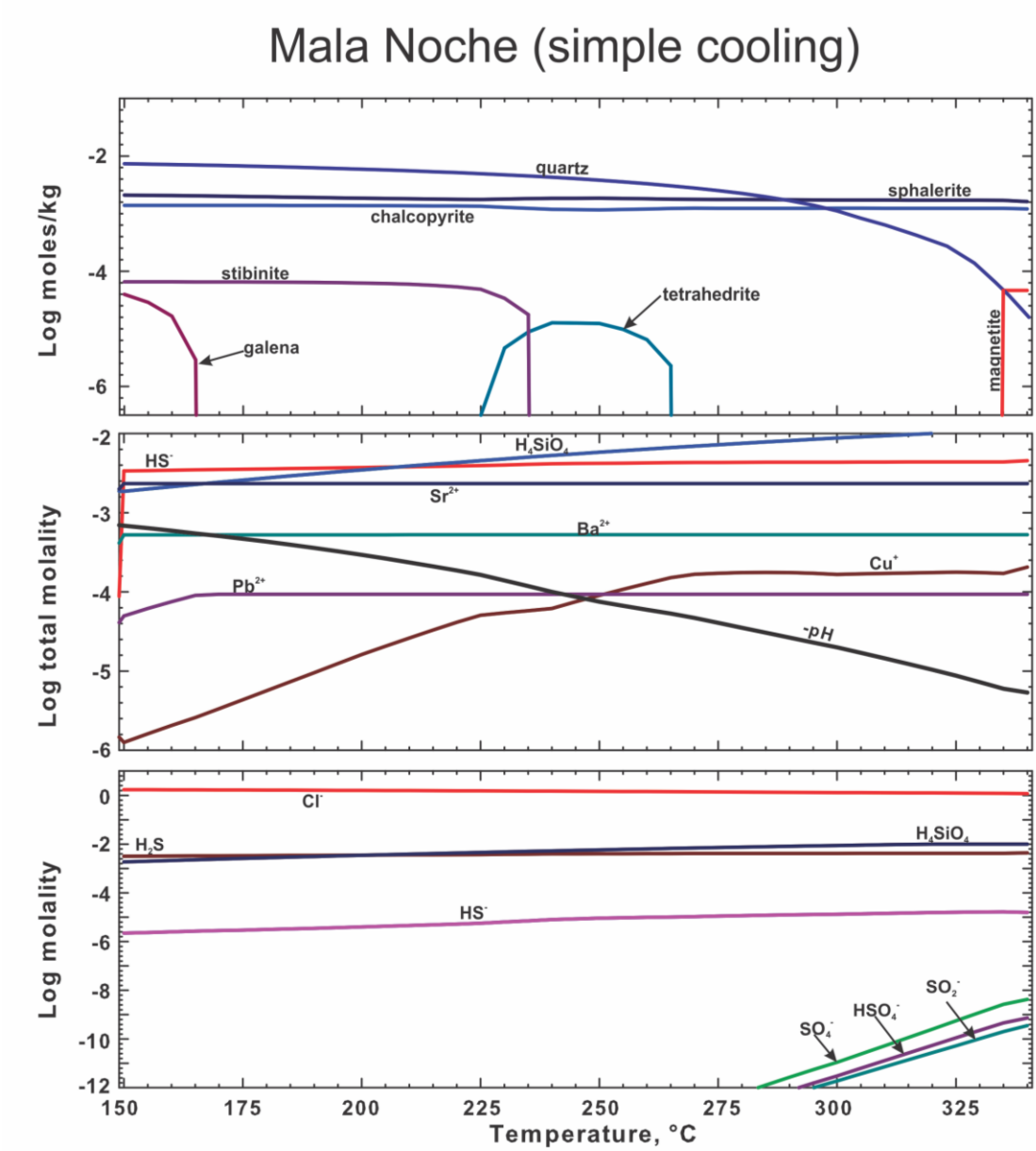

Figure 49. Results of cooling 1 kg of the Mala Noche vein starting solution from 340° to 150 °C. (a) Minerals precipitating from the solution upon cooling. (b) Total concentration of components in the aqueous phase and pH variations along the cooling path. (c) Concentration of individual species in the aqueous phase.

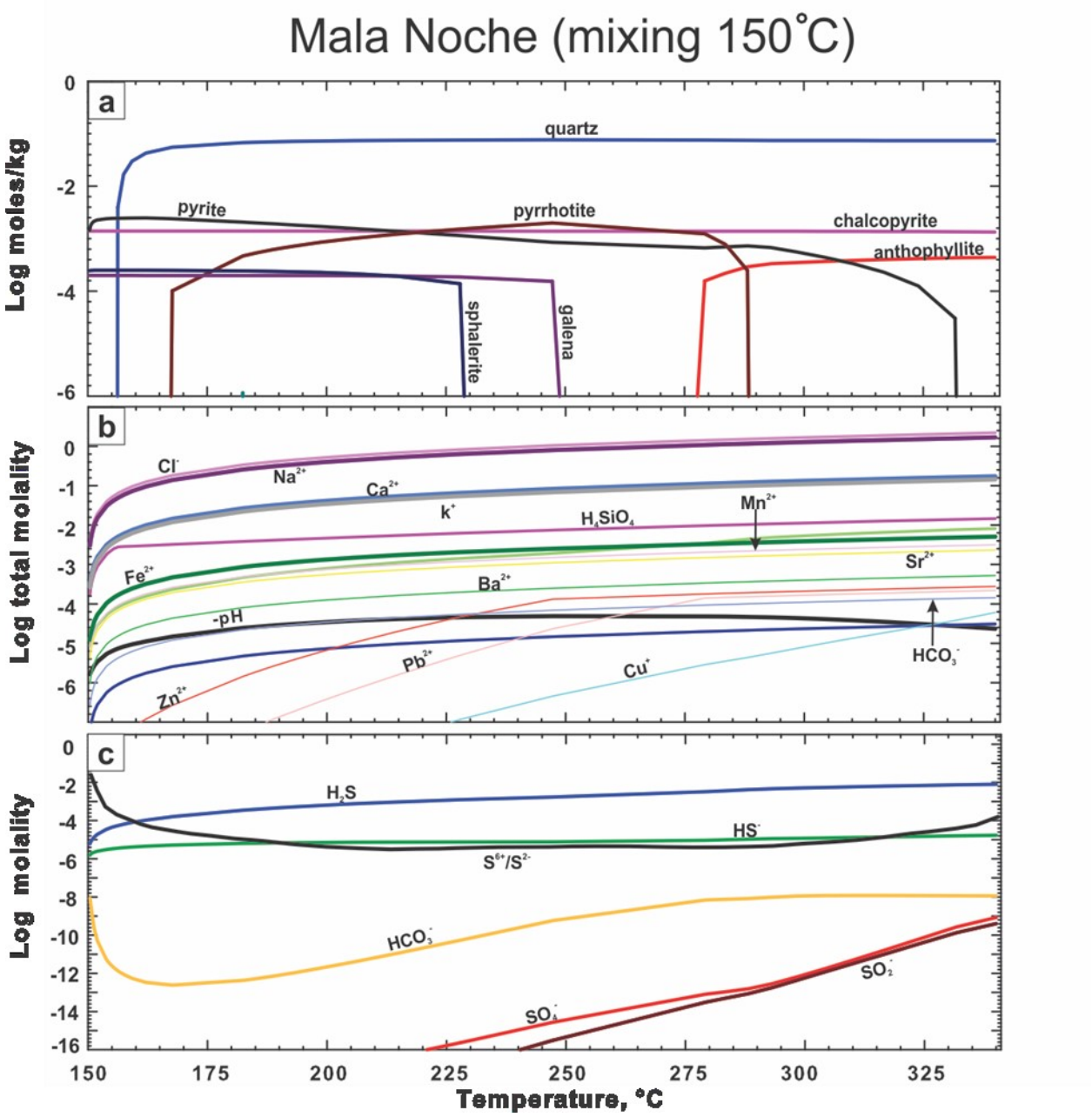

Figure 50. Results of mixing 1 kg of the Mala Noche vein starting solution at 340°C with 0.5 kg of pure water at 150°C. (a) Minerals precipitating from the solution upon gradual mixing and consequent cooling down to 150°C. (b) Total concentration of components in the aqueous phase and pH variations along the mixing path. (c) Concentration of individual species in the aqueous phase.

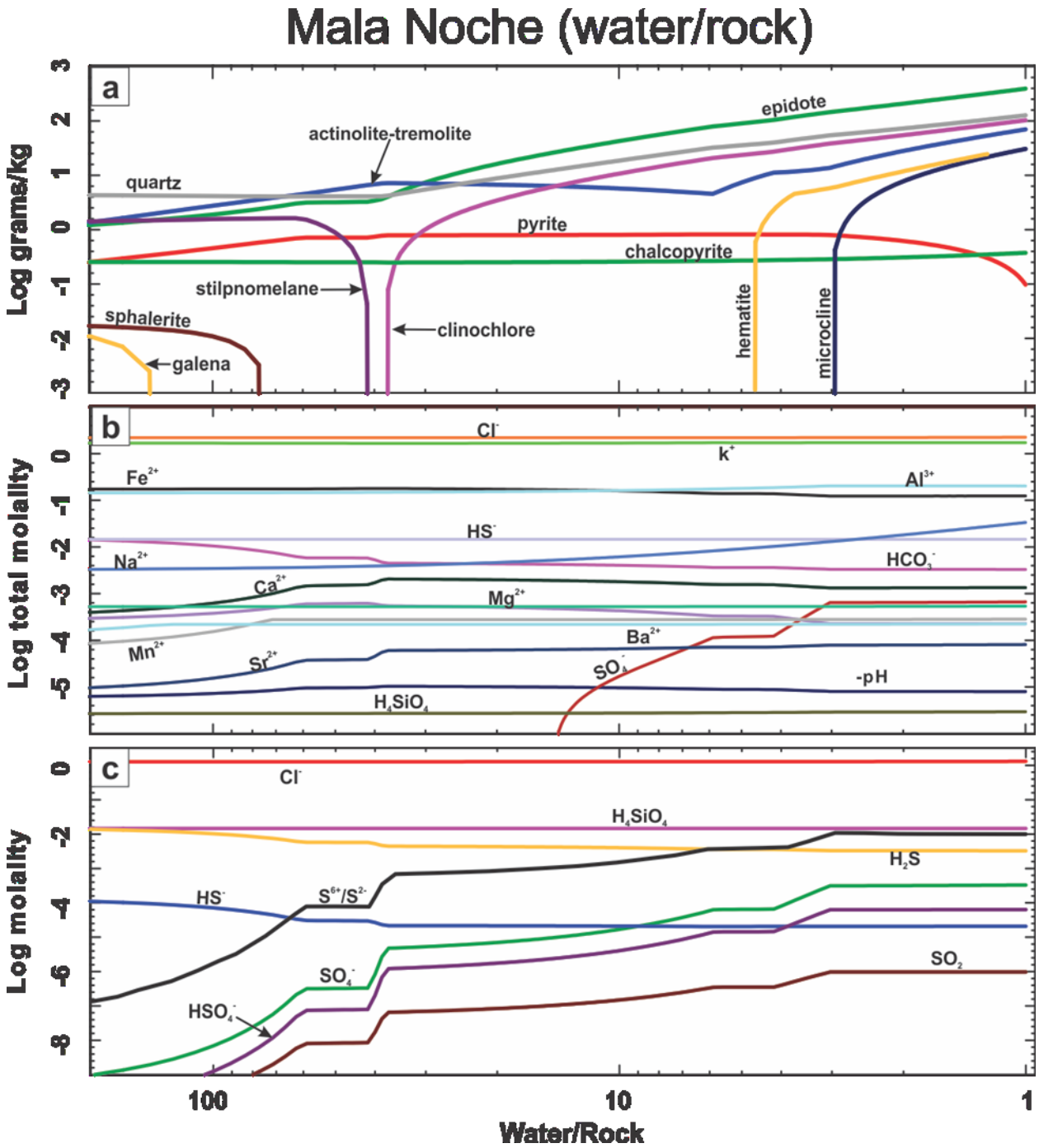

Figure 51. Results of reacting the Mala Noche vein starting solution with basaltic andesite at 340°C and 500 bars. (a) Minerals precipitating from the reaction. (b) Total concentration of components in the aqueous phase and pH variations. (c) Concentration of individual species in the aqueous phase.

5.8.2 Veta Grande

The estimated starting water composition for the Veta Grande vein stage II is shown in Table 4. Based on its isotopic composition ($\delta^{18}O$), salinity, and Th, this water composition is interpreted to represent a magmatic fluid. The temperature range of ore deposition for this stage determined by microthermometry is 180–280 °C. The starting temperature was set slightly higher than this temperature at 320°C and the models were run down to 150°C.

Boiling. Results of the adiabatic boiling simulation for the Veta Grande vein are shown in Figure 52. Quartz, pyrite, and K-feldespar start to precipitate when boiling begins at 320°C. Sphalerite and galena start to precipitate together at 295°C. Chalcopyrite precipitates later, in lower proportions, and only for the interval of temperature between 285–225°, and pyrargyrite starts to precipitate as the temperature drops to 260°C. Stibnite (Sb_2S_3) and bornite are predicted to precipitate at 255°C and 220°C respectively. The pH increases from 5 at 320°C to 5.3 at 260°C due to CO_2 loss, and then decreases again down to 5 because of the effect of continuous cooling (Figs. 52a–b; Reed and Spycher, 1985; Reed, 1998). The S^{6+}/ S^{2-} ratio increases because reduced sulfur (H_2S) is exsolved to the boiling phase.

Cooling. Figure 53 shows the simple cooling simulation results. Berthierite ($Fe^{2+}Sb_2S_4$), pyrite, and quartz, start to precipitate early in the paragenesis, and muscovite, stibnite, and chalcopyrite precipitate between 305°C and 285°C. Galena precipitates at 255°C, but sphalerite does not saturate despite the presence of Zn and HS^- in the solution. Kaolinite replaces muscovite as cooling continues and pH decreases progressively. Argentite and bornite precipitate at low temperature and pH. The pH decreases from 5 to 3 and the S^{6+}/ S^{2-} ratio remains constant throughout the reaction path.

Mixing. The results of mixing of waters for the Veta Grande vein are shown in Figure 54. The simulation yields berthierite from 320–270°C, whereas pyrite and chalcopyrite start to precipitate at the same time and throughout the whole temperature range, with pyrite in higher amounts than chalcopyrite. They are followed by stibnite and galena at 295°C and 285°C, respectively. Argentite saturates at 255°C, quartz saturates at 250°C, and sphalerite at lower temperature (160°C). The pH decreases down to 3.8 and the redox indicator increases slightly.

Water-rock reaction. The reaction between the Veta Grande vein starting solution and basaltic andesite at 320°C produces clinochlore and actinolite-tremolite accompanied by pyrite and galena at low water/rock ratios (Fig. 55). Galena becomes undersaturated as the water/rock ratio increases and then precipitates again at ratios above 10. Microcline precipitates at water/rock ratios between 2 and 9, and stilpnomelane above 6. Quartz, epidote, and lesser chalcopyrite precipitate only at high water/rock ratios (above 60;). Silver minerals and sphalerite do not precipitate in this simulation. The pH remains constant and the S^{6+}/ S^{2-} ratio decreases as the water/rock ratio increases.

Comparison with the observed mineral paragenesis. The observed mineral paragenesis of the Veta Grande mineralization stage II, modelled here, is shown in Figure 19. Ore minerals observed to precipitate significantly are sphalerite, galena, with lesser pyrite, and minor chalcopyrite, pyrargyrite, and acanthite. The main gangue and alteration minerals are quartz and chlorite with hematite, respectively. Other minerals such as bornite, covellite, anglesite, and kaolinite are observed only in the supergene environment.

The ore minerals and their relative sequence and amount of precipitation predicted through the simulation of boiling are similar to the observed mineral paragenesis except that stibnite and hypogene bornite are not observed and acanthite is not predicted to precipitate.

Possibly the estimated concentration of Sb in the starting solution is too high, causing the precipitation of stibnite and silver sulfosalts instead of acanthite. Bornite is predicted to precipitate at lower temperatures than the rest of the minerals, and therefore may have been deposited at higher levels in the crust that have been eroded away. Simple cooling is unlikely to be important because the model fails to predict sphalerite despite of the presence of Zn and HS^-, predicts the stabilization of hypogene kaolinite as a result of highly acidic conditions, and predicts berthierite, which is not observed in the hypogene mineral paragenesis. The mineral sequence and relative quantities produced by the mixing model are not similar to the observed mineral paragenesis, and the water-rock reaction model does not replicate the observed alteration minerals. Therefore, boiling alone could have been the main mechanism of ore formation.

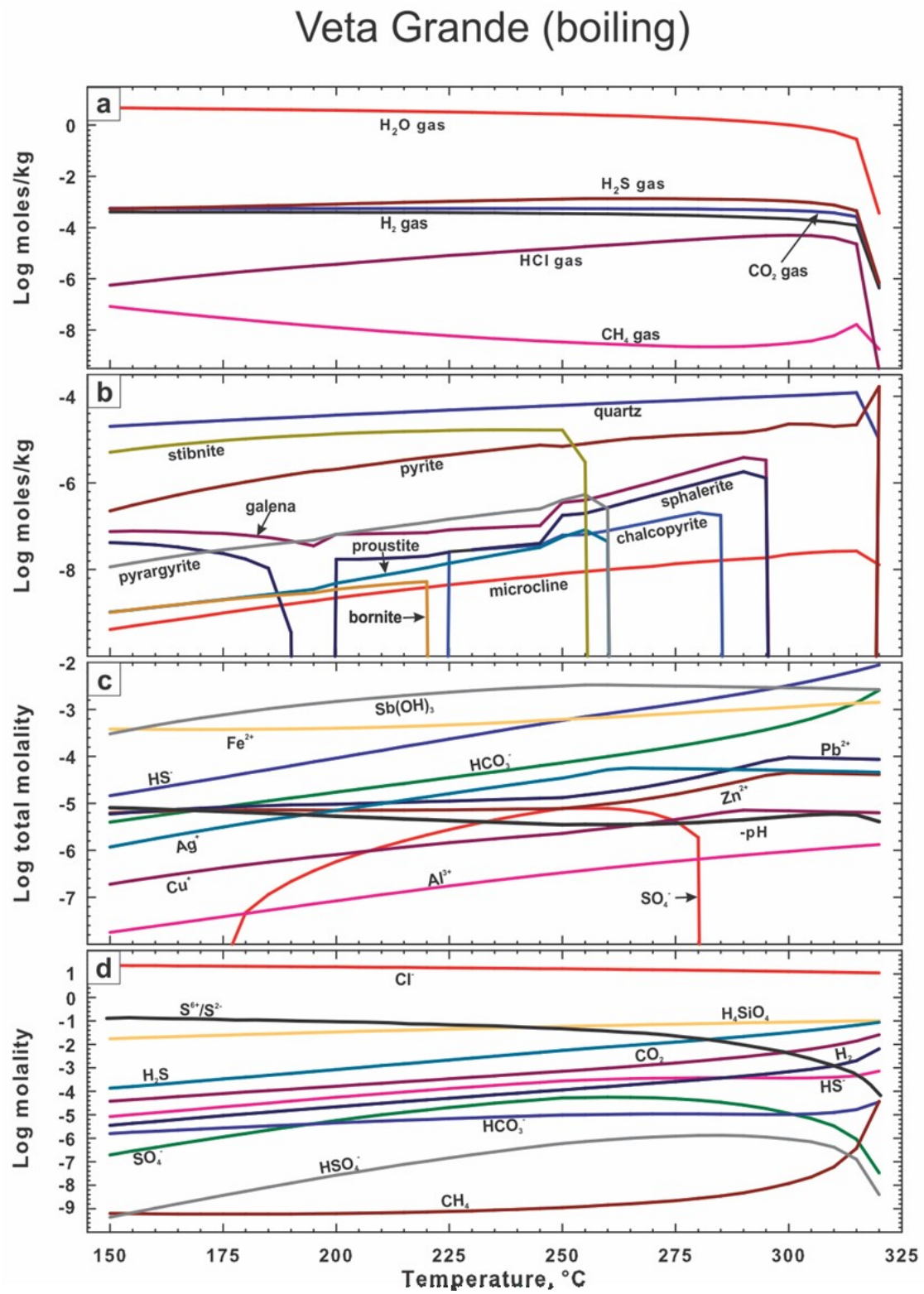

Figure 52. Results of the boiling simulation for 1 kg of the Veta Grande vein starting solution. The reactions procced from 320° to 150 °C at a constant enthalpy. (a) Gases released upon boiling. (b) Minerals precipitating from the solution. (c) Total concentration of components in the aqueous phase and pH variations along the boiling path. (d) Concentration of individual species in the aqueous phase

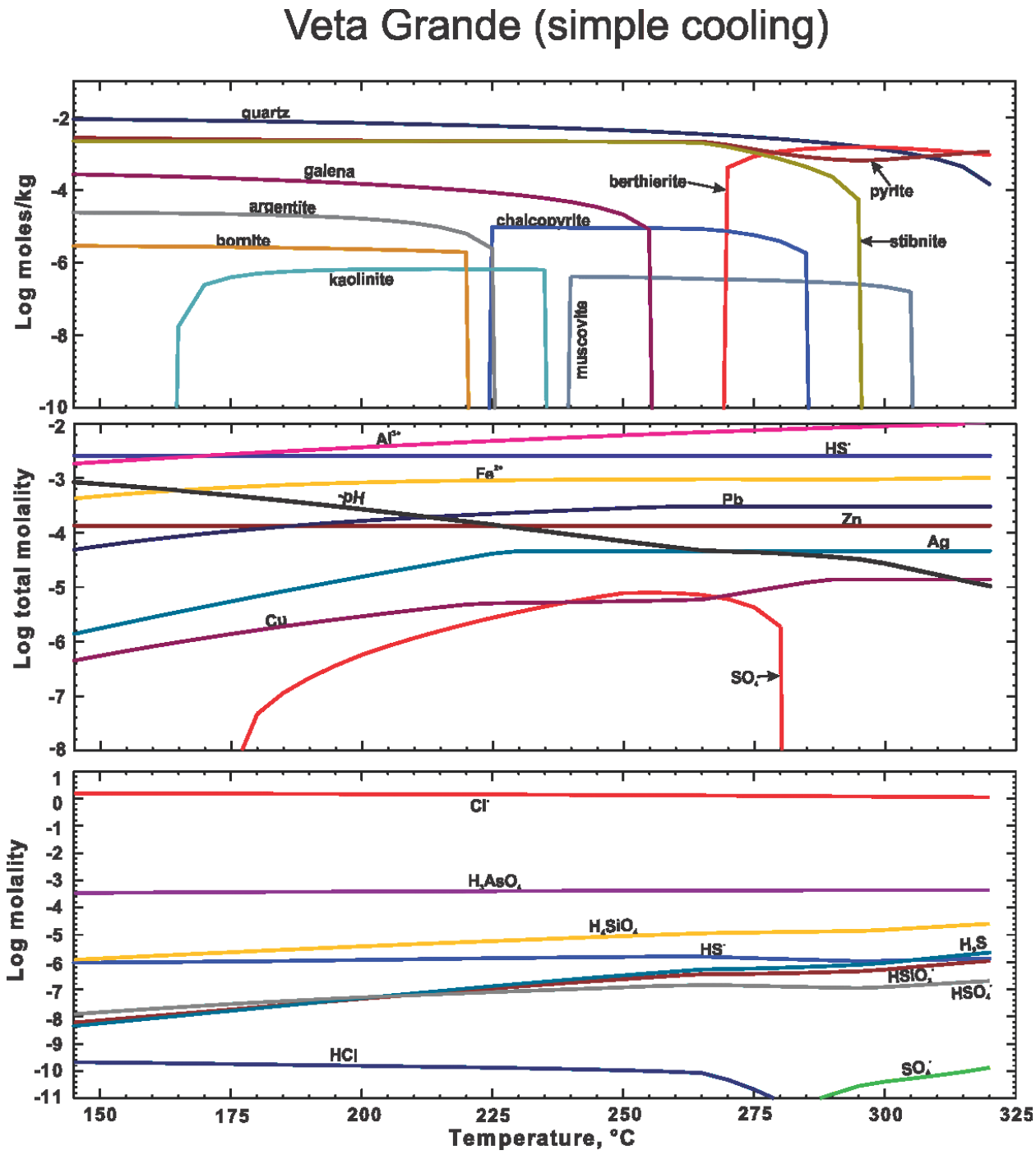

Figure 53. Results of cooling 1 kg of the Veta Grande vein starting solution from 325° to 150 °C. (a) Minerals precipitating from the solution upon cooling. (b) Total concentration of components in the aqueous phase and pH variations along the cooling path. (c) Concentration of individual species in the aqueous phase.

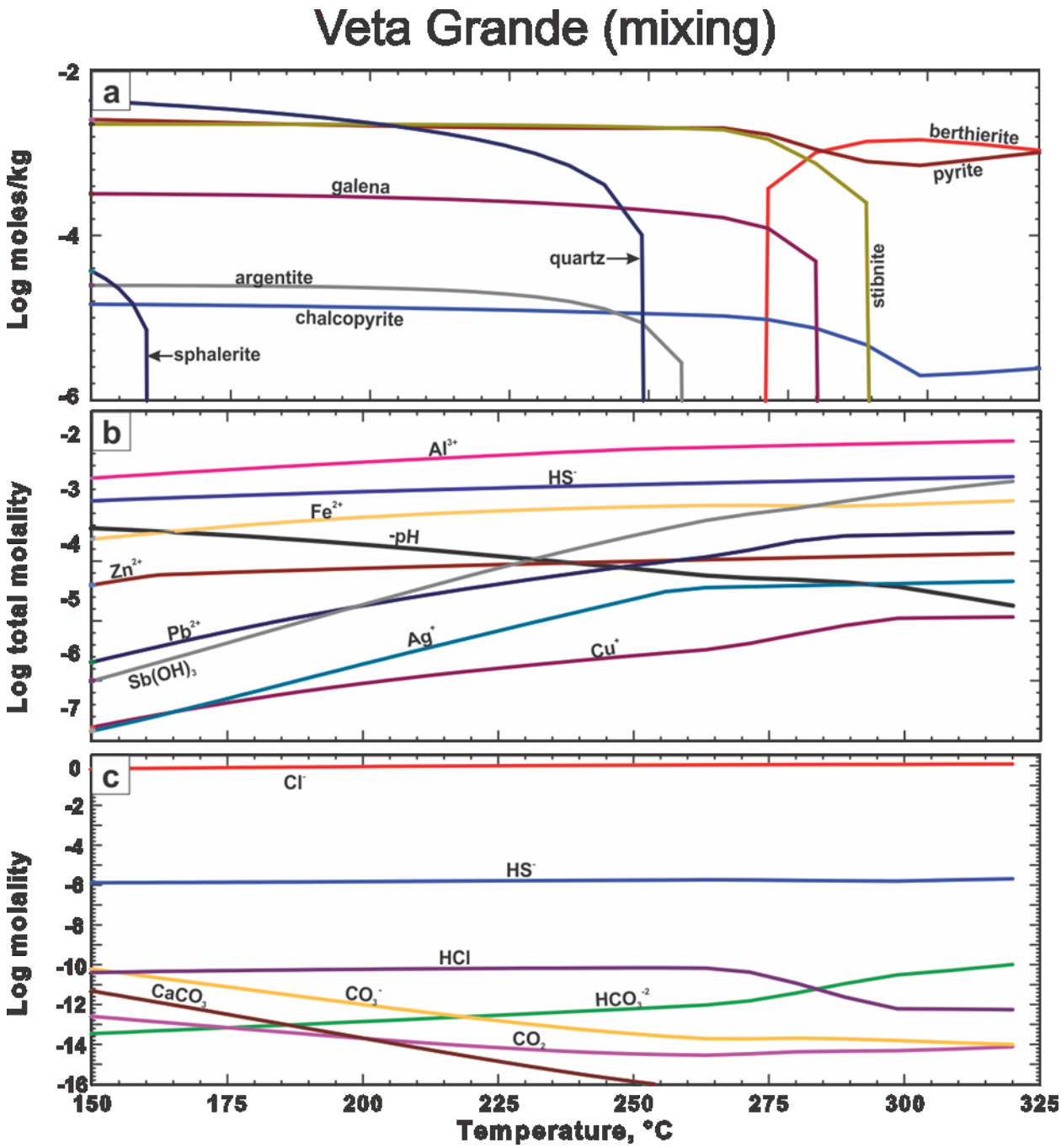

Figure 54. Results of progressively mixing 1 kg of the Veta Grande vein starting solution at 320°C with 0.5 kg of pure water at 25°C. (a) Minerals precipitating from the solution upon gradual mixing and consequent cooling down to 150°C. (b) Total concentration of components in the aqueous phase and pH variations along the mixing path. (c) Concentration of individual species in the aqueous phase.

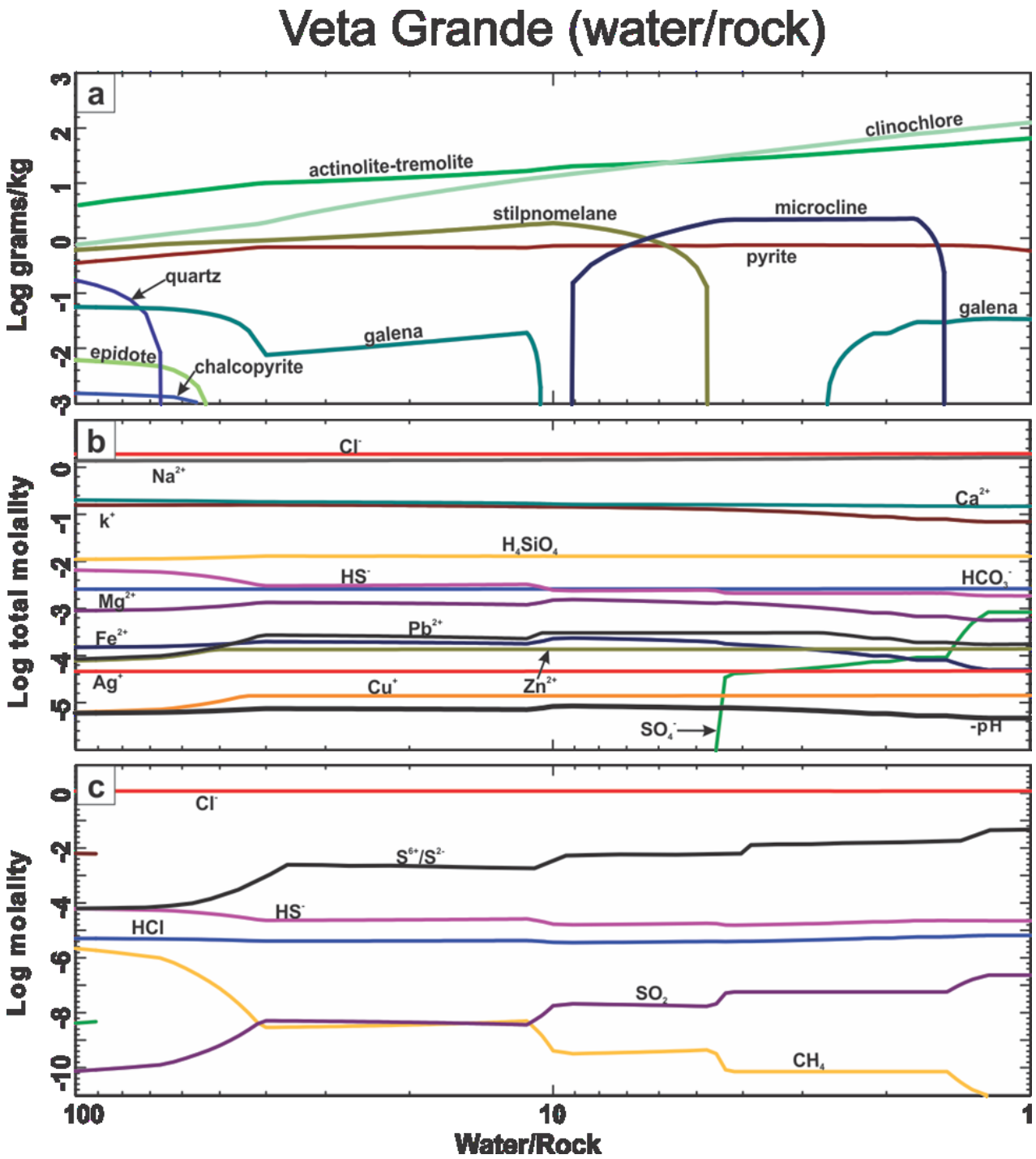

Figure 55. Results of reacting the Veta Grande vein starting solution with basaltic andesite at 320°C and 500 bars. (a) Minerals precipitating from the reaction. (b) Total concentration of components in the aqueous phase and pH variations. (c) Concentration of individual species in the aqueous phase.

6. Discussion

6.1 Geochemical comparison between the Zacatecas district and the southern Mesa Central magmatic rocks

The geochemical and radiogenic isotopic compositions of the Zacatecas Eocene volcanic rocks are compared to those of the upper and lower volcanic sequence rhyolites of the southern Mesa Central in Figures 30, 31, and 56.

Most of the Zacatecas rhyolites show trace-element patterns more similar to rhyolites from the early Oligocene lower volcanic sequence than to the upper volcanic sequence of Orozco-Esquivel et al. (2002; Figs. 30 and 31). Both, the Zacatecas rhyolites and the lower volcanic sequence rocs have distinctive negative anomalies for Nb, Ta, and Ti that are characteristic of subduction-related magmas (Gill, 1981; Brenan et al., 1994; Stolz et al., 1996). However, the Zacatecas rhyolites are slightly more depleted in REE (especially middle-REE; MREE), Sr, P, Eu, and Ti than the lower volcanic sequence, reflecting their more fractionated (SiO_2-rich) compositions, and the La Virgen rhyolite shows a stronger negative anomaly for Nb similar to the upper volcanic sequence (Fig. 31a).

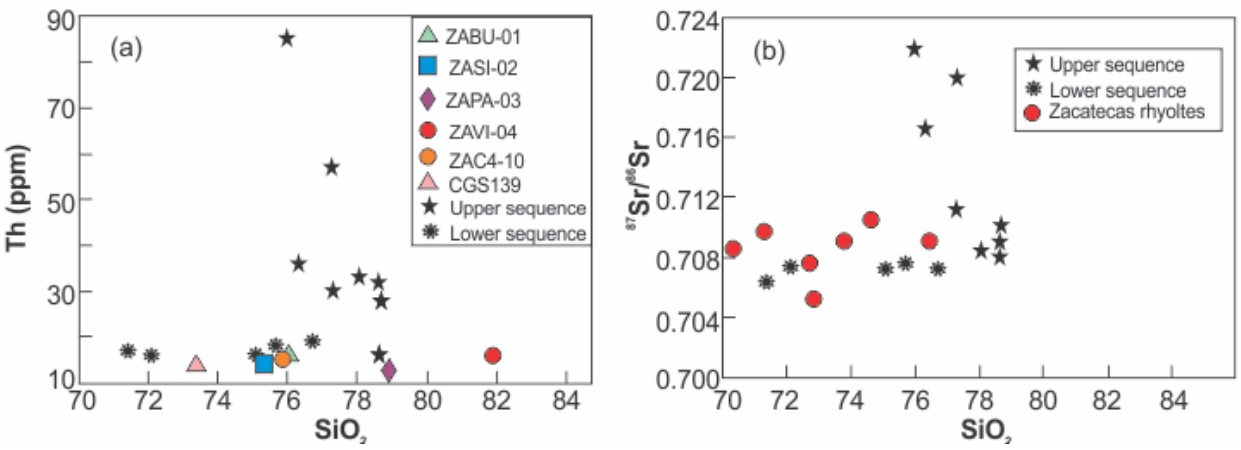

Figure 56. Plot of Th and initial strontium isotope ratios versus silica contents for the Zacatecas district felsic volcanic and subvolcanic intrusive rocks (Verma, 1984) and for the southern Mesa Central (upper and lower sequences; Orozco-Esquivel et al., 2002).

In contrast, the early–late Oligocene upper volcanic sequence rhyolites (Orozco-Esquivel et al., 2002) show different patterns, with flatter REE patterns and large negative Eu anomalies, smaller depletions in Ta and Nb, and prominent depletions in Ba, Sr, and Eu relative to the lower sequence and Zacatecas rhyolites (Fig. 31; Orozco-Esquivel et al., 2002). Furthermore, the Th compositions and $^{87}Sr/^{86}Sr$ ratios show a wide range of values. (Fig. 56; Verma, 1984; Orozco-Esquivel et al., 2002).

The similarity between the Zacatecas rhyolites and the regional lower volcanic rhyolite sequence, and the distinction from the upper volcanic sequence rhyolites, is also shown in the Th content and Sr isotopic composition of these rocks (Fig. 56; Sr isotopic data from Verma, 1984; Th data from Orozco-Esquivel et al., 2002). The high Th contents and radiogenic Sr isotopic compositions of the upper sequence rocks indicates higher degrees of crustal contamination in these younger volcanic rocks or a possible interaction with older crust (Christiansen et al., 1986; Orozco-Esquivel et al., 2002).

These contrasting geochemical and isotopic characteristics are interpreted to reflect a switch from subduction-related magmatism to magmas generated by partial melting of lower-

crustal rocks during Oligocene Basin and Range-type extension. This transition took place over a short period of ~ 1 m.y. at ~30 Ma (Orozco-Esquivel et al., 2002; Rodriguez-Rios et al., 2007).

6.3 Timing, style, and tectonomagmatic setting of mineralization in the Zacatecas district

6.3.1 Eocene magmatism and Cu- and Zn-Pb-Ag-rich mineralization

Figure 57 summarizes the U-Pb and $^{40}Ar/^{39}Ar$ geochronology of igneous rocks and hydrothermal mineralization in the Zacatecas district.

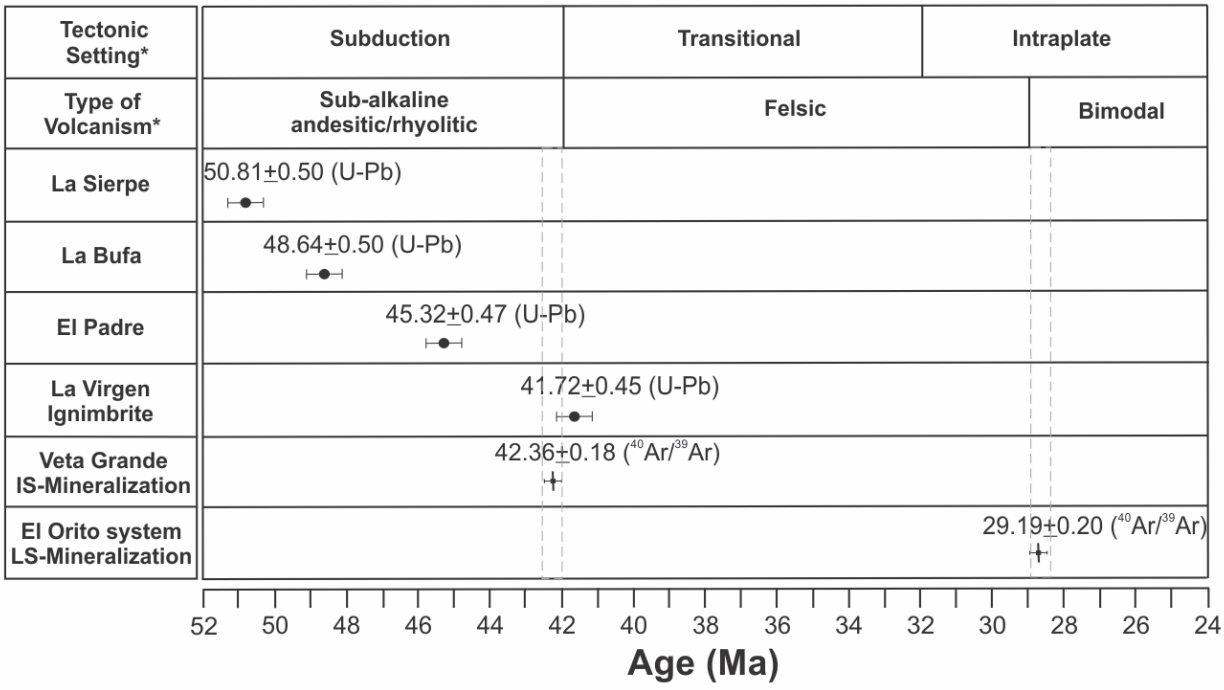

Figure 57. Summary of U-Pb and $^{39}Ar/^{40}Ar$ geochronology from this study; tectonic setting and type of volcanism from Tristan-Gonzalez et al. (2009).

The U-Pb ages for felsic intrusive and volcanic rocks reported in this study constrain continental arc volcanism in the district to between ~50 to 41 Ma. The La Sierpe plug and dike

spatially associated with Cu-rich mineralization in the Mala Noche vein record the oldest Cenozoic magmatic event reported to date in the district. Their ages (50.81 ± 0.50 Ma and 50.19 ± 0.53 Ma, respectively) are similar to that of the El Peñón Blanco granite located ~100 km SE of the Zacatecas district (50.94 ± 0.47 Ma; Aranda-Gomez et al., 2007). Both the granite stock and the rhyolitic hypabyssal rocks intrude marine sedimentary sequences deformed by Laramide shortening, but they show no field or petrographic evidence of deformation. This indicates that they were emplaced after the end of the main compressional phase of the Laramide orogeny. The statistically identical ages of these rocks suggest that the La Sierpe rhyolitic plug and dikes may represent a local hypabyssal expression of deep, regional plutonism.

The Cu-rich mineralization in the Mala Noche vein was likely emplaced during late stages of crystallization of the La Sierpe plug and dikes (~50 Ma). This is suggested by local evidence of contact metamorphism associated with these rocks, and evidence of self-brecciation during or shortly after emplacement that includes hydraulic hydrothermal breccias, and peperitic magmatic breccias with amoeboid shaped fragments (indicating that the fragments were still hot at time of brecciation). This mineralization was sheared up by the ESE- to SE-trending strike-slip faults in which later epithermal mineralization was emplaced. Deformation textures in sulfides have been reported also in the San Martin skarn deposit (Rubin and Kyle, 1988), which is located along a SE regional trend of deposits that contain both skarn-type and epithermal mineralization including San Martin, La Colorada, Francisco I. Madero, Zacatecas, and Guanajuato, suggesting a regional structural control (Fig 4; Rubin and Kyle, 1988; Randall et al., 1994; Moller et al., 2001; Cannet et al., 2009).

In the Zacatecas district, magma was extruded along ESE- to SE-trending strike-slip faults after the emplacement of the La Sierpe plug and dikes. The La Bufa dome was emplaced at

48.64 ± 0.50 Ma along the ESE-trending La Cantera fault system, which is roughly parallel and relatively close to the suture zone of the oceanic Guerrero terrane with the North American continent (Figs. 4 and 7). The fact that felsic calc-alkaline magma was emplaced along a normal fault, synchronous with sedimentary basin formation (deposition of the Zacatecas red conglomerate), indicates that the volcanic arc was under a mild extensional or transtensional stress regime at this time (Tristan-Gonzalez et al., 2009). The La Virgen ignimbrite (41.72 ± 0.45 Ma) overlies the Zacatecas red conglomerate and represents the youngest subalkaline volcanic event in the district.

Because the La Sierpe plug and La Bufa dome are both cut by intermediate-sulfidation polymetallic epithermal veins, they provide a maximum age for hydrothermal activity (≤48.7 Ma). Similarly, the La Virgen ignimbrite is not cut by the ESE- to SE-striking Ag-Pb-Zn veins, and therefore provides a minimum age for this mineralization stage (≥41.7 Ma).

The age of the Ag-rich mineralizing event is provided by a $^{40}Ar/^{39}Ar$ age for adularia from stage I of the Veta Grande intermediate-sulfidation vein (42.36 ± 0.18 Ma). This age is consistent with the constraints noted above, and suggests that this mineralizing event occurred towards the end of this volcanic cycle, shortly prior to emplacement of the La Virgen ignimbrite whose vent is proposed to be located close to this area. This, together with the fact that dikes share the same structures as veins, suggests an intimate relationship between intermediate-sulfidation mineralization and the last stages of subduction-related magmatism in the area, consistently with the model proposed by Sillitoe and Hedenquist (2003). Silver-rich mineralization in other districts within the Mesa Central has been also associated to subduction-related magmas dated between 32–55 Ma (e.g., at the Guanajuato, Sombrerete, La Colorada, and Fresnillo-Fortuna area deposits; Albinson, 1988; Lang et al., 1988; Randall et al., 1994).

The age of the stage II intermediate-sulfidation mineralization in the Veta Grande vein is unknown and it is not clear if the two stages are coeval or not, although we consider they were formed close in time because they share the same structures and structural orientation.

6.3.2 Oligocene Au mineralization

Unlike the earlier Eocene Ag-Pb-Zn mineralization, the low-sulfidation El Orito vein system is not clearly related to magmatism, and occurs in a structurally distinct set of N–S-trending veins. It thus appears to have no temporal or genetic relationship to the intermediate-sulfidation Ag-Pb-Zn veins, contrary to the proposal of Camprubi and Albinson (2007). The El Orito vein system cuts the La Virgen ignimbrite (42.36 ± 0.18 Ma), and our 29.19 ± 0.20 Ma $^{40}Ar/^{39}Ar$ age for adularia from the El Compas vein confirms that the low-sulfidation Au mineralization was formed during a distinct, later event in the Oligocene.

This mineralization was emplaced in dominantly normal faults with a sinistral strike-slip component. Previous studies have used different interpretations to explain the structural contrast between this and the ESE- to SE-striking system. Nelson (2005) suggested that both systems were formed as a result of the same stress field (Fig. 58a), whereby the El Orito faults would represent second-order antithetic structures (R') with a sense of displacement opposite to the bulk movement, and oriented at a high angle (~75°) to the main dextral strike-slip fault plane (M).

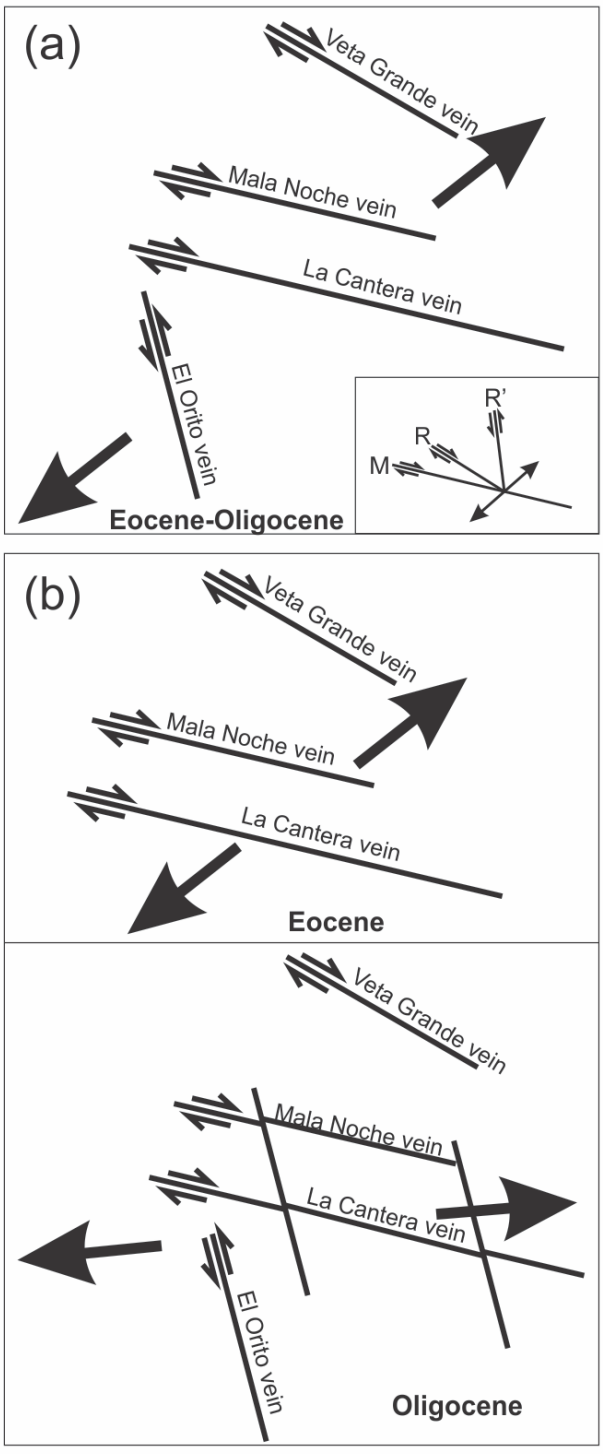

Figure 58. Possible models of fault kinematics and stress field for the Zacatecas fault systems. (a) Transtensional stress regime prevalent in the Eocene-Oligocene. Here, the El Orito vein represents a secondary fault (R') related to the La Cantera main fault. The inset shows a Riedel model for a dextral strike-slip system (Petit, 1987). (b) Model for a transtensional stress regime in the Eocene overprinted by Basin and Range extension in the Oligocene. Abbreviations: M = main fault plane; R = synthetic secondary shears; R' = antithetic secondary shears.

In contrast, other authors have suggested that the NNW-striking El Orito faults might have been formed after the Zacatecas fault system, and in response to a change from a transtensional stress regime in the Eocene to dominantly extensional in the Oligocene related to Basin and Range deformation, with a local sinistral strike-slip component (Fig. 58b). This model implies a rotation of the regional extension direction from NNE in the Eocene to ENE in the Oligocene (Fig. 58c), which is consistent with the ages obtained in this study, and with regional structural interpretations (Tristan-Gonzalez et al., 2009); we therefore favor this model.

The occurrence of selenide minerals in the El Orito system suggests a similarity to the selenide-rich suite of Au-Ag low-sulfidation deposits in the northern Nevada rift (John, 2001). These deposits include Midas, Sleeper, and Mule Canyon, and have been related to the Yellowstone hotspot and Basin and Range extensional tectonics. A detailed $^{40}Ar/^{39}Ar$ study from Midas shows that Au-Ag mineralization was coeval with felsic volcanism and NNW–NW-striking normal faults at 15.4 ± 0.10 Ma ($^{40}Ar/^{39}Ar$ on adularia; Leavitt et al., 2004), although Pb isotope data suggest a source of gold from mafic magmas (Kameov et al., 2007; Saunders et al., 2008). The low-sulfidation El Orito system is not clearly related to magmatism in the Zacatecas area and is older than the Nevada deposits, but its age coincides with the time of change in magma composition across the Mesa Central in response to the onset of Basin and Range tectonics (Orozco-Esquivel et al., 2002; Rodriguez-Rios et al., 2007). The regional effusion of felsic magma (upper volcanic sequence) related to this event was controlled by graben and half-graben structures with similar N–S orientations to the El Orito vein system and other Au-Ag-rich low-sulfidation deposits distributed across the Mesa Central (e.g., Bolañitos in Guanajuato and Pinos in Zacatecas; Figs. 4 and 6; Labarthe-Hernandez et al., 1982; Tristan-Gonzalez et al., 2009; Steel, 2012; Munroe, 2014). Sinter deposits, characteristic of low-sulfidation

mineralization (Sillitoe and Hedenquist, 2003), were deposited in the Oligocene and proximal to N–S graben-bounding normal faults. Thus, we suggest that Oligocene low-sulfidation mineralization in the Zacatecas district was related to the onset of this extensional tectonic regime.

The similar age of Au-Ag-rich mineralization in the Fresnillo SW district (29.75 ± 0.12 and 29.68 ± 0.10 Ma; Velador, 2010; Velador et al., 2010) to the El Orito system (29.19 ± 0.20 Ma), and the similar mineralogy to the Au-rich low-sulfidation mineralization of the Guanajuato district (27–30 Ma; Taylor, 1971; Gross 1975), which is controlled by similar structural systems, suggests that these low-sulfidation hydrothermal systems were related to the onset of Basin and Range extensional tectonics across the Mesa Central in the Oligocene. These observations are consistent with the model proposed by Sillitoe and Hedenquist (2003) for low-sulfidation deposits.

6.4 Source of the hydrothermal fluids and mechanisms of precipitation

6.4.1 Mala Noche vein

6.4.1.1 Source of hydrothermal fluids

Calculated isotopic compositions of fluids help to trace the origin of water involved in ore deposition because different sources of water have characteristic isotopic compositions. The $\delta^{18}O$ value of seawater is relatively uniform (+0.5 to -1.0‰; Sheppard, 1977), whereas the compositions of fresh meteoric waters are negative and vary systematically according to their geographic location down to -55‰ in polar regions. The $\delta^{18}O$ range of present-day meteoric water in central Mexico has been estimated to be between -4.89 and -11.75% (Aguilar-Ramírez

et al., 2017), and tectonic reconstructions show that the paleolatitude of central Mexico on the Eocene–Miocene was similar to the present time latitude (Ferrari et al., 2007). The $\delta^{18}O$ value of magmatic water is typically between +5.5 and +10.0 ‰, which overlaps the wide range of metamorphic waters (+5 to +25 ‰). Formation waters also show a very wide range in $\delta^{18}O$ values (between -15 and +8 ‰; Taylor, 1974). The original isotopic composition of fluids can be modified via isotopic exchange during water-rock or water-water interactions. For instance, the negative values of meteoric water can be shifted towards positive values due to interaction with magmatic rocks, or the magmatic water range of values can be lowered due to dilution with meteoric water.

The correlated Th–salinity arrays for the Mala Noche vein fluid inclusions combined with estimated ore-fluid isotopic compositions, suggest that three different types of fluid were involved in the formation of the mineral deposit (Figs. 39–41 and 45).

The correlation of high homogenization temperatures with high salinities and isotopic values between +5 and +8 ‰ $\delta^{18}O_{fluid}$ located in quartz cores, suggest an early magmatic source of fluid. Conversely, the cooler, lower salinity, and isotopically light fluid suggest a source of meteoric water. The third fluid, dilute, with a range of homogenization temperatures, and isotopic $1\delta^{18}O_{fluid}$ values of between -0.9 and +2.9 may represent either meteoric fluids that underwent variable isotopic exchange with silicate wallrocks or formation waters.

The isotopic composition of sulfides precipitated from ore-forming fluids is a function of the bulk sulfur isotopic composition in the fluid and the physico-chemical conditions during sulfide precipitation (T, pH, and fO_2). Therefore, discussion of the origin of sulfur in the system must be based on determinations of $\delta^{34}S_{\Sigma S}$ (Rye and Ohmoto, 1974). The mineral association of

pyrrhotite, magnetite, and pyrite, and the lack of sulfates in the Mala Noche deposit indicate that reduced sulfur (H_2S) dominated in the fluids, and hence that the $\delta^{34}S$ values of sulfides likely approximates the $\delta^{34}S_{\Sigma S}$ in the fluid (Ohmoto and Rye, 1979). The consistently homogeneous and negative $\delta^{34}S$ value of sulfide minerals (between -12.3 and -14.4 ‰) suggest a source of sulphur from the metasedimentary host rocks.

6.4.1.2 Mechanism of precipitation

Results of the different mechanisms of mineral precipitation modelled for the Mala Noche vein stage I suggest that a combination of boiling, mixing, and water-rock reactions may have been involved in the ore-forming process. Cooling is unlikely to be responsible for the mineral precipitation by itself but occurs as an intrinsic part of the boiling and/or mixing process. A combination of these processes overprinted in space but operating at different time is geologically reasonable, and has been proposed to account for ore formation at other deposits such as Porgera (Ronacher et al., 2004).

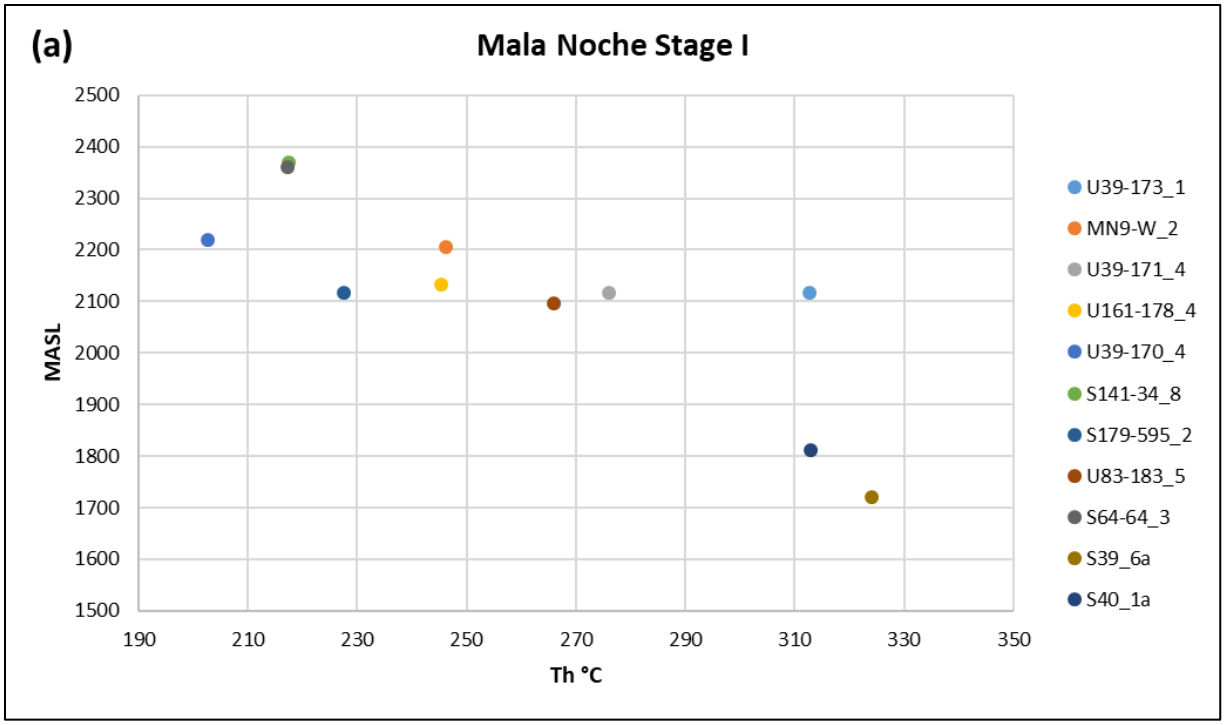

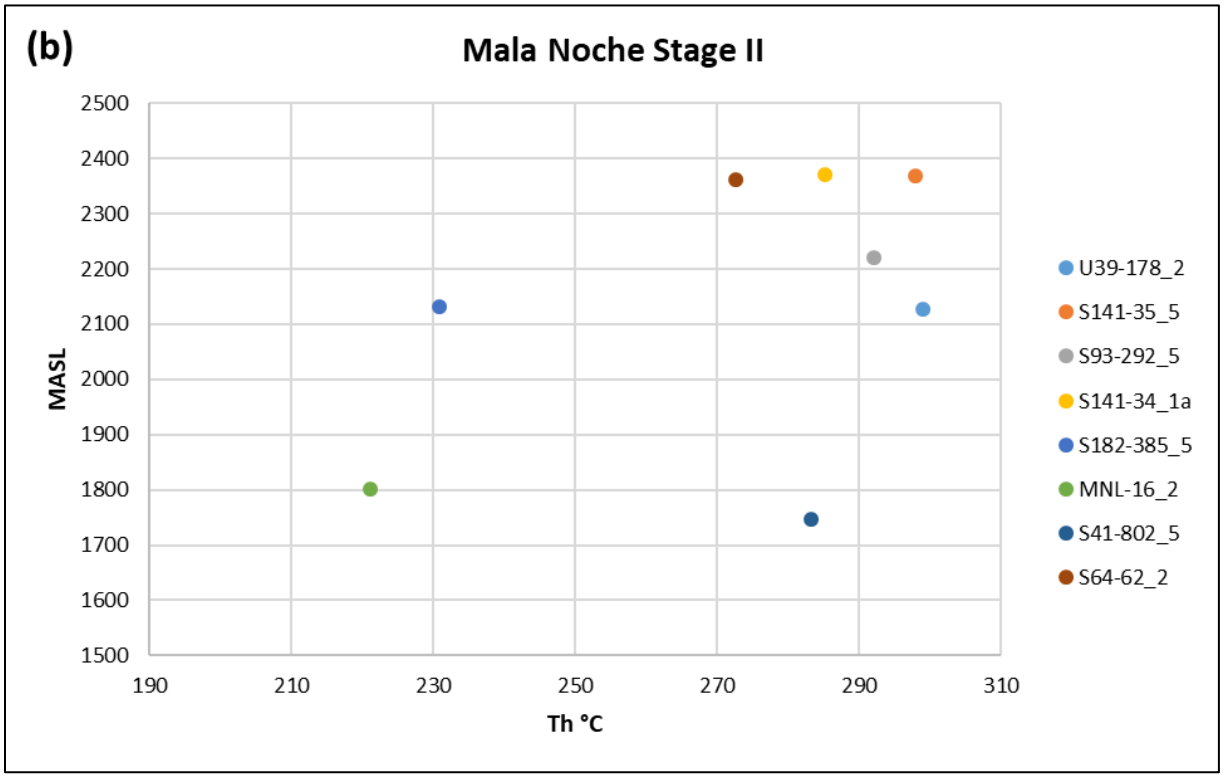

Figure 59. Plot of the maximum temperature FIAs from each sample vs. depth (MASL) for (a) the Mala Noche vein stage I, and (b) stage II samples.

Evidence of boiling observed in fluid inclusions together with the well-constrained depth of sampling (Figs 18a and 59) permit to estimate the paleodepth of trapping. The 310°C, 14 wt. % NaCl eq. stage I FIA, if trapped under boiling conditions, would have formed at a paleodepth of ~950 m (assuming hydrostatic conditions; Fig. 60). Two of these samples from drillholes S39 and S40 were collected at ~700 m below surface (~1750 masl), suggesting uplift and erosion of only ~250 m since formation in the Eocene. This estimate is reasonable considering the preservation of paleosurface features such as sinters and coeval volcanic rocks in the Zacatecas district. Non-boiling liquid-rich fluid inclusion assemblages fall below the 14 wt. % NaCl eq. boiling curve as expected. Scatter in the data that does not allow a simple fit to boiling point–depth curves may reflect pressure fluctuations during vein formation between hydrostatic and lithostatic conditions, and/or differential post-entrapment vertical displacements, such as block faulting along the length of the vein system.

A plot of average temperatures of the highest-Th FIAs in each sample against sampling depth shows that the highest-temperature fluids from Stage I samples do tend to occur at the deepest levels, with lower temperature FIAs at shallower levels (Fig. 59a), as expected from a boiling control. Stage II fluids, however, show minimal discernible trend (Fig. 59b). The reproduction of the observed mineral paragenesis with the boiling mathematical model of stage I fluid, confirms the role of this mechanism of precipitation.

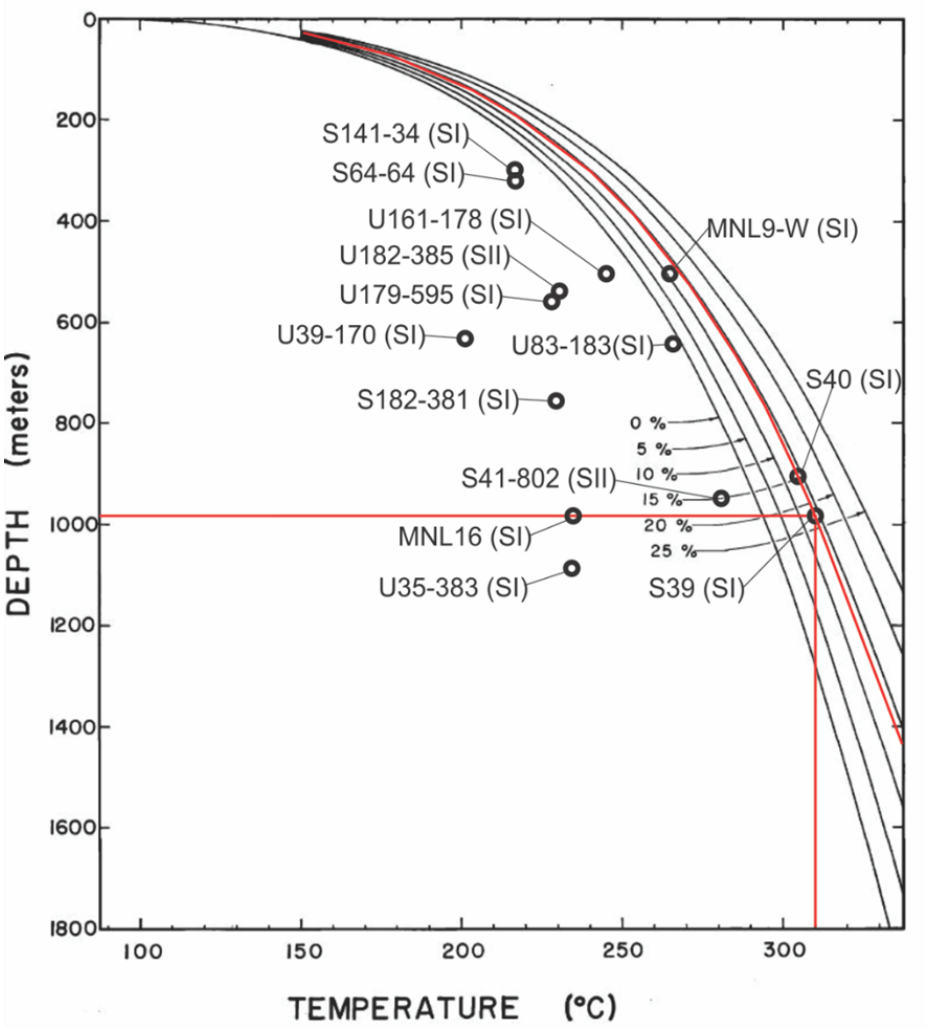

Figure 60. Boiling-point curves for pure H_2O and aqueous brines with salinity compositions up to 25 wt. % NaCl eq. from Hass (1971), showing the inferred depth of formation for a stage I FIA (310°C, 14 wt.% NaCl eq.) with evidence of boiling. Liquid-rich FIA are plotted according to their average homogenization temperatures and reconstructed paleodepth (present depth plus 250 m).

The $\delta^{18}O_{fluid}$ vs salinity correlated array in accordance with arrays of homogenization temperature vs salinity for fluid inclusions within single FIAs, indicate that mixing between hot magmatic fluids and cooler ground water also occurred (Figs. 41 and 45). The mathematical modelling for mixing also predicts the observed mineral paragenesis satisfactorily except for the lack of magnetite. Mixing can also explain the dissolution textures observed on CL images of the Mala Noche vein quartz, although fluctuations on pressure are also plausible (Rusk and Reed,

2002). The mineral paragenesis predicted by mixing complements the paragenesis predicted by boiling to account for the observed mineral paragenesis, and it is possible that the two processes occurred simultaneously or at different times.

6.4.1.3 Wall-Rock Alteration

The mathematical simulation of water-rock reaction shows that the 340°C hydrothermal solution reacting with basaltic andesite can produce some of the observed silicate mineralogy in the wall rock-hosted mineralization, and may account for some of the locally observed skarn-type mineral paragenesis. Reaction of the same hydrothermal fluid with other lithologies from the volcano-sedimentary succession such as limestone lenses or calcareous shales could have locally produced other silicates such as ilvaite, hedenbergite, and possibly garnet. Sulfide mineralization with higher amounts of chalcopyrite precipitation relative to other mechanisms of precipitation (boiling and mixing) is correctly predicted and explains high-copper grades associated with silicate mineralogy and replacement textures. This suggest that water-rock reactions may have played an important role on ore deposition locally and prior to boiling and mixing.

6.4.1.4 Metal Zoning

A lateral and apparently vertical zonation of the metal content in the Mala Noche vein with copper concentrated in the central section and Zn-Pb-Ag extending laterally and upward beyond the Cu core is observed in the Mala Noche vein (Fig. 19). Based on this fact and fluid inclusion analyses, porphyry copper mineralization has been inferred underneath this area (Albinson, 1997). However, high homogenization temperatures in fluid inclusions from the Mala

Noche vein do not necessarily correlate with high salinities and Cu content, and drilling of the La Sierpe plug and dikes targeting this model at the Cozamin mine has failed to intersect porphyry-type alteration or mineralization (Fig. 19a). The apparent zonation of metal content could be an effect of Zn-Pb-Ag epithermal mineralization that overlap and overprints Cu-rich ore shoots, continues laterally, and extends to shallower levels beyond Cu-rich zones giving the impression of outward zonation. The precipitation of high Cu content ore shoots may have been controlled by water-rock reactions independently of depth. The vertical extend of Zn-Pb-Ag distribution could have been controlled by mixing and extended boiling. The presence of gases such as CO_2 and CH_4 documented in the system (Albinson et al., 2001), could have allowed boiling conditions and ore deposition at depths greater than 1 km from surface.

6.4.2 Veta Grande

6.4.2.1 Source of hydrothermal fluids

The low $\delta^{18}O_{fluid}$ values (from +2 to +2.8‰) from the moderately saline (6–10 wt.% NaCl eq.) fluids of the Veta Grande vein stage I suggest a source of isotopically exchanged formation waters, although hydrogen isotopes analyses and an evaluation of mass balance are required for a more definitive assessment (Taylor, 1974). Dilution of isotopically heavy and saline magmatic fluids with cooler, light, and dilute fluids is unlikely because the Th–salinity correlation that would also be expected from mixing of these two fluids is not observed (Fig. 42). Fluid inclusions from the Veta Grande stage II show a clear bimodal distribution of salinities (moderately saline and dilute). The $\delta^{18}O_{fluid}$ values (+4.6 to +10.1 ‰) from regions that contain the saline end member suggest a source of magmatic water (Taylor, 1974). There are no oxygen

isotope analyses of stage II quartz from regions that contain dilute fluid inclusions, however the highly dilute nature of these fluids suggests a meteoric water source, and the petrography of fluid inclusions indicates that they were trapped at different time than the saline end member. Trends between saline high-temperature and dilute low-temperature fluids within single FIAs that may indicate mixing are also not observed in this stage.

The cathodoluminescence images of these samples display crystal growth textures that show no correlation between isotopic values and luminosity (Fig. 46c). Fluctuations in physico-chemical parameters (fluid pressure, temperature, composition, pH, or fO_2) may cause variations in trace element concentrations that yield different cathodoluminescence response (Götze et al., 2001; Rusk et al., 2008). The multiple silica-banding and textures characteristic of this stage have been explained in terms of an opening and sealing mechanism that causes fluctuations in fluid pressure, and consequent boiling during reopening of host structures (Albinson, 1995). This mechanism could also explain the well-developed growth zoning observed in CL-images, as well as the intermittent banding of sulfide precipitation related to boiling, as the mathematical modeling and fluid inclusions evidence for boiling suggest. This evidence was observed in both stages, although mathematical modeling was applied only for the Veta Grande Stage II because of lack of reliable fluid inclusions chemical data for Stage I.

In the Veta Grande vein mineral paragenesis there is no magnetite, and pyrrhotite is minor compared with the Mala Noche vein. However, the lack of hematite and sulfate minerals also suggests that the fluids were dominated by reduced sulfur. The sulfur isotopic compositions of sulfide minerals from both stages of the Veta Grande vein and Mala Noche are very homogeneous and show negative values that suggest a possible common source of sulphur from

the metasedimentary host rock, or oxidation of magmatic sulfur possibly due to boiling (Ohmoto and Rye, 1979; Richards and Kerrich, 1993). However, the oxidation process is likely to be far from equilibrium and would be expected to result in a scattered range of data; a reduced source seems more likely. This is consistent with the relatively high CH_4 concentrations obtained from fluids of the Veta Grande vein (Albinson et al., 2001). At the Fresnillo district, the also homogeneous and negative $\delta^{34}S$ values of sulfides, have been interpreted to be the result of incorporating sedimentary sulfide from the sedimentary host rock into the ore-forming fluid.

6.4.2.1 Mechanism of precipitation

Although there is not enough information to model the mechanisms of precipitation for the Veta Grande stage I, the coexistence of liquid- and vapour-rich fluid FIA's and the brecciated nature of this stage of mineralization suggest that boiling may have played an important role on ore deposition. Rare adularia banded with sulfides and associated with quartz and calcite were fluid inclusions evidence for boiling was observed, may be a product of boiling (Henley et al., 1984; Cooke et al., 1996). Results of the Veta Grande stage II mathematical simulations of different mechanisms of mineral precipitation show that boiling alone produced the observed mineral paragenesis, consistently with fluid inclusions evidence for boiling also observed in this stage. Fluid inclusion evidence and mathematical modelling of ore deposition in the Creede epithermal system, which shares similar characteristics with the Veta Grande vein, indicates that both boiling and mixing processes were responsible for ore deposition and zoning patters of mineral assemblages (Plumlee, 1994).

6.3.3 El Orito System

6.3.3.1 Source of hydrothermal fluids

The $\delta^{18}O_{fluid}$ values (-1.4 to +3.1 ‰) calculated for the El Compas vein combined with the low salinities of these fluids (<1 wt.% NaCl eq.; Figs 43–44) suggest a source of meteoric water. The positive δ^{18}Ofluid values may have been attained by isotopic exchange during interaction of meteoric waters with wall rock, or they may indicate some mixing with magmatic fluid (δ^{18}Ofluid ≈ +5.5 to +10‰; Taylor, 1974). The CL image of quartz from sample VNC4 shows well-defined growth zonation of alternating dark, grey, and bright bands (Fig. 46d), and in general the higher and lower δ^{18}O values correlate with darker and brighter zones, respectively. This sharp CL–isotopic banding suggests that fluids with distinct isotopic compositions flowed through the veins in pulses, which is more consistent with pulsed flow of varying proportions of meteoric and magmatic (?) fluids. A wallrock interaction process would be expected to result in more uniform or gradational changes in fluid isotopic composition, rather than sharp changes.

6.3.3.2 Mechanism of precipitation

Associations of textures that result from rapid mineral precipitation such as colloform quartz, plumose, feathery, and flamboyant among others, have been associated to boiling of hydrothermal fluids (Moncada et al., 2016). Whereas bladed calcite has been considered a characteristic texture formed by boiling due to loss of CO_2 (Simmons and Christenson, 1994). The common presence of these textures in the El Orito system, along with fluid inclusion evidence for boiling (coexisting fluid- and vapour-rich fluid inclusions) and the mineral assemblage of quartz, adularia, and calcite associated to ore minerals (native gold, electrum, and

silver selenides), strongly suggest that boiling was the dominant mechanism of ore precipitation (Henley et al., 1984; Cooke et al., 1996; Simmons et al., 2005). The same mechanism of deposition has been proposed for similar low-sulfidation deposits, including Sleeper in Nevada (Saunders, 1994) and the low-sulfidation Mexican deposits (Camprubí and Albinson, 2007).

7. Conclusions

Polymetallic mineral deposits in central Mexico commonly show combined characteristics of different styles of mineralization including skarn-type, intermediate- and low-sulfidation (e.g. The San Martin, Zacatecas, Fresnillo, and Guanajuato mining districts). Most researchers had attributed this combination of mineralization styles to the evolution of protracted hydrothermal systems related to the emplacement of plutons that have not been identified. However, this study indicates that these different styles of mineralization are related to distinctive tectonic events and were formed from different sources of ore fluids and mechanisms of deposition, rather than to the evolution of a single hydrothermal system.

Base metals mineralization with high-Cu grades in the Zacatecas district was deposited dominantly by water-rock reactions and boiling and mixing of magmatic water related to the last stages of crystallization of ~51 Ma felsic dikes and plugs with ground waters. Magma and fluids were channelized along NW-trending transtensional structures forming localized high-grade skarn-type mineralization and related epithermal veins. Strike-slip reactivation of these structures sheared up this mineralization and allowed the emplacement of a subsequent event of Ag-Pb-Zn-rich epithermal intermediate-sulfidation mineralization at ~42 Ma, apparently associated with the last stages of subduction-related magmatism in the Mesa Central. The main mechanism of

mineral deposition for this stage of mineralization was boiling of dominantly magmatic fluids. During the onset of Basin and Range crustal extensional deformation in the Mesa Central, these deposits were later (~29 Ma) overprinted by Au-rich epithermal low-sulfidation mineralization by boiling of predominantly meteoric fluids along N–S-oriented structures. This two-stage model explains the juxtaposition of intermediate- and low-sulfidation deposits in the Mesa Central, deposit types that are normally found in different tectonic settings and therefore, different locations (Hedenquist et al., 2000; Sillitoe and Hedenquist, 2003).

The distribution of world class mining districts that include combined styles of mineralization aligned along the Guerrero Terrane boundary, suggests that the richness of the Mexican Silver Belt can be explained in terms of the tectonic history of the Mesa Central.

References

Aguirre-Diaz GJ, McDowell FW (1991) The volcanic section at Nazas, Durango, Mexico, and the possibility of widespread Eocene volcanism within the Sierra Madre Occidental; Mid–Tertiary Cordilleran magmatism; plate convergence versus intraplate processes. Journal of Geophysical Research 96:13373–13388

Aguirre-Diaz GJ, McDowell FW (1993) Nature and timing of faulting and synextensional magmatism in the southern Basin and Range, central–eastern Durango, Mexico. Geological Society of America Bulletin 105:1435–1444

Aguirre-Diaz GJ, Labarthe-Hernandez G (2003) Fissure ignimbrites; fissure–source origin for voluminous ignimbrites of the Sierra Madre Occidental and its relationship with basin and range faulting. Geology (Boulder) 31:773–776

Albinson T (1988) Geologic reconstruction of paleosurfaces in the Sombrerete, Colorada, and Fresnillo districts, Zacatecas state, Mexico. Economic Geology 83:1647–1667

Albinson T (1995) Bosquejo de la evolución estructural e hidrotermal del distrito de Zacatecas, *in* Trabajos Técnicos XXI Convención Nacional Asociación de Ingenieros de Minas, Metalurgistas y Geólogos de México, Acapulco, Guerrero: México D.F., Asociación de Ingenieros de Minas, Metalurgistas y Geólogos de México (AIMMGM), p. 143–170.

Albinson T, Norman DI, Cole D, Chomiak B (2001) Controls on formation of low–sulfidation epithermal deposits in Mexico; constraints from fluid inclusion and stable isotope data; New mines and discoveries in Mexico and Central America. Special Publication (Society of Economic Geologists (U.S.)) 8:1–32

Amador MG (1908) Las capas Carnicas de Zacatecas Triassic deposits. Boletin de la Sociedad Geologica Mexicana 29–35

Aranda-Gomez JJ, McDowell FW (1998) Paleogene extension in the southern Basin and Range Province of Mexico; syndepositional tilting of Eocene red beds and Oligocene volcanic rocks in the Guanajuato mining district. International Geology Review 40:116–134

Aranda-Gomez JJ, Henry CD, Luhr JF (2000) Post–Paleocene tectono–magmatic evolution of the Sierra Madre Occidental and the southern part of the Basin and Range tectonic province, Mexico. Boletin de la Sociedad Geologica Mexicana 53:59–71

Aranda-Gomez JJ, Molina-Garza R, McDowell FW, Vassallo Morales LF, Ortega-Rivera MA, Solorio-Munguia JG, Aguillon-Robles A (2007) The relationships between volcanism and extension in the Mesa Central; the case of Pinos, Zacatecas, Mexico. Revista Mexicana de Ciencias Geologicas 24:216–233

Atwater TM (1989) Plate tectonic history of the northeast Pacific and Western North America. In Winterer EL (ed) The Geology of North America, The northeastern Pacific Ocean and Hawaii 21–72

Barboza-Gudiño JR, Tristan-Gonzalez M, Torres-Hernandez JR, (1998) The Late Triassic–Early Jurassic active continental margin of western North America in northeastern Mexico. Geofisica Internacional 37:283–292

Barton, PB, Jr., (1985) High Temperature Calculations Applied to Ore Deposits in: Fluid–Mineral Equilibria in Hydrothermal Systems: Reviews in Economic Geology, v1.

Brenan JM, Shaw HF, Phinney DL, Ryerson FJ, (1994) Rutile–aqueous fluid partitioning of Nb, Ta, Hf, Zr, U and Th: implications for high field strength element depletions in island–arc basalts. Earth and Planetary Science Letters 128:327–339

Burckhardt C (1906) Sobre el descubrimiento del Triasico marino en Zacatecas. Boletin de la Sociedad Geologica Mexicana 43–45

Caballero-Martinez JA (1999) Carta Geologico–Minera, Zacatecas F13–B58. Servicio Geologico Mexicano–Secretaria de Economia 1:50,000 scale

Camprubi A (2009) Major metallogenic provinces and epochs of Mexico. Society for Geology Applied to Mineral Deposits News 25:6–20

Camprubi A, Ferrari L, Cosca MA, Cardellach E, Canals A (2003) Ages of epithermal deposits in Mexico; regional significance and links with the evolution of Tertiary volcanism. Economic Geology and the Bulletin of the Society of Economic Geologists 98:1029–1037

Camprubi A, Albinson T (2007) Epithermal deposits in Mexico; update of current knowledge, and an empirical reclassification; Geology of Mexico; celebrating the centenary of the Geological Society of Mexico. Special Paper – Geological Society of America 422:377–415

Cannet C, Camprubi A, Gonzalez-Partida E, Linares C, Alfonso P, Piñeiro-Fernandez F, Prol-Ledesma RM (2009) Mineral assemblages of the Francisco I. Madero Zn-Cu-Pb-(Ag) deposit, Zacatecas, Mexico: Implications for ore deposit genesis. Ore Geology Reviews 35:423–435

Centeno-Garcia E (2005) Review of upper Paleozoic and lower Mesozoic stratigraphy and depositional environments of central and west Mexico; constraints on terrane analysis and paleogeography; The Mojave–Sonora Megashear hypothesis; development, assessment, and alternatives. Special Paper – Geological Society of America 393:233–258

Centeno-Garcia E, Ruiz J, Coney PJ, Patchett PJ, Ortega–Gutierrez F (1993) Guerrero Terrane of Mexico; its role in the Southern Cordillera from new geochemical data: Geology (Boulder) 21:419–422

Centeno-Garcia E, Silva-Romo G (1997) Petrogenesis and tectonic evolution of central Mexico during Triassic–Jurassic time; Special issue dedicated to the International workshop on The geology of northwestern Sonora. Revista Mexicana de Ciencias Geologicas 14:244–260

Centeno-Garcia E, Guerrero-Suastegui M, Talavera-Mendoza O (2008) The Guerrero composite terrane of western Mexico; collision and subsequent rifting in a supra–subduction zone; Formation and applications of the sedimentary record in arc collision zones. Special Paper – Geological Society of America 436:279–308

Centeno-Garcia E, Busby C, Busby M, Gehrels GE (2011) Evolution of the Guerrero composite terrane along the Mexican margin, from extensional fringing arc to contractional continental arc. Geological Society of America Bulletin 123:1776–1797

Christiansen EH, Sheridan MF, Burt DM (1986) The geology and geochemistry of Cenozoic topaz rhyolites from the Western United States. Special Paper – Geological Society of America 205:01–82

Clark KF, Foster CT, Damon PE (1982) Cenozoic mineral deposits and subduction–related magmatic arcs in Mexico; Symposium on subduction of oceanic plates. Geological Society of America Bulletin 93:533–544

Clark KF, Fitch DC (2009) Evolucion de depositos metalicos en tiempo y espacio en Mexico. In: Clark KF, Salas–Pizá G, Cubillas–Estrada R (ed) Geología Económica de México, II Edición. Servicio Geológico Mexicano 43

Coney PJ, Reynolds SJ, (1977) Cordilleran Benioff zones. Nature (London) 270:403–406

Damon PE, Shafiqullah M, Clark KF (1981) Age trends of igneous activity in relation to metallogenesis in the southern Cordillera; Relations of tectonics to ore deposits in the southern Cordillera. Arizona Geological Society Digest 14:137–154

De Cserna Z (1976) Geology of the Fresnillo area, Zacatecas, Mexico. Geological Society of America Bulletin 87:1191–1199

De Cserna Z (1981) Active continental margin collision in the southwestern part of the Gulf of Mexico. Revista – Instituto de Geologia 5:255–261

Dickinson WR, Snyder WS (1978) Plate tectonics of the Laramide Orogeny. In: Matthews V (ed) Lara– mide folding associated with basement block faulting in the western United States. Geological Society of America Memoir 151:355–366

Dickinson WR (2006) Geotectonic evolution of the Great Basin. Geosphere 2:353–368

Edwards JD (1955) Studies of some early Tertiary red conglomerates of central Mexico. 0264–H:01–153

Einaudi MT, Hedenquist JW, Inan EE (2003) Sulfidation state of fluids in active and extinct hydrothermal systems; transitions from porphyry to epithermal environments; Volcanic, geothermal, and ore–forming fluids; rulers and witnesses of processes within the Earth. Special Publication (Society of Economic Geologists (U.S.)) 10:285–313

Ferrari L, Lopez-Martinez M, Rosas-Elguera J (2002) Ignimbrite flare up and deformation in the southern Sierra Madre Occidental, western Mexico: implications for the late subduction history of the Farallon plate. Tectonics 21:1–24

Ferrari L, Valencia-Moreno M, Bryan S (2007) Magmatism and tectonics of the Sierra Madre Occidental and its relation with the evolution of the western margin of North America; Geology of Mexico; celebrating the centenary of the Geological Society of Mexico. Special Paper – Geological Society of America 422:1–39

Gill JB (1981) Orogenic Andesites and Plate Tectonics. Minerals and Rocks, Springer-Verlag 16:1–390

Goldstein RH and Reynolds TJ (1994) Systematics of fluid inclusions in diagenetic minerals: Society of Economic Paleontologists and Mineralogists, Short Course Handbook, v. 31, 199 p.

Götze J, Plötze M, and Habermann D (2001) Origin, spectral characteristics and practical applica- tions of the cathodoluminescence of quartz— A review: Mineralogy and Petrology, v. 71, p. 225–250.

Gross WH (1975) New ore discovery and source of silver-gold veins, Guanajuato, Mexico. Economic Geology 70:1175–1189

Günther D, Aude´tat A, Frischknecht R, and Heinrich CA (1998) Quantitative analysis of major, minor and trace elements in fluid inclusions using laser ablation inductively coupled plasma mass spectrometry. *J. Anal. At. Spectrom.* **13**(4), 263–270

Harrison TM, McDougall I (1980) Investigations of an intrusive contact, Northwest Nelson, New Zealand; II, Diffusion of radiogenic and excess ^{40}Ar in hornblende revealed by $^{40}Ar/^{39}Ar$ age spectrum analysis. Geochimica et Cosmochimica Acta 44:2005–2020

Hedenquist JW, Arribas RA, Gonzalez-Urien E (2000) Exploration for epithermal gold deposits; Gold in 2000. Reviews in Economic Geology 13:245–277

Heizler MT, Harrison TM (1988) Multiple trapped argon isotope components revealed by $^{40}Ar/^{39}Ar$ isochron analysis. Geochimica et Cosmochimica Acta 52:1295–1303

Heinrich CA, Pettke T, Halter W, Aigner M, Aude´tat A, Günther D, Hattendorf B, Bleiner D, Guillong M, Horn I (2003) Quantitative multi-element analysis of minerals, fluids, and melt inclusions by Laser Ablation Inductively-Coupled-Plasma Mass-Spectrometry. Geochim. Cosmochim. Acta. 67, 3473–3497.

Henry CD, Price JG, James EW (1991) Mid–Cenozoic stress evolution and magmatism in the southern Cordillera, Texas and Mexico; transition from continental arc to intraplate extension. Journal of Geophysical Research 96:545–560

Henry CD, Aranda-Gomez JJ (1992) The real southern Basin and Range; mid– to late Cenozoic extension in Mexico: Geology (Boulder) 20:701–704

Henry CD, Aranda-Gomez JJ, (2000) Plate interactions control middle–late Miocene, proto–Gulf and Basin and Range extension in the southern Basin and Range; The influence of plate interaction on post–Laramide magmatism and tectonics in Mexico. Tectonophysics 318:1–26

Humphreys E, Hessler E, Dueker K, Farmer GL, Erslev E, Atwater T (2003) How Laramide–age hydration of North American lithosphere by the Farallon Slab controlled subsequent activity in the Western United States. International Geology Review 45:575–595

Irvine TN, Baragar WRA (1971) A guide to the chemical classification of the common volcanic rocks. Canadian Journal of Earth Sciences = Revue Canadienne des Sciences de la Terre 8:523–548

John DA (2001) Miocene and early Pliocene epithermal gold–silver deposits in the northern Great Basin, Western United States; characteristics, distribution, and relationship to magmatism. Economic Geology and the Bulletin of the Society of Economic Geologists 96:1827–1853

Jones NW, McKee JW, Anderson TH, Silver LT (1995) Jurassic volcanic rocks in northeastern Mexico; a possible remnant of a Cordilleran magmatic arc; Studies on the Mesozoic of Sonora and adjacent areas. Special Paper – Geological Society of America 301:179–190.

Keenan JH, Keyes FG, Hill PG, and More PG (1969) Steam Tables – thermodynmic properties of water including vapour, liquid, and solid phases (International Edition – metric units): Wiley, NY, 162 p. in: Fluid–Mineral Equilibria in Hydrothermal Systems: Reviews in Economic Geology, v1, Appendix III.

Labarthe-Hernandez G, Tristan-Gonzalez M, Aranda-Gomez J, (1982) Revision estratigrafica del Cenozoico de la parte central del Edo de San Luis Potosi. Instituto de Geologia, Universidad Autonoma de San Luis Potosi 85:1–208

Lang B, Steintz G, Sawkins FJ, Simmons SF (1988) K/Ar age studies in the Fresnillo silver district, Zacatecas, Mexico. Economic Geology 83:1642–1646

Lapierre H, Tardy M, Coulon C, Ortiz-Hernandez E, Bourdier JL, Martinez-Reyes J, Freydier C (1992) Caracterisation, genese et evolution geodynamique du terrain de Guerrero; Mexique occidental. Characterization, genesis, and geodynamic evolution of the Guerrero Terrane, western Mexico. Canadian Journal of Earth Sciences = Revue Canadienne des Sciences de la Terre 29:2478–2489

Leavitt ED, Spell TL, Goldstrand PM, Arehart PM (2004) Geochronology of the Midas low-sulfidation epithermal gold-silver deposit Elko County, Nevada. Economic Geology 99:1665–1686

Le Bas MJ, Le Maitre RW, Streckeisen A, Zanettin BA (1986) Chemical classification of volcanic rocks based on the total alkali–silica diagram. Journal of Petrology 27:745–750.

Maldonado-Koerdell M (1948) Nuevos datos geologicos y paleontologicos sobre el Triasico de Zacatecas Mexico. Anales Esc.Nac.Cien.Biol 5:291–306

Mapes VE (1949) Los Criaderos Minerales de "El Bote,"Zacatecas, Zacatecas, Mexico. Instituto Nacional de Investigacion en Recursos Minerales 24:1–39

Meinert LD, Dipple GM, and Nicolescu S (2005) World skarn deposits: ECONOMIC GEOLOGY 100TH ANNIVERSARY VOLUME, p. 299−336.

Moller, SA, Islas JE, and Davila RT (2001) New discoveries in the La Colorada district, Zacatecas State, Mexico: Society of Economic Geologists Special Publication Series, v. 8, p. 95–104.

Moncada D, Mutchler S, Nieto A, Reynolds TJ, Rimstidt JD, Bodnar RJ (2012) Mineral textures and fluid inclusion petrography of the epithermal Ag–Au deposits at Guanajuato, Mexico: application to exploration. Jour Geochem Explor 114:20–35

Mortensen JK, Hall BV, Bissig T, Friedman RM, Danielson T, Oliver J, Rhys DA, Ross KV, Gabites JE (2008) Age and paleotectonic setting of volcanogenic massive sulfide deposits in the Guerrero terrane of central Mexico:

Constraints from U–Pb age and Pb isotope studies. Economic Geology and the Bulletin of the Society of Economic Geologists 103:117–140

Munroe MJ (2014) Technical Report on the Resource and reserve estimates for the Bolañitos mines project, Guanajuato state, Mexico. NI 43-101 technical report prepared for Endeavour Silver Corp., effective date December 31, 2013.

Nieto-Samaniego AF, Alaniz-Alvarez SA, Labarthe-Hernandez G (1997) The post–Laramide Cenozoic deformation in the southern Mesa Central, Mexico. Revista Mexicana de Ciencias Geologicas 14:13–25

Nieto-Samaniego AF, Alaniz-Alvarez SA, Camprubi, A (2005) La Mesa Central de México: estratigrafía, estructura y evolución tectónica cenozoica. Boletín de la Sociedad Geológica Mexicana. Tomo LVII 3:285–318

Nieto-Samaniego AF, Alaniz-Alvarez SA, Camprubi A (2007) Mesa Central of Mexico; stratigraphy, structure, and Cenozoic tectonic evolution; Geology of Mexico; celebrating the centenary of the Geological Society of Mexico. Special Paper – Geological Society of America 422:41–70

Orozco-Esquivel MT, Nieto-Samaniego AF, Alaniz-Alvarez SA (2002) Origin of rhyolitic lavas in the Mesa Central, Mexico, by crustal melting related to extension; Volcanism and associated regimes; the complexity of volcanic systems. Journal of Volcanology and Geothermal Research 118:37–56

Ortega-Gutierrez F, Ruiz J, Centeno-Garcia E (1995) Oaxaquia, a Proterozoic microcontinent accreted to North America during the late Paleozoic. Geology (Boulder) 23:1127–1130

Pearce, J. A., and J. R. Cann (1973) Tectonic setting of basic volcanic rocks determined using trace element analyses, Earth Planet. Sci. Lett., 19, 290–300,.

Peccerillo A, Taylor SR (1976) Geochemistry of Eocene calc–alkaline volcanic rocks from the Kastamonu area, northern Turkey. Contributions to Mineralogy and Petrology 58:63–81

Perez-Martinez JJ, Mapes-Vazquez E, Pesquera-Velazquez R (1961) Bosquejo geologico del distrito minero de Zacatecas. Boletin – Consejo de Recursos Naturales no Renovables 1–38

Ponce S BF, Clark KF, Salas P (1988) The Zacatecas mining district; a Tertiary caldera complex associated with precious and base metal mineralization; A special issue devoted to the geology and mineral deposits of Mexico. Economic Geology and the Bulletin of the Society of Economic Geologists 83:1668–1682

Rama SNI, Hart SR, Roedder E (1965) Excess radiogenic argon in fluid inclusions. Journal of Geophysical Research 70:509–511

Randall JA, Saldaña E, Clark KF (1994) Exploration in a volcano-plutonic center at Guanajuato, Mexico. Economic Geology 89:1722–1751

Ranson WA, Fernandez LA, Simmons WB (1975) Geology and petrology of the Zacatecas mining district, Zacatecas, Mexico. Abstracts with Programs – Geological Society of America 7:228

Ranson WA, Fernandez LA, Simmons WBJr, de la Vega SE (1982) Petrology of the metamorphic rocks of Zacatecas, Zac., Mexico. Boletin de la Sociedad Geologica Mexicana 43:37–59

Reed MH (1982) Calculation of multicomponent chemical equilibria and reaction processes in systems involving minerals, gases and an aqueous phase: Geochimica et Cosmochimica Acta., v. 46, p. 513–528.

– (1997) Hydrothermal alteration and its relationship to ore fluid composition: *in* Barnes, H.L., ed., Geochemistry of hydrothermal ore deposits: New York, NY, John Wiley and Sons, p. 303–365.

– (1998) Calculation of simultaneous chemical equilibria in aqueous-mineral-gas systems and its application to modeling hydrothermal processes: Reviews in Economic Geology, v. 10, p. 109–124.

Reed MH and Spycher NF (1985) Boiling, cooling, and oxidation in epithermal systems: A numerical modeling approach: Reviews in Economic Geology, v. 2, p. 249–272

Reed MH and Palandri J (2010) SOLTHERM.XPT, a database of equilibrium constants for minerals and aqueous species: Eugene, Oregon, University of Oregon, available from the authors.

Richards JP, McDougall I (1990) Geochronology of the Porgera gold deposit, Papua New Guinea; resolving the effects of excess argon on K–Ar and $^{40}Ar/^{39}Ar$ age estimates for magmatism and mineralization. Geochimica et Cosmochimica Acta 54:1397–1415

Richards JP, Noble SR (1998) Application of radiogenic isotope systems to the timing and origin of hydrothermal processes; Techniques in hydrothermal ore deposits geology. Reviews in Economic Geology 10:195–233

Rodriguez-Rios R, Aguillon-Robles A, Leroy JL (2007) Evolucion petrologica y geoquimica de un complejo de domos topaciferos en el campo volcannico de San Luis Potosi (Mexico). Petrologic and geochemical evolution of a topaz–bearing dome complex in the San Luis Potosi volcanic field (Mexico). Revista Mexicana de Ciencias Geologicas 24:328–343

Roedder, E., 1984, Fluid inclusions: Mineral. Soc. Am., Reviews in Mineralogy, v. 12, 644 p.

Rubin JN, Kyle JR (1988) Mineralogy and geochemistry of the San Martin skarn deposits, Zacatecas, Mexico. Economic Geology 83:1782–1801

Rusk BG and Reed MH (2002) Scanning electron microscope-cathodoluminescenceanalysis of quartz reveals complex growth histories in veins from the Butte porphyry copper deposit, Montana: Geology, v. 30, p. 727–730.

Seedorff E, Dilles JH, Proffett JM Jr., Einaudi MT, Zurcher L, Stavast WJA, Johnson DA, and Barton MD (2005) Porphyry deposits: Characteristics and origin of hypogene features: ECONOMIC GEOLOGY 100TH ANNIVERSARY VOLUME, p. 251−298.

Sillitoe RH, (1999) Styles of high–sulphidation gold, silver and copper mineralisation in porphyry and epithermal environments; PACRIM '99 congress; proceedings [modified]. Publication Series – Australasian Institute of Mining and Metallurgy 4:29–44

Sillitoe RH, Hedenquist JW (2003) Linkages between volcanotectonic settings, ore–fluid compositions, and epithermal precious metal deposits; Volcanic, geothermal, and ore–forming fluids; rulers and witnesses of processes within the Earth. Special Publication (Society of Economic Geologists (U.S.)) 10:315–343

Simmons SF (1991) Hydrologic implications of alteration and fluid inclusion studies in the Fresnillo District, Mexico; evidence for a brine reservoir and a descending water table during the formation of hydrothermal Ag–Pb–Zn orebodies. Economic Geology and the Bulletin of the Society of Economic Geologists 86:1579–1601

Simonetti A, Heaman LM, MacHattie TG, Chacko T, Hartlaub RP, Eccles DR (2005) In–situ petrographic thin section U–Pb dating of zircon and titanite by laser ablation–MC–ICP–MS; Abstracts of the 15th annual V. M. Goldschmidt conference. Geochimica et Cosmochimica Acta 69:381

Smith LD, Jones RL (1979) Thermal Anomaly in Northern Mexico: An extension of the Río Grande Rift (?). In Río Grande Rift: Tectonics and Magmatism RE Rieckers (ed) American Geophysic Union 269–278

Sole J, Salinas JC, Gonzalez-Torres E, Cendejas–Cruz JE (2007) Edades K/Ar de 54 rocas igneas y metamorficas del occidente, Centro y Sur de Mexico. Revista Mexicana de Ciencias Geologicas 24:104–119

Stein G, Lapierre H, Monod O, Zimmermann JL, Vidal R (1993) Petrology and some Mexican Mesozoic plutons–sources and tectonic environments. Journal of South American Earth Sciences 7:1–7

Steel JS (2012) Technical Report on the Catanava Gold Property, Pinos, Zacatecas State, Mexico. NI 43-101 technical report prepared by Mining Insights Inc. for Excalibur Resources Ltd., effective date April 20, 2012

Stewart JH (1998) Regional characteristics, tilt domains, and extensional history of the later Cenozoic Basin and Range Province, western North America; Accommodation zones and transfer zones; the regional segmentation of the Basin and Range Province: Special Paper – Geological Society of America 323:47–74

Stolz AJ, Jochum KP, Spettel B, Hofmann AW (1996) Fluid– and melt–related enrichment in the subarc mantle Evidence from Nb/Ta variations in island–arc basalts. Geology 24:587–590

Sun S, McDonough WF (1989) Chemical and isotopic systematics of oceanic basalts: Implications for mantle composition and processes. In: Saunders AD, Norry MJ (eds) Magmatism in the Ocean Basins. Geological Society of London Special Publication 42:313–345

Tristan-Gonzalez M (1986) Estratigrafia y tectonica del Graben de Villa de Reyes, en los estados de San Luis Potosi y Guanajuato, Mexico. Universidad Autonoma de San Luis Potosi, Instituto de Geologia 107: 1–91

Tristan-Gonzalez M (2008) Evolucion tectono-volcanica durante el Paleogeno en la porcion sur-oriental de la Mesa Central. Universidad Nacional Autonoma de Mexico

Tristan-Gonzalez M, Aguirre-Diaz GJ, Labarthe-Hernandez G, Torres-Hernandez JR, Bellon H (2009) Post–Laramide and pre–Basin and Range deformation and implications for Paleogene (55–25 Ma) volcanism in central Mexico; a geological basis for a volcano–tectonic stress model; Understanding stress and deformation in active volcanoes. Tectonophysics 471:136–152

Velador JM (2010) Timing and origing of intermediate sulfidation epithermal veins and geochemical zoning in the Fresnillo district, Mexico: constrained by $^{40}Ar/^{39}Ar$ geochronology, fluid inclusions, gas analysis, stable isotopes, and metal ratios. The New Mexico Institute of Mining and Technology

Velador JM, Heizler MT, Campbell AR (2010) Timing of magmatic activity and mineralization and evidence of a long–lived hydrothermal system in the Fresnillo silver district, Mexico; constraints from $^{40}Ar/^{39}Ar$ geochronology. Economic Geology and the Bulletin of the Society of Economic Geologists 105:1335–1349

Verma SP (1984) Sr and Nd isotopic evidence for petrogenesis of mid–Tertiary felsic volcanism in the mineral district of Zacatecas, Zac. (Sierra Madre Occidental), Mexico. Chemical Geology – Isotope Geoscience 46:37–53

Wenxin L (2001) Modeling description and spectroscopic evidence of surface acid–base properties of natural illites. Water Res 35: 4111-4125

Appendix A: X-Ray Diffraction Data

Sample #7 La

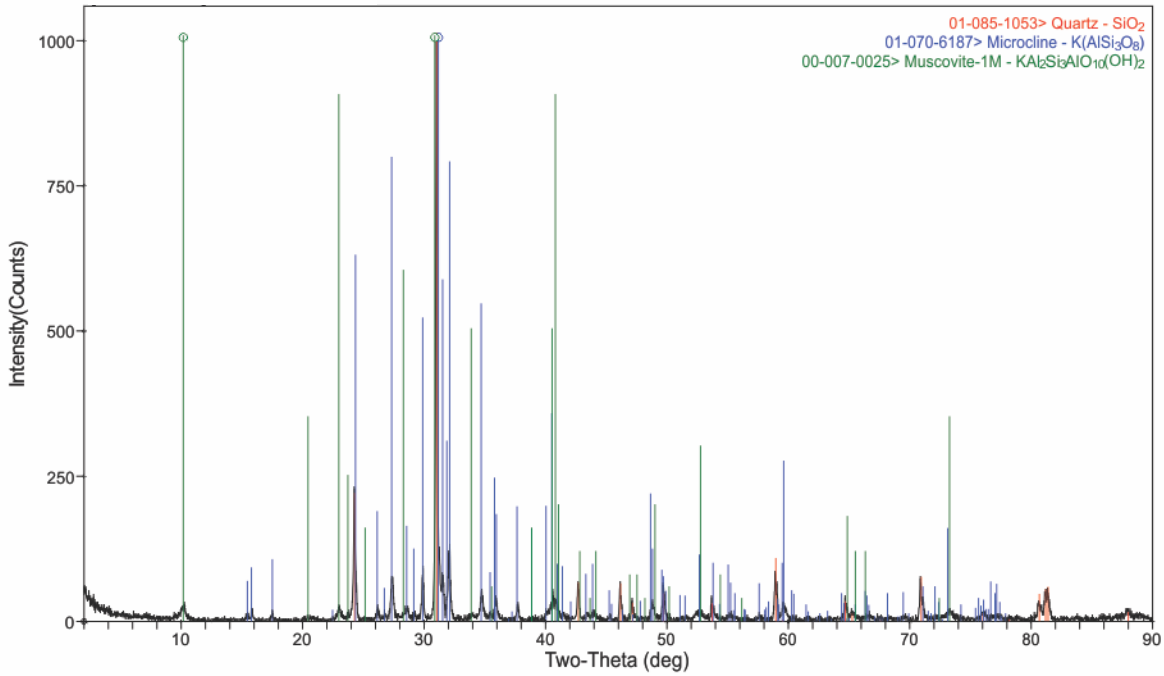

Sample BU-01 La

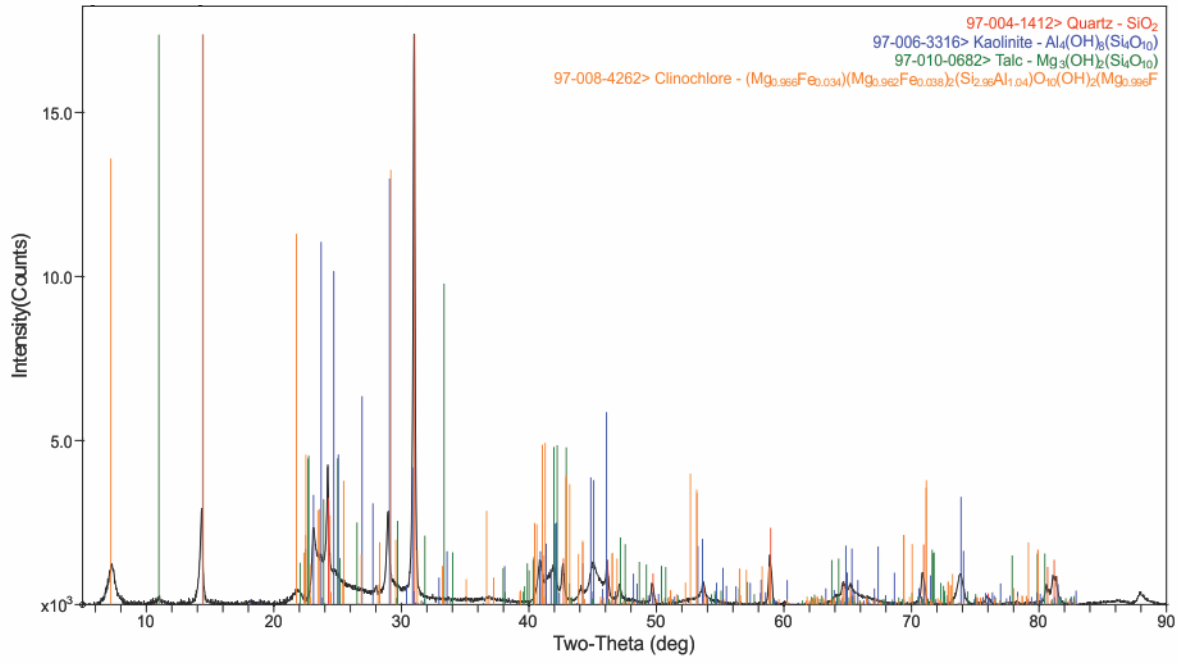

Sample Cos 41-1

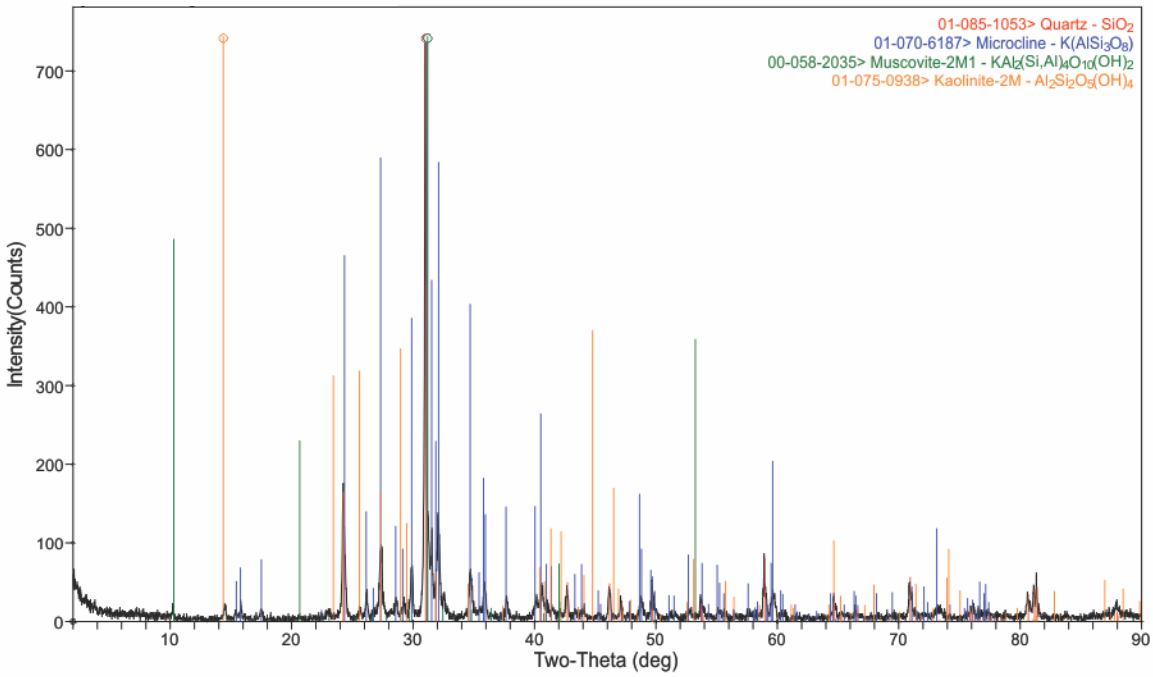

Sample Cos 161_164.73m

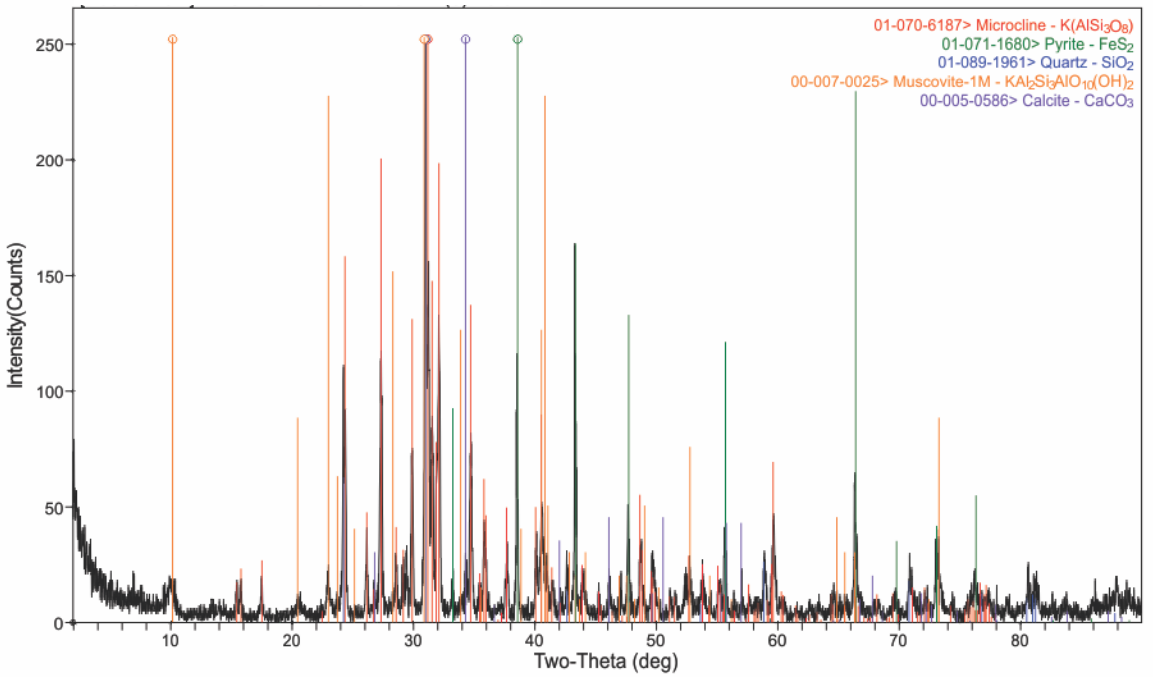

Sample Cos Level 10.3_S4

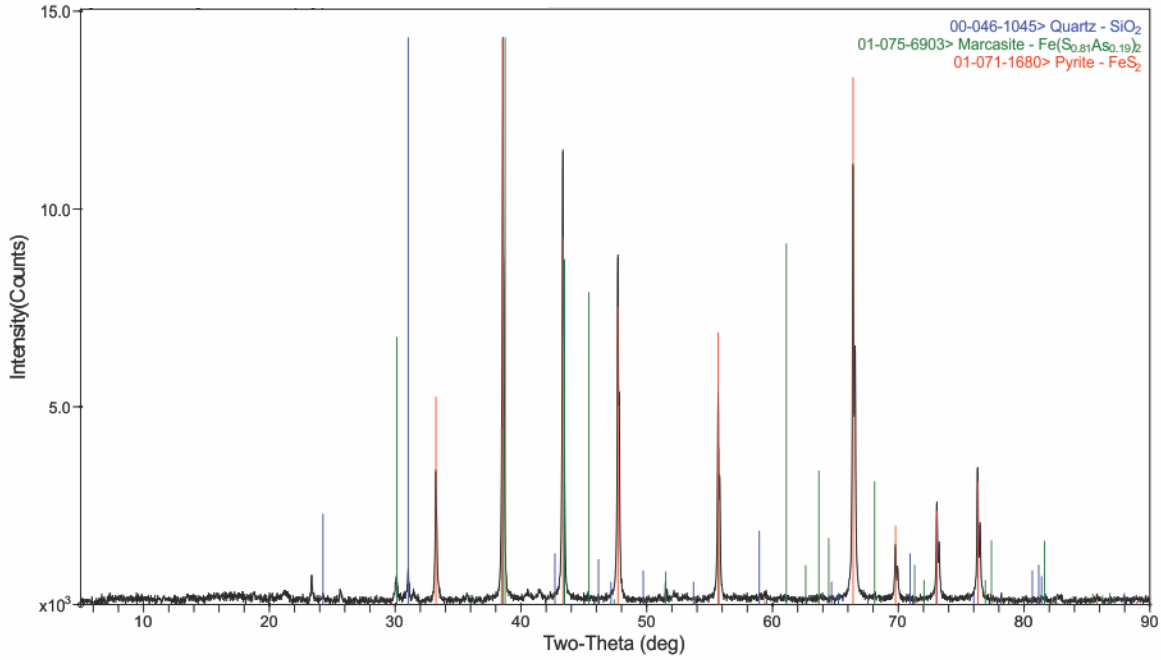

Sample Cos Level 11.6_W

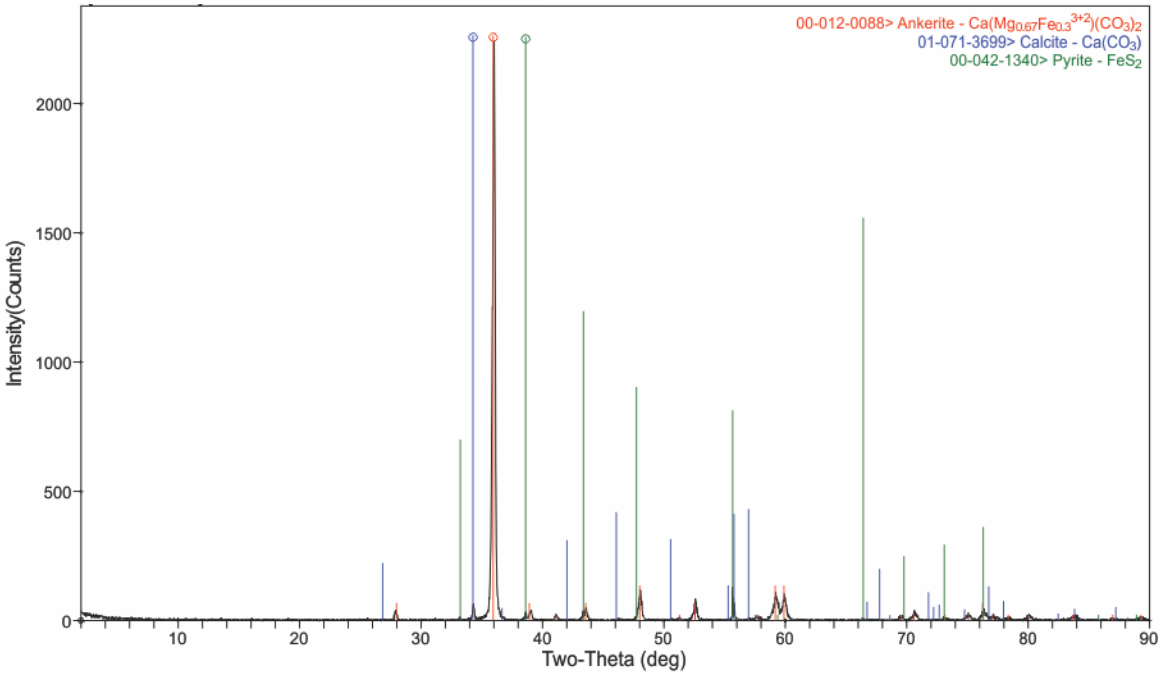

Sample MN_FW zone

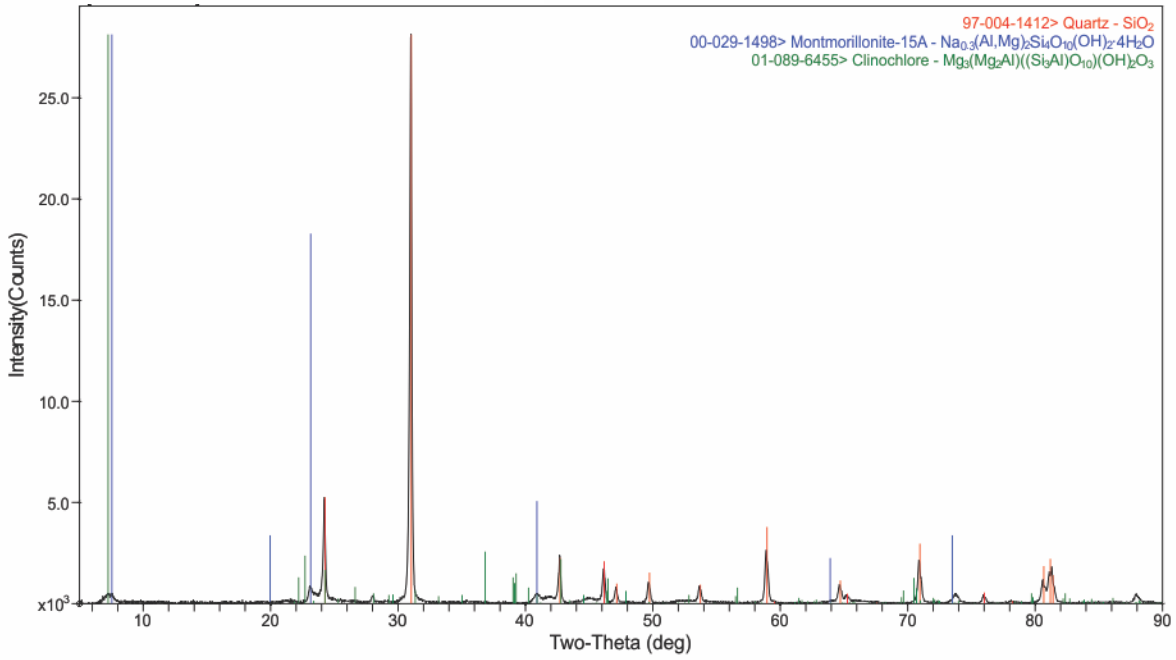

Sample MN_Level 10

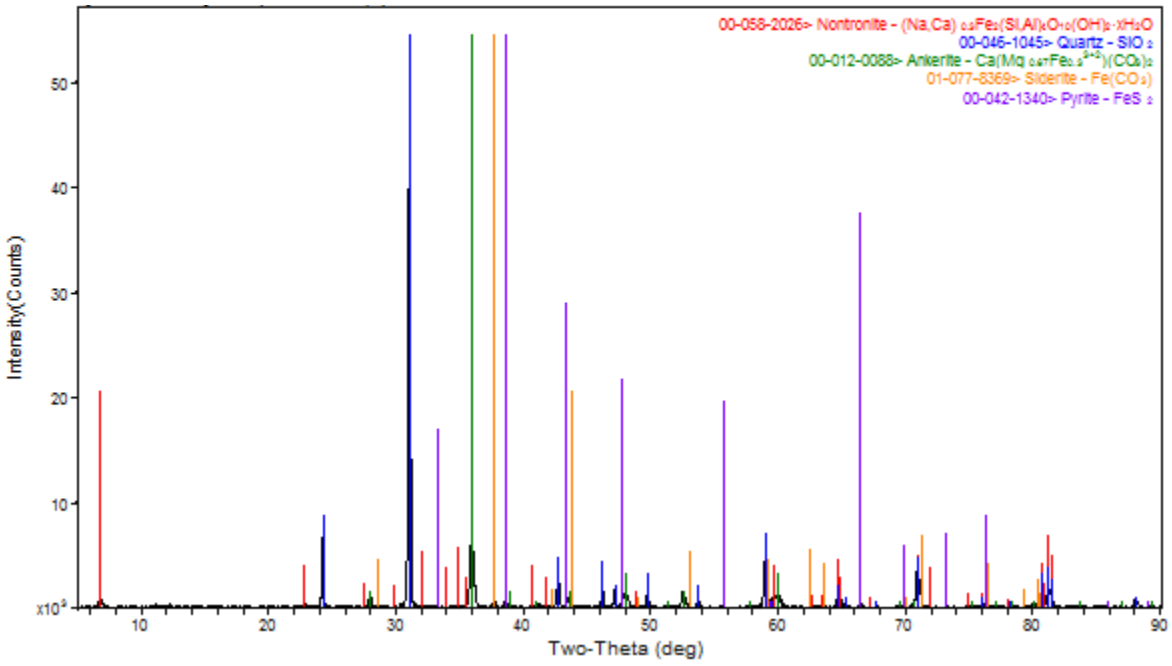

Sample Cos41_754

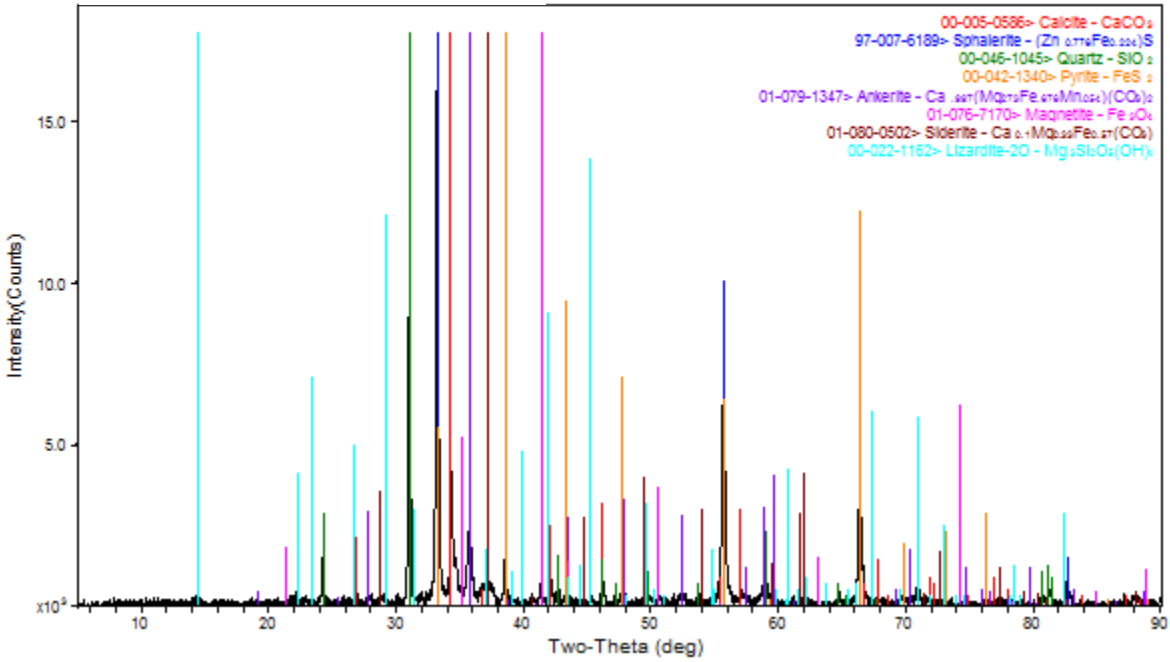

Sample MN_Level 16

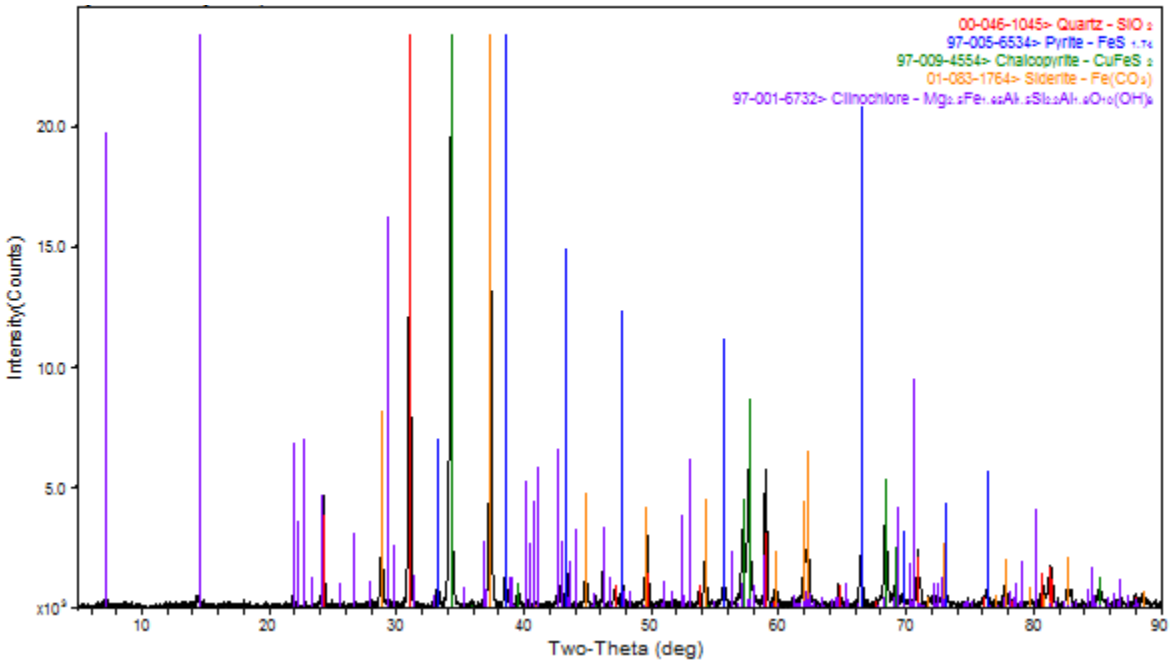

Sample MN_FWZ

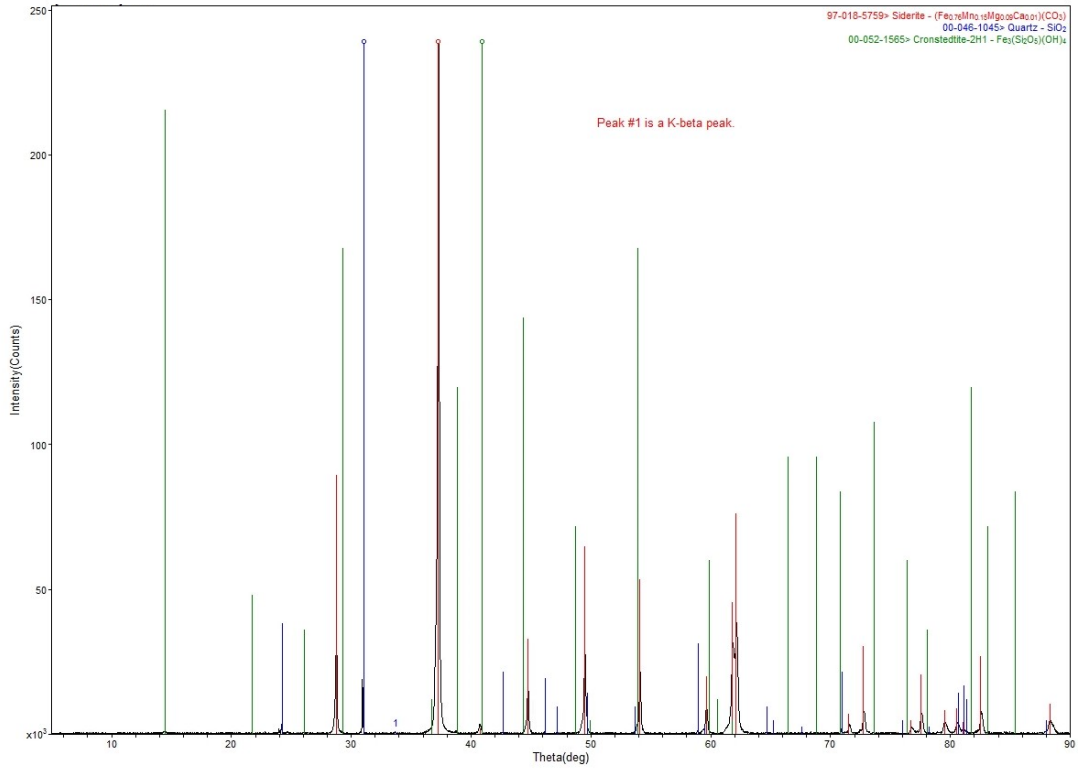

Sample CosU93_171

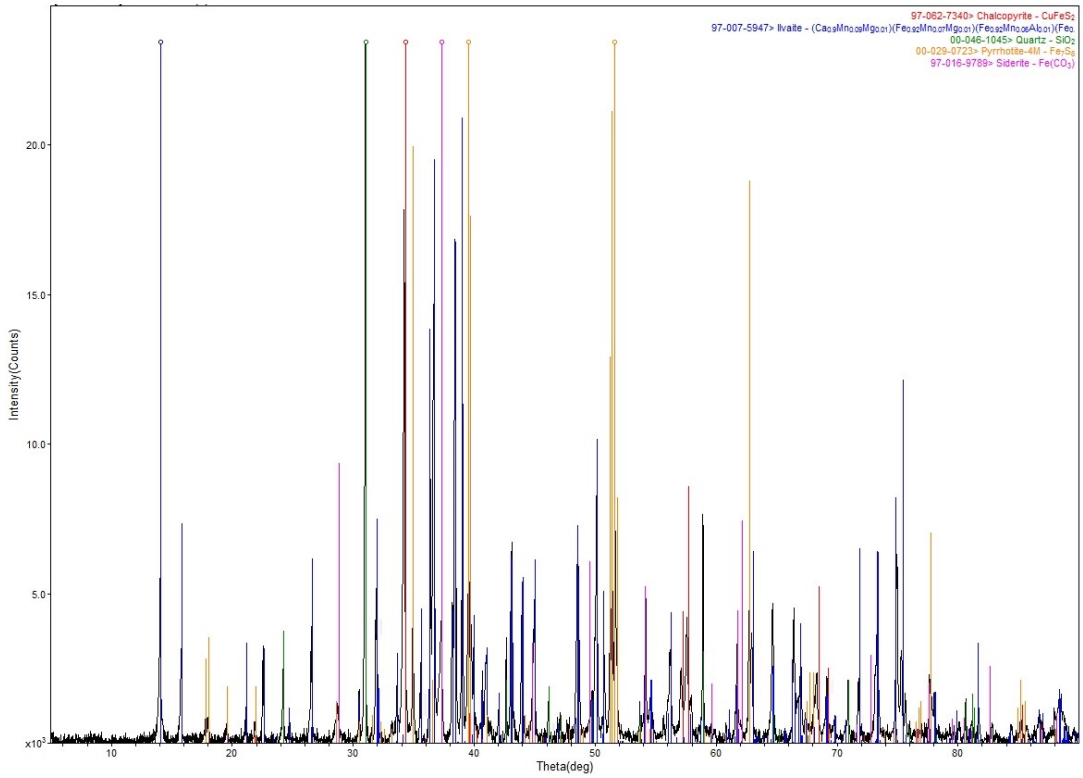

Sample VGDH1B_S14

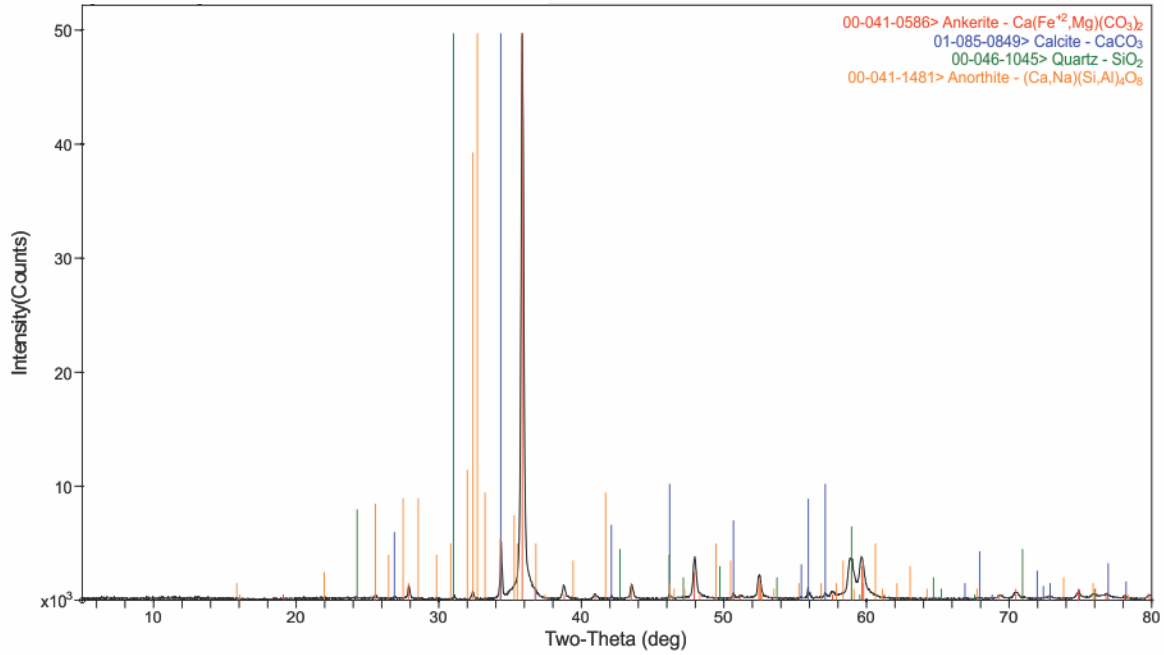

Sample COM_L7

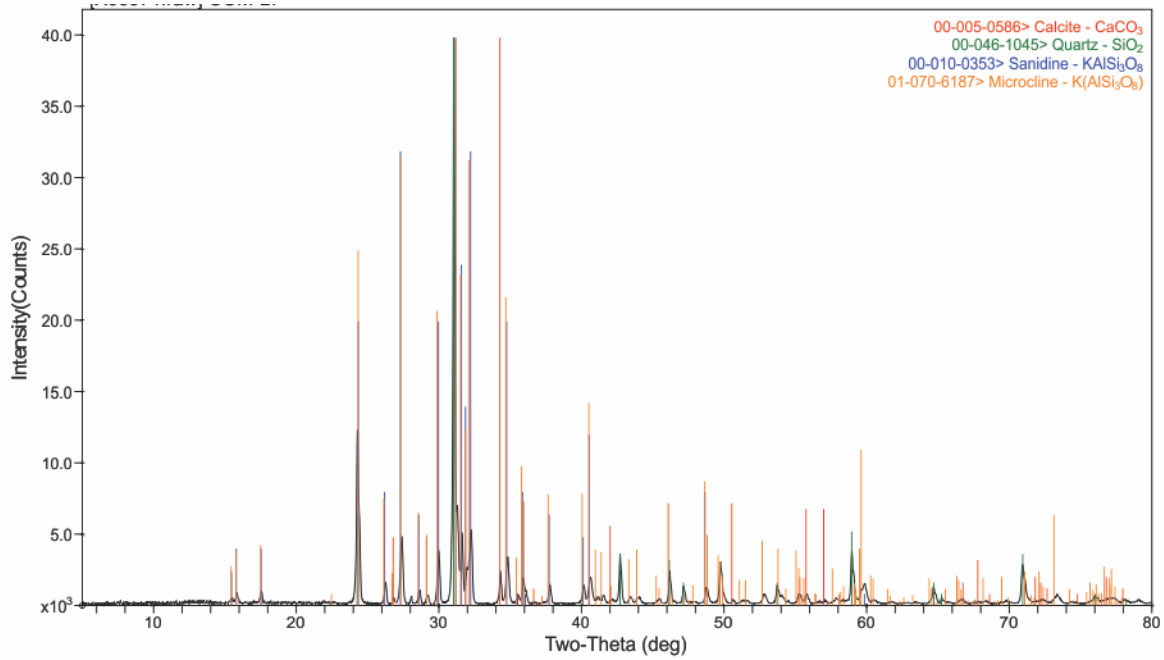

Appendix B: Microprobe Data

Veta Grande

Sample	Mineral	S	As	Ag	Au	W	Pb	Bi	Fe	Sb	Cu	Zn	Total
		W%	W%	W%	W%	W%	W%	W%	W%	W%	W%	W%	W%
SCDH36-S8	Bornite	25.4	0.1	0.7	0.0	n.a	0.0	0.1	10.5	0.0	61.2	0.0	98.1
OSDH1B-S8	Galena	12.6	0.0	0.0	0.0	n.a	80.0	0.3	0.7	0.0	0.0	0.0	93.6
OSDH6-S9	Jamesonite	20.7	0.1	0.0	0.0	n.a	38.1	0.0	2.8	35.8	0.0	0.0	97.5
OSDH6-S9	Galena	13.0	0.1	0.0	0.0	n.a	80.2	0.4	0.0	0.1	0.1	0.0	93.9
OSDH6-S9	Chalcopyrite	32.4	0.1	0.2	0.0	n.a	0.0	0.1	25.4	4.4	29.8	0.0	92.3
OSDH6-S9	Jamesonite	21.1	0.1	0.0	0.0	n.a	38.8	0.2	2.5	35.6	0.0	0.0	98.4
OSDH6-S2	Acanthite	14.2	0.1	81.7	0.1	n.a	0.0	0.0	0.0	0.0	0.1	0.0	96.2
OSDH6-S2	Chalcopyrite	34.0	0.1	0.4	0.0	n.a	0.0	0.1	29.0	0.3	33.6	0.0	97.5
OSDH6-S2	Acanthite	16.5	0.0	79.2	0.0	n.a	0.0	0.1	0.1	0.0	0.7	0.0	96.7
OSDH6-S2	Chalcopyrite	34.5	0.0	0.1	0.0	n.a	0.0	0.1	29.9	0.0	34.0	0.0	98.4
DP-04	Pyrargyrite	17.3	0.2	58.5	0.0	n.a	0.0	0.0	0.3	21.5	0.9	2.8	101.5
DP-04	Pyrrhotite	38.8	0.0	0.0	0.0	n.a	0.0	0.2	58.2	0.0	0.1	2.4	99.7
DP-04	Pyrite	52.6	0.1	0.0	0.0	n.a	0.0	0.2	45.8	0.0	0.0	2.1	100.8
DP-04	Pyrargyrite	17.2	0.2	58.5	0.0	n.a	0.0	0.1	0.4	22.1	0.9	2.8	102.0
DP-04	Sphalerite	33.6	0.0	0.0	0.0	n.a	0.0	0.1	6.4	0.0	0.0	58.8	99.0
TVG	Acanthite	13.0	0.1	73.8	0.2	n.a	0.0	0.0	0.0	0.0	0.2	0.1	87.3
TVG	Anglesite	6.8	0.0	0.0	0.0	n.a	63.1	0.2	0.0	0.0	0.0	0.0	70.1
TVG	Galena	13.2	0.0	0.0	0.0	n.a	82.6	0.0	0.0	0.1	0.0	0.0	96.0
TVG	Acanthite	11.1	0.2	70.6	0.3	n.a	0.0	0.0	0.0	0.0	0.2	0.3	82.6
TVG	Acanthite	13.6	0.0	80.8	0.1	n.a	0.0	0.1	0.0	0.0	0.3	0.0	94.9
TVG	Acanthite	13.9	0.1	77.9	0.1	n.a	0.0	0.0	0.0	0.0	0.3	0.2	92.4

Mala Noche

Sample	Mineral	S	As	Ag	Au	W	Pb	Bi	Fe	Sb	Cu	Zn	Total
		W%	W%	W%	W%	W%	W%	W%	W%	W%	W%	W%	W%
MW9-W-4-2	Sphalerite	34.2	0.0	0.0	n.a	0.0	0.0	0.1	12.5	0.0	0.0	53.0	99.8
MW9-W-4-3	Sphalerite	34.2	0.0	1.5	n.a	0.0	0.0	0.1	12.4	0.0	0.0	53.1	101.3
MW9-W-4-4	Chalcopyrite	34.8	0.0	0.0	n.a	0.0	0.0	0.0	36.7	0.0	29.2	0.1	100.9
MW9-W-1c-1	Chalcopyrite	34.7	0.0	0.0	n.a	0.0	0.0	0.0	36.4	0.0	29.3	0.2	100.7
MW9-W-1c-2	Wolframite	0.0	0.0	7.3	n.a	57.4	0.0	0.1	21.4	0.0	0.0	0.0	86.2
MW9-W-1b-1	Wolframite	0.0	0.0	11.2	n.a	58.6	0.0	0.1	21.3	0.0	0.0	0.0	91.3
MW9-W-1b-2	Pyrite	53.2	0.0	0.0	n.a	0.0	0.0	0.0	45.8	0.0	0.4	0.1	99.5
MW9-W-1a-1	Chalcopyrite	34.5	0.0	0.0	n.a	0.1	0.0	0.0	36.6	0.0	29.4	0.0	100.6
MW9-W-1a-2	Chalcopyrite	34.7	0.0	0.0	n.a	0.0	0.0	0.0	36.2	0.0	29.4	0.1	100.4
MW9-W-1-1	Chalcopyrite	34.7	0.0	0.0	n.a	0.0	0.0	0.0	36.8	0.0	29.3	0.1	100.9
MW9-W-11-1	Pyrite	52.0	0.1	0.0	n.a	0.0	0.0	0.1	44.7	0.0	0.0	0.0	97.0
MW9-W-11-2	Sphalerite	33.9	0.0	0.0	n.a	0.0	0.0	0.0	11.7	0.0	0.0	54.0	99.7
COS37-1-1	Chalcopyrite	34.7	0.0	0.0	n.a	0.0	0.0	0.0	36.4	0.0	29.4	0.2	100.7
COS37-1-2	Pyrrhotite	39.8	0.0	0.0	n.a	0.0	0.0	0.1	55.9	0.0	0.0	0.0	95.8
COS37-1-3	Chalcopyrite	34.6	0.1	0.0	n.a	0.0	0.0	0.0	34.3	0.0	28.2	1.2	98.3
COS37-3-1	Pyrite	53.8	0.0	0.0	n.a	0.0	0.0	0.0	44.4	0.0	0.1	0.1	98.3
COS37-3-2	Pyrrhotite	39.9	0.0	0.0	n.a	0.0	0.0	0.0	56.8	0.0	0.0	0.0	96.8
COS37-2-1	Chalcopyrite	34.5	0.0	0.0	n.a	0.0	0.0	0.0	35.9	0.0	28.9	0.3	99.6
COS37-2-2	Chalcopyrite	34.7	0.0	0.0	n.a	0.0	0.0	0.1	36.5	0.0	29.2	0.1	100.5
COS37-2-3	Pyrrhotite	40.1	0.0	0.0	n.a	0.0	0.0	0.0	56.5	0.0	0.0	0.0	96.8
BOTE21-2b-1	Sphalerite	34.2	0.0	0.0	n.a	0.0	0.0	0.0	10.7	0.0	0.6	54.1	99.7

El Compas

Sample	Mineral	Ag	Au	S	Br	Se	Cl	Hg	Total
		W%	W%	W%	W%	W%	W%	W%	W%
09COM043	Electrum	31.1	67.8	0.1	n.a.	n.a.	n.a.	n.a.	98.9
09COM043	Aguilarite	76.9	0.0	9.1	0.0	10.8	0.2	0.1	97.0
09COM043	Aguilarite	76.7	0.0	6.9	0.0	16.5	0.1	0.2	100.3
09COM043	Aguilarite	76.0	0.0	7.0	0.0	16.5	0.1	0.2	99.8
09COM043	Aguilarite	77.6	0.0	7.4	0.0	15.4	0.1	0.2	100.7
09COM043	Aguilarite	76.6	0.0	7.2	0.0	15.8	0.1	0.0	99.7
09COM043	Aguilarite	78.3	0.2	9.3	0.0	10.5	0.2	0.1	98.6
09COM043	Aguilarite	78.4	0.0	9.6	0.0	10.0	0.2	0.1	98.4
09COM043	Aguilarite	76.9	0.1	7.7	0.0	14.7	0.1	0.2	99.7
09COM043	Aguilarite	77.4	0.0	7.5	0.0	15.1	0.1	0.3	100.5
09COM043	Aguilarite	77.6	0.0	7.7	0.0	14.5	0.1	0.2	100.1
09COM043	Aguilarite	76.9	0.0	7.8	0.0	14.1	0.1	0.2	99.2
09COM043	Aguilarite	77.3	0.0	8.4	0.0	12.6	0.1	0.2	98.7
09COM043	Aguilarite	78.5	0.0	9.0	0.0	10.9	0.1	0.1	98.6

Appendix C: $^{40}Ar/^{39}Ar$ Data

Appendix C $^{40}Ar/^{39}Ar$ Data for samples from the Veta Grande (VG1B-38) and El Compas (COM-L7) veins

Sample VG1B-38, Adularia, 8.40 mg, J = 0.001632 ± 0.20%

4 amu discrimination = 1.0565 ± 0.43%, 40/39K = 0.01738 ± 67.07%, 36/37Ca = 0.0002157 ± 8.78%, 39/37Ca = 0.0006702 ± 1.60%

step	T (C)	^{36}Ar	^{37}Ar	^{38}Ar	^{39}Ar	^{40}Ar	$\%^{40}Ar^*$	$\%^{39}Ar$ rlsd	Ca/K	$^{40}Ar^*/^{39}ArK$	Age (Ma)	1s.d.
1	650	3.21	1.80	1.03	25.67	1267.70	52.3	2.2	0.476	28.148	81.03	0.72
2	750	2.18	2.38	1.11	50.20	1342.77	69.6	4.3	0.322	20.299	58.80	0.43
3	850	0.32	0.28	1.55	111.49	1691.85	96.7	9.5	0.017	16.027	46.58	0.27
4	920	0.23	0.21	1.93	140.97	2087.50	98.1	12.0	0.010	15.882	46.17	0.27
5	990	0.31	0.11	2.26	161.80	2411.93	97.7	13.8	0.005	15.937	46.32	0.27
6	1060	0.32	0.10	2.29	163.62	2440.30	97.7	13.9	0.004	15.937	46.32	0.28
7	1120	0.38	0.08	2.31	166.91	2502.81	97.3	14.2	0.003	15.963	46.40	0.27
8	1160	0.41	0.06	1.72	122.50	1874.66	96.3	10.4	0.003	16.062	46.68	0.28
9	1400	0.98	0.06	3.33	229.85	3577.82	95.2	19.6	0.002	16.164	46.97	0.28
					Cumulative %39Ar rlsd =			100.0		Total gas age =	47.80	0.21
										Plateau age = (steps 3-9)	46.49	0.22
										Isochron age = (steps 1-9)	42.36	0.09

Sample COM-L7, Adularia, 13.80 mg, J = 0.001655 ± 0.20%

4 amu discrimination = 1.0565 ± 0.43%, 40/39K = 0.01738 ± 67.07%, 36/37Ca = 0.0002157 ± 8.78%, 39/37Ca = 0.0006702 ± 1.60%

step	T (C)	^{36}Ar	^{37}Ar	^{38}Ar	^{39}Ar	^{40}Ar	$\%^{40}Ar^*$	$\%^{39}Ar$ rlsd	Ca/K	$^{40}Ar^*/^{39}ArK$	Age (Ma)	1s.d.
1	650	4.20	7.04	2.52	122.72	2404.52	67.1	7.6	0.387	14.382	42.44	0.32
2	750	0.71	6.33	1.94	133.38	1513.66	91.5	8.3	0.320	11.329	33.51	0.20
3	850	0.89	0.16	2.89	202.23	2226.90	92.6	12.5	0.005	11.151	32.99	0.20
4	920	0.80	0.14	3.03	213.52	2302.69	93.6	13.2	0.004	11.034	32.65	0.20
5	990	0.61	0.12	2.89	204.99	2165.62	94.8	12.7	0.004	10.950	32.40	0.19
6	1060	0.79	0.15	3.28	230.16	2457.13	94.0	14.3	0.004	10.982	32.50	0.20
7	1120	1.21	0.14	3.23	223.32	2514.46	91.1	13.8	0.004	11.207	33.15	0.20
8	1160	1.36	0.10	2.28	151.56	1859.16	86.5	9.4	0.005	11.569	34.22	0.22
9	1200	1.26	0.07	1.45	89.60	1231.26	81.2	5.6	0.005	12.110	35.80	0.24
10	1240	0.69	0.05	0.51	28.76	474.38	74.1	1.8	0.012	13.007	38.42	0.27
11	1290	0.29	0.05	0.18	9.29	170.25	77.2	0.6	0.039	14.183	41.86	0.31
12	1400	0.25	0.05	0.10	3.68	101.40	62.1	0.2	0.083	14.033	41.42	0.47
					Cumulative %39Ar rlsd =			100.0		Total gas age =	34.02	0.14
										Plateau age = (steps 3-6)	32.63	0.20
										Isochron age = (steps 1-11)	29.19	0.10

note: isotope beams in mV, rlsd = released, error in age includes J error, all errors 1 sigma
(^{36}Ar through ^{40}Ar are measured beam intensities, corrected for decay for the age calculations)

Appendix D: U/Pb Data

Sample ZABU-01	^{206}Pb (cps)	^{204}Pb (cps)	^{207}Pb/^{206}Pb	2 σ	^{207}Pb/^{235}U	2 σ	^{206}Pb/^{238}U	2 σ	ρ	^{207}Pb*/^{206}Pb* age (Ma)	2 σ error (Ma)	^{207}Pb*/^{235}U age (Ma)	2 σ error (Ma)	^{206}Pb*/^{238}U age (Ma)	2 σ error (Ma)
ZABU-36	51632	2	0.04515	0.00078	0.04477	0.00262	0.00719	0.00040	0.956	-47	41	44	3	46	3
ZABU-40	31336	14	0.04579	0.00162	0.04622	0.00361	0.00732	0.00051	0.892	-13	83	46	3	47	3
ZABU1-23	28949	24	0.04440	0.00079	0.04497	0.00243	0.00735	0.00037	0.944	-89	43	45	2	47	2
ZABU1-5	44010	0	0.04500	0.00080	0.04566	0.00304	0.00736	0.00047	0.964	-56	43	45	3	47	3
ZABU1-30	20559	4	0.04127	0.00076	0.04203	0.00355	0.00739	0.00061	0.976	-271	46	42	3	47	4
ZABU1-6	192877	14	0.04740	0.00071	0.04872	0.00398	0.00745	0.00060	0.983	69	35	48	4	48	4
ZABU1-9	90600	0	0.04570	0.00067	0.04706	0.00254	0.00747	0.00039	0.962	-18	35	47	2	48	2
ZABU1-16	42882	51	0.04493	0.00083	0.04630	0.00253	0.00747	0.00038	0.942	-59	44	46	2	48	2
ZABU-34	36579	4	0.04321	0.00092	0.04454	0.00243	0.00748	0.00038	0.921	-155	52	44	2	48	2
ZABU1-19	27825	39	0.04349	0.00094	0.04486	0.00257	0.00748	0.00040	0.926	-140	53	45	2	48	3
ZABU1-28	44212	7	0.04520	0.00083	0.04663	0.00269	0.00748	0.00041	0.948	-45	44	46	3	48	3
ZABU1-11	36142	30	0.04447	0.00083	0.04610	0.00261	0.00752	0.00040	0.945	-85	45	46	3	48	3
ZABU1-15	68055	26	0.04579	0.00066	0.04750	0.00248	0.00752	0.00038	0.962	-13	34	47	2	48	2
ZABU-39	57419	5	0.04553	0.00065	0.04725	0.00271	0.00753	0.00042	0.968	-27	34	47	3	48	3
ZABU-33	52907	3	0.04448	0.00098	0.04621	0.00260	0.00753	0.00039	0.920	-84	53	46	3	48	2
ZABU-35	182311	5	0.04770	0.00070	0.04958	0.00412	0.00754	0.00062	0.984	85	34	49	4	48	4
ZABU1-13	35060	16	0.04441	0.00107	0.04624	0.00331	0.00755	0.00051	0.941	-88	58	46	3	48	3
ZABU1-29	24067	7	0.04194	0.00092	0.04370	0.00257	0.00756	0.00041	0.928	-230	54	43	2	49	3
ZABU1-17	103982	66	0.04646	0.00061	0.04842	0.00261	0.00756	0.00039	0.970	22	31	48	3	49	3
ZABU1-22	32668	29	0.04492	0.00077	0.04692	0.00261	0.00758	0.00040	0.951	-60	41	47	3	49	3
ZABU1-18	92784	47	0.04700	0.00070	0.04944	0.00254	0.00763	0.00038	0.957	49	35	49	2	49	2
ZABU1-14	187305	49	0.04931	0.00095	0.05192	0.00327	0.00764	0.00046	0.952	163	45	51	3	49	3
ZABU-32	109418	2	0.04725	0.00065	0.05010	0.00291	0.00769	0.00043	0.971	62	33	50	3	49	3
ZABU-31	53351	85	0.07233	0.00488	0.07671	0.00662	0.00769	0.00041	0.623	995	131	75	6	49	3
ZABU1-7	44730	1	0.04545	0.00097	0.04830	0.00293	0.00771	0.00044	0.936	-31	51	48	3	49	3
ZABU1-24	32313	30	0.04582	0.00083	0.04869	0.00293	0.00771	0.00044	0.954	-12	43	48	3	49	3
ZABU1-26	77294	24	0.04729	0.00068	0.05054	0.00290	0.00775	0.00043	0.968	64	34	50	3	50	3
ZABU1-10	91228	0	0.04564	0.00082	0.04917	0.00265	0.00781	0.00040	0.942	-22	43	49	3	50	3
ZABU1-12	95524	40	0.04744	0.00066	0.05171	0.00387	0.00791	0.00058	0.983	72	33	51	4	51	4
ZABU1-8	78847	0	0.04788	0.00085	0.05329	0.00331	0.00807	0.00048	0.958	93	41	53	3	52	3

Sample ZASI-02	^{206}Pb (cps)	^{204}Pb (cps)	^{207}Pb/^{206}Pb	2 σ	^{207}Pb/^{235}U	2 σ	^{206}Pb/^{238}U	2 σ	ρ	^{207}Pb*/^{206}Pb* age (Ma)	2 σ error (Ma)	^{207}Pb*/^{235}U age (Ma)	2 σ error (Ma)	^{206}Pb*/^{238}U age (Ma)	2 σ error (Ma)
ZASI2-1	74278	76	0.04755	0.00084	0.05061	0.00232	0.00772	0.00033	0.923	77	41	50	2	50	2
ZASI2-2	100847	76	0.04714	0.00079	0.05140	0.00242	0.00791	0.00035	0.934	56	40	51	2	51	2
ZASI2-3	50396	72	0.04714	0.00082	0.05262	0.00240	0.00810	0.00034	0.924	56	41	52	2	52	2
ZASI2-4	22524	65	0.04754	0.00091	0.05429	0.00254	0.00828	0.00035	0.913	76	45	54	2	53	2
ZASI2-5	25028	40	0.04706	0.00091	0.05178	0.00218	0.00798	0.00030	0.888	52	45	51	2	51	2
ZASI2-6	54616	56	0.04688	0.00076	0.05004	0.00251	0.00774	0.00037	0.947	43	38	50	2	50	2
ZASI2-7	70725	57	0.04698	0.00077	0.05178	0.00235	0.00799	0.00034	0.932	48	39	51	2	51	2
ZASI2-8	32616	53	0.04602	0.00091	0.05023	0.00243	0.00792	0.00035	0.913	-1	47	50	2	51	2
ZASI2-9	53429	69	0.04642	0.00081	0.05116	0.00252	0.00799	0.00037	0.935	20	42	51	2	51	2
ZASI2-10	80163	73	0.04735	0.00074	0.05230	0.00228	0.00801	0.00033	0.933	67	37	52	2	51	2
ZASI2-11	54436	89	0.04624	0.00082	0.05155	0.00251	0.00808	0.00037	0.931	10	42	51	2	52	2
ZASI2-12	54365	141	0.04696	0.00077	0.05107	0.00213	0.00789	0.00030	0.919	47	39	51	2	51	2
ZASI2-13	99085	157	0.04705	0.00074	0.05156	0.00224	0.00795	0.00032	0.932	52	37	51	2	51	2
ZASI2-14	76927	140	0.04705	0.00075	0.05107	0.00206	0.00787	0.00029	0.918	52	38	51	2	51	2
ZASI2-15	80536	152	0.04794	0.00098	0.05116	0.00250	0.00774	0.00034	0.909	96	48	51	2	50	2
ZASI2-16	104742	146	0.04691	0.00071	0.04966	0.00213	0.00768	0.00031	0.936	45	36	49	2	49	2
ZASI2-17	30785	135	0.04703	0.00162	0.04873	0.00281	0.00751	0.00035	0.803	51	80	48	3	48	2
ZASI2-18	62986	136	0.04849	0.00105	0.05346	0.00293	0.00800	0.00040	0.918	123	50	53	3	51	3
ZASI2-19	70231	132	0.04714	0.00075	0.05192	0.00244	0.00799	0.00035	0.942	56	37	51	2	51	2
ZASI2-20	29470	118	0.04760	0.00091	0.05211	0.00232	0.00794	0.00032	0.902	79	45	52	2	51	2
ZASI2-21	73792	19	0.04870	0.00142	0.05467	0.00274	0.00814	0.00033	0.813	133	67	54	3	52	2
ZASI2-23	52991	19	0.04614	0.00098	0.05151	0.00345	0.00810	0.00051	0.949	5	50	51	3	52	3
ZASI2-24	77002	18	0.04619	0.00080	0.04873	0.00302	0.00765	0.00046	0.960	8	41	48	3	49	3
ZASI2-25	77184	45	0.04717	0.00074	0.05047	0.00300	0.00776	0.00044	0.964	58	37	50	3	50	3
ZASI2-28	51491	50	0.04582	0.00080	0.04912	0.00245	0.00777	0.00036	0.937	-12	42	49	2	50	2
ZASI2-31	102374	19	0.04711	0.00079	0.05326	0.00407	0.00820	0.00061	0.976	55	40	53	4	53	4
ZASI2-32	54837	33	0.04610	0.00075	0.04958	0.00218	0.00780	0.00032	0.929	3	39	49	2	50	2
ZASI2-36	85335	33	0.04690	0.00076	0.05039	0.00217	0.00779	0.00031	0.927	44	38	50	2	50	2
ZASI2-37	26769	27	0.04777	0.00141	0.05252	0.00276	0.00797	0.00035	0.827	88	69	52	3	51	2

Sample ZAPA-03	^{206}Pb (cps)	^{204}Pb (cps)	^{207}Pb/^{206}Pb	2 σ	^{207}Pb/^{235}U	2 σ	^{206}Pb/^{238}U	2 σ	ρ	^{207}Pb*/^{206}Pb* age (Ma)	2 σ error (Ma)	^{207}Pb*/^{235}U age (Ma)	2 σ error (Ma)	^{206}Pb*/^{238}U age (Ma)	2 σ error (Ma)
ZAPA03-13	36325	111	0.05081	0.00095	0.04736	0.00313	0.00676	0.00043	0.959	232	43	47	3	43	3
ZAPA03-23	35858	105	0.04989	0.00078	0.04731	0.00186	0.00688	0.00025	0.917	190	36	47	2	44	2
ZAPA03-25	21305	71	0.05178	0.00107	0.04912	0.00217	0.00688	0.00027	0.884	276	47	49	2	44	2
ZAPA03-6	32147	83	0.05470	0.00112	0.05196	0.00301	0.00689	0.00037	0.935	400	45	51	3	44	2
ZAPA03-8	22932	63	0.05192	0.00091	0.04969	0.00256	0.00694	0.00034	0.940	282	40	49	2	45	2
ZAPA03-20	37853	137	0.05579	0.00222	0.05350	0.00289	0.00696	0.00025	0.678	444	86	53	3	45	2
ZAPA03-21	44709	140	0.04985	0.00083	0.04784	0.00203	0.00696	0.00027	0.919	188	38	47	2	45	2
ZAPA03-1	30275	138	0.04980	0.00194	0.04797	0.00480	0.00699	0.00064	0.921	186	88	48	5	45	4
ZAPA03-26	31613	123	0.06130	0.00238	0.05916	0.00333	0.00700	0.00029	0.725	650	81	58	3	45	2
ZAPA03-7	107779	84	0.04920	0.00071	0.04802	0.00224	0.00708	0.00031	0.950	157	34	48	2	45	2
ZAPA03-2	32670	92	0.05004	0.00080	0.04891	0.00232	0.00709	0.00032	0.942	197	37	48	2	46	2
ZAPA03-5	172927	71	0.04717	0.00052	0.04626	0.00210	0.00711	0.00031	0.971	58	26	46	2	46	2
ZAPA03-18	50234	183	0.05398	0.00256	0.05297	0.00324	0.00712	0.00027	0.631	370	103	52	3	46	2
ZAPA03-9	40495	46	0.05027	0.00116	0.04959	0.00247	0.00716	0.00032	0.886	207	53	49	2	46	2
ZAPA03-19	82227	101	0.04999	0.00096	0.04943	0.00211	0.00717	0.00027	0.892	194	44	49	2	46	2
ZAPA03-10	44496	92	0.05398	0.00149	0.05344	0.00278	0.00718	0.00032	0.847	370	61	53	3	46	2
ZAPA03-4	33905	75	0.05012	0.00099	0.04983	0.00268	0.00721	0.00036	0.930	201	45	49	3	46	2
ZAPA03-16	38811	138	0.05651	0.00265	0.05622	0.00322	0.00722	0.00024	0.576	473	100	56	3	46	2
ZAPA03-27	39044	88	0.05418	0.00166	0.05418	0.00269	0.00725	0.00028	0.786	378	68	54	3	47	2
ZAPA03-28	120340	147	0.05640	0.00283	0.05650	0.00339	0.00726	0.00024	0.550	468	107	56	3	47	2
ZAPA03-12	30594	223	0.08636	0.00631	0.08734	0.00730	0.00733	0.00030	0.485	1346	135	85	7	47	2
ZAPA03-15	65649	244	0.06702	0.00594	0.06972	0.00670	0.00754	0.00028	0.387	838	174	68	6	48	2
ZAPA03-22	109232	154	0.04877	0.00086	0.05105	0.00404	0.00759	0.00059	0.975	137	41	51	4	49	4
ZAPA03-11	25152	213	0.07978	0.00863	0.08532	0.01029	0.00776	0.00041	0.443	1191	200	83	10	50	3
ZAPA03-14	27151	97	0.05492	0.00135	0.15374	0.01033	0.02030	0.00127	0.930	409	54	145	9	130	8
ZAPA03-17	96133	120	0.04985	0.00059	0.14236	0.00569	0.02071	0.00079	0.956	188	27	135	5	132	5
ZAPA03-3	32339	78	0.05278	0.00070	0.15689	0.01089	0.02156	0.00147	0.982	319	30	148	10	137	9
ZAPA03-29	116974	352	0.07898	0.00740	0.25617	0.02636	0.02352	0.00100	0.413	1172	175	232	21	150	6

Sample ZAVI-04	^{206}Pb (cps)	^{204}Pb (cps)	^{207}Pb/^{206}Pb	2 σ	^{207}Pb/^{235}U	2 σ	^{206}Pb/^{238}U	2 σ	ρ	^{207}Pb*/^{206}Pb* age (Ma)	2 σ error (Ma)	^{207}Pb*/^{235}U age (Ma)	2 σ error (Ma)	^{206}Pb*/^{238}U age (Ma)	2 σ error (Ma)
ZAVI04-26	16332	96	0.05191	0.00121	0.04395	0.00315	0.00614	0.00042	0.946	282	52	44	3	39	3
ZAVI04-9	15059	97	0.05341	0.00115	0.04554	0.00263	0.00618	0.00033	0.928	346	48	45	3	40	2
ZAVI04-15	15539	95	0.05786	0.00210	0.04938	0.00371	0.00619	0.00041	0.876	524	78	49	4	40	3
ZAVI04-6	16265	106	0.05329	0.00159	0.04631	0.00310	0.00630	0.00038	0.895	341	66	46	3	41	2
ZAVI04-18	10764	91	0.05705	0.00141	0.04982	0.00270	0.00633	0.00031	0.890	494	54	49	3	41	2
ZAVI04-28	17007	103	0.05162	0.00113	0.04522	0.00276	0.00635	0.00036	0.933	269	50	45	3	41	2
ZAVI04-10	16310	100	0.05275	0.00143	0.04653	0.00330	0.00640	0.00042	0.924	318	60	46	3	41	3
ZAVI04-16	19620	115	0.05118	0.00086	0.04559	0.00260	0.00646	0.00035	0.956	249	38	45	3	42	2
ZAVI04-24	16825	93	0.05227	0.00127	0.04691	0.00313	0.00651	0.00040	0.931	297	55	47	3	42	3
ZAVI04-30	13684	90	0.05271	0.00098	0.04734	0.00238	0.00651	0.00030	0.929	316	42	47	2	42	2
ZAVI04-29	15442	116	0.05609	0.00190	0.05069	0.00399	0.00655	0.00047	0.903	456	73	50	4	42	3
ZAVI04-13	17836	98	0.05377	0.00167	0.04879	0.00290	0.00658	0.00033	0.854	362	68	48	3	42	2
ZAVI04-31	11075	92	0.05518	0.00141	0.05010	0.00282	0.00658	0.00033	0.891	420	56	50	3	42	2
ZAVI04-8	19302	106	0.05291	0.00157	0.04804	0.00295	0.00659	0.00035	0.875	325	66	48	3	42	2
ZAVI04-21	11846	94	0.05517	0.00136	0.05023	0.00300	0.00660	0.00036	0.911	419	54	50	3	42	2
ZAVI04-3	13127	82	0.05414	0.00156	0.04934	0.00339	0.00661	0.00041	0.907	377	64	49	3	42	3
ZAVI04-22	15589	103	0.05295	0.00139	0.04827	0.00246	0.00661	0.00029	0.856	326	59	48	2	42	2
ZAVI04-1	12509	112	0.05530	0.00208	0.05045	0.00393	0.00662	0.00045	0.876	424	82	50	4	43	3
ZAVI04-25	8260	92	0.05855	0.00177	0.05363	0.00286	0.00664	0.00029	0.824	551	65	53	3	43	2
ZAVI04-7	12676	109	0.05618	0.00196	0.05199	0.00343	0.00671	0.00038	0.849	460	76	51	3	43	2
ZAVI04-20	11470	95	0.05575	0.00122	0.05163	0.00268	0.00672	0.00032	0.906	442	48	51	3	43	2
ZAVI04-17	14293	109	0.05381	0.00103	0.05003	0.00277	0.00674	0.00035	0.938	363	43	50	3	43	2
ZAVI04-5	14242	106	0.05468	0.00216	0.05109	0.00375	0.00678	0.00042	0.843	399	86	51	4	44	3
ZAVI04-2	11397	90	0.05575	0.00140	0.05209	0.00306	0.00678	0.00036	0.904	442	55	52	3	44	2
ZAVI04-14	10957	109	0.05744	0.00221	0.05452	0.00340	0.00688	0.00034	0.786	508	83	54	3	44	2

sample CGS139_210	^{206}Pb (cps)	^{204}Pb (cps)	^{207}Pb/^{206}Pb	2 σ	^{207}Pb/^{235}U	2 σ	^{206}Pb/^{238}U	2 σ	ρ	^{207}Pb*/^{206}Pb* age (Ma)	2 σ error (Ma)	^{207}Pb*/^{235}U age (Ma)	2 σ error (Ma)	^{206}Pb*/^{238}U age (Ma)	2 σ error (Ma)
S139-210-1	17973	47	0.04954	0.00162	0.05394	0.00282	0.00790	0.00032	0.780	173	75	53	3	51	2
S139-210-4	23406	75	0.05039	0.00219	0.05428	0.00338	0.00781	0.00035	0.715	213	98	54	3	50	2
S139-210-5	22583	83	0.04914	0.00133	0.05115	0.00247	0.00755	0.00030	0.828	155	62	51	2	48	2
S139-210-6	53498	97	0.04780	0.00048	0.05142	0.00191	0.00780	0.00028	0.963	89	24	51	2	50	2
S139-210-8	17626	102	0.06353	0.00504	0.06800	0.00585	0.00776	0.00026	0.388	726	160	67	6	50	2
S139-210-9	11754	73	0.05243	0.00390	0.05618	0.00484	0.00777	0.00034	0.504	304	161	55	5	50	2
S139-210-10	44922	71	0.04794	0.00060	0.05131	0.00210	0.00776	0.00030	0.952	96	29	51	2	50	2
S139-210-11	16568	57	0.05055	0.00131	0.05442	0.00274	0.00781	0.00034	0.857	220	59	54	3	50	2
S139-210-12	98659	51	0.04920	0.00076	0.05309	0.00179	0.00783	0.00023	0.887	157	36	53	2	50	1
S139-210-13	23230	56	0.05230	0.00115	0.05469	0.00257	0.00758	0.00032	0.884	298	49	54	2	49	2
S139-210-14	22298	68	0.04837	0.00090	0.05280	0.00197	0.00792	0.00026	0.867	117	43	52	2	51	2
S139-210-15	43504	65	0.04785	0.00062	0.05249	0.00216	0.00796	0.00031	0.950	92	30	52	2	51	2
S139-210-16	13698	57	0.05109	0.00264	0.05431	0.00348	0.00771	0.00029	0.591	245	115	54	3	50	2
S139-210-17	5013	63	0.07084	0.00327	0.07557	0.00468	0.00774	0.00032	0.667	953	92	74	4	50	2
S139-210-18	40635	55	0.04954	0.00077	0.05482	0.00228	0.00803	0.00031	0.928	174	36	54	2	52	2
S139-210-19	18050	71	0.04869	0.00160	0.05233	0.00317	0.00780	0.00040	0.841	133	75	52	3	50	3
S139-210-20	4545	53	0.06694	0.00480	0.07292	0.00572	0.00790	0.00025	0.402	836	143	71	5	51	2
S139-210-21	7316	62	0.05222	0.00276	0.05853	0.00388	0.00813	0.00032	0.601	295	117	58	4	52	2
S139-210-23	33283	42	0.04818	0.00076	0.05420	0.00217	0.00816	0.00030	0.920	108	37	54	2	52	2
S139-210-24	136273	66	0.04824	0.00052	0.05324	0.00256	0.00800	0.00038	0.975	111	25	53	2	51	2
S139-210-25	35324	68	0.04953	0.00094	0.05615	0.00333	0.00822	0.00046	0.947	173	44	55	3	53	3
S139-210-28	11197	67	0.05270	0.00261	0.05909	0.00414	0.00813	0.00040	0.706	316	109	58	4	52	3
S139-210-30	17940	45	0.05211	0.00247	0.05638	0.00361	0.00785	0.00034	0.671	290	105	56	3	50	2

sample CGS139_288	^{206}Pb (cps)	^{204}Pb (cps)	^{207}Pb/^{206}Pb	2 σ	^{207}Pb/^{235}U	2 σ	^{206}Pb/^{238}U	2 σ	ρ	^{207}Pb*/^{206}Pb* age (Ma)	2 σ error (Ma)	^{207}Pb*/^{235}U age (Ma)	2 σ error (Ma)	^{206}Pb*/^{238}U age (Ma)	2 σ error (Ma)
S139-288-1	12194	148	0.05421	0.00544	0.05820	0.00625	0.00779	0.00030	0.356	380	211	57	6	50	2
S139-288-2	27682	106	0.04971	0.00169	0.05369	0.00291	0.00783	0.00033	0.779	181	77	53	3	50	2
S139-288-4	47568	67	0.04795	0.00119	0.05306	0.00287	0.00803	0.00039	0.888	97	58	52	3	52	2
S139-288-5	38040	83	0.04848	0.00126	0.05450	0.00300	0.00815	0.00040	0.882	123	60	54	3	52	3
S139-288-6	15265	26	0.04797	0.00089	0.05084	0.00238	0.00769	0.00033	0.919	98	43	50	2	49	2
S139-288-7	217563	101	0.05169	0.00072	0.05749	0.00243	0.00807	0.00032	0.944	272	32	57	2	52	2
S139-288-8	24414	26	0.04962	0.00147	0.05457	0.00281	0.00798	0.00034	0.818	177	68	54	3	51	2
S139-288-10	59996	28	0.04929	0.00103	0.05364	0.00225	0.00789	0.00029	0.867	162	48	53	2	51	2
S139-288-11	23394	21	0.04918	0.00064	0.05282	0.00226	0.00779	0.00032	0.952	156	30	52	2	50	2
S139-288-12	228065	366	0.06184	0.00572	0.06749	0.00670	0.00791	0.00029	0.363	669	187	66	6	51	2
S139-288-13	51856	19	0.05054	0.00141	0.05620	0.00276	0.00806	0.00033	0.824	220	63	56	3	52	2
S139-288-14	51856	22	0.04986	0.00141	0.05277	0.00267	0.00768	0.00032	0.830	188	64	52	3	49	2
S139-288-15	94147	24	0.04870	0.00068	0.05096	0.00262	0.00759	0.00038	0.963	134	32	50	3	49	2
S139-288-16	15796	21	0.04902	0.00112	0.05180	0.00303	0.00766	0.00041	0.921	149	53	51	3	49	3
S139-288-18	29892	27	0.04831	0.00065	0.05255	0.00283	0.00789	0.00041	0.968	114	31	52	3	51	3
S139-288-20	119873	103	0.06085	0.00201	0.07082	0.00355	0.00844	0.00032	0.752	634	70	69	3	54	2
S139-288-21	25834	14	0.05095	0.00189	0.05490	0.00289	0.00781	0.00029	0.711	239	83	54	3	50	2
S139-288-22	105200	5	0.04843	0.00047	0.05172	0.00260	0.00774	0.00038	0.981	120	23	51	3	50	2
S139-288-23	50393	11	0.04902	0.00100	0.05300	0.00236	0.00784	0.00031	0.890	149	47	52	2	50	2
S139-288-24	37161	34	0.07659	0.00439	0.08753	0.00622	0.00829	0.00035	0.591	1111	110	85	6	53	2
S139-288-25	101341	11	0.04775	0.00055	0.05174	0.00212	0.00786	0.00031	0.959	87	27	51	2	50	2
S139-288-26	26318	2	0.04851	0.00095	0.05147	0.00228	0.00770	0.00031	0.896	124	46	51	2	49	2
S139-288-28	76552	8	0.04766	0.00051	0.05180	0.00229	0.00788	0.00034	0.970	83	25	51	2	51	2
S139-288-29	26784	1	0.05432	0.00105	0.05757	0.00260	0.00769	0.00031	0.904	384	43	57	2	49	2
S139-288-30	171197	403	0.07550	0.01194	0.08369	0.01369	0.00804	0.00034	0.256	1082	288	82	13	52	2

Note: ^{207}Pb/^{206}Pb ratios are not corrected for common lead.

Appendix E: Fluid Inlcusions Data

Sample	DDH	MASL	Vein stage	Ore minerals	Host mineral	FIA number	FIA type	Th (°C)	Wt.% NaCl eq.	N
S141-35	S141	1993	MN/Stage I	py+cpy	Quartz	S141-35_10	P (L+V)	259.5	11.5	2
U39-173	U39	2117	MN/Stage I	cpy-po	Quartz	U39-173_1	P (L)	312.6	11.9	8
"	"	"	"	"	"	U39-173_2	"	288.9	10.2	7
"	"	"	"	"	"	U39-173_3	"	250.2	10.8	5
"	"	"	"	"	"	U39-173_3a	"	190.5	10.6	4
"	"	"	"	"	"	U39-173_4	"	151.9	4.0	3
"	"	"	"	"	"	U39-173_4a	PS (L)	176.7	0.8	10
"	"	"	"	"	"	U39-173_5	"	192.1	7.2	5
MN9-W	Underground	2206	MN/Stage I	py-cpy-mag	Quartz	MN9-W_1	P (L)	242.0	0.0	11
"	"	"	"	"	"	MN9-W_2	PS (L)	246.3	0.0	4
U375-383	U375		I	cpy+py	Quartz	U375-383_1	P (L)	229.8	8.9	11
"	"	"	"	"	"	U375-383_1a	PS (L+V)	235.6	10.7	4
U39-171	U39	2117	MN/Stage I	cpy-po	Quartz	U39-171_3	P (L)	213.0	6.3	2
"	"	"	"	"	"	U39-171_4	"	276.1	9.9	5
"	"	"	"	"	"	U39-171_5	"	245.4	11.2	5
U161-178	U161	2132	MN/Stage I	py+cpy	Quartz	U161-178_4	P (L)	245.3	0.0	8
"	"	"	"	"	"	U161-178_2	PS (L+V)	245.7	0.4	8
"	"	"	"	"	"	U161-178_5	P (L)	240.8	0.4	8
U39-170	U39	2220	MN/Stage I	cpy-po	Quartz	U39-170_4	P (L)	202.7	0.0	7
S141-34	S141	2369	MN/Stage I	"	"	S141-34_8	P (L)	217.4	2.3	6
"	"	"	"	"	"	S141-34_13	P (L+V)	208.5	3.4	10
S179-595	S179	2117	MN/Stage I	py+cpy	Quartz	S179-595_1	P (L)	217.0	8.8	5
"	"	"	"	"	"	S179-595_2	"	227.6	6.6	3
"	"	"	"	"	"	S179-595_2a	"	187.7	6.7	5
U83-183	U83	2096	MN/Stage I	cpy-po-mag	Quartz	U83-183_1	P (L+Sp)	257.5	8.7	3
"	"	"	"	"	"	U83-183_2	"	196.7	5.3	5
"	"	"	"	"	"	U83-183_4	"	250.8	11.2	10
"	"	"	"	"	"	U83-183_5	"	266.0	9.2	10
"	"	"	"	"	"	U83-183_9	"	231.1	1.3	5
S64-64	S64	2361	I	py+cpy	"	S64-64_3	P (L)	217.3	2.9	13
"	"	"	"	"	"	S64-64_4	"	207.9	9.5	4
COS-S39	S39	1721	MN/Stage I	cpy+py	Quartz	COS-S39_1a	P (L)	235.9	11.8	4
"	"		"	"	"	COS-S39_1b	"	223.7	0.2	5
"	"		"	"	"	COS-S39_11a	"	262.5	9.0	12
"	"		"	"	"	COS-S39_16b	"	250.5	9.0	11
"	"		"	"	"	COS-S39_2a	"	299.1	12.6	10
"	"		"	"	"	COS-S39_2b	"	275.3	1.7	4
"	"		"	"	"	COS-S39_3a	"	306.0	10.5	6
"	"		"	"	"	COS-S39_6a	"	324.0	12.2	17
COS-S40	S40	1811	MN/Stage I	Cpy+py	Quartz	COS-S40_1a	P (L)	313.4	12.2	12
"	"		"	"	"	COS-S40_3a	"	298.8	10.6	10
"	"		"	"	"	COS-S40_3b	"	227.4	0.8	9
	"					COS-S40_4a	PS (L)	246.6	0.9	7
U39-178	U39	2128	MN/Stage II	sph+gn+py	Quartz	U39-178_1	P (L)	289.3	13.3	5
"	"	"	"	"	"	U39-178_1a	PS (L)	282.8	13.2	3
"	"	"	"	"	"	U39-178_2	PS (L+V)	299.1	9.3	5
"	"	"	"	"	"	U39-178_5	P (L)	283.8	15.0	4
"	"	"	"	"	"	U39-178_7	P (L+sp)	294.5	9.1	5
S141-35	S141	2368	MN/Stage II	Barren	Amethyst Qz	S141-35_1	P (L)	250.2	0.5	3
"	"	"	"	"	"	S141-35_2	PS (L+V)	339.6	0.0	4
"	"	"	"	"	"	S141-35_3	PS (L+V)	294.0	13.2	3
"	"	"	"	"	"	S141-35_5	P (L+V)	298.1	13.5	5
S93-292	S93	2220	MN/Stage II	sph+gn	Amethyst Qz	S93-292_2	PS (L)	279.3	13.8	5
"	"	"	"	"	"	S93-292_3	"	269.0	11.1	6
"	"	"	"	"	"	S93-292_5	"	292.2	12.2	8
S141-34	S141	2369	MN/Stage II	sph+gn	Quartz	S141-34_1	P (L)	206.8	2.0	7
"	"	"	"	"	"	S141-34_1a	PS (L+V)	285.4	13.1	6
"	"	"	"	"	"	S141-34_3	PS (L)	205.9	0.0	5
"	"	"	"	"	"	S141-34_4	PS (L+V)	249.4	11.4	11
"	"	"	"	"	"	S141-34_5	P (L)	210.7	6.4	13
S182-385	S182	2131	MN/Stage II	sph+cpy	Quartz	S182-385_3	PS (L)	222.8	0.0	12
"	"	"	"	"	"	S182-385_5	"	231.0	0.0	8
"	"	"	"	"	"	S182-385_6	"	205.6	0.0	3
MNL-16	underground	1800	MN/Stage II	cpy-po-sph+gn	Quartz	MNL-16_2	PS (L)	221.3	8.6	10
S41-802	S41	1745	MN/Stage II	sph	Quartz	S41-802_2	P (L)	216.0	7.1	6
"	"	"	"	"	"	S41-802_3	P	227.4	9.4	3
"	"	"	"	"	"	S41-802_4	P (L)	226.1	9.4	7
"	"	"	"	"	"	S41-802_5	P (L)	283.4	11.5	7
S64-62	S64	2361	MN/Stage II	sph+gn	Quartz	S64-62_2	PS	272.7	13.4	5

Sample	Sample type	Vein stage	Host mineral	FIA number	FIA type	Th (°C)	Wt.% NaCl eq.	N
SA2	Surface	VG/Stage I	Quartz	SA2_1	P (L)	232.5	9.3	9
"	"	"	"	SA2_5b	"	239.3	7.7	7
"	"	"	"	SA2_6	"	238.4	9.0	4
OSDH1B-S11	Drillhole	VG/Stage I	Calcite	OSDH1B_1a	P (L)	231.0	9.4	7
"	"	"	"	OSDH1B_2	P (L+V)	242.6	9.0	9
"	"	"	"	OSDH1B_4	"	249.5	9.6	6
"	"	"	"	OSDH1B_9	P (L)	238.7	10.1	8
Sample 4	surface	VG/Stage II	Quartz	Sample 4_1	P (L)	227.5	8.5	9
"	"	"	"	Sample 4_2	"	223.0	9.3	5
"	"	"	"	Sample 4_3	"	215.4	9.6	5
"	"	"	"	Sample 4_3a	"	198.3	0.3	5
"	"	"	"	Sample 4_5	"	188.4	0.4	18
"	"	"	"	Sample 4_6	"	207.9	0.2	4
"	"	"	"	Sample 4_9	"	215.2	10.3	9
"	"	"	"	Sample 4_9a	"	220.4	11.1	5
"	"	"	"	Sample 4_10	"	225.6	0.8	6
"	"	"	"	Sample 4_12	"	224.1	9.8	11
"	"	"	"	Sample 4_18	"	210.7	10.2	8
"	"	"	"	Sample 4_21	"	217.6	8.9	7
SA3-a	surface	VG/Stage II	Quartz	SA3-a_9	P (L)	193.8	9.1	4
"	"	"	"	SA3-a_7	"	222.3	10.1	10
"	"	"	"	SA3-a_6	"	201.7	10.6	4
SA3-b	surface	VG/Stage II	Quartz	SA3-b_1	"	209.8	8.4	3
"	"	"	"	SA3-b_2	"	220.3	10.5	5
SA3-c	surface	VG/Stage II	Quartz	SA3-c_5	"	223.1	11.1	14
"	"	"	"	SA3-c_6	"	220.5	10.9	19
"	"	"	"	SA3-c_9	"	221.4	9.3	6
SA3-d	surface	VG/Stage II	Quartz	SA3-d_1	"	207.7	9.3	6
"	"	"	"	SA3-d_3	"	214.2	8.2	7
TVG	surface	VG/Stage II	Quartz	TVG_5	"	212.9	9.6	13
"	"	"	"	TVG_10	"	215.8	10.7	8
"	"	"	"	TVG_10a	P (L)	224.6	9.2	9
VECN1-S1	UG_Level 1	COM/Stage I	Quartz	VECN1-S1_1	"	201.5	0.6	3
"	"	"	"	VECN1-S1_2	"	210.8	0.4	4
VECN4-S2	UG_Level 4	COM/Stage I	Quartz	VECN4-S2_1	"	195.1	0.0	3
"	"	"	"	VECN4-S2_2	"	205.0	0.0	4
"	"	"	"	VECN4-S2_3	"	226.3	0.3	5
VECN7-S3	UG_Level 7	COM/Stage I	Calcite	VECN7-S3_1	"	210.4	0.4	4
"	"	"	"	VECN7-S3_2	P (L+V)	220.4	0.0	4
"	"	"	"	VECN7-S3_3	P (L)	207.0	0.7	5
COM43-63	DHCOM43	COM/Stage I	Quartz	COM43-63_1	"	217.7	0.1	4
"	"	"	"	COM43-63_2	"	204.1	0.1	5
"	"	"	"	COM43-63_3	"	198.4	0.3	4
"	"	"	"	COM43-63_4	"	206.0	0.1	6

Appendix F: Oxygen Isotopes Data

Vein	Method	$\delta^{18}O$ (SMOW)	2σ (‰) inter-session	Th°C	$\delta^{18}O_{fluid}$
Mala Noche	In-situ	12.1	0.15	280	4.5
"	"	12.2	0.19	280	4.5
"	"	15.6	0.17	280	8.0
"	"	15.8	0.18	280	8.1
"	"	11.9	0.16	280	4.3
"	"	11.6	0.17	280	4.0
"	"	11.7	0.15	280	4.1
"	"	11.5	0.19	280	3.8
"	"	11.8	0.15	280	4.1
"	"	12.1	0.22	313	5.6
"	"	12.6	0.19	313	6.2
"	"	12.5	0.20	313	6.1
"	"	12.4	0.24	313	6.0
"	"	12.4	0.20	313	6.0
"	"	12.3	0.16	313	5.9
"	"	12.2	0.18	313	5.7
"	"	12.1	0.18	313	5.6
"	"	12.6	0.22	313	6.1
"	"	12.2	0.18	313	5.8
"	"	12.3	0.21	289	5.0
"	"	12.3	0.19	289	5.0
"	"	13.7	0.19	289	6.4
"	"	12.8	0.18	289	5.5
"	"	19.8	0.19	289	12.5
"	"	12.3	0.18	289	5.0
"	"	12.4	0.21	289	5.1
"	"	12.5	0.16	289	5.2
"	"	17.6	0.16	258	9.1
"	"	12.9	0.18	258	4.3
"	"	12.7	0.18	258	4.1
"	"	13.4	0.17	258	4.8
"	"	12.8	0.27	258	4.3
"	"	13.3	0.23	258	4.7
"	"	13.0	0.17	258	4.4
"	"	13.2	0.20	258	4.7
"	"	11.7	0.20	233	1.9
"	"	11.8	0.20	233	2.0
"	"	11.6	0.17	233	1.8
"	"	11.5	0.21	233	1.7
"	"	15.0	0.14	233	5.2
"	"	11.5	0.19	233	1.7
"	"	11.5	0.17	233	1.7
"	"	11.9	0.22	233	2.1
"	"	11.5	0.19	233	1.7
"	"	11.7	0.18	233	1.9
"	"	14.5	0.22	246	5.3
"	"	12.3	0.21	246	3.2
"	"	12.1	0.15	246	2.9
"	"	13.0	0.15	246	3.9
"	"	12.3	0.17	246	3.2
"	"	15.0	0.21	246	5.8
"	"	12.2	0.17	246	3.1
"	"	12.2	0.17	246	3.1
"	"	12.4	0.23	246	3.3
"	"	12.5	0.16	227	2.4
"	"	13.2	0.21	227	3.1
"	"	12.2	0.19	227	2.1
"	"	12.9	0.18	227	2.8
"	"	12.8	0.20	227	2.7
"	"	12.3	0.15	227	2.2
"	"	12.5	0.20	227	2.3
"	"	11.9	0.21	227	1.8
"	"	13.5	0.17	281	5.8
"	"	13.9	0.20	281	6.3
"	"	14.0	0.20	281	6.4
"	"	13.2	0.20	281	5.5
"	"	13.3	0.14	281	5.7
"	"	13.1	0.15	281	5.5
"	"	13.4	0.21	281	5.8
"	"	13.4	0.17	281	5.8
"	"	13.3	0.17	281	5.7
"	"	14.2	0.21	281	6.6
"	"	13.7	0.18	281	6.1
"	"	14.4	0.17	281	6.7
"	"	13.7	0.20	281	6.0

Vein	Method	$\delta^{18}O$ (SMOW)	2σ (‰) inter-session	Th°C	$\delta^{18}O_{fluid}$
El Compas	In-situ	13.3	0.18	193	1.1
"	"	14.7	0.16	193	2.5
"	"	13.9	0.21	193	1.7
"	"	14.3	0.17	193	2.1
"	"	14.3	0.17	193	2.2
"	"	13.8	0.17	193	1.7
"	"	13.7	0.14	193	1.5
"	"	15.2	0.17	193	3.1
"	"	14.7	0.19	193	2.6
"	"	11.9	0.18	193	-0.2
"	"	13.2	0.19	193	1.0
"	"	10.8	0.17	193	-1.4
Veta Grande (SII)	"	17.0	0.20	227	6.9
"	"	17.3	0.20	227	7.2
"	"	18.3	0.22	227	8.2
"	"	17.3	0.17	227	7.2
"	"	17.1	0.22	227	7.0
"	"	20.3	0.21	227	10.1
"	"	18.0	0.20	227	7.9
"	"	16.2	0.21	227	6.0
"	"	16.6	0.24	227	6.5
"	"	16.7	0.20	227	6.6
"	"	16.0	0.21	227	5.9
"	"	18.2	0.17	227	8.1
"	"	16.4	0.19	217	5.7
"	"	17.3	0.20	217	6.6
"	"	16.4	0.15	217	5.7
"	"	16.9	0.17	217	6.2
"	"	15.7	0.19	217	5.0
"	"	15.4	0.19	217	4.7
"	"	15.3	0.20	217	4.6
"	"	15.5	0.18	217	4.9
"	"	16.4	0.19	217	5.7
"	"	16.4	0.15	217	5.7
"	"	16.0	0.16	217	5.3
"	"	15.7	0.16	217	5.0
"	"	15.9	0.15	217	5.2
"	"	16.3	0.17	217	5.6
"	"	15.9	0.16	217	5.2
"	"	16.3	0.18	217	5.6
Veta Grande (SII)	BrF_5	16.3	0.10	195	4.3
"	"	16.0	0.10	195	4.0
"	"	16.4	0.10	195	4.4
"	"	16.3	0.10	195	4.3
"	"	16.4	0.10	210	5.3
"	"	16.4	0.10	210	5.3
"	"	16.4	0.10	210	5.3
"	"	15.5	0.10	210	4.4
Veta Grande (SI)	In-situ	12.0	0.17	232	2.1
"	"	12.3	0.19	232	2.4
"	"	12.1	0.21	232	2.3
"	"	12.0	0.15	232	2.2
"	"	12.5	0.21	232	2.7
"	"	12.1	0.21	232	2.2
"	"	11.8	0.21	232	2.0
"	"	12.5	0.15	232	2.6
"	"	12.6	0.23	232	2.8
"	"	12.2	0.20	232	2.3

Appendix G: LA-ICP Data

Sample:	COS39_6-P5.txt	Host Correction Factor:	-
Date:	03/16/2015 09:12	Wt % NaCl eq:	13.1
Internal Standard:	Na		
Standard Method:	Microthermometry		
Region:	207.0 : 227.0 seconds		

Element	Con. (ppm)	LOD (ppm)	Weight %	Sample (cps)	Bkg (cps)	Std (cps)	Bkg (cps)	Mix (ppm)	Host (ppm)	Known (ppm)	Diff (%)
Li (7)	6.399	1.471	0	684,644	10,367,997	24,324,402	12,943,434	-	-	-	-
B (11)	21.678	0.306	0.02	955,137	77,952	7,699,447	140,390	-	-	-	-
Na (23)	1,338.249	0.277	0.34	405,928,987	2,788,360	14,115,031,1..	3,380,019	-	-	-	-
Mg (25)	-	0.989	-	5,087	180,886	4,515,772	168,413	-	-	-	-
Si (28)	20,796.568	1.664	12.58	1,429,220,188	5,156,179	10,529,535,3..	15,132,498	-	-	-	-
K (39)	126.831	0.432	0.02	40,030,805	7,550,832	68,613,913	7,525,607	-	-	-	-
Ca (40)	352.162	0.167	0.1	117,742,918	1,503,641	12,733,194,7..	1,317,980	-	-	-	-
Sc (45)	5.694	0.198	0	2,557,087	3,240,446	91,418,665	4,135,481	-	-	-	-
Mn (55)	-	0.085	-	23,259	511,363	80,276,874	589,369	-	-	-	-
Fe (56)	-	0.068	-	18,305	207,578	66,352,298	229,117	-	-	-	-
Cu (63)	-	0.215	-	8,045	195,526	19,574,695	201,508	-	-	-	-
Zn (66)	1.304	0.18	0	79,823	49,610	13,171,586	75,904	-	-	-	-
As (75)	0.112	0.087	0	5,738	8,012	7,774,385	10,383	-	-	-	-
Se (82)	-	0.374	-	3,263	14,910	781,953	17,152	-	-	-	-
Rb (85)	2.054	0.048	0	795,462	147,901	77,400,053	185,395	-	-	-	-
Sr (88)	7.389	0.004	0	3,318,012	2,048	108,350,140	2,014	-	-	-	-
Zr (90)	-	0.008	-	527	723	30,279,560	1,076	-	-	-	-
Nb (93)	-	0.011	-	0	2,832	46,020,646	2,569	-	-	-	-
Mo (98)	-	0.015	-	503	843	15,059,342	1,319	-	-	-	-
Ag (107)	-	0.008	-	452	2,560	18,833,032	3,912	-	-	-	-
Sn (120)	-	0.023	-	841	15,603	47,163,796	24,722	-	-	-	-
Sb (121)	0.11	0.043	0	27,308	42,501	43,302,918	61,876	-	-	-	-
Cs (133)	1.543	0.003	0	1,031,983	1,386	113,014,988	1,667	-	-	-	-
Ba (138)	0.964	0.002	0	429,396	241	94,854,285	555	-	-	-	-
W (182)	0	0	0	0	0	22,128,854	139	-	-	-	-
Au (197)	-	0.003	-	14	217	1,269,128	222	-	-	-	-
Pb (208)	-	0.007	-	2,084	3,012	76,477,437	3,334	-	-	-	-

Sample:	COS39 6-P7.txt	Host Correction Factor:	-
Date:	03/17/2015 06:53	Wt % NaCl eq:	13.4
Internal Standard:	Na		
Standard Method:	Microthermometry		
Region:	66.5 : 70.5 seconds		

Element	Con. (ppm)	LOD (ppm)	Weight %	Sample (cps)	Bkg (cps)	Std (cps)	Bkg (cps)	Mix (ppm)	Host (ppm)	Known (ppm)	Diff (%)
Li (7)	-	25.731	-	102,471.	9,964,837.	24,324,402.	12,943,434.	-	-	-	-
B (11)	21.138	5.785	0.02	104,775.	74,676.	7,699,447.	140,390.	-	-	-	-
Na (23)	1,745.559	5.34	0.44	59,479,987.	2,648,017.	##########	3,380,019.	-	-	-	-
Mg (25)	-	19.317	-	0.	192,498.	4,515,772.	168,413.	-	-	-	-
Si (28)	21,125.07	28.777	12.78	163,349,673.	4,713,680.	##########	15,132,498.	-	-	-	-
K (39)	254.16	7.85	0.05	9,015,246.	7,563,155.	68,613,913.	7,525,607.	-	-	-	-
Ca (40)	313.527	3.458	0.09	11,781,898.	1,536,005.	##########	1,317,980.	-	-	-	-
Sc (45)	11.745	3.521	0.	596,326.	3,181,024.	91,418,665.	4,135,481.	-	-	-	-
Mn (55)	7.843	1.661	0.	350,871.	504,502.	80,276,874.	589,369.	-	-	-	-
Fe (56)	25.045	1.458	0.01	875,538.	212,990.	66,352,298.	229,117.	-	-	-	-
Cu (63)	4.393	4.353	0.	48,545.	203,154.	19,574,695.	201,508.	-	-	-	-
Zn (66)	7.188	3.248	0.	49,586.	48,759.	13,171,586.	75,904.	-	-	-	-
As (75)	-	1.593	-	2,712.	8,954.	7,774,385.	10,383.	-	-	-	-
Se (82)	-	6.947	-	4,181.	16,372.	781,953.	17,152.	-	-	-	-
Rb (85)	2.403	0.963	0.	104,514.	149,419.	77,400,053.	185,395.	-	-	-	-
Sr (88)	9.175	0.075	0.	463,087.	1,503.	108,350,140.	2,014.	-	-	-	-
Zr (90)	-	0.199	-	0.	1,242.	30,279,560.	1,076.	-	-	-	-
Nb (93)	-	0.181	-	0.	2,320.	46,020,646.	2,569.	-	-	-	-
Mo (98)	-	0.378	-	0.	1,242.	15,059,342.	1,319.	-	-	-	-
Ag (107)	-	0.154	-	893.	2,255.	18,833,032.	3,912.	-	-	-	-
Sn (120)	-	0.431	-	1,996.	14,118.	47,163,796.	24,722.	-	-	-	-
Sb (121)	0.794	0.717	0.	22,193.	42,254.	43,302,918.	61,876.	-	-	-	-
Cs (133)	2.188	0.06	0.	164,349.	1,765.	113,014,988.	1,667.	-	-	-	-
Ba (138)	3.252	0.031	0.	162,555.	229.	94,854,285.	555.	-	-	-	-
W (182)	-	0.131	-	0.	261.	22,128,854.	139.	-	-	-	-
Au (197)	-	0.058	-	517.	262.	1,269,128.	222.	-	-	-	-
Pb (208)	0.87	0.142	0.	36,925.	3,627.	76,477,437.	3,334.	-	-	-	-

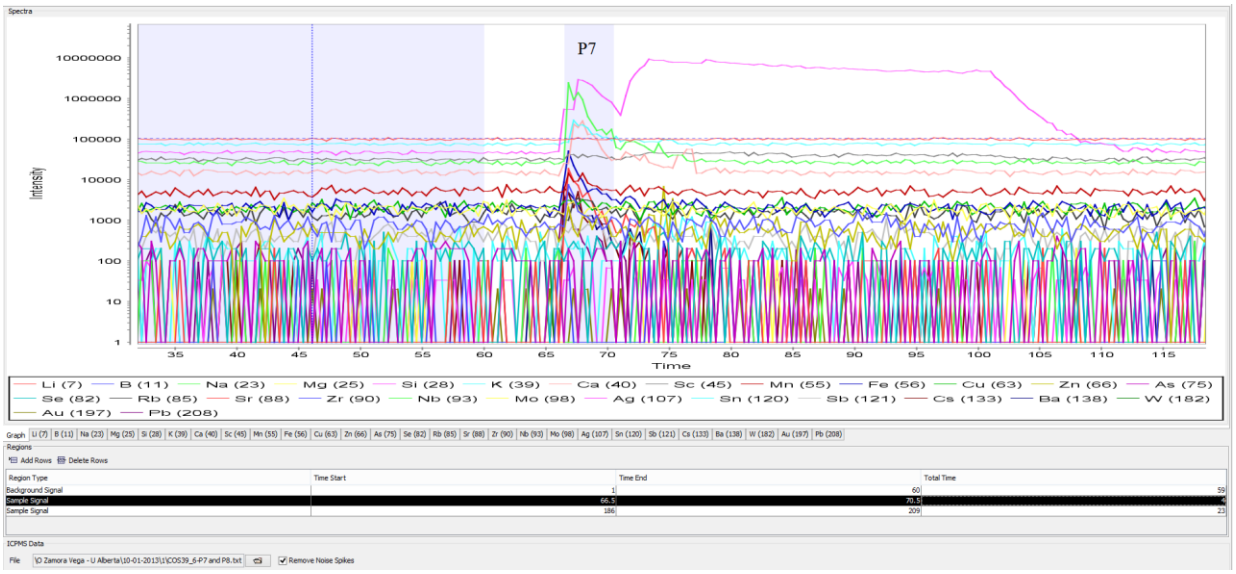

Sample:	COS39 6-P8.txt	Host Correction Factor:	-
Date:	03/17/2015 06:53	Wt % NaCl eq:	13.4
Internal Standard:	Na		
Standard Method:	Microthermometry		
Region:	186.0 : 213.0 seconds		

Element	Con. (ppm)	LOD (ppm)	Weight %	Sample (cps)	Bkg (cps)	Std (cps)	Bkg (cps)	Mix (ppm)	Host (ppm)	Known (ppm)	Diff (%)
Li (7)	1.921	1.249	0.	209,710.	9,964,837.	24,324,402.	12,943,434.	-	-	-	-
B (11)	2.409	0.281	0.	108,677.	74,676.	7,699,447.	140,390.	-	-	-	-
Na (23)	104.958	0.259	0.03	32,521,728.	2,648,017.	##########	3,380,019.	-	-	-	-
Mg (25)	-	0.938	-	0.	192,498.	4,515,772.	168,413.	-	-	-	-
Si (28)	22,071.41	1.397	13.35	1,552,310,125.	4,713,680.	##########	15,132,498.	-	-	-	-
K (39)	17.499	0.381	0.	5,644,711.	7,563,155.	68,613,913.	7,525,607.	-	-	-	-
Ca (40)	34.607	0.168	0.01	11,826,754.	1,536,005.	##########	1,317,980.	-	-	-	-
Sc (45)	5.937	0.171	0.	2,743,603.	3,181,024.	91,418,665.	4,135,481.	-	-	-	-
Mn (55)	0.551	0.081	0.	224,246.	504,502.	80,276,874.	589,369.	-	-	-	-
Fe (56)	0.369	0.071	0.	117,485.	212,990.	66,352,298.	229,117.	-	-	-	-
Cu (63)	-	0.211	-	4,905.	203,154.	19,574,695.	201,508.	-	-	-	-
Zn (66)	0.295	0.158	0.	18,488.	48,759.	13,171,586.	75,904.	-	-	-	-
As (75)	-	0.077	-	1,843.	8,954.	7,774,385.	10,383.	-	-	-	-
Se (82)	-	0.337	-	0.	16,372.	781,953.	17,152.	-	-	-	-
Rb (85)	0.214	0.047	0.	84,514.	149,419.	77,400,053.	185,395.	-	-	-	-
Sr (88)	0.958	0.004	0.	439,610.	1,503.	108,350,140.	2,014.	-	-	-	-
Zr (90)	-	0.01	-	0.	1,242.	30,279,560.	1,076.	-	-	-	-
Nb (93)	-	0.009	-	1,086.	2,320.	46,020,646.	2,569.	-	-	-	-
Mo (98)	-	0.018	-	0.	1,242.	15,059,342.	1,319.	-	-	-	-
Ag (107)	-	0.008	-	185.	2,255.	18,833,032.	3,912.	-	-	-	-
Sn (120)	-	0.021	-	665.	14,118.	47,163,796.	24,722.	-	-	-	-
Sb (121)	-	0.035	-	1,732.	42,254.	43,302,918.	61,876.	-	-	-	-
Cs (133)	0.18	0.003	0.	122,588.	1,765.	113,014,988.	1,667.	-	-	-	-
Ba (138)	0.18	0.002	0.	81,804.	229.	94,854,285.	555.	-	-	-	-
W (182)	-	0.006	-	173.	261.	22,128,854.	139.	-	-	-	-
Au (197)	-	0.003	-	28.	262.	1,269,128.	222.	-	-	-	-
Pb (208)	0.049	0.007	0.	18,910.	3,627.	76,477,437.	3,334.	-	-	-	-

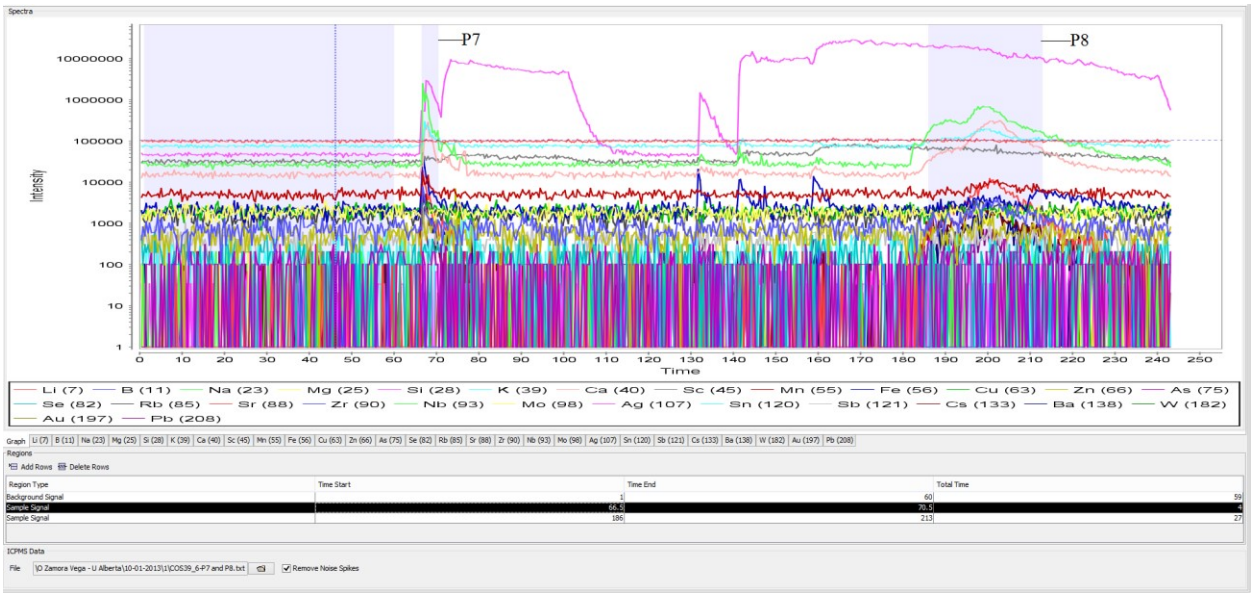

Sample:	MN10.3S4 9-P15.txt	Host Correction Factor:	-
Date:	03/17/2015 01:16	Wt % NaCl eq:	11.8
Internal Standard:	Na		
Standard Method:	Microthermometry		
Region:	122.5 : 139.8 seconds		

Element	Con. (ppm)	LOD (ppm)	Weight %	Sample (cps)	Bkg (cps)	Std (cps)	Bkg (cps)	Mix (ppm)	Host (ppm)	Known (ppm)	Diff (%)
Li (7)	7.856	0.874	0.	1,480,277.	9,091,018.	24,183,134.	12,943,434.	-	-	-	-
B (11)	3.992	0.138	0.	314,697.	68,106.	7,668,210.	140,390.	-	-	-	-
Na (23)	211.803	0.154	0.05	113,884,514.	2,375,414.	##########	3,380,019.	-	-	-	-
Mg (25)	4.448	0.6	0.	164,898.	187,431.	4,491,183.	168,413.	-	-	-	-
Si (28)	19,378.173	0.836	11.72	2,380,064,336.	3,981,226.	##########	15,132,498.	-	-	-	-
K (39)	53.795	0.285	0.01	30,149,374.	7,640,352.	68,239,032.	7,525,607.	-	-	-	-
Ca (40)	40.198	0.113	0.01	23,881,564.	1,591,492.	##########	1,317,980.	-	-	-	-
Sc (45)	4.959	0.124	0.	4,074,179.	2,938,788.	90,800,839.	4,135,481.	-	-	-	-
Mn (55)	0.39	0.053	0.	277,682.	516,208.	79,835,790.	589,369.	-	-	-	-
Fe (56)	10.364	0.041	0.	5,790,201.	201,620.	66,000,020.	229,117.	-	-	-	-
Cu (63)	0.155	0.146	0.	27,793.	213,022.	19,478,354.	201,508.	-	-	-	-
Zn (66)	4.945	0.103	0.	545,004.	47,451.	13,108,979.	75,904.	-	-	-	-
As (75)	0.105	0.048	0.	9,642.	7,745.	7,745,645.	10,383.	-	-	-	-
Se (82)	-	0.222	-	0.	14,706.	777,422.	17,152.	-	-	-	-
Rb (85)	0.404	0.027	0.	276,357.	143,045.	76,975,599.	185,395.	-	-	-	-
Sr (88)	0.782	0.002	0.	623,918.	1,536.	107,695,587.	2,014.	-	-	-	-
Zr (90)	0.014	0.005	0.	3,599.	719.	30,129,605.	1,076.	-	-	-	-
Nb (93)	-	0.006	-	278.	2,222.	45,784,237.	2,569.	-	-	-	-
Mo (98)	-	0.014	-	1,369.	1,699.	14,983,508.	1,319.	-	-	-	-
Ag (107)	0.035	0.004	0.	10,626.	1,950.	18,748,499.	3,912.	-	-	-	-
Sn (120)	0.015	0.014	0.	6,689.	14,674.	46,937,034.	24,722.	-	-	-	-
Sb (121)	0.117	0.023	0.	51,716.	33,628.	43,072,044.	61,876.	-	-	-	-
Cs (133)	0.32	0.002	0.	378,398.	1,830.	112,268,129.	1,667.	-	-	-	-
Ba (138)	0.227	0.001	0.	178,343.	196.	94,271,334.	555.	-	-	-	-
W (182)	0.004	0.004	0.	713.	196.	22,008,031.	139.	-	-	-	-
Au (197)	-	0.002	-	102.	353.	1,262,812.	222.	-	-	-	-
Pb (208)	0.698	0.005	0.	464,475.	3,432.	76,077,957.	3,334.	-	-	-	-

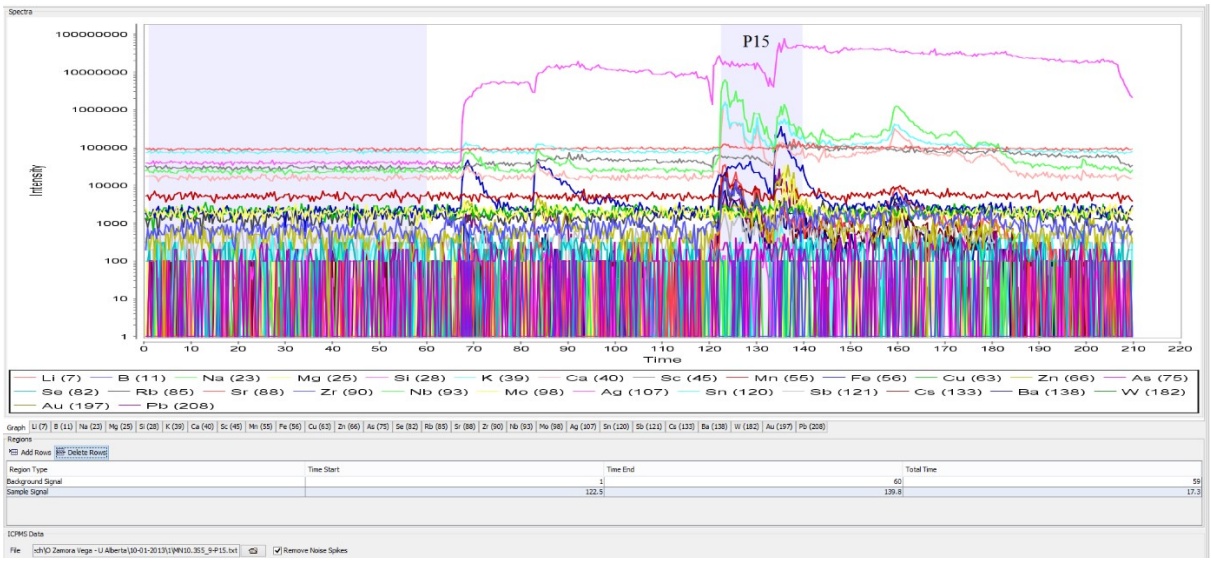

Sample:	MN10.3S4 15-P16.txt	Host Correction Factor:	-
Date:	03/17/2015 02:18	Wt % NaCl eq:	13.9
Internal Standard:	Na		
Standard Method:	Microthermometry		
Region:	73.0 : 76.0 seconds		

Element	Con. (ppm)	LOD (ppm)	Weight %	Sample (cps)	Bkg (cps)	Std (cps)	Bkg (cps)	Mix (ppm)	Host (ppm)	Known (ppm)	Diff (%)
Li (7)	-	9.668	-	70,994.	8,931,929.	24,183,134.	12,943,434.	-	-	-	-
B (11)	-	1.9	-	18,270.	65,067.	7,668,210.	140,390.	-	-	-	-
Na (23)	131.743	1.554	0.03	13,880,306.	2,323,758.	##########	3,380,019.	-	-	-	-
Mg (25)	66.627	6.818	0.03	484,655.	187,204.	4,491,183.	168,413.	-	-	-	-
Si (28)	22,618.964	9.759	13.68	545,000,550.	3,887,528.	##########	15,132,498.	-	-	-	-
K (39)	376.306	3.255	0.07	41,337,487.	7,565,850.	68,239,032.	7,525,607.	-	-	-	-
Ca (40)	278.074	1.17	0.08	32,383,384.	1,604,251.	##########	1,317,980.	-	-	-	-
Sc (45)	8.134	1.38	0.	1,315,809.	2,857,123.	90,800,839.	4,135,481.	-	-	-	-
Mn (55)	2.333	0.617	0.	326,561.	505,418.	79,835,790.	589,369.	-	-	-	-
Fe (56)	64.849	0.466	0.01	7,115,470.	198,970.	66,000,020.	229,117.	-	-	-	-
Cu (63)	32.784	1.732	0.01	1,157,127.	213,711.	19,478,354.	201,508.	-	-	-	-
Zn (66)	74.956	1.17	0.02	1,622,434.	45,884.	13,108,979.	75,904.	-	-	-	-
As (75)	-	0.631	-	11,160.	8,007.	7,745,645.	10,383.	-	-	-	-
Se (82)	-	3.13	-	3,924.	16,078.	777,422.	17,152.	-	-	-	-
Rb (85)	-	0.319	-	41,094.	142,263.	76,975,599.	185,395.	-	-	-	-
Sr (88)	1.604	0.033	0.	250,648.	1,896.	107,695,587.	2,014.	-	-	-	-
Zr (90)	0.633	0.058	0.	32,553.	784.	30,129,605.	1,076.	-	-	-	-
Nb (93)	-	0.076	-	1,240.	2,091.	45,784,237.	2,569.	-	-	-	-
Mo (98)	-	0.132	-	685.	981.	14,983,508.	1,319.	-	-	-	-
Ag (107)	0.38	0.053	0.	22,473.	2,244.	18,748,499.	3,912.	-	-	-	-
Sn (120)	0.704	0.147	0.	61,869.	12,321.	46,937,034.	24,722.	-	-	-	-
Sb (121)	-	0.28	-	0.	32,551.	43,072,044.	61,876.	-	-	-	-
Cs (133)	-	0.014	-	851.	817.	112,268,129.	1,667.	-	-	-	-
Ba (138)	0.447	0.015	0.	68,712.	458.	94,271,334.	555.	-	-	-	-
W (182)	-	0.035	-	0.	131.	22,008,031.	139.	-	-	-	-
Au (197)	-	0.02	-	85.	248.	1,262,812.	222.	-	-	-	-
Pb (208)	1.922	0.052	0.	250,507.	3,726.	76,077,957.	3,334.	-	-	-	-

Sample:	MN10.3S4 15-P17.txt	Host Correction Factor:	-
Date:	03/17/2015 02:18	Wt % NaCl eq:	13.9
Internal Standard:	Na		
Standard Method:	Microthermometry		
Region:	84.0 : 86.8 seconds		

Element	Con. (ppm)	LOD (ppm)	Weight %	Sample (cps)	Bkg (cps)	Std (cps)	Bkg (cps)	Mix (ppm)	Host (ppm)	Known (ppm)	Diff (%)
Li (7)	5.671	2.336	0.	865,412.	8,931,929.	24,183,134.	12,943,434.	-	-	-	-
B (11)	-	0.459	-	14,936.	65,067.	7,668,210.	140,390.	-	-	-	-
Na (23)	53.095	0.376	0.01	23,141,972.	2,323,758.	##########	3,380,019.	-	-	-	-
Mg (25)	24.414	1.648	0.01	734,784.	187,204.	4,491,183.	168,413.	-	-	-	-
Si (28)	22,873.001	2.359	13.84	2,280,232,406.	3,887,528.	##########	15,132,498.	-	-	-	-
K (39)	119.874	0.787	0.02	54,477,390.	7,565,850.	68,239,032.	7,525,607.	-	-	-	-
Ca (40)	121.21	0.283	0.03	58,397,368.	1,604,251.	##########	1,317,980.	-	-	-	-
Sc (45)	6.597	0.334	0.	4,416,990.	2,857,123.	90,800,839.	4,135,481.	-	-	-	-
Mn (55)	0.367	0.149	0.	212,267.	505,418.	79,835,790.	589,369.	-	-	-	-
Fe (56)	35.349	0.113	0.01	16,049,531.	198,970.	66,000,020.	229,117.	-	-	-	-
Cu (63)	7.115	0.419	0.	1,039,482.	213,711.	19,478,354.	201,508.	-	-	-	-
Zn (66)	12.455	0.283	0.	1,115,536.	45,884.	13,108,979.	75,904.	-	-	-	-
As (75)	0.95	0.152	0.	71,162.	8,007.	7,745,645.	10,383.	-	-	-	-
Se (82)	1.199	0.756	0.	25,590.	16,078.	777,422.	17,152.	-	-	-	-
Rb (85)	0.2	0.077	0.	111,097.	142,263.	76,975,599.	185,395.	-	-	-	-
Sr (88)	0.559	0.008	0.	361,507.	1,896.	107,695,587.	2,014.	-	-	-	-
Zr (90)	0.223	0.014	0.	47,551.	784.	30,129,605.	1,076.	-	-	-	-
Nb (93)	-	0.018	-	2,909.	2,091.	45,784,237.	2,569.	-	-	-	-
Mo (98)	0.04	0.032	0.	4,853.	981.	14,983,508.	1,319.	-	-	-	-
Ag (107)	0.094	0.013	0.	23,034.	2,244.	18,748,499.	3,912.	-	-	-	-
Sn (120)	0.438	0.036	0.	159,360.	12,321.	46,937,034.	24,722.	-	-	-	-
Sb (121)	0.083	0.068	0.	29,951.	32,551.	43,072,044.	61,876.	-	-	-	-
Cs (133)	0.008	0.003	0.	7,516.	817.	112,268,129.	1,667.	-	-	-	-
Ba (138)	0.177	0.004	0.	112,882.	458.	94,271,334.	555.	-	-	-	-
W (182)	0.027	0.009	0.	4,036.	131.	22,008,031.	139.	-	-	-	-
Au (197)	0.008	0.005	0.	1,418.	248.	1,262,812.	222.	-	-	-	-
Pb (208)	1.942	0.013	0.	1,047,010.	3,726.	76,077,957.	3,334.	-	-	-	-

Sample:	MN10.3S4 15-P18.txt	Host Correction Factor:	-
Date:	03/17/2015 02:18	Wt % NaCl eq:	13.9
Internal Standard:	Na		
Standard Method:	Microthermometry		
Region:	151.7 : 157.5 seconds		

Element	Con. (ppm)	LOD (ppm)	Weight %	Sample (cps)	Bkg (cps)	Std (cps)	Bkg (cps)	Mix (ppm)	Host (ppm)	Known (ppm)	Diff (%)
Li (7)	9.731	2.809	0.01	839,392.	8,931,929.	24,183,134.	12,943,434.	-	-	-	-
B (11)	2.339	0.552	0.	84,606.	65,067.	7,668,210.	140,390.	-	-	-	-
Na (23)	77.739	0.451	0.02	19,154,672.	2,323,758.	##########	3,380,019.	-	-	-	-
Mg (25)	-	1.981	-	0.	187,204.	4,491,183.	168,413.	-	-	-	-
Si (28)	22,976.177	2.835	13.9	1,295,027,651.	3,887,528.	##########	15,132,498.	-	-	-	-
K (39)	10.057	0.946	0.	2,583,865.	7,565,850.	68,239,032.	7,525,607.	-	-	-	-
Ca (40)	16.443	0.34	0.	4,478,529.	1,604,251.	##########	1,317,980.	-	-	-	-
Sc (45)	5.395	0.401	0.	2,043,048.	2,857,123.	90,800,839.	4,135,481.	-	-	-	-
Mn (55)	0.288	0.179	0.	94,380.	505,418.	79,835,790.	589,369.	-	-	-	-
Fe (56)	-	0.135	-	16,718.	198,970.	66,000,020.	229,117.	-	-	-	-
Cu (63)	-	0.503	-	0.	213,711.	19,478,354.	201,508.	-	-	-	-
Zn (66)	-	0.34	-	117.	45,884.	13,108,979.	75,904.	-	-	-	-
As (75)	0.283	0.183	0.	11,993.	8,007.	7,745,645.	10,383.	-	-	-	-
Se (82)	-	0.909	-	0.	16,078.	777,422.	17,152.	-	-	-	-
Rb (85)	0.204	0.093	0.	64,084.	142,263.	76,975,599.	185,395.	-	-	-	-
Sr (88)	0.411	0.01	0.	150,119.	1,896.	107,695,587.	2,014.	-	-	-	-
Zr (90)	0.024	0.017	0.	2,883.	784.	30,129,605.	1,076.	-	-	-	-
Nb (93)	-	0.022	-	0.	2,091.	45,784,237.	2,569.	-	-	-	-
Mo (98)	-	0.038	-	353.	981.	14,983,508.	1,319.	-	-	-	-
Ag (107)	-	0.016	-	0.	2,244.	18,748,499.	3,912.	-	-	-	-
Sn (120)	-	0.043	-	3,014.	12,321.	46,937,034.	24,722.	-	-	-	-
Sb (121)	0.398	0.081	0.	81,125.	32,551.	43,072,044.	61,876.	-	-	-	-
Cs (133)	0.135	0.004	0.	72,854.	817.	112,268,129.	1,667.	-	-	-	-
Ba (138)	0.059	0.004	0.	21,211.	458.	94,271,334.	555.	-	-	-	-
W (182)	-	0.01	-	536.	131.	22,008,031.	139.	-	-	-	-
Au (197)	-	0.006	-	485.	248.	1,262,812.	222.	-	-	-	-
Pb (208)	0.032	0.015	0.	9,608.	3,726.	76,077,957.	3,334.	-	-	-	-

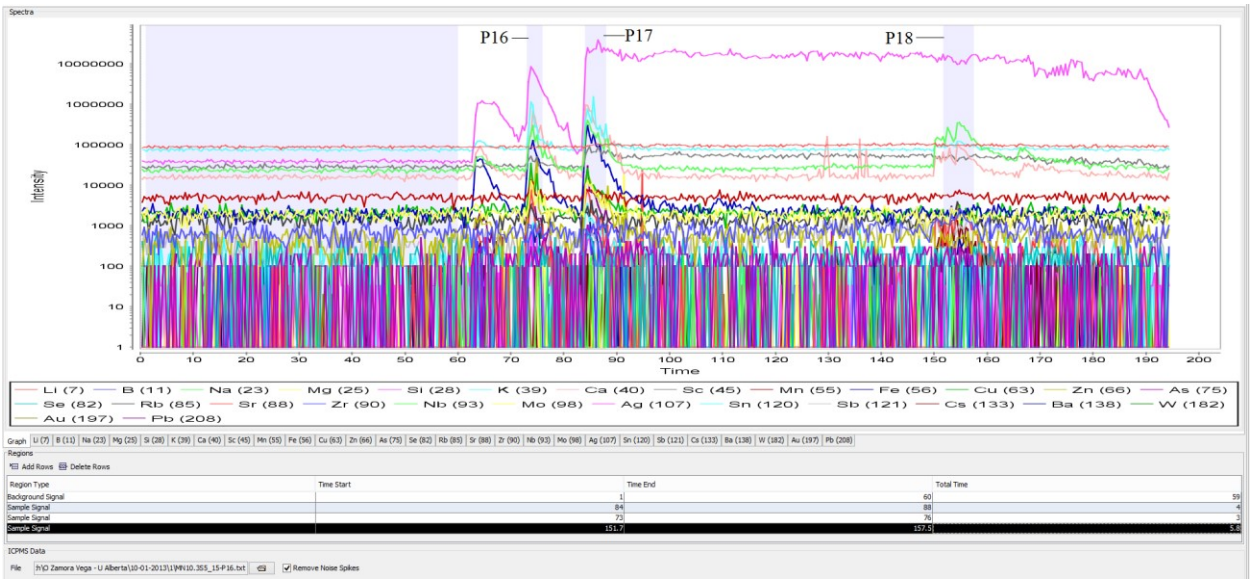

Sample:	TVG 9-P10.txt	Host Correction Factor:	-
Date:	03/17/2015 02:30	Wt % NaCl eq:	9.2
Internal Standard:	Na		
Standard Method:	Microthermometry		
Region:	175.0 : 184.74 seconds		

Element	Con. (ppm)	LOD (ppm)	Weight %	Sample (cps)	Bkg (cps)	Std (cps)	Bkg (cps)	Mix (ppm)	Host (ppm)	Known (ppm)	Diff (%)
Li (7)	7.432	1.095	0.	1,349,772.	9,621,979.	24,183,134.	12,943,434.	-	-	-	-
B (11)	6.865	0.224	0.01	516,866.	73,009.	7,668,210.	140,390.	-	-	-	-
Na (23)	358.374	0.207	0.09	185,010,245.	2,577,431.	##########	3,380,019.	-	-	-	-
Mg (25)	-	0.921	-	0.	185,958.	4,491,183.	168,413.	-	-	-	-
Si (28)	14,988.405	1.254	9.07	1,758,267,708.	4,583,507.	##########	15,132,498.	-	-	-	-
K (39)	94.769	0.337	0.02	50,927,701.	7,523,330.	68,239,032.	7,525,607.	-	-	-	-
Ca (40)	69.239	0.147	0.02	39,427,948.	1,531,588.	##########	1,317,980.	-	-	-	-
Sc (45)	3.948	0.17	0.	3,047,556.	3,080,177.	90,800,839.	4,135,481.	-	-	-	-
Mn (55)	0.101	0.071	0.	68,658.	510,456.	79,835,790.	589,369.	-	-	-	-
Fe (56)	1.88	0.054	0.	998,103.	200,606.	66,000,020.	229,117.	-	-	-	-
Cu (63)	0.185	0.17	-	400,030.	201,585.	19,478,354.	201,508.	-	-	-	-
Zn (66)	0.431	0.136	-	100,223.	47,778.	13,108,979.	75,904.	-	-	-	-
As (75)	0.437	0.067	0.	38,419.	7,582.	7,745,645.	10,383.	-	-	-	-
Se (82)	-	0.324	-	309.	13,693.	777,422.	17,152.	-	-	-	-
Rb (85)	0.658	0.035	0.	433,290.	145,106.	76,975,599.	185,395.	-	-	-	-
Sr (88)	1.354	0.004	0.	1,034,756.	2,091.	107,695,587.	2,014.	-	-	-	-
Zr (90)	-	0.006	-	612.	588.	30,129,605.	1,076.	-	-	-	-
Nb (93)	-	0.007	-	0.	2,484.	45,784,237.	2,569.	-	-	-	-
Mo (98)	-	0.012	-	1,615.	784.	14,983,508.	1,319.	-	-	-	-
Ag (107)	0.013	0.007	-	4,970.	2,636.	18,748,499.	3,912.	-	-	-	-
Sn (120)	-	0.018	-	765.	14,837.	46,937,034.	24,722.	-	-	-	-
Sb (121)	5.76	0.029	0.	2,442,813.	38,563.	43,072,044.	61,876.	-	-	-	-
Cs (133)	0.481	0.002	0.	546,552.	2,092.	112,268,129.	1,667.	-	-	-	-
Ba (138)	0.389	0.001	0.	294,207.	261.	94,271,334.	555.	-	-	-	-
W (182)	-	0.004	-	0.	131.	22,008,031.	139.	-	-	-	-
Au (197)	-	0.002	-	204.	196.	1,262,812.	222.	-	-	-	-
Pb (208)	0.311	0.006	0.	7,332.	3,268.	76,077,957.	3,334.	-	-	-	-

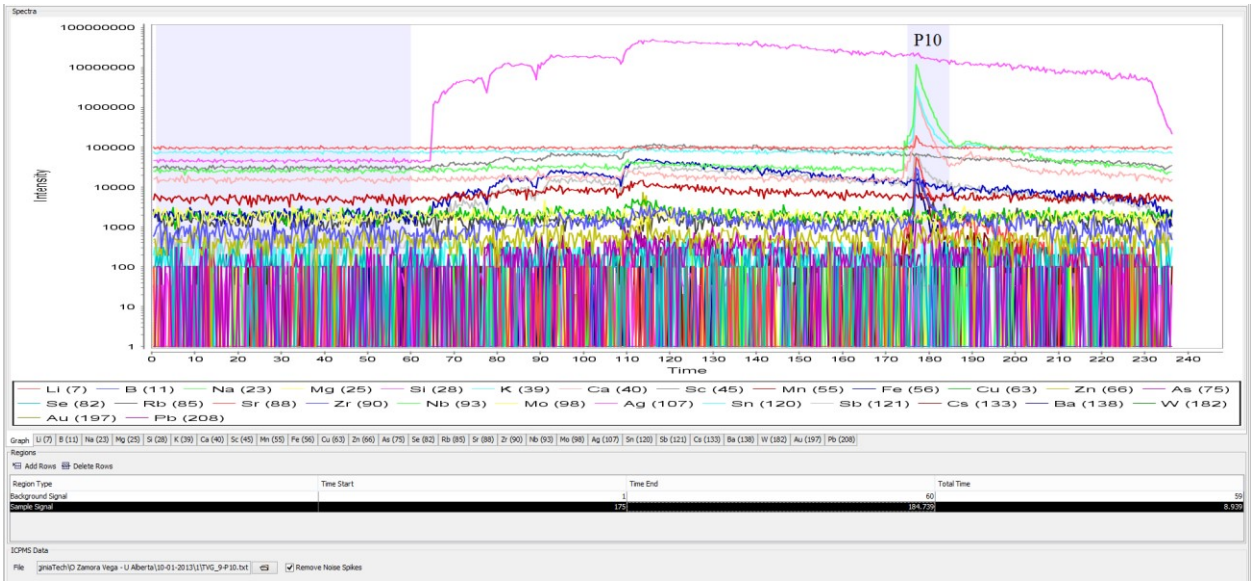

Sample:	TVG 9-P11.txt	Host Correction Factor:	-
Date:	03/17/2015 02:37	Wt % NaCl eq:	9.2
Internal Standard:	Na		
Standard Method:	Microthermometry		
Region:	155.4 : 160.5 seconds		

Element	Con. (ppm)	LOD (ppm)	Weight %	Sample (cps)	Bkg (cps)	Std (cps)	Bkg (cps)	Mix (ppm)	Host (ppm)	Known (ppm)	Diff (%)
Li (7)	-	1.052	-	209,138.	9,481,166.	24,183,134.	12,943,434.	-	-	-	-
B (11)	0.597	0.236	0.	62,250.	70,262.	7,668,210.	140,390.	-	-	-	-
Na (23)	31.061	0.193	0.01	22,177,123.	2,536,113.	##########	3,380,019.	-	-	-	-
Mg (25)	-	0.761	-	2,043.	185,471.	4,491,183.	168,413.	-	-	-	-
Si (28)	15,199.503	1.108	9.19	2,468,878,213.	4,337,725.	##########	15,132,498.	-	-	-	-
K (39)	7.041	0.34	0.	5,234,819.	7,572,828.	68,239,032.	7,525,607.	-	-	-	-
Ca (40)	4.944	0.135	0.	3,895,152.	1,553,861.	##########	1,317,980.	-	-	-	-
Sc (45)	3.754	0.146	0.	4,027,778.	3,103,193.	90,800,839.	4,135,481.	-	-	-	-
Mn (55)	0.074	0.071	0.	70,004.	504,279.	79,835,790.	589,369.	-	-	-	-
Fe (56)	1.738	0.05	0.	1,279,438.	205,115.	66,000,020.	229,117.	-	-	-	-
Cu (63)	-	0.181	-	16,256.	205,013.	19,478,354.	201,508.	-	-	-	-
Zn (66)	-	0.14	-	0.	49,021.	13,108,979.	75,904.	-	-	-	-
As (75)	0.111	0.067	0.	13,479.	7,354.	7,745,645.	10,383.	-	-	-	-
Se (82)	-	0.339	-	0.	15,327.	777,422.	17,152.	-	-	-	-
Rb (85)	-	0.034	-	21,659.	140,433.	76,975,599.	185,395.	-	-	-	-
Sr (88)	0.122	0.003	0.	129,385.	1,863.	107,695,587.	2,014.	-	-	-	-
Zr (90)	-	0.007	-	752.	915.	30,129,605.	1,076.	-	-	-	-
Nb (93)	-	0.008	-	1,355.	2,810.	45,784,237.	2,569.	-	-	-	-
Mo (98)	-	0.015	-	1,388.	1,111.	14,983,508.	1,319.	-	-	-	-
Ag (107)	-	0.007	-	0.	2,887.	18,748,499.	3,912.	-	-	-	-
Sn (120)	-	0.016	-	0.	13,334.	46,937,034.	24,722.	-	-	-	-
Sb (121)	2.599	0.03	0.	1,526,492.	38,595.	43,072,044.	61,876.	-	-	-	-
Cs (133)	0.044	0.002	0.	69,241.	1,176.	112,268,129.	1,667.	-	-	-	-
Ba (138)	0.04	0.002	0.	41,694.	392.	94,271,334.	555.	-	-	-	-
W (182)	-	0.006	-	0.	327.	22,008,031.	139.	-	-	-	-
Au (197)	-	0.003	-	0.	333.	1,262,812.	222.	-	-	-	-
Pb (208)	-	0.006	-	3,511.	3,987.	76,077,957.	3,334.	-	-	-	-

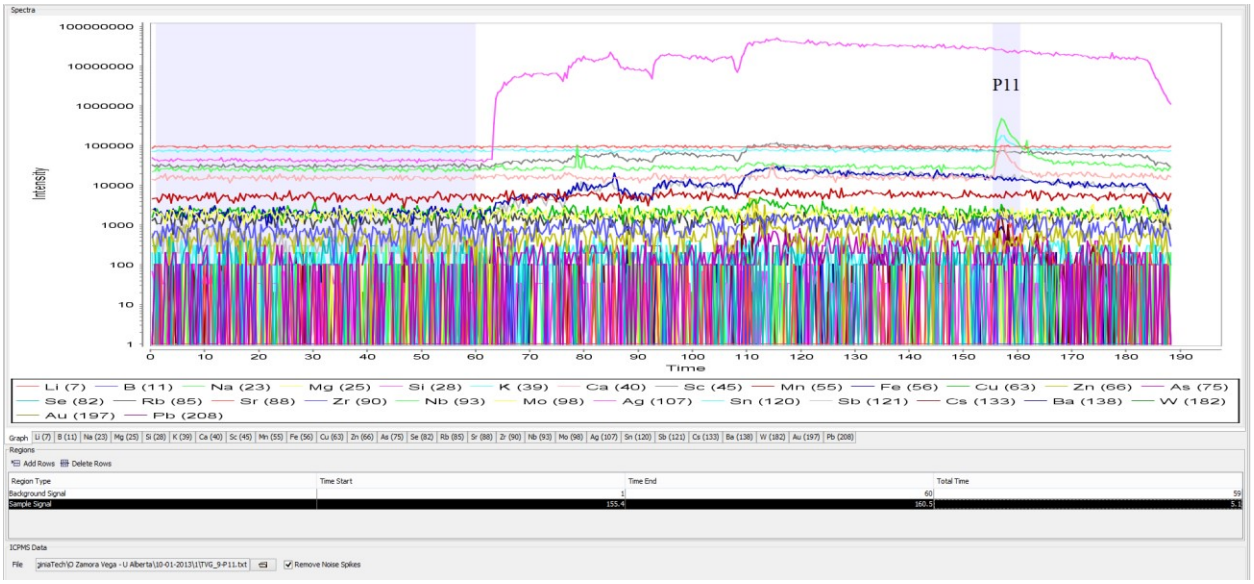

Sample:	TVG 9-P12.txt	Host Correction Factor:	-
Date:	03/17/2015 04:13	Wt % NaCl eq:	9.2
Internal Standard:	Na		
Standard Method:	Microthermometry		
Region:	153.2 : 162.0 seconds		

Element	Con. (ppm)	LOD (ppm)	Weight %	Sample (cps)	Bkg (cps)	Std (cps)	Bkg (cps)	Mix (ppm)	Host (ppm)	Known (ppm)	Diff (%)
Li (7)	10.705	0.575	0.01	3,631,601.	9,345,219.	24,183,134.	12,943,434.	-	-	-	-
B (11)	4.922	0.12	0.	694,830.	70,845.	7,668,210.	140,390.	-	-	-	-
Na (23)	129.665	0.108	0.03	125,230,037.	2,456,642.	##########	3,380,019.	-	-	-	-
Mg (25)	-	0.44	-	0.	186,881.	4,491,183.	168,413.	-	-	-	-
Si (28)	15,111.265	0.633	9.14	3,323,287,860.	4,219,471.	##########	15,132,498.	-	-	-	-
K (39)	53.55	0.192	0.01	53,864,550.	7,526,852.	68,239,032.	7,525,607.	-	-	-	-
Ca (40)	39.529	0.08	0.01	42,139,132.	1,564,218.	##########	1,317,980.	-	-	-	-
Sc (45)	3.721	0.084	0.	5,420,864.	3,053,655.	90,800,839.	4,135,481.	-	-	-	-
Mn (55)	0.376	0.04	0.	478,926.	511,663.	79,835,790.	589,369.	-	-	-	-
Fe (56)	2.478	0.034	0.	2,470,954.	212,790.	66,000,020.	229,117.	-	-	-	-
Cu (63)	-	0.097	-	13,749.	205,585.	19,478,354.	201,508.	-	-	-	-
Zn (66)	-	0.079	-	8,787.	44,398.	13,108,979.	75,904.	-	-	-	-
As (75)	0.21	0.042	0.	34,704.	8,253.	7,745,645.	10,383.	-	-	-	-
Se (82)	-	0.178	-	4,418.	13,766.	777,422.	17,152.	-	-	-	-
Rb (85)	0.342	0.022	0.	421,233.	151,305.	76,975,599.	185,395.	-	-	-	-
Sr (88)	0.759	0.002	0.	1,085,849.	1,687.	107,695,587.	2,014.	-	-	-	-
Zr (90)	-	0.005	-	0.	1,205.	30,129,605.	1,076.	-	-	-	-
Nb (93)	-	0.006	-	0.	2,892.	45,784,237.	2,569.	-	-	-	-
Mo (98)	-	0.009	-	159.	1,205.	14,983,508.	1,319.	-	-	-	-
Ag (107)	-	0.004	-	189.	2,841.	18,748,499.	3,912.	-	-	-	-
Sn (120)	-	0.009	-	4,352.	12,921.	46,937,034.	24,722.	-	-	-	-
Sb (121)	3.147	0.016	0.	2,502,503.	33,585.	43,072,044.	61,876.	-	-	-	-
Cs (133)	0.272	0.001	0.	578,055.	934.	112,268,129.	1,667.	-	-	-	-
Ba (138)	0.197	0.001	0.	278,793.	181.	94,271,334.	555.	-	-	-	-
W (182)	-	0.004	-	548.	361.	22,008,031.	139.	-	-	-	-
Au (197)	-	0.001	-	159.	205.	1,262,812.	222.	-	-	-	-
Pb (208)	0.015	0.003	0.	17,655.	3,253.	76,077,957.	3,334.	-	-	-	-

Sample:	TVG 9-P13.txt	Host Correction Factor:	-
Date:	03/17/2015 04:13	Wt % NaCl eq:	9.2
Internal Standard:	Na		
Standard Method:	Microthermometry		
Region:	299.0 : 308.5 seconds		

Element	Con. (ppm)	LOD (ppm)	Weight %	Sample (cps)	Bkg (cps)	Std (cps)	Bkg (cps)	Mix (ppm)	Host (ppm)	Known (ppm)	Diff (%)
Li (7)	5.511	0.778	0.	1,332,727.	9,345,219.	24,183,134.	12,943,434.	-	-	-	-
B (11)	4.644	0.162	0.	467,637.	70,845.	7,668,210.	140,390.	-	-	-	-
Na (23)	139.023	0.146	0.04	95,743,926.	2,456,642.	##########	3,380,019.	-	-	-	-
Mg (25)	-	0.595	-	2,299.	186,881.	4,491,183.	168,413.	-	-	-	-
Si (28)	15,115.993	0.856	9.14	2,371,439,492.	4,219,471.	##########	15,132,498.	-	-	-	-
K (39)	45.982	0.259	0.01	32,984,925.	7,526,852.	68,239,032.	7,525,607.	-	-	-	-
Ca (40)	36.728	0.108	0.01	27,922,903.	1,564,218.	##########	1,317,980.	-	-	-	-
Sc (45)	3.685	0.113	0.	3,834,057.	3,053,655.	90,800,839.	4,135,481.	-	-	-	-
Mn (55)	0.531	0.054	0.	482,474.	511,663.	79,835,790.	589,369.	-	-	-	-
Fe (56)	2.85	0.046	0.	2,028,413.	212,790.	66,000,020.	229,117.	-	-	-	-
Cu (63)	-	0.131	-	4,433.	205,585.	19,478,354.	201,508.	-	-	-	-
Zn (66)	-	0.107	-	9,145.	44,398.	13,108,979.	75,904.	-	-	-	-
As (75)	0.259	0.057	0.	30,495.	8,253.	7,745,645.	10,383.	-	-	-	-
Se (82)	-	0.24	-	0.	13,766.	777,422.	17,152.	-	-	-	-
Rb (85)	0.384	0.029	0.	337,340.	151,305.	76,975,599.	185,395.	-	-	-	-
Sr (88)	0.712	0.003	0.	726,931.	1,687.	107,695,587.	2,014.	-	-	-	-
Zr (90)	-	0.007	-	462.	1,205.	30,129,605.	1,076.	-	-	-	-
Nb (93)	-	0.008	-	0.	2,892.	45,784,237.	2,569.	-	-	-	-
Mo (98)	-	0.013	-	46.	1,205.	14,983,508.	1,319.	-	-	-	-
Ag (107)	-	0.006	-	630.	2,841.	18,748,499.	3,912.	-	-	-	-
Sn (120)	-	0.012	-	4,583.	12,921.	46,937,034.	24,722.	-	-	-	-
Sb (121)	4.423	0.022	0.	2,508,701.	33,585.	43,072,044.	61,876.	-	-	-	-
Cs (133)	0.25	0.001	0.	378,937.	934.	112,268,129.	1,667.	-	-	-	-
Ba (138)	0.207	0.001	0.	208,802.	181.	94,271,334.	555.	-	-	-	-
W (182)	-	0.005	-	0.	361.	22,008,031.	139.	-	-	-	-
Au (197)	-	0.002	-	0.	205.	1,262,812.	222.	-	-	-	-
Pb (208)	0.034	0.004	0.	29,247.	3,253.	76,077,957.	3,334.	-	-	-	-

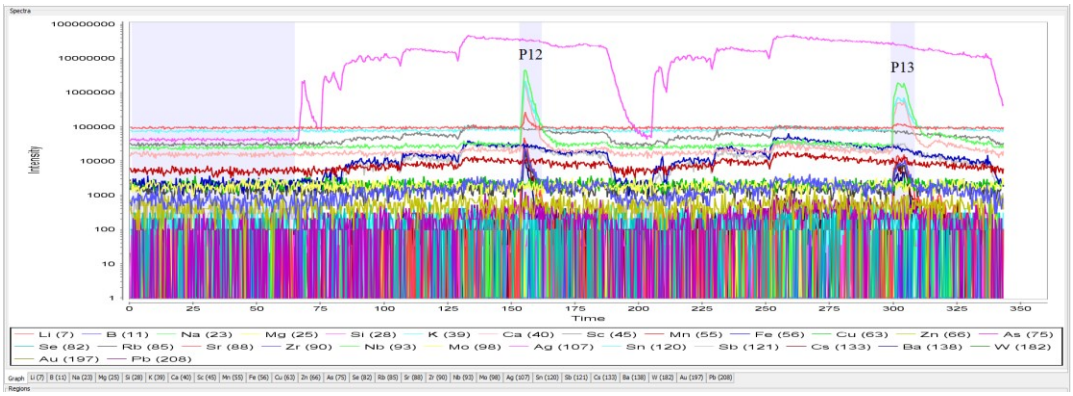

Sample: VCN4S3 9-P17.txt
Date: 03/17/2015 05:03
Internal Standard: Na
Standard Method: Microthermometry
Region: 112.0 : 117.5 seconds

Host Correction Factor: -
Wt % NaCl eq: 0.9

Element	Con. (ppm)	LOD (ppm)	Weight %	Sample (cps)	Bkg (cps)	Std (cps)	Bkg (cps)	Mix (ppm)	Host (ppm)	Known (ppm)	Diff (%)
Li (7)	0.235	0.061	0.	1,007,500.	8,792,632.	24,183,134.	12,943,434.	-	-	-	-
B (11)	0.014	0.013	0.	24,336.	67,584.	7,668,210.	140,390.	-	-	-	-
Na (23)	0.871	0.011	0.	10,693,687.	2,310,735.	##########	3,380,019.	-	-	-	-
Mg (25)	-	0.042	-	18,224.	195,634.	4,491,183.	168,413.	-	-	-	-
Si (28)	1,451.977	0.061	0.88	4,083,432,581.	3,775,273.	##########	15,132,498.	-	-	-	-
K (39)	0.219	0.017	0.	2,805,176.	7,587,972.	68,239,032.	7,525,607.	-	-	-	-
Ca (40)	0.136	0.008	0.	1,845,702.	1,588,148.	##########	1,317,980.	-	-	-	-
Sc (45)	0.337	0.008	0.	6,395,824.	2,795,594.	90,800,839.	4,135,481.	-	-	-	-
Mn (55)	0.005	0.004	0.	76,078.	502,123.	79,835,790.	589,369.	-	-	-	-
Fe (56)	0.298	0.003	0.	3,817,352.	201,419.	66,000,020.	229,117.	-	-	-	-
Cu (63)	0.011	0.011	0.	47,132.	219,038.	19,478,354.	201,508.	-	-	-	-
Zn (66)	0.056	0.007	0.	141,663.	40,654.	13,108,979.	75,904.	-	-	-	-
As (75)	0.009	0.004	0.	17,975.	8,562.	7,745,645.	10,383.	-	-	-	-
Se (82)	-	0.018	-	3,439.	16,177.	777,422.	17,152.	-	-	-	-
Rb (85)	-	0.002	-	1,905.	138,863.	76,975,599.	185,395.	-	-	-	-
Sr (88)	0.001	0.	0.	14,970.	1,568.	107,695,587.	2,014.	-	-	-	-
Zr (90)	-	0.	-	2,097.	980.	30,129,605.	1,076.	-	-	-	-
Nb (93)	-	0.	-	0.	1,862.	45,784,237.	2,569.	-	-	-	-
Mo (98)	-	0.001	-	1,352.	1,340.	14,983,508.	1,319.	-	-	-	-
Ag (107)	0.013	0.	0.	91,628.	2,603.	18,748,499.	3,912.	-	-	-	-
Sn (120)	0.002	0.001	0.	21,237.	10,686.	46,937,034.	24,722.	-	-	-	-
Sb (121)	0.005	0.002	0.	52,306.	31,928.	43,072,044.	61,876.	-	-	-	-
Cs (133)	0.001	0.	0.	15,362.	1,176.	112,268,129.	1,667.	-	-	-	-
Ba (138)	0.001	0.	0.	15,134.	261.	94,271,334.	555.	-	-	-	-
W (182)	0.001	0.	0.	5,891.	261.	22,008,031.	139.	-	-	-	-
Au (197)	0.004	0.	0.	18,879.	196.	1,262,812.	222.	-	-	-	-
Pb (208)	0.08	0.	0.	1,217,578.	4,085.	76,077,957.	3,334.	-	-	-	-

Sample: VCN4S3 9-P18.txt
Date: 03/17/2015 05:03
Internal Standard: Na
Standard Method: Microthermometry
Region: 112.0 : 117.5 seconds

Host Correction Factor: -
Wt % NaCl eq: 0.9

Element	Con. (ppm)	LOD (ppm)	Weight %	Sample (cps)	Bkg (cps)	Std (cps)	Bkg (cps)	Mix (ppm)	Host (ppm)	Known (ppm)	Diff (%)
Li (7)	0.235	0.061	0.	1,007,500.	8,792,632.	24,183,134.	12,943,434.	-	-	-	-
B (11)	0.014	0.013	0.	24,336.	67,584.	7,668,210.	140,390.	-	-	-	-
Na (23)	0.871	0.011	0.	10,693,687.	2,310,735.	##########	3,380,019.	-	-	-	-
Mg (25)	-	0.042	-	18,224.	195,634.	4,491,183.	168,413.	-	-	-	-
Si (28)	1,451.977	0.061	0.88	4,083,432,581.	3,775,273.	##########	15,132,498.	-	-	-	-
K (39)	0.219	0.017	0.	2,805,176.	7,587,972.	68,239,032.	7,525,607.	-	-	-	-
Ca (40)	0.136	0.008	0.	1,845,702.	1,588,148.	##########	1,317,980.	-	-	-	-
Sc (45)	0.337	0.008	0.	6,395,824.	2,795,594.	90,800,839.	4,135,481.	-	-	-	-
Mn (55)	0.005	0.004	0.	76,078.	502,123.	79,835,790.	589,369.	-	-	-	-
Fe (56)	0.298	0.003	0.	3,817,352.	201,419.	66,000,020.	229,117.	-	-	-	-
Cu (63)	0.011	0.011	0.	47,132.	219,038.	19,478,354.	201,508.	-	-	-	-
Zn (66)	0.056	0.007	0.	141,663.	40,654.	13,108,979.	75,904.	-	-	-	-
As (75)	0.009	0.004	0.	17,975.	8,562.	7,745,645.	10,383.	-	-	-	-
Se (82)	-	0.018	-	3,439.	16,177.	777,422.	17,152.	-	-	-	-
Rb (85)	-	0.002	-	1,905.	138,863.	76,975,599.	185,395.	-	-	-	-
Sr (88)	0.001	0.	0.	14,970.	1,568.	107,695,587.	2,014.	-	-	-	-
Zr (90)	-	0.	-	2,097.	980.	30,129,605.	1,076.	-	-	-	-
Nb (93)	-	0.	-	0.	1,862.	45,784,237.	2,569.	-	-	-	-
Mo (98)	-	0.001	-	1,352.	1,340.	14,983,508.	1,319.	-	-	-	-
Ag (107)	0.013	0.	0.	91,628.	2,603.	18,748,499.	3,912.	-	-	-	-
Sn (120)	0.002	0.001	0.	21,237.	10,686.	46,937,034.	24,722.	-	-	-	-
Sb (121)	0.005	0.002	0.	52,306.	31,928.	43,072,044.	61,876.	-	-	-	-
Cs (133)	0.001	0.	0.	15,362.	1,176.	112,268,129.	1,667.	-	-	-	-
Ba (138)	0.001	0.	0.	15,134.	261.	94,271,334.	555.	-	-	-	-
W (182)	0.001	0.	0.	5,891.	261.	22,008,031.	139.	-	-	-	-
Au (197)	0.004	0.	0.	18,879.	196.	1,262,812.	222.	-	-	-	-
Pb (208)	0.08	0.	0.	1,217,578.	4,085.	76,077,957.	3,334.	-	-	-	-

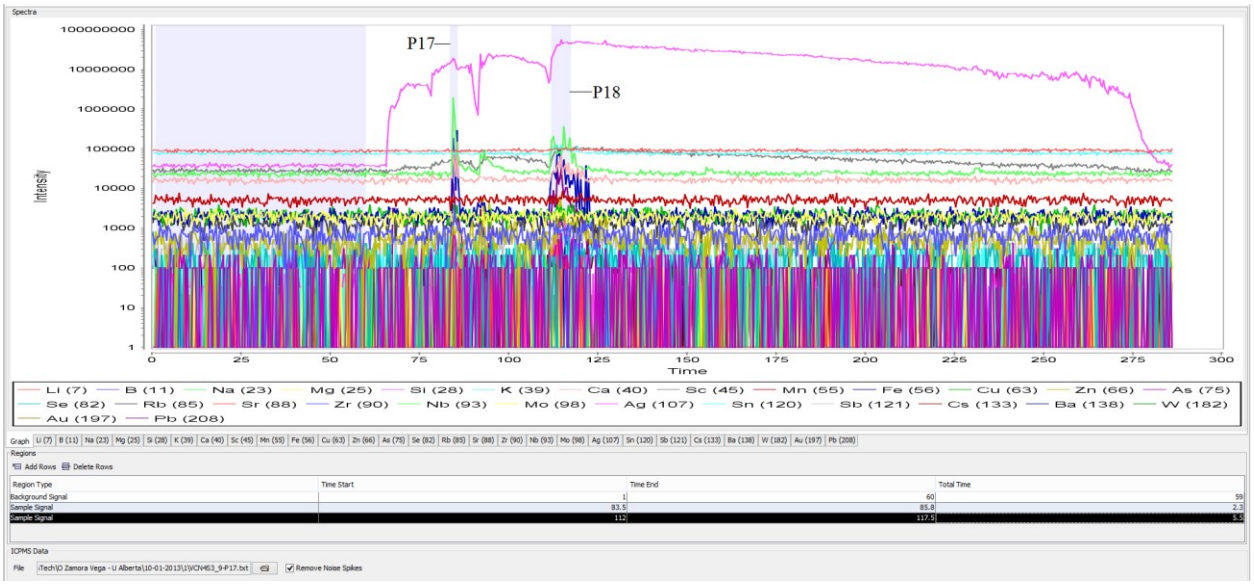
Spectra
P17
P18
Intensity
Time
Li (7) B (11) Na (23) Mg (25) Si (28) K (39) Ca (40) Sc (45) Mn (55) Fe (56) Cu (63) Zn (66) As (75)
Se (82) Rb (85) Sr (88) Zr (90) Nb (93) Mo (98) Ag (107) Sn (120) Sb (121) Cs (133) Ba (138) W (182)
Au (197) Pb (208)
Graph
Regions
Add Rows
Delete Rows
Region Type
Time Start
Time End
Total Time
Background Signal
Sample Signal
Sample Signal
ICPMS Data
File
Remove Noise Spikes